

**Development of a New Hybrid Photochemical/
Electrocatalytic Water Splitting Reactor for Hydrogen
Production: Design, Analysis and Experiments**

By

EHSAN BANIASADI

A Thesis Submitted in Partial Fulfillment
of the Requirements for the degree of Doctor of Philosophy
in
Mechanical Engineering

Faculty of Engineering and Applied Science
University of Ontario Institute of Technology

Oshawa, Ontario, Canada, 2012

© Ehsan Baniasadi

Development of a New Hybrid Photochemical/ Electrocatalytic Water Splitting Reactor for Hydrogen Production: Design, Analysis and Experiments

By

EHSAN BANIASADI

Supervisory Committee

1. **Dr. Ibrahim Dincer**, Supervisor (Faculty of Engineering and Applied Science, University of Ontario Institute of Technology)
2. **Dr. Greg F. Naterer**, Co-Supervisor (Faculty of Engineering and Applied Science, Memorial University of Newfoundland)
3. **Dr. Alan Fung**, External Member (Department of Mechanical and Industrial Engineering, Ryerson University)
4. **Dr. Franco Gaspari**, External Member (Faculty of Science, University of Ontario Institute of Technology)
5. **Dr. Bale Reddy**, Faculty Member (Faculty of Engineering and Applied Science, University of Ontario Institute of Technology)
7. **Dr. Zhaolin Wang**, Faculty Member (Faculty of Engineering and Applied Science, University of Ontario Institute of Technology)
7. **Dr. Ramiro Liscano**, Chair (Faculty of Engineering and Applied Science, University of Ontario Institute of Technology)

Abstract

Solar-driven water splitting combines several attractive features for sustainable energy utilization. The conversion of solar energy to a type of storable energy has crucial importance. An alternative method to hydrogen production by solar energy without consumption of additional reactants is a hybrid system which combines photochemical and electro-catalytic reactions. The originality of this research lies in the engineering development of a novel photo-catalytic water splitting reactor for sustainable hydrogen production, and verification of new methods to enhance system efficiency.

The scope of this thesis is to present a thorough understanding of complete photo-catalytic water splitting system performance under realistic working conditions. In this dissertation, an experimental apparatus for hydrogen and oxygen production is designed and built at UOIT to simulate processes encountered in photo-catalytic and electro-catalytic water splitting systems. The hybridization of this system is investigated, and scale-up analysis is performed based on experimental data using a systematic methodology. The hydrogen production rate of approximately 0.6 mmol h^{-1} corresponds to a quantum efficiency of 75% is measured through illumination of zinc sulfide suspensions in a dual-cell reactor. Utilization of ZnS and CdS photo-catalysts to simultaneously enhance quantum yield and exergy efficiency is performed. The production rate is increased by almost 30% as compared with ZnS performance.

In the next step, an oxygen production reactor is experimentally investigated to simulate processes encountered in electro-catalytic water splitting systems for hydrogen production. In this research, the effects of ohmic, concentration and activation losses on the efficiency of hydrogen production by water electrolysis are experimentally investigated. The electrochemical performance of the system is examined by controlling the current density, temperature, space, height, and electrolyte concentration. The experimental results show that there exists an optimum working condition of water electro-catalysis at each current density, which is determined by the controlling parameters. A predictive mathematical model based on experimental data is developed, and the optimized working conditions are determined.

The oxygen evolving half-cell is also analyzed for different complete systems including photo-catalytic and electro-catalytic water splitting. An electrochemical model is developed to evaluate the over-potential losses in the oxygen evolving reaction and the effects of key parameters are analyzed. The transient diffusion of hydroxide ions through the membrane and bulk electrolyte is modeled and simulated for improved system operation.

In addition, a new seawater electrolysis technique to produce hydrogen is developed and analyzed from energy and exergy points of view. In this regard, the anolyte feed after oxygen evolution to the cathode compartment for hydrogen production is examined. An inexpensive and efficient molybdenum-oxo catalyst with a turn-over frequency of 1,200 is examined for the hydrogen evolving reaction. The electrolyte flow rate and current density are parametrically studied to determine the effects on both bulk and surface precipitate formation. The mixing electrolyte volume and electrolyte flow rate are found to be significant parameters as they affect cathodic precipitation.

Furthermore, a new hybrid system for hydrogen production via solar energy is developed and analyzed. In order to decompose water into hydrogen and oxygen without the net consumption of additional reactants, a steady stream of reacting materials must be maintained in consecutive reaction processes, to avoid reactant replenishment or additional energy input to facilitate the reaction. Supramolecular complexes $[\{(bpy)_2Ru(dpp)\}_2RhBr_2](PF_6)_5$ are employed as the photo-catalysts, and an external electric power supply is used to enhance the photochemical reaction. A light-driven proton pump is used to increase the photochemical efficiency of both O_2 and H_2 production reactions. The maximum energy conversion of the system can be improved up to 14% by incorporating design modification that yields a corresponding 25% improvement in exergy efficiency.

Moreover, a photocatalytic water splitting system is designed and analyzed for continuous operation on a large pilot-plant scale. A Compound Parabolic Concentrator (CPC) is presented for the sunlight-driven hydrogen production system. Energy and exergy analyses and related parametric studies are performed, and the effect of various parameters are analyzed, including catalyst concentration, flow velocity, light intensity, reactor surface absorptivity, and ambient temperature. Two methods of photo-catalytic water splitting and solar methanol steam reforming are investigated as two potential solar-based methods of catalytic hydrogen production. The exergy efficiency, exergy destruction, environmental impact and sustainability index are investigated for these systems, as well as exergo-environmental analyses. The results show that a trade-off exists in terms of exergy efficiency improvement and CO_2 reduction of the photo catalytic hydrogen production system. The exergo-economic study reveals the maximum hydrogen exergy price of 2.12, 0.85, and 0.47 \$ kg^{-1} for production capacities of 1, 100, and 2000 ton day^{-1} , respectively. These results are well below the DOE 2012 target and confirm the viability of this technology.

Acknowledgements

I would like to express my sincere gratitude to my supervisors, Prof. Ibrahim Dincer and Prof. Greg Naterer, for giving me the great opportunity to work on this interesting subject at UOIT. I also appreciate their unwavering guidance, steady encouragement, and support throughout my PhD study.

I would like to sincerely thank all my committee members, Dr. Franco Gaspari, Dr. Bale Reddy, Dr. Zhaolin Wang, Dr. Alan Fung, and Dr. Ramiro Liscano for their valuable time in reading this thesis and providing comments to improve it further. Also, I thank the UOIT ESL specialist, Mrs. Catherin Lee, for her valuable time in proofreading this dissertation.

I would also like to extend my thanks to all my colleagues at the Clean Energy Research Laboratory (CERL), especially Dr. Calin Zamfirescu and Mr. Edward Secnik for their kind attention, and helpful suggestions throughout these years. Also, I like to acknowledge the solar hydrogen production group members Mr. Ron Roberts, Mr. Musharaf Rabbani, and Mr. Rafay Shamim for their assistance during this research.

Furthermore, the financial support by the Phoenix Canada Oil Company Ltd. and the Natural Sciences and Engineering Research Council of Canada (NSERC) is gratefully acknowledged.

Last but not least, I would like to express my eternal gratitude to my parents for their consistent support throughout my life. I would like to acknowledge my appreciation of my wife for her patience, understanding, and positive inspiration during my PhD study.

Contents

Abstract	iii
List of Tables	x
List of Figures	xi
Nomenclature	xix
Chapter 1: Introduction	1
1.1 Clean energy sources	1
1.2 Motivation	3
1.3 Scope of research and objectives	4
1.4 Thesis outline	6
Chapter 2: Background	8
2.1 Solar water splitting	8
2.2 Photoelectrochemistry of water splitting	10
2.3 Heterogeneous photo-catalysis	12
2.4 Homogeneous Photo-catalysis	14
2.5 Design and scale-up of photo-reactors for photo-catalytic water splitting	15
2.5.1. Parabolic trough reactors	16
2.5.2. Inclined plate collectors	17
2.5.3. Optical fiber photo-reactors	19
2.5.4. Optical fiber photo-reactors	19
Chapter 3: Literature Review	21
3.1 Photo-catalytic water splitting	22
3.2 Photoelectrochemical water splitting	24
3.3 Photocathodes for hydrogen evolving reaction	26
3.4 Photo-anodes for oxygen evolving reaction	27
3.5 Electro-catalytic water splitting	28

3.6	Photocatalytic overall water splitting	30
3.7	Photo-reactors for photo-catalytic water splitting	32
	3.7.1. Photoelectrode configurations	32
	3.7.2. Dual-cell photo-reactor	33
3.8	Hydrogen production via seawater catalysis	34
3.9	Modeling of photo-catalytic hydrogen production process	35
Chapter 4: Experimental Apparatus and Methodology		37
4.1.	Photo-reactor in batch operation	37
4.2.	Dual-cell reactor for quasi-steady operation	40
4.3.	Integrated system setup	42
4.4.	Materials	43
4.5.	Electrolyte	43
4.6.	Membrane	44
4.7.	Oxygen evolving reaction electrodes	44
4.8.	Linear mode DC power supply	46
4.9.	TriSOL solar simulator	47
4.10.	Experimental methodology of photo-catalytic process	47
4.11.	Experimental apparatus and method for oxygen production reactor	48
4.12.	Uncertainty analysis of experimental data	49
Chapter 5: Conceptual Design and Scale-up Study		52
5.1	Conceptual designs	52
	5.1.1. Water splitting reactor-hybrid photochemical conversion of solar energy	52
	5.1.2. Dual-cell reactor for seawater electro-catalysis	54
	5.1.3. Conceptual design for large-scale continuous flow photo-reactor	55
	5.1.4. Exergo-environmental study of large-scale solar reactors	57
5.2	Scaling-up study	60
	5.2.1. Methodology	60
	5.2.2. Modeling of photo-reactor	62
	5.2.2.1. Light absorption model	62
	5.2.2.2. Fluid-dynamics model	64
	5.2.2.3. Intrinsic kinetic model	64
	5.2.2.4. Mass balance	64

5.3	Scale-up relationships and methods	65
5.3.1.	Scaling factors	65
5.3.2.	Scale-up methods	67
Chapter 6: Analysis and Optimization		69
6.1	Photo-catalytic hydrogen production	69
6.1.1.	Photo-catalysis and quantum efficiency models	70
6.2	Fitting rate data and thermodynamics	73
6.2.1.	Fitting CSTR data	74
6.2.2.	Fitting batch reactor data	75
6.3	Hybridization	75
6.3.1.	Utilization of electrodes instead of electron donors	75
6.3.2.	Use of multiple catalysts to utilize wide range of spectrum	76
6.4	Oxygen production reactor design	77
6.4.1.	Electrochemical cell model	77
6.4.2.	Mathematical modelling of mass transport	78
6.4.3.	Hydroxide ion transfer	79
6.4.4.	Effects of pH change	81
6.5	Electrochemical analysis of seawater electro-catalysis	81
6.6	Energy and exergy analyses	84
6.6.1.	Energy of solar radiation	85
6.6.2.	Energy radiation exchange at the reactor surface	86
6.6.3.	Exergy of solar radiation exchange	86
6.6.4.	Exergy of radiation exchange at a surface	87
6.6.5.	Energy balance for photo-reactor system	87
6.6.6.	Exergy balance for photo-reactor system	87
6.6.7.	Analyses of continuous flow photo-catalysis process	88
6.7	Environmental impact assessment	89
6.8	Exergo-economic study	90
Chapter 7: Results and Discussion		93
7.1	Experimental results of photo-catalytic water splitting	93
7.1.1.	Photo-reactor operation	93
7.1.2.	Dual-cell operation	96

7.1.3. Model validation	106
7.1.4. Dual-cell experiments with CdS catalyst	107
7.1.5. Hybridization of photocatalytic water splitting	110
7.1.6. Scale up results for photocatalytic reactor	114
7.2 Oxygen production reactor	119
7.2.1. Experimental study	119
7.2.2. Predictive model	122
7.2.3. Optimization of OER overpotential	123
7.2.4. Reaction-diffusion formulation	125
7.2.5. Oxygen evolving reactor overpotentials and ion diffusion	129
7.3 Performance of a water splitting reactor	136
7.3.1. Hybrid photochemical water splitting reactor	137
7.3.2. Conversion efficiency of light energy based on energy balance	146
7.3.3. Analysis of molecular molybdenum-oxo catalyst hydrogen production	149
7.3.3.1. Post-processing of controlled potential electrolysis (CPE) experiments	149
7.3.3.2. Electrical circuit analogy	152
7.3.3.3. Seawater electrolysis	153
7.3.3.4. Effects of pH change	155
7.3.3.5. Oxygen evolving reactor design	156
7.3.3.6. Electrolyte concentration	158
7.4 Electrochemical analysis of seawater electrolysis	159
7.5 Radiative heat transfer and catalyst performance	164
7.6 Exergo-environmental assessment results of continuous flow photo-reactor	171
7.6.1. Solar thermal methanol reforming	173
7.7 Exergo-economic study results of photo-catalytic water splitting plants	176
7.8 Comparison of electro-catalysis methods	182
Chapter 8: Conclusions and Recommendations	184
8.1 Conclusions	184
8.2 Recommendations for future research	190
References	191
Appendix I: Optimization method	210
Appendix II: Sample codes-simulation of hydrogen and oxygen evolution process	212

List of Tables

Table 1.2: A DOE roadmap for hydrogen economy transition (modified from [5]).	2
Table 4.1: Comparison of different metal electrodes for oxygen evolving reaction.	45
Table 4.2: Comparison of electrochemical prosperities of three OER electrodes.	46
Table 4.3: Precision and bias errors of measurement devices.	50
Table 4.4: Cumulative precision errors of measurements.	51
Table 5.1: Scale-up factors for tubular reactor operating with constant properties.	66
Table 5.2: Scale-up factors for tubular reactor operating with constant properties.	68
Table 6.3: Inputs and fitting parameters used in this study.	78
Table 7.1: Efficiencies of photo-catalytic water splitting using CdS catalyst.	110
Table 7.2: Geometry characteristics of Scaled up photo-reactor.	116
Table 7.3: Kinetic and physical characteristics of scaled-up photo-reactor.	117
Table 7.4: Productivity enhancement of scaled-up reactor with 2,000 W m ⁻² light intensity.	117
Table 7.5: Productivity enhancement of scaled-up reactor with 5,000 W m ⁻² light intensity.	118
Table 7.6: Productivity enhancement of scaled-up reactor with 10,000 W m ⁻² light intensity.	118
Table 7.7: Optimization results for J = 150 mA cm ⁻² , ΔC = 2% (w/v).	124
Table 7.8: Optimization results for J = 300 mA cm ⁻² , ΔC = 2% (w/v).	125
Table 7.9: Input values and parameters.	127
Table 7.10: Comparison between experimentally and theoretically obtained efficiencies for the photo-catalysis of water.	146
Table 7.11: Comparison of HER over-potentials of different metal electrodes and catalysts.	152
Table 7.12: Comparison of electrochemical properties of three OER electrodes.	158
Table 7.13: Inputs and fitting parameters used in this study.	161
Table 7.14: Cost assessment assumptions and intermediate results.	178
Table 7.15: Economic analysis results for cost of hydrogen (\$/kg).	182
Table 7.16: Comparison of different technologies of water electrolysis.	183

List of Figures

Figure 1.1: Technical routes for solar-to-hydrogen conversion.	2
Figure 1.2: A flowchart of the accomplished objectives.	5
Figure 2.1: Technical routes for solar-to-hydrogen conversion; STCH: Solar Thermochemical, CST: Concentrating Solar Thermal.	8
Figure 2.2: Analogy of the photocatalytic water splitting (artificial photosynthesis) with photosynthesis of the green plants.	9
Figure 2.3: Basics of photocatalytic water splitting: (a) Photo-excitation and subsequent processes on catalyst surface (b) Photo-excitation and electron-hole generation.	10
Figure 2.4: General configurations for photo-catalytic water splitting; (a) electrode-based, and (b) particle-based.	11
Figure 2.5: (a) Heterogeneous photo-catalysis mechanism, (b) Reduction reaction	13
Figure 2.6: Relationship between band structure of semiconductor and redox potentials of water splitting (modified from [23]).	14
Figure 2.7: Homogeneous photo-catalysis process with complex molecular structure.	14
Figure 2.8: Reflector profile and typical reactor layout for a (a) parabolic trough reactor and (b) compound parabolic collector (modified from [25]).	17
Figure 2.9: A reactor layout for an inclined plate collector (modified from [25]).	18
Figure 3.1: Schematic representation of homogeneous multi-electron photo-catalysis for light-driven water splitting.	22
Figure 3.2: Photochemical scheme for H ₂ fuel production from H ₂ O using [{(bpy) ₂ Ru(dpp)} ₂ RhBr ₂] ⁵⁺ photo-initiated electron collector (modified from [70]).	24
Figure 3.3: Diagram of required potential for photochemical water splitting at pH = 0: (a) single semiconductor system; (b) dual semiconductor system (z scheme) using a redox shuttle (modified from Ref [73]).	25
Figure 3.4: Proposed electrocatalytic cycle for water reduction to release hydrogen and	29

hydroxide anions (modified from [10]).	
Figure 3.5: Sketch of the dual-cell for photocatalytic water splitting, with separate H ₂ and O ₂ evolution (modified from [116]).	30
Figure 3.6: Photo-electrode arrangements for photoelectrochemical water splitting (modified from [133]).	33
Figure 3.7: Schematic of a dual-cell photoreactor (modified from [133]).	33
Figure 4.1: Schematic of the experimental photo-reactor apparatus.	38
Figure 4.2: Experimental setup for photo-reactor measurements [185].	40
Figure 4.3: Experimental apparatus for photo-catalytic water reduction with zinc sulfide.	41
Figure 4.4: Experimental apparatus for photo-catalytic water reduction with cadmium sulfide.	41
Figure 4.5: Integrated system setup for photo-catalytic water splitting.	42
Figure 4.6: Integrated water splitting system with illuminated zinc sulfide suspensions.	43
Figure 4.7: Linear mode DC power supply.	46
Figure 4.8: TriSOL solar simulator.	47
Figure 4.9: Experimental apparatus for electro-catalytic water splitting.	49
Figure 5.1: Schematic of water splitting photochemical reactor with external power source.	53
Figure 5.2: Photoreactions based on reductive and oxidative quenching of the photo-excited [Ru(bpy) ₃] ^{2+*} .	54
Figure 5.3: (a) Seawater electro-catalysis system and (b) modified seawater electro-catalysis system.	55
Figure 5.4: Pilot plant scale hybrid photo-reactor for continuous operation, under sunlight and artificial illumination.	56
Figure 5.5: Schematic of hybrid photo-reactor.	56
Figure 5.6: Pilot plant scale hybrid photo-catalytic system for continuous operation, under sunlight and artificial illumination.	58

Figure 5.7: Schematic of solar thermal hydrogen production by methanol steam reforming.	60
Figure 5.8: Scale-up methodology.	61
Figure 5.9: Schematic representation of light distribution in (a) externally illuminated cuboidal photo-reactor, (b) externally illuminated cylindrical photo-reactor, I_0 , incident light intensity; I , light intensity inside the photo-reactor; L , Length of photo-reactor; D , diameter of the cylindrical photo-reactor.	63
Figure 6.1: Schematic illustration of the possible reactions resulting from the irradiation of zinc sulfide in a sodium sulfide solution, H,L: heat and light due to electron-hole recombination.	70
Figure 6.2: Hybridization method for photo-catalytic hydrogen production.	76
Figure 6.3: Schematic representation of the oxygen evolving half-cell.	80
Figure 7.1: Effect of ZnS concentration on hydrogen production (Uncertainty $\pm 3.1\%$).	94
Figure 7.2: Effect of light intensity on hydrogen production (Uncertainty $\pm 3.5\%$).	95
Figure 7.3: Effect of sacrificial agent concentration on hydrogen production for ZnS 2% w/v- $I = 1000 \text{ W m}^{-2}$ (Uncertainty $\pm 3.4\%$).	96
Figure 7.4: Polarization curve for catalyst aqueous solution (Uncertainty $\pm 2\%$).	97
Figure 7.5: Amount of hydrogen and oxygen evolved versus illumination time for ZnS concentration 1.5% w/v and light intensity 1000 W m^{-2} (Uncertainty $\pm 3.6\%$).	98
Figure 7.6: Amount of hydrogen and oxygen evolved versus illumination time for ZnS concentration 3% w/v and light intensity 1000 W m^{-2} (Uncertainty $\pm 4.1\%$).	98
Figure 7.7: Amount of hydrogen and oxygen evolved versus illumination time for ZnS concentration 1% w/v and light intensity 900 W m^{-2} (Uncertainty $\pm 4.3\%$).	99
Figure 7.8: Amount of hydrogen evolved versus illumination time for light intensity of 1000 W m^{-2} and different catalyst concentrations (Uncertainty $\pm 4.3\%$).	100
Figure 7.9: Amount of hydrogen evolved versus illumination time for light intensity of 900 W m^{-2} and different catalyst concentrations (Uncertainty $\pm 4.8\%$).	100
Figure 7.10: Dissolved gas ratio versus time for ZnS concentration 3% w/v and light intensity 1000 W m^{-2} (Uncertainty $\pm 4.9\%$).	101

Figure 7.11: Effect of ZnS concentration on Hydrogen production rate.	102
Figure 7.12: Effect of light intensity on hydrogen production rate (Uncertainty \pm 3.6%).	103
Figure 7.13: Effect of ZnS concentration on quantum efficiency.	103
Figure 7.14: Effect of ZnS concentration on energy and exergy efficiency.	104
Figure 7.15: Effect of light intensity on quantum efficiency.	105
Figure 7.16: Effect of light intensity on energy and exergy efficiency.	105
Figure 7.17: Measured (solid dots) and predicted (solid line) values of hydrogen production rate versus catalyst concentration.	106
Figure 7.18: Measured (solid dots) and predicted (solid line) values of hydrogen production rate versus light intensity.	107
Figure 7.19: Amount of hydrogen and oxygen evolved versus illumination time for CdS concentration 1% w/v, and light intensity 1000 W m^{-2} (Uncertainty \pm 4.9%).	108
Figure 7.20: Effect of CdS concentration on hydrogen production (Uncertainty \pm 3.9%).	109
Figure 7.21: Effect of light intensity on hydrogen production (Uncertainty \pm 4.1%).	109
Figure 7.22: Hybrid utilization of solar spectrum.	111
Figure 7.23: Productivity of ZnS and CdS catalysts in stand-alone and mixture operation (Uncertainty \pm 3.99%).	111
Figure 7.24: Amount of hydrogen and oxygen evolved versus illumination time for ZnS 1% w/v mixed with CdS 1% w/v at light intensity of 1000 W m^{-2} (Uncertainty \pm 4.91%).	112
Figure 7.25: Effect of catalytic hybridization on hydrogen production for different ZnS concentrations.	113
Figure 7.26: Effect of catalytic hybridization on hydrogen production for different light intensities.	114
Figure 7.27: Estimation of kinetic parameters n (a) and m (b) for photo-catalytic hydrogen production.	115

Figure 7.28: OER over-potential versus current density for $H = 1.5$ cm, $S = 1$ cm.	119
Figure 7.29: OER over-potential versus current density for $H = 1.5$ cm and $S = 1.5$ cm.	120
Figure 7.30: OER over-potential versus temperature for different electrode distances.	120
Figure 7.31: Effect of concentration gradient and electrode height on electrochemical performance (at working conditions $T = 300$ K, $S = 1$ cm, $J = 250$ mA cm ⁻²).	121
Figure 7.32: OER overpotential contours at different concentration gradients and current densities (at working conditions $T = 350$ K, $H = 5$ cm, $S = 10$ mm).	122
Figure 7.33: OER overpotential contours at different electrode distances and current densities (at working conditions $J = 250$ mA cm ⁻² , $T = 350$ K, $H = 5$ cm).	123
Figure 7.34: OER overpotential contours at different electrode distances and electrode heights (at working conditions $J = 250$ mA cm ⁻² , $T = 350$ K, $\Delta C = 2\%$ w/v).	123
Figure 7.35: Schematic representation of electrode surface processes.	125
Figure 7.36: Time-dependent spatial variation of hydroxide ion concentration ($k = 0.01$ M ⁻¹ s ⁻¹).	127
Figure 7.37: Time-dependent spatial variation of water concentration ($k = 0.01$ M ⁻¹ s ⁻¹).	128
Figure 7.38: Time-dependent spatial variation of charge carrier concentration ($k = 0.01$ M ⁻¹ s ⁻¹).	128
Figure 7.39: Time-dependent spatial variation of hydroxide ion concentration ($k = 0.001$ M ⁻¹ s ⁻¹).	129
Figure 7.40: Time-dependent spatial variation of water concentration ($k = 0.001$ M ⁻¹ s ⁻¹).	129
Figure 7.41: Time-dependent spatial variation of charge carrier concentration ($k = 0.001$ M ⁻¹ s ⁻¹).	129
Figure 7.42: Activation over-potential versus current density for graphite and nickel electrodes.	130
Figure 7.43: Activation over-potential versus current density at different temperatures.	131
Figure 7.44: Ohmic over-potential versus current density at different temperatures.	131
Figure 7.45: Concentration over-potential versus current density at different temperatures.	132

Figure 7.46: OER over-potential versus current density for different electrolyte concentrations.	132
Figure 7.47: OER over-potential versus electrolyte concentrations for different electrode-membrane distances.	133
Figure 7.48: Hydroxide ion diffusion between membrane and anode.	134
Figure 7.49: Hydroxide ion concentration at $t = 60$ s for different electric potentials.	134
Figure 7.50: Hydroxide ion concentration at $t = 60$ s for different current densities.	135
Figure 7.51: Energy efficiency of complete photo-catalytic system.	136
Figure 7.52: Energy efficiency of complete electro-catalytic system.	136
Figure 7.53: Equivalent schematic diagram of the electric circuit for water splitting reactors.	138
Figure 7.54: Schematic diagram of the light-induced proton pump across the lipid bilayer in a liposomic membrane. A molecular triad A-BC-D is symmetrically inserted in the lipid bilayer. A refers to acceptor, D for donor, and S for shuttle.	139
Figure 7.55: Effect of external electric potential on maximum energy conversion efficiency.	140
Figure 7.56: Energy efficiency and supplied electric energy versus external voltage.	141
Figure 7.57: Exergy efficiency and supplied electric energy versus external voltage.	142
Figure 7.58: Effect of external power supply on maximum energy efficiency.	143
Figure 7.59: Effect of external power supply on exergy efficiency.	143
Figure 7.60: Comparison between energy and exergy efficiencies for different water splitting methods.	145
Figure 7.61: Comparison between energy and exergy efficiencies for different photo-sensitizers.	145
Figure 7.62: Energy flow of the photo-catalytic system.	147
Figure 7.63: Energy efficiency of light based energy balance.	149
Figure 7.64: Exergy efficiency of photo-catalytic system.	149

Figure 7.65: Over-potential vs. current density for water electrocatalysis with 7.7 μ M solution of [(PY5Me ₂)MoO](PF ₆) ₂ .	151
Figure 7.66: System energy efficiency based on molybdenum-oxo function in HER.	152
Figure 7.67: Electrical circuit analogy of water electrolysis system.	153
Figure 7.68: Qualitative comparison of energy losses between MoO catalyst and alkaline electrolyser.	153
Figure 7.69: Over-potential versus current density for electrocatalysis of seawater in 7.7 μ M solution of [(PY5Me ₂)MoO](PF ₆) ₂ .	155
Figure 7.70: System energy efficiency based on molybdenum-oxo function in HER of seawater.	155
Figure 7.71: Effects of pH change on HER over-potential and energy efficiency of the electrolysis cell.	156
Figure 7.72: Energy and exergy efficiency of electrolysis cell with different OER electrodes.	157
Figure 7.73: Effect of electrolyte concentration on energy efficiency versus current density.	158
Figure 7.74: Polarization curve for the molybdenum-oxo catalyst at different pH differences.	159
Figure 7.75: Turnover frequency of molybdenum-oxo catalyst at different pH differences (Δ pH).	160
Figure 7.76: Turnover frequency of molybdenum-oxo catalyst at different salinities.	161
Figure 7.77: Anolyte flow rate required at different anodic pH values.	162
Figure 7.78: Magnesium hydroxide formation rate versus catholyte pH for different diameters.	163
Figure 7.79: Effect of electrolyte flow rate on total precipitate formation.	164
Figure 7.80: Effect of current density and concentration gradient on effective diffusion layer.	164
Figure 7.81: Energy and exergy efficiencies versus catalyst concentration.	165
Figure 7.82: Energy and exergy efficiencies of photo-reactor at different flow rates.	166

Figure 7.83: Distribution of exergy losses in the photo-reactor system.	167
Figure 7.84: Exergy efficiency variations for light absorptivity of catalyst.	167
Figure 7.85: Energy and exergy efficiencies of photo-reactor for different light intensities.	168
Figure 7.86: Energy and exergy efficiencies of photo-reactor for different ambient temperatures.	168
Figure 7.87: Exergy destruction ratios of photo-reactor at different ambient temperatures.	169
Figure 7.88: Variation of exergy destruction ratio by flow rate.	170
Figure 7.89: Variation of exergy destruction ratio by light intensity.	170
Figure 7.90: Energy and exergy efficiencies of photo-reactor for different mixed-metal supramolecular complexes.	171
Figure 7.91: Exergy efficiency versus catalyst concentration at different ambient temperatures.	172
Figure 7.92: Exergy efficiency and CO ₂ emissions reduction of water splitting photo-reactor.	173
Figure 7.93: Exergy destruction rate and sustainability index of water splitting photo-reactor.	173
Figure 7.94: Mass flow and exergy rate of solar-thermal methanol reforming for hydrogen production.	174
Figure 7.95: Exergy efficiency variations versus mole ratio of water and methanol.	175
Figure 7.96: CO ₂ emissions variations versus mole ratio of water and methanol.	175
Figure 7.97: Exergy efficiency and CO ₂ emissions of photo-catalytic methanol steam reforming.	176
Figure 7.98: CO ₂ emissions of photo-catalytic methanol steam reforming at different feeding rates.	176
Figure 7.99: Hydrogen exergy cost versus production capacity for different insolation.	182

Nomenclature

A	Surface area (m^2)
b	Tafel slope (mV dec^{-1})
c	Cost per unit of exergy ($\$ \text{GJ}^{-1}$)
C	Molar concentration (mol dm^{-3})
\dot{C}	Cost rate ($\$ \text{kg}^{-1}$)
d	Catalytic active centre thickness (m); Diameter (m)
D	Diffusion coefficient ($\text{m}^2 \text{s}^{-1}$)
De	Reactor equivalent diameter (m)
\bar{e}	Molar specific energy (kJ kmol^{-1})
$\bar{e}x$	Molar specific exergy (kJ kmol^{-1})
ex	Specific exergy (kJ kg^{-1})
E	Thermodynamic voltage (V); Electric field ($\text{kg m s}^{-3} \text{A}^{-1}$)
Ex	Exergy (kJ)
$\dot{E}x_s$	Exergy rate of solar radiation (W m^{-2})
En	Energy (kJ)
$\dot{E}n_s$	Energy rate of solar radiation (W m^{-2})
f	Proportionality factor
F	Faraday constant (C mol^{-1})
\bar{g}	Molar specific Gibbs free energy (kJ kmol^{-1})
G	Gibbs function (kJ)
Gz	Graetz number
H	Electrode height (m)
h	Specific enthalpy (kJ kg^{-1}); Liquid level height (m)
\bar{h}^0	Molar specific enthalpy at reference state (kJ kmol^{-1})
\bar{h}_f^0	Molar specific enthalpy of formation (kJ kmol^{-1})
\bar{h}	Molar specific enthalpy (kJ kmol^{-1})
h_{con}	Convective heat transfer coefficient ($\text{kW m}^{-2} \text{K}^{-1}$)
i	Electric current (A)
I	Light intensity (W m^{-2})
j	Current density (A m^{-2})

j_0	Exchange current density ($A\ m^{-2}$)
j_L	Limiting Current density ($A\ m^{-2}$)
J	Ion flux ($mole\ cm^{-2}$)
k	Specific conductivity ($\mu S\ cm^{-1}$); Rate constant ($M^{-1}\ s^{-1}$)
K	Monochromatic intensity of radiation ($kW\ m^{-3}\ srd^{-1}$)
L	Length (m)
\dot{m}	Mass flow rate ($kg\ s^{-1}$)
\mathcal{M}_{GHG}	Carbon mitigation factor ($kg\ kWh^{-1}$)
n	Charge career
\dot{n}	Molar flow rate ($mole\ s^{-1}$)
p	Pressure (Pa)
P	Power (W); Product
q	Heat flux ($kW\ m^{-2}$)
\bar{q}	Molar specific reaction heat ($kJ\ kmol^{-1}$)
Q	Heat (kJ); Flow rate ($m^3\ s^{-1}$)
r	Reaction rate ($M\ s^{-1}$)
R	Universal gas constant ($J\ mol^{-1}\ K^{-1}$); Reactant; Radius (m)
Re	Reynolds number
Rv	Revenue ($\$ day^{-1}$)
R^2	Coefficient of determination
\bar{s}^0	Molar specific entropy at reference state ($kJ\ kmol^{-1}\ K^{-1}$)
\bar{s}	Molar specific entropy ($kJ\ kmol^{-1}\ K^{-1}$)
s	Specific entropy ($kJ\ kg^{-1}\ K^{-1}$)
S	Electrode space (cm); scaling factor
\dot{S}_{gen}	Entropy generation rate ($kW\ K^{-1}$)
\dot{S}_λ	Entropy rate of the monochromatic intensity of radiation ($kW\ m^{-3}\ K^{-1}\ srd^{-1}$)
Sc	Schmidt number
Sh	Sherwood number
t	Time (s)
tn	Transport number
\bar{t}	Mean residence time (s)
t_{el}	Thickness (m)
T	Temperature (K, °C)

\bar{u}	Average velocity (m s^{-1})
U	Over-potential (V); Voltage (V)
v	Velocity (m s^{-1})
V	Volume (m^3)
w	Width (m)
W	Work (J)
x	Distance (m)
z	Elevation (m); Valence number
\dot{Z}	Cost rate of owning and operating cycle ($\text{\$ kg}^{-1}$)

Greek Letters

α	Transfer coefficient; absorptivity ($\text{cm}^2 \text{g}^{-1}$)
Λ	Absorption coefficient averaged over the spectrum (m^{-1})
γ	Radiation weakening factor; activity coefficient
ε_b	Stefan–Boltzmann radiation constant ($\text{W m}^{-2} \text{K}^{-4}$)
δ	Diffusion layer
η	Efficiency
λ	Wavelength (m)
ζ	Radiosity (kW m^{-2})
ξ	Henry constant ($\text{dm}^3 \text{bar mol}^{-1}$)
μ	Dynamic viscosity ($\text{kg m}^{-1} \text{s}^{-1}$)
μ_{OH^-}	Hydroxide ion mobility ($\text{cm}^2 \text{V}^{-1} \text{s}^{-1}$)
ρ	Density (kg m^{-3})
σ	Specific mass scattering coefficient ($\text{cm}^2 \text{g}^{-1}$)
τ	Time factor (s)
ω	Rotational velocity (rev s^{-1}); scattering albedo coefficient
Ψ	Medium mass attenuation coefficient ($\text{cm}^2 \text{g}^{-1}$)
φ	Incident energy fraction
ϕ	Quantum

Subscripts & Superscripts

0	Environments
act	Activation

ads	Adsorbed
av	Average
b	Bulk
c	Conversion
C	Capital investment
ch	Chemical
con	Concentration
conv	Convection
e	Electron
EC	Electrochemical
EL	Electrical
eff	Effective
el	Electrolyte
en	Energy
enc	Encounter
em	Emission
et	Electron transfer
ex	Exergy
gen	Generation
init	Initial
L	Loss
ls	Large scale
M	Maintenance
nv	Non-visible wavelength range
ohm	Ohmic
PC	Photo-catalytic
ph	Physical/photon
R	Radius
Rev	Reversible
s	Surface
S	Solar
ss	Small scale
t	Total
thc	Thermochemical

UV	Ultraviolet
v	Visible wavelengths range (400-700 nm)
w	Water

Acronyms

AC	Annual capital cost ($\$ \text{ year}^{-1}$)
AT	Annual hydrogen production capacity (ton year^{-1})
CF	Concentration factor
CPC	Compound parabolic concentrator
CRF	Capital recovery factor
CSTR	Continuous stirred-tank reactor
CT	Carbon taxation ($\$$)
ED	Electron Donor
FIT	Feed-in-tariff factor (¢ kWh^{-1})
HER	Hydrogen Evolving Reaction
IF	Incentive factor ($\text{¢ kg}^{-1} \text{ H}_2$)
ir	Interest rate (%)
LHV	Lower Heating Value (kJ mol^{-1})
LOF	Land occupancy factor
LT	Life time (years)
HHV	Higher heating value (kJ mol^{-1})
OER	Oxygen Evolving Reaction
OL	Optical losses (%)
PW	Present worth ($\$$)
PWF	Present worth factor
RCD	Relative Cost Difference ($\$$)
SF	Scaling factor
SI	Sustainability index
SS	Sum of squares
TDS	Total dissolved solids (mg L^{-1})
TLA	Total land area (ha)
TOF	Turnover frequency (s^{-1})

Chapter 1

Introduction

1.1. Clean energy sources

Conventional fossil fuel energy resources, which are used to meet most of the world's energy requirements, have been depleted to a great extent. Almost all resources of green energy involve variation, regional, or seasonal limitations. Following the quick rise in world energy demand, the consumption of chemicals, materials, and fuels is an increasing necessity for each society. It is therefore necessary to produce an alternative fuel that should be pollution-free, storable, and economical. Recent global climate changes have raised many concerns and led to extensive research and development on alternative, clean energy sources. Hydrogen is envisioned as an attractive candidate for a clean, sustainable fuel and underpins the intense interest in creating artificial systems that use catalysts which are based on the Earth's abundant elements to achieve efficient hydrogen production from water [1-3].

With respect to hydrogen economy, hydrogen has emerged as the ideal energy carrier to store and distribute renewable energy resources. One of the most reliable ways of utilizing solar energy is to convert and store it in the form of an energy carrier such as hydrogen. This valuable chemical compound can be utilized in fuel cell or combustion engine facilities to generate power or heat with zero carbon emission, providing water as a reusable by-product.

Today, electricity is the principal energy carrier and will be still considered as a remarkable commodity in the long term future. However, the promising role of hydrogen as a complementary carrier in large scale storage and long distance distribution should not be ignored. The U.S. Department of Energy (DOE) has proposed a roadmap for the transition to a hydrogen economy, as illustrated in Table 2.1.

Currently, the industry market demand for hydrogen is more than 5,000,000 kg consumption per year [4]. The low density, high thermal conductivity and strong chemical reducing properties make hydrogen the major applicant for industries, including the chemical production, semiconductor processing, and generator cooling. The current application of hydrogen to upgrade conventional petroleum products, large-scale ammonia and methanol

production, and production of pharmaceuticals is quickly rising. As the global population continues to increase, the demand for hydrogen will significantly increase.

Table 1.1: A DOE roadmap for hydrogen economy transition (modified from [5]).

		Hydrogen Industry Segments				
	Public Policy Framework	Production process	Delivery	Storage Technologies	Conversion Technologies	End-Use Energy Market
2000	<ul style="list-style-type: none"> • Security • Climate • H₂ Safety 	Natural gas reforming/ biomass	<ul style="list-style-type: none"> • Pipeline • Trucks, rail, garages 	Pressurized tanks	Combustion	<ul style="list-style-type: none"> • Fuel reforming • Portable power
2010		Gasification of coal				
2020	↓ Outreach & acceptance	Electrolysis using renewables and nuclear	Onsite distributed facilities	Solid state (hydrides)	<ul style="list-style-type: none"> • Fuel cells • Advanced combustion 	<ul style="list-style-type: none"> • Stationary distributed power • Government fleets
2030	Public confidence in hydrogen gas as an energy carrier	Thermo-chemical water splitting				
2040		Photo catalytic water splitting	Integrated central distributed network	Mature technologies for mass production Solid state	Mature technologies for mass production	<ul style="list-style-type: none"> • Commercial fleets • CHPs Utility systems

To meet the rising demands, current H₂ production technologies based on fossil fuel conversions are mainly in use. Steam reforming of natural gas supplies almost 50% of the global demand for hydrogen, oil/naphtha reforming in refinery industries provides about 30%, and the rest is mainly produced by coal gasification, and water electrolysis. Steam reaction with methane at a high temperature as a high efficiency method, known as steam methane reforming (SMR), is highly invested in North America [6].

The common methods of hydrogen production impose several concerns regarding fossil fuel sources declination, CO₂ emission, and ecological impacts. Subsequently, all the downstream industries that consume hydrogen involve the aforementioned drawbacks and risks. Therefore, H₂ production technologies with almost zero greenhouse gas emissions are the ideal candidates to address the hydrogen supply issue. In one approach, biomass gasification can be utilized to release hydrogen and carbon monoxide. Considering the CO₂ adsorption characteristics during a photosynthesis process, this method is basically carbon neutral. Alternatively, water electrolysis using renewable power sources, such as geothermal, wind, and solar cells, can be utilized.

1.2. Motivation

The emerging concerns regarding energy security, and the maintenance of our global ecosystem, has kindled the search for efficient and environment friendly processes that are economical and practical for large-scale production of hydrogen. Hydrogen is distinguished as an important energy carrier to supply future energy demands. However, the production process of hydrogen should have sustainability attributes such as low or no associated greenhouse gas emissions, affordability, and availability. Hydrogen is found chemically in bound form on the Earth. However, the bond should be broken into element form to be useful as an energy carrier. Therefore, a sustainable source of energy is required as an input to the consequence of the chemical reaction energies for obtaining unbound hydrogen.

Natural gas steam reforming and electrolysis are the major routes of hydrogen production on a large-scale. The thermochemical water splitting process is also being improved through transition status to a complete renewable based hydrogen technology. The fossil-fuel-based hydrogen is not environmentally benign and does not satisfy low greenhouse gas emissions criteria. In order to avoid the environmental damages and depletion of fossil-fuel resource, hydrogen has to be produced from water, and clean energy sources.

Among the viable renewable hydrogen production technologies, photo-catalytic water splitting is known as one of the most intriguing, yet still one of the immature approaches. A photo-catalytic system consists of solar energy harnessing and splitting water in a single semiconductor-based device. The solar energy can be directly converted into electrochemical energy for water splitting, by immersing a semiconductor device in a water-based solution. However, to meet the practical criteria, the semiconductor material must efficiently absorb sunlight and generate electron-hole pairs to sustain the hydrogen and oxygen gas evolution reactions on the catalyst surface. Furthermore, the stability of the photo-catalyst in the solution should be sufficiently high, and it should be cost-effective to be suitable for large-scale deployment.

Solar water splitting appears to be one of the most effective solutions of today's crucial energy, environmental and sustainability issues. While the use of photochemical and catalytic hydrogen production systems is widespread, the feasibility of these techniques at scaled up production rates is uncertain. Photo initiated and economic photo-catalysts, such as zinc sulfide and cadmium sulfide [7-8], should be investigated. Investigation of the performance of a solar reactor for heterogeneous water splitting is the main interest of this research. A homogenous photo-catalytic water splitting system based on supramolecular complexes such as $\{[(bpy)_2Ru(dpp)]_2 2RhBr_2\}(PF_6)_5$ [9], and also efficient catalysts such

as $[(\text{PY5Me}_2)\text{MoO}](\text{PF}_6)_2$ [10] for electro-catalysis is also considerable. There is little research available to guide regulatory agencies and industry towards designs and installations of photo-catalytic hydrogen production systems that maximize their sustainability and minimize possible energy and exergy losses.

1.3. Scope of research and objectives

The general aim of the ongoing studies into photo-catalytic hydrogen production is to overcome the lack of knowledge of engineering scale-up and to enhance system efficiency to ensure further development and commercialization. In this view, there is a necessity to assess the uncertainties of the light distribution and mass transfer inside a photo-reactor to develop scale-up methodologies based on the illuminated surface area of catalysts in liquid-phase photo-catalysis. Therefore, the scope of this thesis is focused on experimental evaluation, modeling, and scale-up analysis of a complete photo-induced water splitting system with emphasis on engineering challenges.

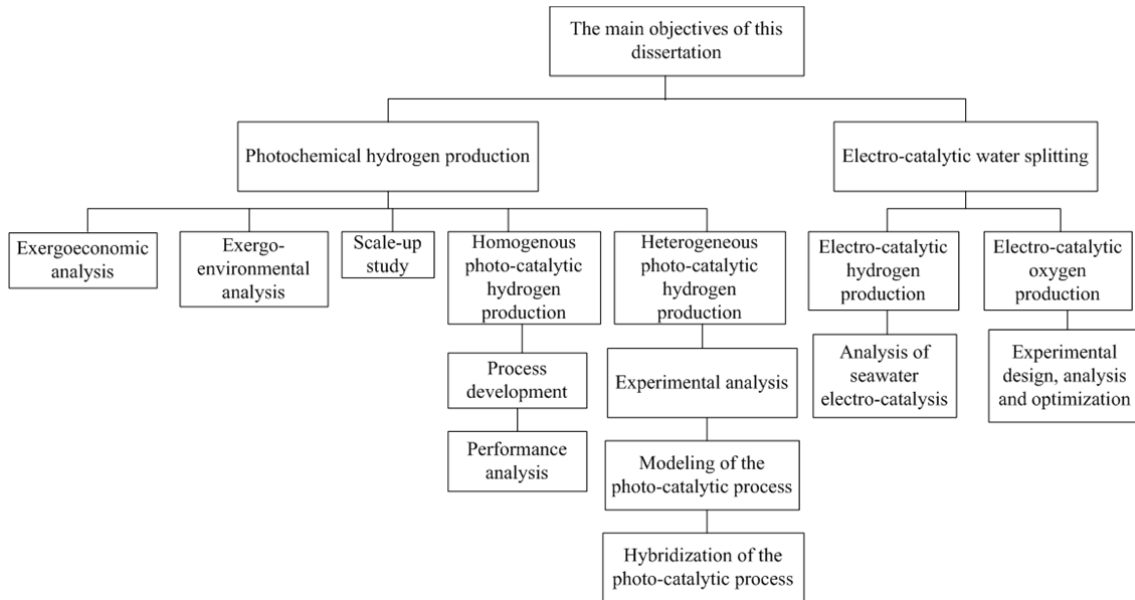
Most previous studies on photo-catalytic hydrogen production have focused on either chemical processes of photo-catalyst fabrication or modeling of radiation fields in photo-reactors. Design and scale-up analysis of a photo-reactor for water splitting requires a comprehensive analysis to integrate all various aspects of photo-induced hydrogen production complexity from the radiation field to kinetic reactions to charge transfer kinetics and diffusion. This type of analysis requires experimental and mathematical methods to gather enough information for a complete system of water splitting which is functional, economically feasible, and scalable for mass production.

In this regard, the characteristics of a complete water splitting system, including photo-catalytic hydrogen evolution and electro-catalytic oxygen evolution, are examined. For each half cell, a number of parameters exists that affect the performance of the system and the resultant effect should be considered in an engineering design. The intra-molecular charge transfer and ionic diffusion in the hydrogen production reactor are directly affected by light intensity, and photocatalyst concentration. In the case of an oxygen evolution reactor, however, electrolyte concentration, electrode and membrane performance, and temperature affect the limiting over-voltage parameter. Hybridization of a photo-catalytic water splitting system, through alternative approaches to enhance the productivity rate and prevent replenishment of intervening chemicals, is crucial.

In essence, the specific objective of this thesis is to analyze the photo-electrochemistry of a solar water splitting system to address some of the design and scale-up

challenges of such a system from an engineering stand point and enhance the understanding of complex physical and chemical phenomena occurring inside the photo-reactor. The accomplished objectives of this research are shown in Figure 1.2.

Figure 1.2: A flowchart of the accomplished objectives.



More explanations are provided as follows:

- (a) Performance analysis of the homogeneous photo-catalytic water splitting reactor based on $[(bpy)_2Ru(dpp)]_2RhBr_2(PF_6)_5$ photo-catalyst and also electrochemical performance of seawater electro-catalysis for hydrogen production by the molybdenum-oxo catalyst.
- (b) Experimental design, analysis, and optimization of an oxygen production reactor. The analysis is mostly based on a modeling of ion diffusion and energetic performance of the hydroxide decomposition process.

The oxygen production reactor is investigated through several individual experiments to evaluate the effects of reaction overpotential on the efficiency of hydrogen production. The electrochemical performance of the system is examined by controlling the current density, temperature, space, height, and electrolyte concentration; thus the optimized working conditions are determined. A predictive mathematical model is developed to simulate the dominant processes involved in hydrogen and oxygen production.

- (c) Experimental analysis of photo-catalytic water splitting using zinc sulfide and cadmium sulfide in a batch and dual-cell (quasi-steady operation) reactor to investigate the effect of radiation intensity, and photo-catalyst concentration on hydrogen and oxygen production rate.

The main objective of this analysis is to pursue an engineering approach toward development, analysis, and scale up of a photo-catalytic water splitting system to produce hydrogen and oxygen in separate manifolds. Considering all the ambiguities that are involved in a photo-induced diffusion process, any design and modeling step includes several unknown coefficients that should be derived by experiments. In this regard, an experimental hydrogen and oxygen production reactor is designed and built to perform photo-catalytic and electro-catalytic water splitting processes. Photocatalytic hydrogen evolution using zinc sulfide and cadmium sulfide is tested in the dual-cell reactor to verify the effect of light intensity and catalyst concentration as the main influential parameters in the photo-induced diffusion reaction.

- (d) Comparison of experimental results with a theoretical model that is derived from the kinetics and quantum processes of photo-catalytic water splitting reaction.

Following the experimental steps, all the results are evaluated for possible uncertainties and compared with theoretical results. The validated results provide important details and serves as the foundation to extract specific correlations that are utilized in this scale-up study. MATLAB software is used for mathematical workloads, developing an optimization routine, as well as regression analysis to obtain a good fit to a set of experimental measurements.

- (e) Hybridization of the photo-catalytic process using multi catalysts and electric potential bias to enhance the productivity of the reactor and sustain the reaction rate.

- (f) Scale-up analysis of the dual-cell photo reactor based on a kinetic and radiation model and mass balance of reactants.

- (g) Thermodynamic study and greenhouse gas emissions assessment of photo-catalytic conversion of light energy in terms of energy and exergy efficiencies to investigate the solar radiation characteristics and catalyst performance of a large-scale continuous flow photo-reactor.

Energy and exergy efficiency analysis as an effective method to elucidate the deficiencies of the photo-catalytic water splitting process is utilized. The analysis is further extended to evaluate the performance of a continuous flow photo-reactor with large scale production capacity.

- (h) Exergo-economic analysis of photo-catalytic water splitting plants with different production capacities is performed to provide detailed information on the economic aspects of the engineered hydrogen production process.

1.4. Thesis outline

This thesis is organized into seven chapters and two appendices.

Chapter 2 presents the corresponding background, including an introduction to solar hydrogen production and related photo-catalytic processes.

Chapter 3 includes a comprehensive literature review on the existing technologies of photo-catalytic hydrogen production and related details with regard to their achievements and future prospects.

Chapter 4 introduces the system description of experimental and theoretical analysis accomplishments of this thesis. It contains all the introductory information that is taken into account during this research.

Chapter 5 explains the conceptual designs and scale-up study methodology which are followed for analysis of photo-catalytic water splitting process.

Chapter 6 contains the detail information about design and modeling of the hydrogen and oxygen production systems. The main assumptions and theoretical procedure are included.

Chapter 7 explains the results of experimental and theoretical analysis of the system with corresponding discussions.

Chapter 8 summarizes the conclusions and some recommendations for future work.

The optimization routine and modeling codes for both mathematical and thermodynamic assessments are presented in the appendices.

Chapter 2

Background

2.1. Solar water splitting

Water as the most available source on the earth is one of the major sources of hydrogen. Various procedures may be utilized to extract hydrogen including electrolysis, photolysis, water purification, etc. Hydrogen production from water splitting requires two molecules of water to donate four-valence electrons to the oxygen nucleus and protons in a general reaction according to: $2\text{H}_2\text{O} \rightarrow 2\text{H}_2 + \text{O}_2$. This process consumes at least 4.92 eV of energy to generate 1 molecule of oxygen and two molecules of hydrogen. Additionally, a hydrogen separation method should be utilized to distinct a pure hydrogen and oxygen stream [11-12].

Among various water splitting technologies, water electrolysis is more maturely developed. Water splitting via sunlight to produce hydrogen can be achieved through several conversion routes, as shown in Figure 2.1. However, more progress with regard to efficiency improvement and water impurities is required. The energy required for water splitting can be supplied through thermal, electrical, photonic, and biological sources plus hybridization of these possibilities [13-14].

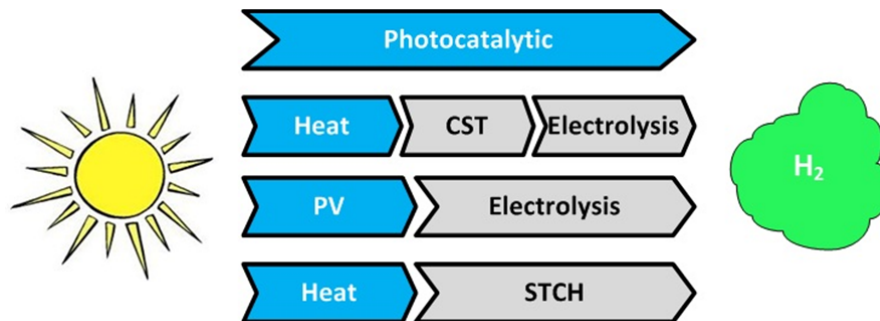


Figure 2.1: Technical routes for solar-to-hydrogen conversion; STCH: Solar Thermochemical, CST: Concentrating Solar Thermal

High-temperature direct thermo-electrolysis of water ($> 2500\text{ K}$) [15], and lower-grade thermal energy thermochemical methods (below 1000 K) are mainly developed to split the water molecule and separate the products by conducting a series of chemical reactions through intermediate compounds [16]. Photonic radiation can be used in several routes to split the water molecule, either through photolysis or in hybrid manner such as photoelectrochemical processes.

As shown in Figure 2.1, the so-called solar thermochemical (STCH) approach triggers by a photon-to-thermal conversion step followed by a thermal-to-chemical process. In another two-step route, photon-to-electric process initiates the process and an electric-to-chemical conversion step accomplishes afterward. The concentrating solar thermal (CST) electrolysis pathway comprises three steps of photon-to-heat, heat-to-electricity, and electric-to-chemical conversions. The direct process of photon-to-chemical conversion, so-called photo-electrochemical, is another alternative pathway.

Hydrogen and electricity play a key role as effective energy carriers in the future of energy economics. Therefore, the hydrogen production routes such as PV-electrolysis and CST-electrolysis that implement both could be more beneficial. Recent progresses in science indicate the viability of producing inexpensive electricity and hydrogen using semiconductors in near future. The high energy losses associated with the multistep conversion pathways of the aforementioned techniques has to be treated in a way. From this perspective, the single-stage techniques such as photo-catalysis could be beneficial in terms of minimum process irreversibilities (Figure 2.2). The direct conversion processes for hydrogen production, as one of the most promising alternatives, mimics photosynthesis to absorb light and convert water into H_2 and O_2 using inorganic semiconductors through water-splitting reaction [17].

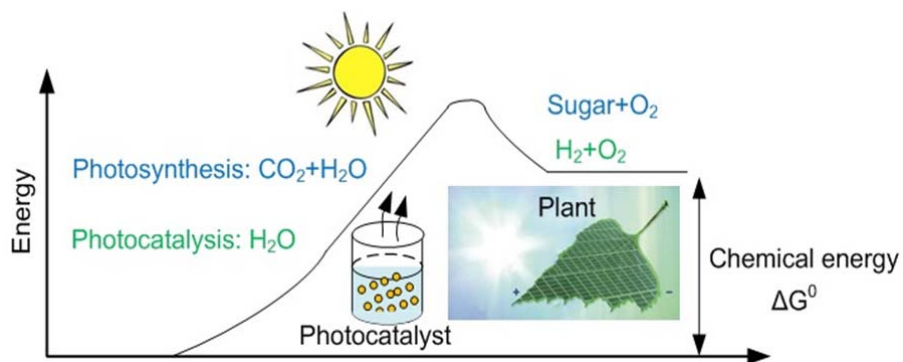


Figure 2.2: Analogy of the photocatalytic water splitting (artificial photosynthesis) with photosynthesis of the green plants.

The pioneering efforts by Fujishima and Honda [18] in 1972 on the semiconductors, that are capable of absorbing light energy, introduced this type of materials as effective means of water splitting reaction for hydrogen generation. Since then, numerous studies are undertaken to develop various types of semiconductors for photo-catalytic water dissociation and to enhance their performance under visible light by more efficient utilization of the solar spectrum [19-20].

2.2. Photoelectrochemistry of water splitting

The possibility to transmit energy to every point of a volume using photonic radiation is applicable to water cleavage process. Since pure water does not absorb radiation in the visible and near-ultraviolet ranges, the dissociation of water is technically possible by either electromagnetic rays, e.g. exposing water to higher-frequency radiation such as extreme UV, X and gamma rays, or using molecular photosensitizers dissolved/suspended in water, to capture the solar radiation in the visible and UV ranges. The latter approach constitutes important paths for solar driven water splitting. In this regard, the interaction of photonic radiation with photo-catalyst and water molecules is important for technology development.

The theoretical potential for water splitting process is 1.23 eV per molecule. This energy corresponds to the wavelength of 1,010 nm that makes about 70% of the solar irradiated photons eligible for deriving water cleavage reaction. However, the amount of the energy per photon should be higher than the minimum value of 1.23 eV in order to compensate the intrinsic energy losses associated with the redox reactions on the surface of the photo-catalyst [21].

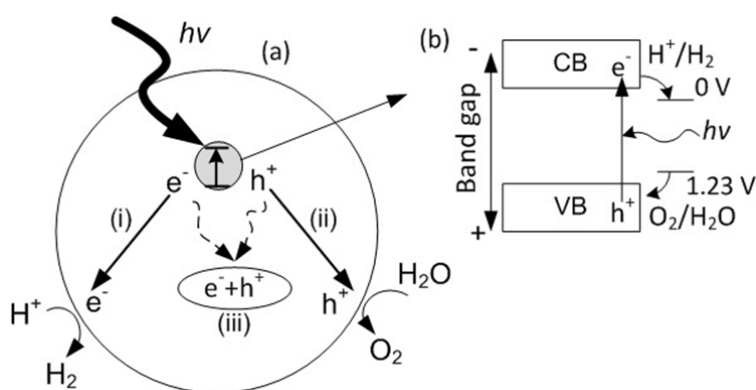


Figure 2.3: Basics of photocatalytic water splitting: (a) Photo-excitation and subsequent processes on catalyst surface (b) Photo-excitation and electron-hole generation.

The photo-catalytic water splitting is initiated with the absorption of light photons with energies higher than the band-gap energy (E_g) of a semiconductor. As depicted in Figure 2.3, following the absorption process excited photoelectrons are generated in the conduction band (CB) and holes in the valence band (VB) of the semiconductor. Once the photo-excited electron-hole pairs are created in the material bulk, they migrate to the surface separately (represented by routes i and ii).

This process is in continuous competition with the electron-hole recombination process (route iii in Figure 2.3) that leads to heat generation. Eventually, the water molecules in vicinity of catalytic active sites are reduced and oxidized by photo-induced electrons and holes to produce gaseous hydrogen and oxygen, respectively. The decomposition of water into H_2 and O_2 requires a large positive change in the Gibbs free energy ($\Delta G_0=237 \text{ kJ mol}^{-1}$, 2.46 eV per molecule). The following reactions are performed in an acidic medium:



The water dissociation process refers to either half-processes such as water reduction to hydrogen and hydroxyl ions or water oxidation to oxygen and protons, or to the complete conversion of water to hydrogen and oxygen. The photochemical process of water splitting does not necessarily involve a complete water splitting process. Photo induced half-reactions to generate hydrogen mainly occur according to $[2H_2O + 2e^- \xrightarrow{h\nu} H_2(g) + 2OH^-]$ in alkaline medium. The hydroxide ion by-product can be further processed through electro-catalytic oxidation to generate oxygen.

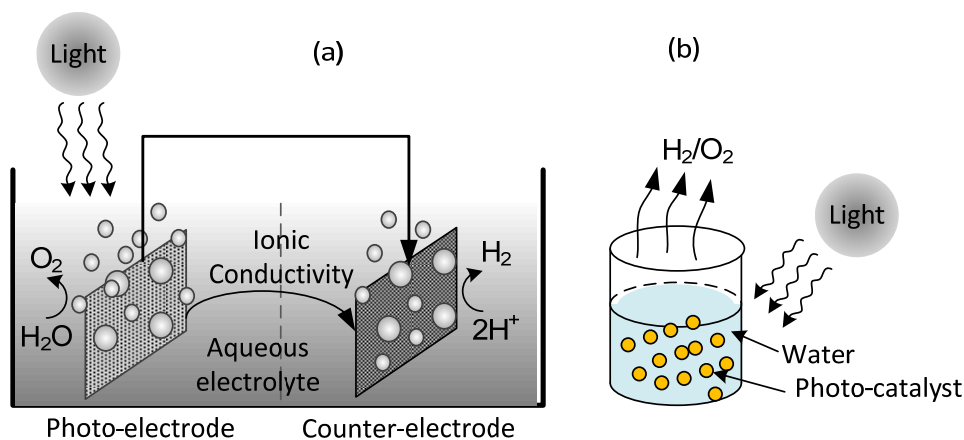


Figure 2.4: General configurations for photo-catalytic water splitting; (a) electrode-based, and (b) particle-based.

Two major configurations of photo-catalytic technique for water cleavage are electrode-based, and particle-based. The first method implements two electrodes immersed in an aqueous electrolyte, one is the semiconductor photo-catalyst exposed to light and the other is a counter-electrode to facilitate the electron flow circuit (Figure 2.4a). The second system is based on photo-catalysts in the form of suspended particles in an electrolyte (Figure 2.4b).

In this system, each particle acts as a micro-photo-electrode to conduct redox active sites for splitting water. In comparison, particle based configuration has some disadvantages with respect to electron-hole separation efficiency and reverse reaction of the products on the surface of the photo-catalyst, that leads to lower conversion rates. However, photo-catalysts in particle form have the advantage of much simpler and less expensive synthesise. Aside from these two configurations that undergo heterogeneous catalysis, another approach of homogenous catalysis based on interaction of complex molecular structures in a solution is also feasible.

2.3. Heterogeneous photo-catalysis

The photo-catalysts in solid phase implemented in reaction of water dissociation in liquid phase, is denoted as heterogeneous. These catalysts are applied in powder and electrode form. Photo-electrodes are widely being developed to enhance the efficiency of water catalysis. The photo-electrode structure consists of a conductive material such as noble metals doped with photo-catalysts. The conductivity of electrode material facilitates the migration of electrons from its conduction band to valence band and eventually to the active catalytic sites where water electrolysis is performed. The photo-electrodes in a photo-reactor configuration are exposed to solar radiation through transparent windows. Direct incident light together with electrical potential bias, supplied by an external electrical power supply, are utilized to activate active sites.

The small band gap between the valence and conduction bands of semiconductors make them suitable to develop heterogeneous photo-catalysis. Some semiconductors such as titanium dioxide have both photosensitization and photo-catalytic attributions. So when semiconductor is exposed to light, it absorbs photons and dislocates electrons from the valence band to the conduction band. It eventually facilitates redox reactions at the photo-catalyst surface. The performance of photo-catalysts is usually enhanced to overcome the redox potentials through two possible routes:

- (i) Applying a bias voltage to the electrode via an external power supply;
- (ii) Electrode coating or doping with photo-synthesizer materials.

The heterogeneous photo-catalysis process is illustrated in Figure 2.5. The reaction mechanism is introduced in Fig. 2.5a, and the reduction pathway is shown in Figure 2.5b, respectively. Following the light absorption and activation of catalytic sites heterogeneous catalysis occurs at the solid surface. The catalyst reduces the activation energy without being consumed. In order to quantify its ability of photo-catalyst to interact with reactant molecules the turnover number (TON) is defined as the number of reactants that are treated with catalyst before degradation. The turnover frequency (TOF) is also an indicative parameter that represents the number of converted reactants by photo-catalyst per unit of time.

A layer of ionized solvent molecules called Helmholtz layer hosts the electron transfer from the active site to the reactant molecules. This layer is adjacent to the solid-liquid interface with a thickness of 1 Å. The electrons migrate to the reacting molecules through the Helmholtz layer. The semiconductor has the same Fermi energy levels of Helmholtz layer, therefore the process of electron transfer is iso-energetic. The dislocated electron in the conduction band then falls into a lower energetic level to accomplish the reduction reaction (Figure 2.5a).

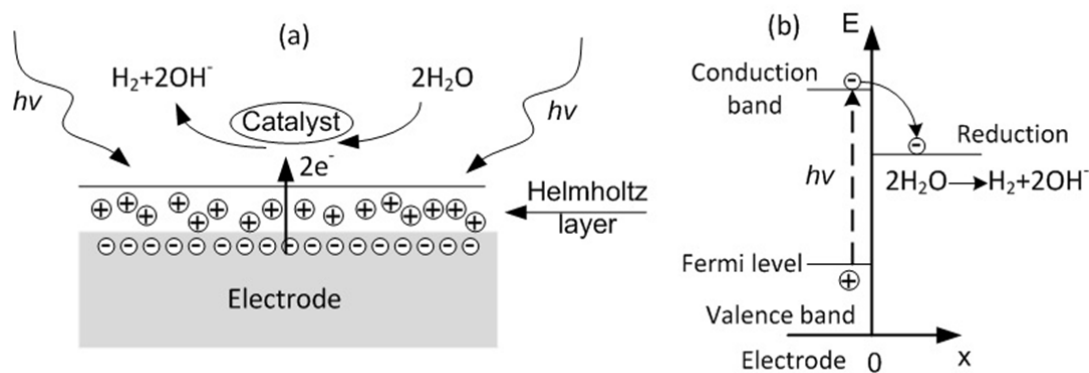


Figure 2.5: (a) Heterogeneous photo-catalysis mechanism, (b) Reduction reaction.

Figure 2.6 shows the band levels of various semiconductor materials. The pH of the solution usually changes the band levels by -0.059 V/pH for oxide materials. According to the information in Figure 2.6, ZrO_2 , $KTaO_3$, $SrTiO_3$ and TiO_2 have suitable band structures for water splitting. These materials are usually modified with co-catalysts to be active for water splitting.

The n-type semiconductors such as cadmium sulfide or zinc sulfide are recognized as potential photo-catalyst for large scale hydrogen production. However, they involve anodic

photo-corrosion in aqueous solutions that leads to the formation of sulfur and/or sulfate ions according to:



However, they are promising photo-catalysts for H₂ evolution under visible and ultra-violet light irradiation if reducing agents acting as hole scavengers, such as S²⁻, SO₃²⁻, or S₂O₃²⁻ exist in the aqueous solution to stabilize cadmium sulfide and zinc sulfide efficiently [22].

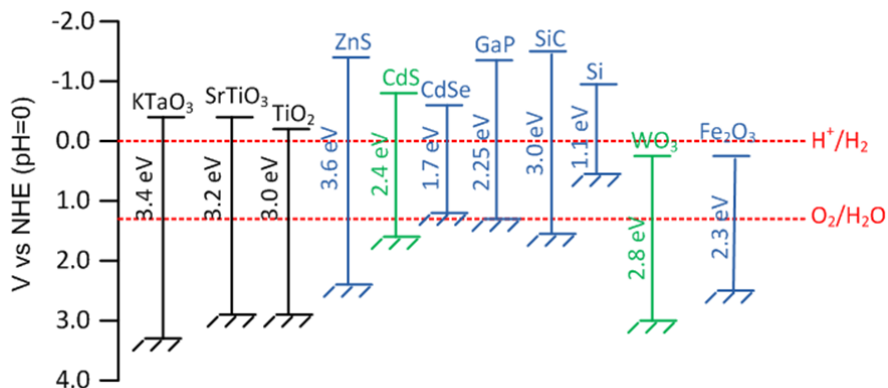


Figure 2.6: Relationship between band structure of semiconductor and redox potentials of water splitting (modified from [23]).

2.4. Homogeneous photo-catalysis

Homogeneous photo-catalysts consist of complex molecular structures that perform photo-catalytic water splitting starting from photosensitization. Subsequently, charge separation, charge transfer, and catalysis processes are conducted by the molecular structure. Figure 2.7 shows the process of homogeneous photo-catalysis for hydrogen-evolution.

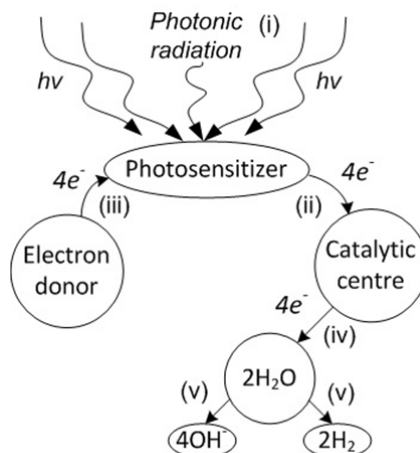


Figure 2.7: Homogeneous photo-catalysis process with complex molecular structure.

The series of events initiates with photon absorption of the photo-sensitizers that turns to its excited state. The excited state form of photo-sensitizer interacts with the catalyst and it translocates an electron to the active catalytic center. The photo-sensitizers returns to reactive state by absorbing an electron from the electron donor dissolved in the solution. The electron donor remains stable in the solution. Water reduction reaction is then accomplished by electron transfer through catalytic active centers. Four catalytic cycles are performed following four times photon absorption to complete a water dissociation reaction,

2.5. Design and scale-up of photo-reactors for photo-catalytic water splitting

Among industrial applications photocatalytic water splitting is limited due to process efficiency and the lack of knowledge on engineering scale-up. Comparing with conventional reactors, the design and scale-up of photo-reactors involve more complexity due to intervention of radiation transfer along with mass, momentum, and heat transfers. The catalysts in liquid-phase photocatalytic systems are either suspended or immobilized in reactors.

In general, the efficiency of suspended systems is higher than immobilized systems. However, the attenuation of light intensity through absorption and scattering by suspended particles creates a challenge from design stand point. This also makes difficulties to simulate the kinetic model and subsequently in the scale-up of reactors. The kinetic model of suspended systems cannot be extrapolated to another reactor size and configurations unless it accompanies an explicit light irradiation model. Dealing with radiation transfer in immobilized systems is quite simpler than suspended systems since absorption and scattering effects are not involved. Hence, the kinetic modeling and scale-up analysis of immobilized surface area of catalysts under illumination are simpler. Due to the uncertainties of the light and mass transfer effect, photo-reactor scale-up methodologies based on the illuminated surface area of catalysts in liquid-phase photo-catalysis are still immature.

In order to develop industrial photo-reactors, a device with high capability of capturing photons and bringing the reactants into contact with the photo-catalyst, as well collecting the reaction product should be designed. The critical importance of reactor geometry to ensure the effective collection of photons makes a significant difference between photo-reactors and traditional chemical reactors. Various aspects of photo-catalytic systems have been investigated, however, photo-reactor design has not been standardized and each research team in obeying individual designs. In fact, any performance difference is attributed to specific number of variables which differ between studies. The solar photo-reactors for

hydrogen production are mainly distinguished in either form of parabolic trough system, inclined plate collectors, optical fiber photo-reactors, and fluidized bed photo-reactors.

2.5.1. Parabolic trough reactors

Despite the significant difference between operational requirements of solar photo-reactors and solar thermal collectors, the well-established parabolic reflectors in solar thermal engineering can be implemented for efficient collection and absorption of photons on a specific area or volume of a solar photo-reactor. Adopting the solar thermal collector design, parabolic trough reactor is developed that consists of a long, reflective, parabolic surface to concentrate solar radiation on a transparent tube. This tube conveys reactant fluid flows and along the parabolic focal line. Since the surface area of the reflecting surface is essentially larger than absorber tube, the light intensity on the photo-catalyst is increases through concentration of the photons.

The direct concentration of sunlight onto the photo-catalyst creates both an advantage and disadvantage for parabolic trough reactors. The greatest benefit attributes to the increase of light intensity, which reduces the photo-catalyst consumption comparing to non-concentrating photo-reactors with the same light collecting area [24]. Consequently, it provides the capability of utilizing absorber tube with smaller diameters, greater operating pressures and higher quality materials without high increase of the capital investment.

Industrial-scale plants incorporate several absorber tubes and associated components with significant pressure losses. Therefore, the advantage of operating at higher pressures is accounted as a significant benefit. A reduction in the quantity of required photo-catalyst is in favour of reducing operating costs. It reduces particle agglomeration and simplifies the separation process and recycling of the suspended photo-catalyst as well as material handling requirements.

Utilization of compound parabolic collector overcomes some of the problems associated with parabolic trough reactors. The reflector geometry of these components has the advantage of reflecting the indirect light onto the absorber tube surface. There is a concentration factor associated with each compound parabolic collector according to:

$$CF = \frac{1}{\sin \theta_a} = \frac{w}{2\pi r} \quad (2.3)$$

where CF is the concentration factor, θ_a is the acceptance half angle, w is the width of the reflector aperture, and r is the radius of the absorber tube. Therefore, an acceptance half angle of 90° makes a concentration factor of 1 sun that means all direct and diffuse light entering

the aperture is reflected onto the absorber tube. Figure 2.8 shows the reflector profile of parabolic trough reactor and compound parabolic collector.

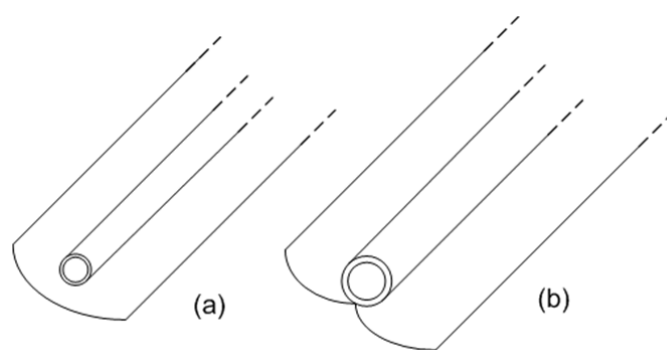


Figure 2.8: Reflector profile for (a) a parabolic trough reactor and (b) a compound parabolic collector.

This aperture increases the total quantity of photons comparing to a parabolic trough reactor and also provide the capability of working on cloudy days when direct light is unavailable. A parabolic trough reactor concentrates the light on the bottom hemisphere of the absorber tube, whereas compound parabolic collector distributes the incident light over the entire surface of the absorber tube homogeneously.

2.5.2. Inclined plate collectors

The main design considerations of the concentrating parabolic and non-concentrating compound-parabolic reactors have roots in commercial solar thermal technologies. The photo-catalytic processes based on these systems seems to be viable, it does not necessarily offer the optimal design. If a solar photo-catalytic reactor is designed specifically for convenient accommodation the photo-catalyst and maximizing the mass transfer between the photo-catalyst and the reactant fluid through effective illumination of the photo-catalyst higher efficiency than conventional parabolic reflecting reactors can be achieved.

An inclined plate collector is basically an assembly of a flat, inclined surface for thin film reactant fluid flows. This design in particular matches the supported photo-catalyst on the surface of the inclined plate. The photons essentially migrate through the reactant fluid and eventually reach the photo-catalyst. Different types of material can be used to fabricate the backing plate [26].

This design is extensively used in research facilities because of the relative simplicity, low cost materials, and suitability for supported photo-catalyst. It has the advantage of eliminating efficiency losses due to reflective surface in parabolic trough reactor and

compound parabolic collector. Although the lack of concentration of the incoming photons, does not allow capturing diffuse light. To further increase the efficiency the reactor may be fabricated with open face to the atmosphere to eliminate light adsorption by the reactor covering and prevent forming an opaque film by suspended photo-catalyst. The maximum diffusion thickness is essentially limited to the thickness of the film, and thin-fluid film enable the maximum mass-transfer rates between the different phases of the reactor [27]. Figure 2.9 illustrates a typical layout of an inclined plate reactor.

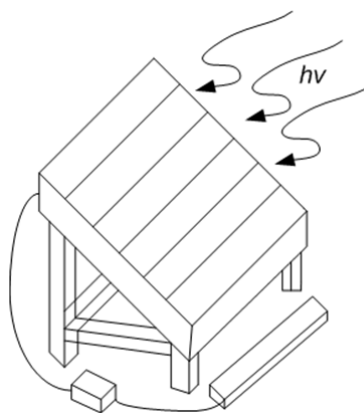


Figure 2.9: A reactor layout for an inclined plate collector (modified from [25]).

The effectiveness of inclined plate collectors at commercial scale is limited due to some practical drawbacks regarding the thin fluid film. The thin fluid film for this type of photo-reactors are typically in the range of 100-200 μm , that requires maintaining flow rates of about $0.15\text{-}1 \text{ L min}^{-1} \text{ m}^{-2}$ collection plate area. In contrast to parabolic trough reactor and compound parabolic collector, the reactant fluid is not enclosed over the surface, and adjusting the flow rate or pressurizing through an open surface plate cannot be easily handled. Increase of the flow rate causes decrease of the residence time of the reactant fluid on the collector plate which leads to increase of the fluid film thickness [28]. The mass-transfer constraint is then ignored and the efficiency of the reactor decreases. The use of a transparent covering may help in a way but it adsorb some photons and reduces the efficiency of the photo-reactor. There is also a potential for suspended solids to form an opaque solid film on the interior surface of the covering and enhance the photonic absorption.

The simplicity of inclined plate collector in fabrication, and design and their compatibility with a supported photo-catalyst makes them ideally suitable for small scale productions with low fluid volumes.

2.5.3. Optical fiber photo-reactors

The solar photo-reactors are basically designed to utilize an external light source. This introduces a drawback of effective access of photo-catalyst to light. In fact, light scattering and adsorption phenomenon by photo-catalyst suspensions makes it difficult to provide homogeneous external illumination, and also supported photo-catalysts with compacted surface areas require an un-obscured path for arriving light.

These issues can be addressed by accommodating artificial light sources within the reactor volume. This can be done either by direct immersion of lamp in the reactant fluid or install it within an inner annulus. In an alternative approach, an optical fiber can be implemented to conduct the light from an external light source into the fluid bulk of reactants. In these types of reactors, supporting the photo-catalyst on either the internal lamps or waveguides is superior to a suspended photo-catalyst because the surface area to volume ratios will be significantly enhanced. The implementation of optical fibers with artificial light has been well addressed [29].

Peill et al. has extensively investigated an optical fiber photo-reactor using a bundle of 537 quartz optical fibers at concentration point of a 24 in. parabolic dish with 3.5 in. convex secondary reflector. The fiber is coated with a photo-catalyst and immersed in the reactant fluid. This configuration provided almost 300 suns concentration factor at the entrance of the fiber bundle and lead to a two order-of magnitude reduction in 4 L of a 13 mg L⁻¹ solution of 4-chlorophenol during 13 h solar radiation [30].

The advantage of optical fiber photo-reactor over other photo-reactor designs is related to isolation of light gathering process from photocatalytic components of the reactor. This allows remote collecting the light and transmitting over a long distance through the optical fibers to the photo-reactor that contains solution of reactants and photo-catalyst. Therefore, this design is suitable for indoor facilities, providing appropriate light gathering device and connecting fiber optics. The mechanical complexity and low efficiency of these reactors compared to other photo-reactor designs limited wider application of this technology.

2.5.4. Fluidized and fixed bed photo-reactors

A hybrid approach in photo-catalyst handling is to support photo-catalyst particles on larger particles such as glass beads, to have both advantages of suspended and supported photo-catalysts. Supporting the photo-catalyst on packing materials provides high photo-catalyst surface areas and consequently high mass-transfer rates. Also, the separation process as in supported systems is not necessary anymore. Therefore, Fluidized and fixed bed photo-

reactors can effectively serve the gas-phase photoreactions due to the intensive interaction between the reactant and photo-catalyst particles.

The supporting particles or packing has a strong interaction with the incoming light, and leads to a heterogeneous radiation field within the reactor. The major portion of light is absorbed by the particles at around the edge of the photo-reactor within a relatively thin region, and results in poor illumination of the majority of the reaction volume. This effect varies depending on the void fraction and expansion of the bed.

Solar packed/fixed bed photo-reactors are relatively very common in use. Fluidized/fixed bed photo-reactors may introduce an optimal method of photo-catalyst handling as very high quantum efficiency is achievable using this technology [31]. However, the current status of fluidized/fixed bed reactors with solar radiation is limited. In fact, homogeneous illumination of particles throughout the fluidized bed volume is a significant challenge. This issue can be addressed by use of a compound parabolic collector at the exterior of the bed and use of internal reflectors or waveguides to provide homogeneous illumination. However, this configuration has not been investigated so far. The fluidized bed photo-reactors may be introduced as an effective option in water photo-catalysis if the challenges with regard to optimum particle size and photo-catalyst attachment methods are addressed.

Chapter 3

Literature Review

To be an economical and sustainable pathway, hydrogen should be produced from a renewable energy source, i.e. solar energy. Photo-catalytic water splitting is the most promising technology for this purpose, since H₂ could be obtained directly from abundant and renewable water and sunlight from the process. If successfully developed with economic viability, this could be the ultimate technology that could solve both energy and environmental problems altogether in the future [32-34].

Compared to hydrogen production methods based on fossil fuels, the high investment cost of solar hydrogen generation is a challenging issue. Production of hydrogen in a regenerative fashion such as photochemical splitting of water has been studied [35]. Photo-catalytic water splitting has been introduced as an efficient and cost effective way to produce hydrogen, in which sunlight is absorbed and water is split directly into hydrogen and oxygen. Many efforts in photo-catalytic water splitting is focused on increasing the efficiency and stability of the photoactive materials [36,37] to achieve the required efficiency target to be viable for commercialization [38].

The reductive side of this process requires the development of catalysts that promote the reduction of protons to molecular hydrogen, facilitated by direct excitation by a photo-sensitizer. Recently, molecular platinum- and palladium-based systems have been developed as heterogeneous catalysts [39-40]. Supramolecular complexes in a photo-catalytic hydrogen production scheme that results in high turnover rates and numbers are promising [41].

Catalytic hydrogen evolution from a neutral aqueous solution using hydrogenase enzymes that possess iron and/or nickel cofactors shows turnover frequencies of 100 to 10,000 moles of H₂ per mole of catalyst per second at their thermodynamic potential [42-44]. However, the large size of these enzymes and instability under aerobic, ambient conditions has encouraged new searches for alternative molecular complexes to produce H₂ from water in a non-biological setting. Despite the high catalytic activity of precious metals for water reduction at a low over-potential, the high cost challenged their widespread application.

Therefore, the main challenge in catalytic hydrogen production from water is to create Earth-abundant molecular systems with high catalytic activity and stability.

This review is focused on the efforts to develop water splitting devices in which the energy inputs, which are either sunlight and/or electricity, handle a catalytic hydrogen evolving reaction in an aqueous environment.

3.1. Photo-catalytic water splitting

The development of an energy scenario based on the use of two natural resources, water and sunlight, is a challenging solution to the energy crisis in the world. Conversion of solar energy into chemical energy through light-driven water splitting generates the environmentally benign oxygen gas and hydrogen, a carbon free fuel with the highest energy output relative to its molecular weight. Moreover, this approach provides an attractive solution for storing the tremendous amount of sunlight energy falling on earth. In that context, natural photosynthesis is a great source of interest for the scientific community. Light to chemical energy conversion is indeed achieved by photosynthetic organisms. As far as the energetic aspect is concerned, the photosynthetic process is a fascinating example of efficiency [45-46].

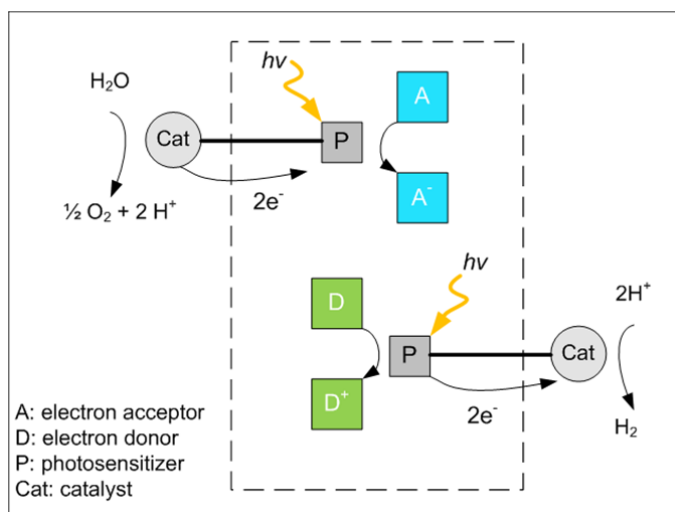


Figure 3.1: Schematic representation of homogeneous multi-electron photo-catalysis for light-driven water splitting.

Methods derived from natural photosynthesis are therefore highly attractive for the development of novel hydrogen production technologies. Understanding this biological process and exploiting this knowledge for designing original synthetic molecular systems

achieving light-to-chemical energy conversion is the basis of a large field of research called “artificial photosynthesis” [47-48]. Molecular light harvesting arrays have been developed to mimic the antennae effect, which is collecting energy of many photons to transfer it directionally to a final acceptor achieving charge separation. Dyad and triad models based on the association of a photosensitizer to either an electron donor or an electron acceptor or both components have been designed to reproduce light-induced spatial charge separation. These first two topics have been the core of artificial photosynthesis, and also the subject of comprehensive reviews [49-54].

Currently, research is often focused on the independent development of the two half-reactions, through the combination of a photosensitizer with a suitable catalyst for either the oxidation or the reduction of water, together with a sacrificial electron acceptor or donor, respectively (Figure 3.1). The efforts have also been devoted toward the synthesis of single-component photocatalysts, either by supramolecular assembly or by covalent linking of the light harvesting unit to the catalyst. This design can improve electron transfers between these two units and it is relevant to the spatially controlled assembly of the various photosynthetic components in the membrane, largely responsible for the efficiency of the natural photosynthetic process. Supramolecular complexes in a photocatalytic hydrogen production scheme that result in high turnover rates and numbers are an area of interest [55]. Supramolecular solar H₂ photocatalysts usually consist of Ru or a light absorption metal LA coupled to a metal-based catalyst including Pt, Pd, Rh, Co, bio-inspired di-iron dithiolates, or single-component dirhodium or Pt systems [56-58].

Encouraging results have been obtained by Fihri et al. [59-60], and Li et al. [61] with cobalt-based supramolecular photocatalysts including supramolecular photocatalysts for H₂ production based on cobaloxime centers. Some series of ruthenium-based photocatalytic assemblies has established that a conjugated bridge is not required for the activity. The long lived metal-to-ligand charge-transfer (MLCT) excited state of [Ru(bpy)₃]²⁺ has motivated photochemical and photophysical studies leading to light to energy conversion processes [62]. The MLCT excited state of [Ru(bpy)₃]²⁺ and its analogs have the required energy to split water into hydrogen and oxygen, but it requires complicated multi-component systems for operation.

Recently, progress has been achieved in H₂ production using homogeneous molecular catalysts powered by the sensitization of a molecular light absorber (LA) [63-66]. More recently, multicomponent systems have been identified that use Ir LAs with Rh catalysts or a Pt LA with a Co catalyst of 1000 ton in 10 hrs [67-69].

Brewer et al. [3,70] have developed photochemical water splitting catalysts using supramolecular devices, which are able to capture the incident solar radiation, and generate electrons or holes at the active centre where water reduction or oxidization occurs, respectively. Such systems mimic natural photosynthesis and mainly consist of supramolecular complexes of organic molecules which possess active metallic centers. Photo-initiated electron collection affords Rh species that provides reducing equivalents to H₂O to make H₂ fuel (Figure 3.2). They have reported a photo-catalytic system for H₂ production using the [$\{(\text{bpy})_2\text{Ru}(\text{dpp})\}_2\text{RhBr}_2\}^{5+}$] photo-catalyst, DMA, H₂O, and DMF solvent that provides a catalyst with 280 turnover number in 19.5 hours and maximum quantum efficiency of $\eta_\phi = 0.023$.

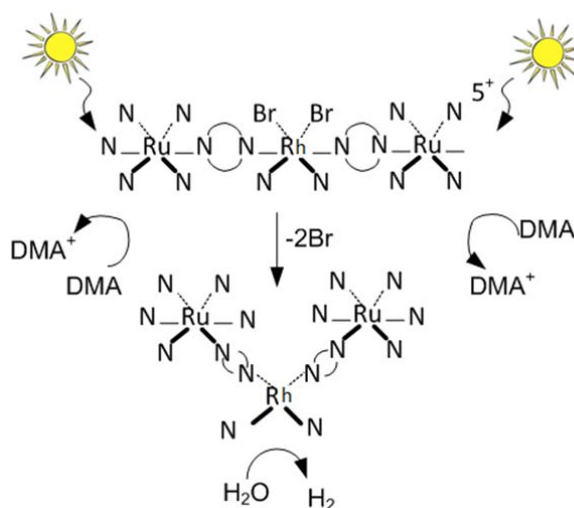


Figure 3.2: Photochemical scheme for H₂ fuel production from H₂O using [$\{(\text{bpy})_2\text{Ru}(\text{dpp})\}_2\text{RhBr}_2\}^{5+}$] photo-initiated electron collector (modified from [70]).

3.2. Photoelectrochemical water splitting

The free energy change for the conversion of one molecule of H₂O to H₂ and 1/2 O₂ under standard conditions is $\Delta G = 237.2$ kJ/mol, which, according to the Nernst equation, corresponds to $\Delta E^\circ = 1.23$ V per electron transferred. For photochemical water reduction to occur, the flat-band potential of the semiconductor (for highly doped semiconductors, this equals the bottom of the conductance band) must exceed the oxidation potential of water of +1.23 V vs NHE at pH = 0 (+0.82 V at pH = 7) (Figure 1.3a). A single band gap device requires, at a minimum, a semiconductor with a 1.6 to 1.7 eV band gap in order to generate the open circuit potential required to split water. Once other voltage-loss mechanisms (i.e.,

catalysis) are accounted for, a band gap above 2 eV is generally necessary [71]. The smallest band gap achieved so far in a functional catalyst is 2.30 eV in NiO/RuO₂-Ni:InTaO₄ [72]. Semiconductors with smaller band gaps or lower flat-band potentials require a bias voltage or external redox reagents to drive the reaction. Alternatively, two or more small band-gap semiconductors can be combined to drive water oxidation/reduction processes separately via multi photon processes (Figure 3.3b).

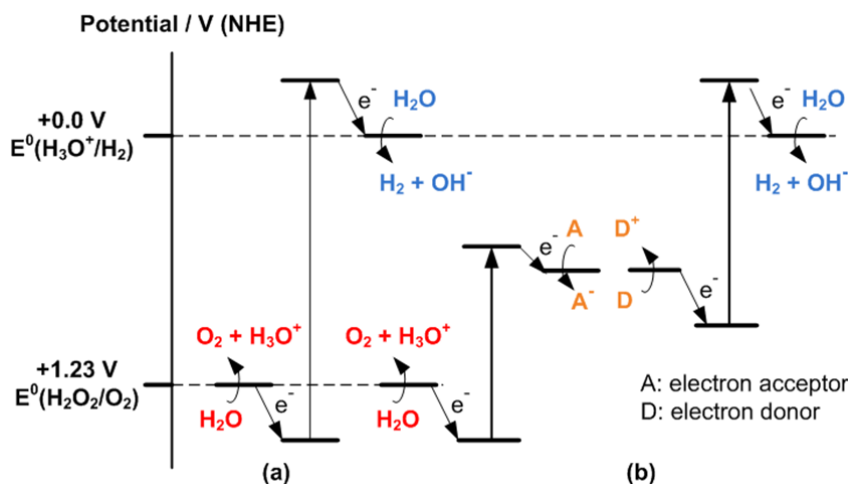


Figure 3.3: Diagram of required potential for photochemical water splitting at pH = 0: (a) single semiconductor system; (b) dual semiconductor system (z scheme) using a redox shuttle (modified from Ref [73]).

Water splitting reaction to hydrogen and oxygen can be facilitated by many inorganic semiconductors, such as TiO₂, which was discovered in 1971 by Fujishima and Honda [74]. During the past decade, over 130 materials and derivatives are developed for overall water catalysis to hydrogen and oxygen or water oxidation or reduction by employing the external redox agents. The best compounds in terms of quantum efficiencies (η_ϕ) are NiO-modified La/KTaO₃ ($\eta_\phi = 56\%$, pure water, UV light) [75], ZnS ($\eta_\phi = 90\%$, aqueous Na₂S/Na₂SO₃, light with $\lambda > 300$ nm) [76], and Cr/Rh-modified GaN/ZnO ($\eta_\phi = 2.5\%$, overall pure water splitting, visible light) [77-78]. Since now, no material has been developed to catalyze water splitting with visible light at quantum efficiency larger than 10%. Here, 10% is the goal for commercial applications [79].

The use of two semiconductor materials remains an attractive option for capturing a large portion of the solar spectrum, with the two band gaps tuned to absorb complementary portions of the solar spectrum [71]. A dual band gap cell configuration consists of an n-type

material (photo-anode) with a p-type semiconductor (photocathode) in series. The n-type material is capable of water oxidation with sufficiently positive valence band and reasonable photocurrent, and p-type material has a smaller band gap, that would drive the hydrogen evolution reaction.

3.3. Photocathodes for hydrogen evolving reaction

Photocathodes used for a water splitting cell need to supply sufficient cathodic current to reduce protons to H_2 and must be stable in aqueous environments. In addition, to successfully reduce protons to H_2 , the potential of the conduction band edge of the photocathode must be more negative than the hydrogen redox potential. GaP has an indirect band gap of 2.26 eV, with band edges that straddle the hydrogen reduction potential. The n-type form of this material is unstable in an aqueous solution, but p-GaP is stable for extended periods of time under reducing conditions [80].

InP has a band gap of 1.35 eV, which makes it a good solar absorber; however the scarcity and high demand of indium limit the commercial viability of the material, at least in traditional wafer format [81]. Using Ru catalyst islands on the surface of oxidized InP, Heller et al. [82] were able to achieve 12% solar to chemical conversion for the production of H_2 . By electrodepositing Rh and Re on p-InP electrodes, efficiencies of 13.3% and 11.4% were obtained, respectively (efficiencies were calculated as the ratio of energy that could be produced in an ideal fuel cell using the photoelectrochemically produced H_2 and the solar irradiance striking the photocathode).

With a band gap of 1.12 eV, p-Si is a desirable p-type small band gap absorber for possible use in dual band gap p/n-PEC water splitting configurations [83]. Several groups have demonstrated that planar p-Si photocathodes, combined with a variety of metal catalysts, can be used to reduce the voltage required to electrochemically produce H_2 . Photon to hydrogen conversion efficiencies as high as 6% (under low level monochromatic 633 nm illumination) have been reported for p-Si with Pt nanoparticles [84]. Si is stable in acidic conditions, but surface oxidation can occur over extended periods of time. Passivation of the Si surface by covalent attachment of methyl groups has been shown to improve the stability of p-Si photocathodes [83, 85].

Currently, II-VI semiconductors such as CdTe and $CdIn_{1-x}Ga_xSe_2$ (CIGS) dominate the thin film photovoltaic market. These materials have band gaps that can be controlled by modifying their composition and processing. Several different groups have investigated the properties of II-VI semiconductors, and have used them to split HI and HBr with relatively

high efficiencies. Bard and co-worker [86] made single crystals of the group VI selenides and used them to split HI in water, using methyl viologen as a redox shuttle for the hydrogen evolution process.

3.4. Photoanodes for oxygen evolving reaction

The photoanode materials for oxygen evolving must be an n-type semiconductor, and drive the holes toward the surface under the electric field generated by band bending. The materials with a suitable band gap and band-edge positions for a single or multiple band gap system are used to supply the electrical property requirements such as doping and resistivity that allow for efficient collection of charge carriers. Because of the stability requirement under oxidizing conditions, photoanode materials are mostly investigated among the metal oxides or metal oxide anions, in pure, mixed, or doped forms.

The WO_3 has band gap of 2.7 eV that results in a slightly positive CB edge potential to NHE. Also, WO_3 as a photoanode or with sacrificial oxidants can oxidize water to oxygen without any additional OER cocatalyst [87]. In_2O_3 as an efficient photoanode material is well-known to be responsive to near-UV light [88]. Litharge ($\alpha\text{-PbO}$) with band gap of 1.9 eV enhances the photocurrent over a wide range of the visible spectrum ($400 \text{ nm} < \lambda < 650 \text{ nm}$) using and a redox couple [89]. However, PbO is converted into metallic PbO_2 during water splitting without any oxygen evolution [90].

Group 7-10 transition metal oxides have scarcity properties and some of them have the tendency to form partially filled d shells. Therefore, they have been mostly utilized as OER cocatalysts than as bulk photoanode materials. The optical measurements on hematite ($\alpha\text{-Fe}_2\text{O}_3$) have revealed that below the main absorption edge, e.g. 2.2 eV, two weak peaks, at 1.4 and 2.0 eV, exist that can be attributed to crystal field transitions [91]. As the result, the intrinsic charge recombination rate is high, and the hole diffusion length is only 2-4 nm, that negatively affect the performance of this material as a photoanode [92].

Thus, Substantial efforts have been directed toward fabrication of thin layers [93] and nanoparticles [94] of hematite, to promote charge collection capability. Silicon doping of hematite can develop dendritic nanostructures and enhance electrical conductivity, as reported by Gratzel et al. [95]. These researchers have shown that a short-circuit current density of $> 3 \text{ mA cm}^{-2}$ under AM 1.5G sunlight can be achieved [96]. Recently, Sivula et al. have sintered mesoporous films on SnO_2 glass electrodes at high temperatures ($\sim 800 \text{ }^\circ\text{C}$) that show photoactivity and confirms the ability to form efficient hematite photoanodes from colloidal suspensions [97].

The attractive feature of CdS, e.g. direct band gap of 2.4 eV, makes the overall water splitting thermodynamically viable. In practice, the oxidation products are usually elemental sulfur or polysulfides [98]. It is demonstrated that by applying a Nafion film that employs a Ru complex as the OER co-catalyst, the photo-induced harvested holes at the CdS surface are rapidly passed on for O₂ evolution [99]. GaP has the valence band edge potential of ($E_g > 2.3$ eV) almost equal to the standard OER potential, but GaP as a photoanode for water oxidation can function only in neutral or basic water. In order to prevent photo-corrosion, GaP has to be treated by a protective layer, such as Sn-doped In₂O₃ (ITO), before doping with an OER co-catalyst such as RuO₂ [100].

3.5. Electrocatalytic water splitting

In water splitting device, a suitable HER or OER catalyst must satisfy two basic requirements. First, the catalyst must be highly active toward its respective reaction, meaning it must be capable of producing, at a minimum over-potential, large quantities of hydrogen or oxygen as quickly as the absorber can supply electrons or holes to the catalyst. Second, an effective catalyst must be robust enough to maintain its efficiency over time scales relevant to commercial use. Catalysts described in the electrolysis literature largely meet these requirements, although continued research in the area demonstrates that improvements are still needed.

Electrochemists have studied several pure metal catalysts, as well as materials for efficient, low-cost hydrogen evolution [101]. These materials are categorized into two categories of metal composites/alloys and non-metallic elements incorporated compounds. Nickel metal with specific treatments to increase its active surface area, has demonstrated high performance [102]. Therefore, the majority of investigated mixed-metal catalysts include additions of another metal, or metals, to nickel. The binary mixtures of Ni-Mo [103] and Ni-Co [103-104] as well as the ternary systems Ni-Mo-Cd [105] and Ni-Mo-Fe [106] are some instances.

High-activity, low-cost catalysts have been developed employing mixtures of metals with non-metal components. The electrochemistry and HER catalytic properties of RuO₂ and other metal oxides have been studied by Trasatti [107], which show high catalytic activity. The ternary mixture Sr_xNbO_{3-δ} shows promising properties due to its low-cost components and high apparent stability among the oxides [108]. Sulfides such as nickel sulfide have also been pursued, and exhibit higher activity and stability under alkaline conditions comparing

with pure nickel [109]. Tungsten carbide takes advantage of inhibition by carbon to avoid formation of a deactivating surface oxide and shows a photo-activity for the HER [110].

In proof-of-concept of photoelectrochemical HER systems, platinum and other noble metals have been extensively utilized as catalysts that achieved $\sim 13\%$ solar conversion efficiency [111]. However, very few photocathodes for photoelectrochemical HER have been reported that employ catalysts other than noble metals. MoS₂ cocatalyst has been reported by Zong et al. [112], along with CdS that produces hydrogen more efficiently than platinized cadmium sulfide, under illumination and under the presence of a sacrificial reductant.

Recently, Karunadasa et al. [10] have developed a water reduction catalyst based on a molybdenum-oxo metal complex that is about 70 times cheaper than platinum. The molecular catalyst reduces water molecule to generate hydrogen without any additional acids or organic co-solvents. Turnover frequency of this molybdenum-oxo complex is reported as 2.4 moles of H₂ per mole of catalyst per second and a turnover number of 7.1×10^5 moles of H₂ per mole of catalyst in neutral buffered water or sea water. The high activity and stability of this metal-oxo complex in water introduces a distinct molecular system for reduction catalysis.

Figure 3.4 shows the catalytic cycle of molybdenum-oxo for the generation of hydrogen from water. According to the proposed cycle, one electron reduction of [(PY5Me₂)MoO]²⁺ turns to [(PY5Me₂)MoO]¹⁺, and eventually to a putative [(PY5Me₂)MoO] species with the addition of a second electron. These reduction processes weaken the Mo–O bond and enhance its nucleophilicity, that leads to deprotonating to reactive intermediate [(PY5Me₂)Mo(H₂O)]²⁺ nearby water molecules to and release two hydroxide anions.

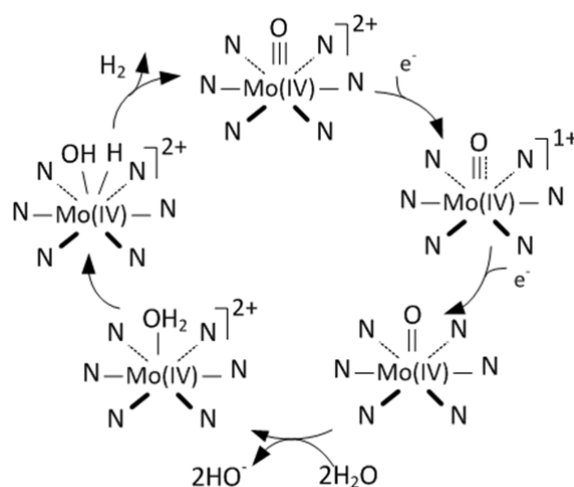


Figure 3.4: Proposed electrocatalytic cycle for water reduction to release hydrogen and hydroxide anions (modified from [10]).

The catalyst developed at the University of California, Berkeley (UCal) [10] simulates the process of an alkaline cell, where the water is introduced at the cathode and it is decomposed into hydrogen and OH^- . But the main difference is that instead of hydrogen evolution on the electrode surface, the heterogeneous solution of molybdenum-oxo complexes dissociates the water molecules to hydrogen and hydroxide ions. The OH^- ions travel through the electrolytic material to the anode where oxygen is formed.

3.7. Photocatalytic overall water splitting

Development of new types of photocatalysts for water splitting to produce hydrogen by visible incident light has been extensively studied in the past decade [113-114]. Traditionally, water splitting with photocatalysts in powder form produces a mixture of H_2 and O_2 . Therefore, efficient devices must be designed based on the use of heterogeneous or homogenous photocatalysts to separate H_2 and O_2 in water photo splitting processes [115].

Selli et al. [116] have developed a photocatalytic water splitting process by the use of a new two-compartment Plexiglas cell. This design provides an effective decomposition of H_2O into H_2 and O_2 , where oxygen evolves in a separate half-cell by illuminating photoactive Ti electrode (Figure 3.5). Hydrogen production under irradiation with a UV lamp at a wavelength above 300 nm was performed without use of any sacrificial reagent. The photonic efficiency is reported as 2.1%, whereas it reduces to 0.36% under irradiation with a visible wavelength lamp ($\lambda > 350$ nm) [116].

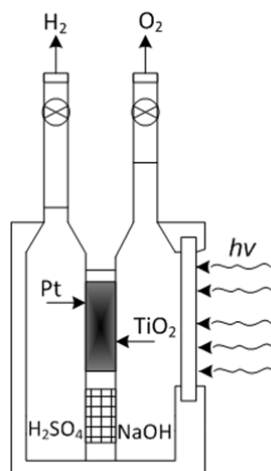


Figure 3.5: Sketch of the dual-cell for photocatalytic water splitting, with separate H_2 and O_2 evolution (modified from [116]).

Sun et al. [117] have designed a photoelectrochemical device by an assembly of a molecular Ru catalyst with pH-modified Nafion on a dye-sensitized nanostructured TiO₂ film as the anode to split water into O₂ and H₂ under visible light. A Pt foil has been used as the cathode. A small bias of -0.325 V vs. Ag/AgCl is required to boost the conduction band of TiO₂ for direct reduction of protons to hydrogen, and perform the complete water splitting. The strong acidity of commercial Nafion is found as the reason for an increase of overpotential associated with water oxidation, and the rapid decay of photocurrent.

Due to band-gap limitation, many of visible-light driven photocatalysts can only evolve H₂ or O₂ with a low yield. A novel photocatalytic system called a Z-scheme is developed to overcome this drawback, which mimics the Z-scheme mechanism in natural photosynthesis of green plants to generate hydrogen and oxygen simultaneously [118]. The Z-scheme basically consists of a dual-photocatalyst system that performs water reduction and oxidation using an H₂-photocatalyst and O₂-photocatalyst, respectively [119].

In the Z-scheme, photocatalytic water splitting produces H₂ and O₂ as a mixture due to use of photocatalysts in a mixed format in a single reactor. To address this issue, a novel twin reactor was designed that employs Pt/SrTiO₃:Rh (H₂-photocatalyst) and WO₃ (O₂-photocatalyst) discretely in two compartments of a reactor. The reactor is separated by a modified Nafion ion-exchange membrane to perform the water-splitting reaction under visible-light irradiation [120]. An aqueous solution containing Fe³⁺/Fe²⁺ is used to fill the compartments of the connected twin reactor. The ions act as the electron-transfer mediator. Consequently, hydrogen and oxygen can be generated separately. The average production rate of H₂ and O₂ was 0.71 and 0.35 mmol g⁻¹h⁻¹, respectively.

Preparation of TiO₂ thin films for water splitting have been extensively investigated using several deposition methods. However, most of the reported hydrogen production yields generally do not correspond to an actual water-splitting reaction. Huang et al. [121] have performed a physical deposition technique, called electron beam-induced deposition, for preparing a photo-catalytic TiO₂ thin film that facilitates a water-splitting reaction. A photocurrent of 2.1 mA was measured for the TiO₂ thin film with post-calcination at 500 °C under UV irradiation. The hydrogen and oxygen yields were 59.8 and 30.6 mmol, respectively, after 8 h illumination of reactor under UV light.

Photoelectrochemical (PEC) water splitting for hydrogen generation has been performed using crystalline silicon, group III–V compounds as well as α -Si:H [122-123]. Photoelectrochemical solar-to-hydrogen conversion involves efficient PEC cells that are expensive and cheaper cells are not adequately efficient. CIGS₂ polycrystalline thin-film solar

cells have been recently introduced for efficient PEC water splitting [124]. Compared with III–V based and α -Si:H solar cells, CIGS₂ thin-film solar cells have several advantages such as lower cost, higher tolerance against intrinsic degradation, and easier large-area depositions. The PEC configuration is an assembly of two ~ 0.43 cm² CIGS₂/CdS thin film solar cells used in series with the RuS₂ anode for oxygen production and platinum for hydrogen generation. The series connected PV cells were not inside the electrolyte. The infrared rays which are not absorbed during PV conversion are exposed to the RuS₂ photo-anode in contact with the electrolyte which enhances hydrogen and oxygen generation by water splitting. The efficiency of overall PV electrolysis using this configuration was 8.78%, respectively.

3.7. Photo-reactors for photo-catalytic water splitting

Different configurations of photo-reactor are in use to verify the performance of the photoactive materials. An apparatus for photo-catalytic heterogeneous water splitting is essentially a photo-reactor with either immobilized photoactive material on a substrate or suspended photo-catalyst particles. The photo-reactor geometry should facilitate enough light exposure and penetration to ensure maximum photons can reach the photo-catalyst. The light source usually provides irradiation perpendicular to the photo-reactor surface [125]. Some studies are conducted to investigate the photon to hydrogen conversion efficiency for photo-electro-catalytic water splitting [126-128]. The photo-reactors for particular applications based on UV light are commercially available, but a photo-reactor for heterogeneous photo-catalytic water splitting is not readily available.

3.7.1. Photoelectrode configurations

The photoactive material used for photo-catalytic water splitting is mainly semiconductor in two classified forms of metal oxide and conventional photovoltaic (PV) material. Figure 3.6 illustrates different general configurations of photoelectrochemical water splitting reactor. The semiconductor can be utilized in form of n-type such as TiO₂ [18] (Figure 3.6a), p-type such as InP [129], (Figure 3.6b) or coupling of n-type and p-type as in n-GaAs/p-InP [130-131] (Figure 3.6c). In order to utilize maximum possible portion of spectrum, layers of several n-types or p-types with different band gaps can be sandwiched together (Fig. 3.6d). In an alternative way, combination of different layers of n- and p-types can be implemented under internal biased in a monolithic structure [132]. It is accomplished by depositing the anode on one side of a metal substrate and cathode on the other and sealing

the edges or stacking the anode and cathode on their own substrates with an electrical connection between the two.

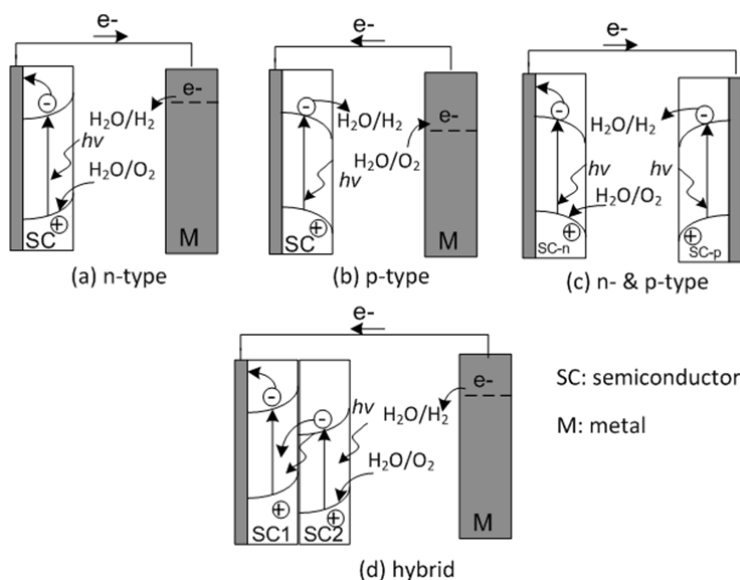


Figure 3.6: Photo-electrode arrangements for photoelectrochemical water splitting (modified from [133]).

3.7.2. Dual-cell photo-reactor

In a complete system two photo-reactors are joined together where each photo-catalytic cell has half of the electrochemical potential for water splitting, as shown in Figure 3.7 [134-135]. The apparatus consist of two flat containers with immobilized photo-catalytic particles on the bed of the bottom plate or grids. An alkaline solution that contains the redox mediators is usually being supplied between the two chambers. In order to eliminate pumping a large volume of solution between two chambers, anion exchange membranes can be installed between the two cells to allow the crossover of mediator ions. Due to separation of two half cells, in this case, the photo-catalyst can be used in suspension instead of immobilized form [136].

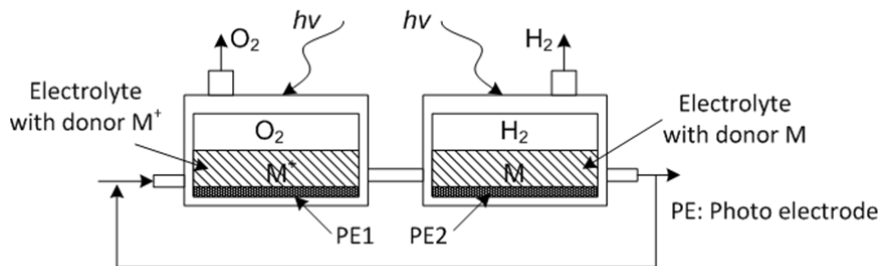


Figure 3.7: Schematic of a dual-cell photo-reactor (modified from [133]).

3.8. Hydrogen production via seawater catalysis

Electrolysis of seawater, as an abundant available resource on the earth, is one of the most promising ways to produce hydrogen. The electrolysis of seawater has received increasing attention recently [137]. Purified alkaline chloride solutions have been used for the generation of hypochlorite. Direct seawater electrolysis has been used commercially for reducing organic fouling in process cooling water [138], for disinfecting sewage streams, and for sterilizing water used in pressure injection in oil and gas formations. In these cases, only the anodic reactions were examined. There has also been interest in the cathodic release of hydrogen for onsite use as a reducing agent or as part of the overall hydrogen economy [139]. Some of the problems encountered in adapting seawater electrolysis to hydrogen production have been identified by Williams [140].

However, as described by Bockris et al. [141], the usual electrode materials and conditions of electrolysis favours the anodic evolution of chlorine rather than oxygen. Large quantities of the by-product chlorine would be generated by a major power plant. These could not be discharged to the environment and would be costly to convert back to chloride. Hashimoto and co-workers developed efficient anodes for oxygen evolution in seawater electrolysis [142-150].

The main difficulty in using seawater, whether intended for hypochlorite, chlorine or hydrogen production, is the gradual build-up of insoluble precipitates on the cathode surface [140]. These precipitates result in increased operational costs and reduced production because of increased hydrogen over-potentials and lower active surface area at the cathode. This problem is encountered with traditional hypochlorite generation, but is even more pronounced with untreated seawater because of the large number and concentration of metal impurities. Typically, high electrolyte flow rates are used to scour the electrode surfaces and reduce the fouling, but this also increases pumping costs. Periodic cleaning of the cathode surfaces is required to maintain efficiency.

Another feature of the direct use of seawater is the problem of low conductivity of the electrolyte and subsequent high power requirements. In conventional hypochlorite cells, hydrochloric acid is often added to adjust pH and to improve the conductivity by reducing the ohmic resistance [151]. By using electrolyte recirculation for seawater electrolysis, more concentrated product solutions can be achieved, which would reduce power requirements. However, this improvement may be offset by increased maintenance costs resulting from electrode fouling. Most of the scientific contributions to seawater research have been focused

on the development of electrode materials such as manganese dioxide-coated IrO₂ anodes with high selectivity for the oxygen evolution reaction over chlorine evolution [152-154].

3.9. Modeling of photo-catalytic hydrogen production process

The design and modeling of water splitting through photo-catalysis is a relatively new research scope but essential for the effective exploitation of hydrogen production photo-reactors. The modeling of photo-catalytic reactors involves a rigorous analysis of the radiation field in the photo-reactor [155-156]. This analysis is linked to the modeling of the reaction kinetics and fluid dynamics that leads to differential equations which usually require numerical solutions. Further development of photo-reactors for an industrial scale is facilitated by the availability of mathematical models that can be used for scale-up and design. Different approaches for the analysis of photo-catalytic reactors have been presented, which include complete and experimentally validated dimensionless models for falling film and fountain photo-catalytic reactors [157-160].

The analysis of a complete water splitting system requires investigation of an oxygen evolution reactor as it consumes almost 40% of input energy for the whole process. Most investigations on catalytic hydrogen production focus on the development of new catalysts [161-162] and development of new membrane electrolytes [163]. However, there has been a relative lack of thermodynamic and electrochemical modeling of oxygen evolving half-cells for a complete system analysis of catalytic hydrogen production. This is important for better understanding of the working mechanisms as well as design optimization. Ni et al. [164] developed an electrochemical model to provide the current–voltage (J-V) characteristics of a PEM electrolyser. The kinetics and energetics of electron transfer across semiconductor/electrolyte junctions are examined by Gerischer [165-166]. The characteristic of the semiconductor space-charge layer in vicinity of the semiconductor/electrolyte interface is also explored. However, the understanding phenomena occurring in a complete cell and the contribution of different intervening mechanisms require development of a systematic and integrated transient phenomenological model.

The mass transfer is the main mechanism that requires detailed understanding of hydrogen production at a gas evolving electrode. The concentration of the reaction products is the determining factor of mass transfer, which can be evaluated by experiment. Although many past studies examined mass transfer at hydrogen evolving electrodes [167-169], very few studies exist to deal with concentration profiles of hydrogen at a gas evolving cathode [170]. In these experiments, the transfer of a tracer to the electrode was monitored. Therefore,

the mass transfer of the reaction product from the electrode into the liquid bulk was not directly measured.

Electron transfer has an important role in the chemical processes. The main objective is to explore the intermolecular electron-transfer and temporal dependencies of intramolecular species. Photo-induced charge transfer has a particular interest in the areas of photosynthesis, photochemical reactions, and technical applications. The kinetics of light initiated electron transfer is examined in a variety of experimental studies [171-173], as well as a number of theoretical studies to predict the rates of photo-induced charge separation [174-175]. Intramolecular photo-induced electron transfer is described for some systems with a donor and a single acceptor at a fixed distance [176-177]. However, a donor in liquid solutions can interact with many acceptors, and the diffusion of the donors and acceptors affects the rates of reaction. Therefore, investigation of systems with intermolecular transfer through a solvent is more complex.

Furthermore, there are relatively few thermodynamic studies of photo-catalytic conversion of light energy in terms of energy and exergy efficiencies [178]. Currently, there exist several approaches to the exergy analysis with some minor differences, i.e. Moran and Shapiro [179], and Bejan [180].

Solar energy transfer is basically conducted in the form of thermal radiation. Planck [181] proposed the quantum hypothesis for blackbody thermal radiation, and derived Planck's Law to describe spectral blackbody radiation. There exist different expressions of exergy and entropy of photon gas [182-184]. The review by Petela [182] of different theories of thermal radiation exergy is summarized in three main theories: (i) exergy equation for blackbody radiation proposed by Petela [182], (ii) the equation to approximate the direct solar radiation derived exergy by Spanner [183] and (iii) the theory by Jeter [184] that implies that Carnot efficiency determines the available energy (exergy) of thermal radiation on the basis of an analysis for a heat engine.

Chapter 4

Experimental Apparatus and Methodology

In order to evaluate the performance of a complete water splitting reactor and extract unknown characteristics associated with each component that contributes to water dissociation, a number of experiments are performed. Two different setups are utilized for photo-catalytic water splitting in batch and quasi-steady operation. Different photo-catalysts are examined to study the performance and characteristics of a complete water splitting system that is scalable and capable of producing hydrogen and oxygen in separate chambers. The characteristic of the experimental setups and the methodologies for performing experiments are described in this chapter.

4.1. Photo-reactor in batch operation

The schematic of the experimental apparatus (photo-reactor) is presented in Figure 4.1. Its main components and features are described in Table 4.1. Related components are named in Table 4.1. This reactor was fabricated by a senior capstone group at UOIT [185]. It has been further modified to serve the purposes of this research. The modifications are mostly related to sensor positioning, data acquisition system and LabVIEW software integration. In the present study the performance of the photo-reactor is enhanced for more precise measurements and, a hybrid production system is accommodated using an external power supply.

The system comprises the reaction vessel made of thin transparent glass, which contains an immersed thermocouple and two electrodes. The produced gas is collected from the upper side and drawn automatically in a cylinder actuated by a servomotor. A pressure sensor is installed, through which the displacement of the piston is controlled, such that the pressure remains constant. A digital calibre is fixed to the piston rod to monitor its movement and thus determine the collected gas volume.

This photo-reactor operates in batch mode, and accommodates only the hydrogen evolution reaction. Therefore hydroxide ions due to splitting of water molecules are

accumulated inside the aqueous solution and limit the rate of production. The experiments are conducted with various solution compositions, pH values, molar concentrations of photo-catalysts and the presence or absence of electron donors.

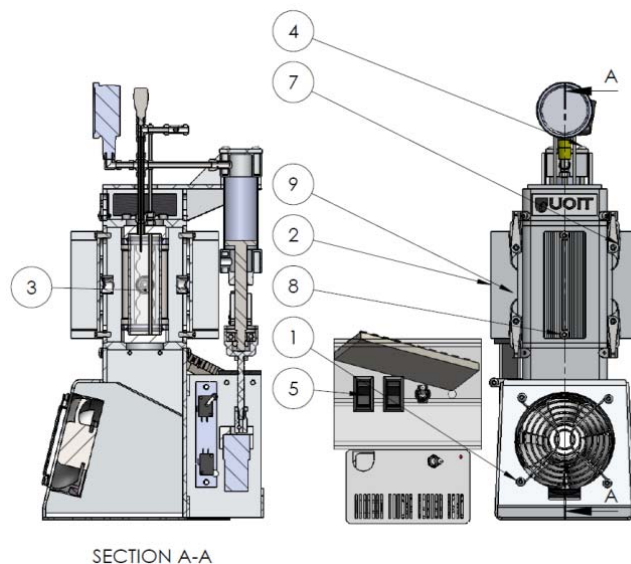


Figure 4.1: Schematic of the experimental photo-reactor apparatus (1: Stacking Reactor Assembly, 2: LED and Heat Sink Assembly, 3: Tube Assembly, 4: Upper Module Assembly, 5: Electrical Assembly, 6: Motor Assembly, 7: Reactor Housing Assembly, 8: B18.3.4M-6×1.0×16 SBHCS, and 9: Cylinder Rod Assembly) [185].

The reactor has the following features:

- The reactor has a liquid capacity of 105 mL, 21 times the volume of Brewer’s early work [9] and 5 times the volume of their more recent reactor.
- The reactor includes a hydrogen variable stroke cylinder that can measure and store up to 50 mL of gas at pressures between vacuum and 1 atmosphere positive pressure. This will allow testing at varying pressures to establish the impact of pressure on catalyst reaction rates. Gas production can be bled off and the cylinder stroke is reset during production with minimal impact on the system, allowing 100 mL, 150 mL, 200 mL etc. volumes to be collected and measured.
- Light is supplied by an array of 20 blue (470 nm) LEDs totalling 100 W. The intensity of each LED is adjustable and the entire array’s intensity can also be adjusted, allowing testing to be performed to establish the impact of light intensity on catalyst reaction rates. The LEDs can be replaced with LEDs of different colours (wavelength) to further test the

impact of wavelength on reaction rates. The reactor can be exposed to solar simulator to study the photo-catalytic reaction under full spectrum.

- The reactor has two built-in electrodes. This will allow ways of eliminating the electron donor materials.
- The reactor can be used for oxygen production to facilitate testing of the various oxygen evolving reactions that is a necessary companion reaction to the reaction for hydrogen.
- Use a digital thermocouple with its output as an input to the controller.
- Use a pressure transducer in place of the analog pressure gauge with its output as an input to the NI controller.

Use NI Lab View software to set up the controller to automatically control the apparatus.

The system allows flexibility in the experiments. At least three ways to conduct hydrogen evolution tests are envisaged as follows:

- Water photolysis – light is applied and the evolved hydrogen is generated by a photo-catalyst such as supramolecular complexes, zinc sulfide, etc.;
- Water electrolysis – electricity is applied under the absence of light and the composition and quantity of the resulting gas (hydrogen/oxygen mixture) is measured; and
- Hybrid process of water electrolysis and photolysis – both electricity and light are applied.

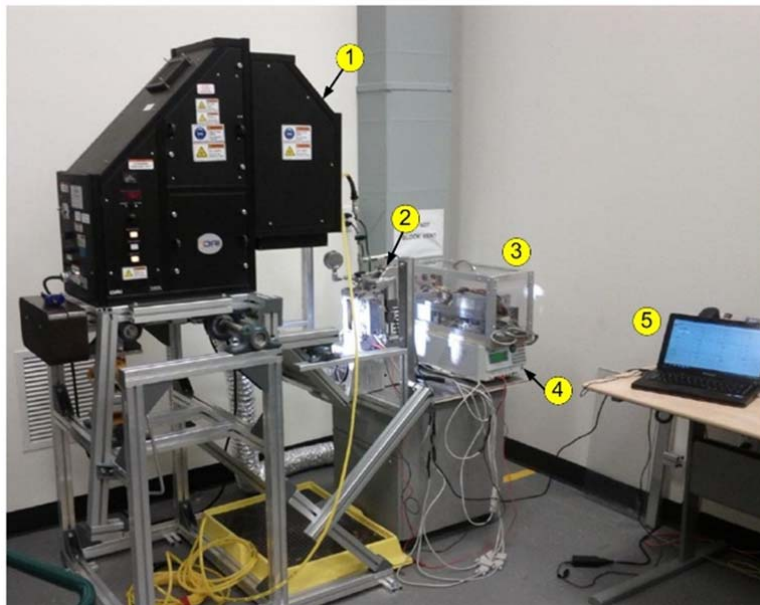


Figure 4.2: Experimental setup for photo-reactor measurements (1: Photo-reactor, 2: Reactor control system, 3: Tube Assembly, 4: DC Power supply, and 5: Data acquisition system).

In order to perform the photo-catalysis experiments with zinc sulfide catalyst under the solar spectrum, the photo-reactor is exposed to light under a solar simulator. The photo-reactor in operation, under illumination by a solar simulator is shown in Figure 4.2.

4.2. Dual-cell reactor for quasi-steady operation

As mentioned in the previous section, performing the photo-catalytic experiments in batch mode is associated with a rate limiting effect of hydroxide ions. Furthermore, batch mode operation is not considered as a practical design for large scale production. In this regard, a dual-cell water splitting system is designed and fabricated for quasi-steady operation under various working conditions. This reactor is designed to decompose the hydroxide ion by-products in order to maintain the reaction rates and produce oxygen as a product in a separate cell. Two half cells are assembled with a flange connection where a membrane is placed in a groove to keep the HER and OER reactants separated. The dual-cell can accommodate both electro-catalytic and photo-catalytic water splitting experiments.

Figure 4.3 illustrates the dual-cell in operation under illumination by the solar simulator. The hydrogen production half-cell contains zinc sulfide suspensions. The dual-cell containing cadmium sulfide photo-catalyst is shown in Figure 4.4. Sacrificial agents are supplied to the aqueous solution to maintain the reaction rate constant. However, the amount of chemicals that should be replenished over time is less than a batch reactor. This is due to implementation of an electric power supply and an anion exchange membrane that facilitates neutralization of negative ions.

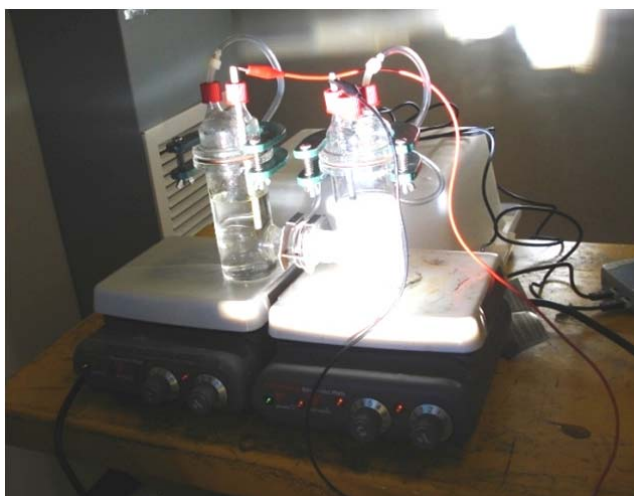


Figure 4.3: Experimental apparatus for photo-catalytic water reduction with zinc sulfide.



Figure 4.4: Experimental apparatus for photo-catalytic water reduction with cadmium sulfide.

The cell features the anode and cathode electrodes connected in a circuit to a power supply. An electrochemical workstation is a power supply capable of controlling and measuring both current and voltage in a variety of electrochemical methods. Only the difference in voltage between the anode and cathode can be measured in a two-electrode system. A reference electrode is a third electrode that is required to measure the voltage for the electrode of interest. In a three electrode system, the electrode being measured by the reference electrode is the working electrode and the remaining electrode is the counter electrode. The electrodes are immersed in an electrolyte. The electrolyte contains mobile ions so as to help conduct an ionic current. The anion exchange membrane between two half-cells is capable of passing the negative ions from HER to OER reactions. The integration of a negative charge supply and the performance of an anion exchange membrane avoids rate limiting species such as hydroxide and disulfide ions. However, it partially compensates the replenishment of sacrificial agents. These chemicals are supplied to the reactor at specific time intervals to keep the solution volume constant. It leads to a quasi-steady operation of this water splitting system.

4.3. Integrated system setup

In another approach to prevent hydroxide ion accumulation in photo-reactor and transition from batch mode to continuous operation, an integrated system for photo-catalytic water splitting is assembled, as shown in Figure 4.5. Hydroxyl ions are formed by the reduction of water to hydrogen gas during the photochemical reaction. The aqueous solution

inside the photo-reactor is pumped to a dual-cell where the OH^- ions diffuse to the vicinity of anode surface and further oxidized to produce oxygen gas. The transport of hydroxyl ions occurs in two different regions of the complete cell: through the membrane, and within the free volume between the membrane-electrolyte interface and the OER-electrode. The neutralized solution will be pumped back to the reactor. The system in operation is illustrated in Figure 4.6.

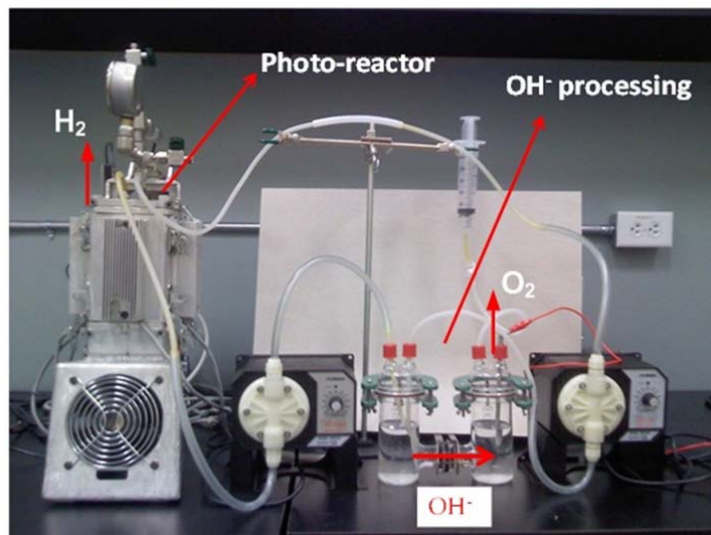


Figure 4.5: Integrated system setup for photo-catalytic water splitting.



Figure 4.6: Integrated water splitting system with illuminated zinc sulfide suspensions.

In this setup, the main challenge to run the experiments is to pump the aqueous solution that contains suspended catalyst from photo-reactor to dual-cell and vice versa. This setup requires more catalyst consumption. Also the fluid flow into and out of reactor disturb the evolved gas pressure and causes measurement errors, Figure 4.6. Therefore, the results from direct illumination of dual-cell, described in Section 4.2, become more reliable.

4.4. Materials

The zinc sulfide and cadmium sulfide powders are mainly used in this work as supplied by Alfa Aesar Ltd. (pure grade, 99.99% metal basis, -325 Mesh powder). Sodium sulfide is purchased from Ricca Chemical in a 3% (w/v) aqueous solution form and diluted based on each experiment requirement. Deionized water is used for the experiments.

4.5. Electrolyte

Choosing an appropriate electrolyte for the oxygen evolving reactor, and investigation of the effects of electrolyte concentration on electrochemical performance of the electrode, are essential. Acids, bases, and salts dissociate into ions when dissolved in water (or in other solvents). This dissociation can be complete or partial. The fraction of the original molecules that have dissociated is known as the degree of dissociation, α . Substances that exhibit a low degree of dissociation in solution are called weak electrolytes, whereas when the value of α is close to unity, it indicates strong electrolytes.

Most of the commercial electrolyzers have adopted alkali (potassium or sodium hydroxide) solutions as the electrolyte. Aqueous alkaline electrolytes of approximately 30-50 wt% KOH or NaOH are widely used. The liquid electrolyte is not consumed in the reaction. It must be replenished over time because of other system losses primarily during hydrogen recovery.

4.6. Membrane

Ion exchange membranes are thin films of polymeric chains containing electrically charged functional sites. These selectively charged membranes can separate ions: if the membrane is positively charged (e.g. with quaternary ammonium groups), only anions will be allowed through and it is called an anion-exchange membrane. Similarly, negatively charged membranes (i.e. with sulfonate groups) are called cation-exchange membranes. This

membrane property is named perm-selectivity and it can be customized to meet specific requirements.

There are also membranes that only allow monovalent cations or anions through and reject multivalent ions: these are called monovalent-selective membranes. Such selectivity is typically obtained by adding a thin ion-exchange layer of opposite sign at the surface of the membrane. Note that all ion-exchange membranes are not 100% permselective: most Neosepta membranes have a permselectivity of 98% or higher.

An anion-exchange membrane is utilized for the dual-cell experiments. It facilitates the transfer of OH⁻ ions, generated at the cathode during hydrogen evolution, into the anolyte chamber where neutralization of hydroxide ions occurs, and thus a pH differential to be set up in the cell. AMI-7001 anion exchange membrane is purchased from Membrane International Inc., with electrical resistance of 40 Ohm cm² in 0.5 mol L⁻¹ NaCl, Total Exchange Capacity of 1.3 meq g⁻¹, and thermal stability of 90 °C. Membranes are preconditioned by emersion in a 5% NaCl solution at 40 °C for 24 hours to allow for membrane hydration and expansion.

4.7. Oxygen evolving reaction electrodes

At practical current densities, anodes of RuO₂ or IrO₂ have the lowest OER overpotentials. However, these oxides suffer from poor chemical stability in alkaline media [186]. The oxides of the first row transition metals, in particular nickel and cobalt, offer a fair electrocatalytic activity for the OER, and they display excellent long term corrosion resistance in aqueous alkaline solutions. They have the advantage of being relatively inexpensive [186-187]. Nickel hydroxides [188], spinels (ABO₃) including Co₃O₄ [189], Ni-Co₂O₄ [190], perovskites (ABO₃, A is a lanthanide, B is a first row transition metal) [191], and transition metal based amorphous alloys [192], have all been proposed for OER anode applications. The aforementioned oxides were prepared from inorganic precursor materials using a wide variety of approaches, including thermal decomposition, spray pyrolysis, sol-gel routes, freeze drying, precipitation or electro-deposition from a solution.

Polycrystalline nickel anodes have been commercially utilised in water electrolysis and consequently there exists significant ongoing research on this system [193-194]. In contrast, electrochemical performance of oxidised cobalt and oxidised iron anodes is compared with nickel in this report. Alloys with different electronic distributions in the metal are adopted to improve the activity of electrodes. For example, alloys of Mo and Pt were found to be a significant upgrade of the electrolytic efficiency in comparison with its individual components and conventional cathode materials [195].

Nanostructures have also received much attention as they enlarge the material surface area and enable a unique electronic property. A 25% reduction in over-potential and 20% reduction in energy consumption were achieved by the use of the Ru nano-rod cathode compared to the planar Ru cathode. The improvement was attributed to the increased active area of the nanostructured electrode, which reduces the operating current density of the electrolyser [196].

Table 4.1 shows a list of several electrocatalysts which are found helpful to reduce the over-potential or stabilise the electrodes of the industrial water electrolysis, specifically for the oxygen evolving reaction. A comparison of over-potential (U) values at a similar current density (J) indicates the superiority of Ni and Ni alloys for the OER half-cell. It can also be concluded that increasing the working temperature from 25 °C to 90 °C can decrease the over-potential drastically.

Table 4.1: Comparison of different metal electrodes for oxygen evolving reaction.

Composition formula	Method	T (°C)	Electrolyte	C (mol dm ⁻³)	J(A m ⁻²)	U (mv)
Co	N/A	25	NAOH	1	1000	540
Fe	N/A	25	NAOH	1	1000	580
Ni	N/A	25	NAOH	1	1000	530
Ni	N/A	90	KOH	50 wt%	1000	300
Ni + Spinel type Co ₃ O ₄	Thermo-decomposition	25	KOH	1	1000	235
Ni + La doped Co ₃ O ₄	Thermo-decomposition	25	KOH	1	1000	224
Ni _{0.2} Co _{0.8} LaO ₃	Plasma jet projection	90	KOH	50 wt%	1000	270

Table 4.2 compares the relative activities of the three electrodes for the OER in terms of the real current density at a potential in the lower Tafel region. The values of $i_{(E=0.57\text{ V})}$ suggest that catalytic performance decreases in the order Ni > Co > Fe. Caution is however required because there is a greater electrical contribution to the current density at a given potential for the Ni and Fe electrodes, owing to the higher transfer coefficient of $\alpha = 3/2$ for these systems, compared to the value of a $\alpha = 5/4$ that prevails for Co. Ni and graphite electrodes are utilized for electro-catalytic experiments of this research.

Table 4.2: Comparison of electrochemical prosperities of three OER electrodes.

Electrode	b (mV dec ⁻¹)	$i_{(E=0.57V)}$ (Am ⁻²)
Co	47.1	1.05×10^{-5}
Fe	37.9	9.1×10^{-7}
Ni	38.2	2.78×10^{-5}

4.8. Linear mode DC power supply

The electrochemical experiments are powered with the PSU505 with 3 programmable outputs and 12-bit resolution, as shown in Figure 4.7. The total output power is 210 W: channels 1 and 2, 30 V/3 A, provide 90 W each; channel 3, 10 V/5 A, puts out 30 W at a constant rate. Channel 1 provides outputs in serial and parallel modes, but channel 2 in serial mode only. For channel 3, the user can perform auto-ranging. This feature is not found in traditional power supplies.



Figure 4.7: Linear mode DC power supply.

The user can monitor OVP (overvoltage protection) and OCP (overcurrent protection) on the front-panel LCD. Because of its 0.01% load-and-line regulation and 50 ms maximum response time, the PSU505 remains stable even when the voltage source and loads change. The PSU505 is also highly efficient, with an average measurement time of 50 ms.

4.9. TriSOL solar simulator

The OAI solar simulator was acquired to produce highly collimated uniform light, as shown in Figure 4.8. This simulator has an output rated at 3,500W. The solar simulator is calibrated with special air mass filters and lamps to reproduce the sun's solar spectrum. Solar

simulators are necessary for testing virtually any material or product that is exposed to sunlight for long or short periods.

A reflecting mirror is installed under the solar simulator lamp in a rotating mechanism to facilitate different irradiation angles. This feature helps to simulate different light intensities due to changes in climate or attitude difference of various areas. The solar simulator also has the capability to adjust the light intensity in range of $\pm 20\%$ of reference value, e.g. 1000 W m^{-2} .

The existing solar simulator is able to provide a full range of light wavelengths corresponding to 1.5 air mass solar spectral irradiance. Therefore, the experiments can be performed under a light source similar to actual solar conditions.

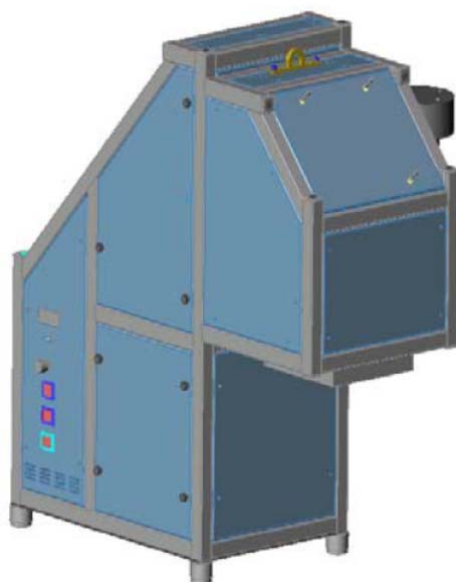


Figure 4.8: TriSOL solar simulator.

4.10. Experimental methodology of photo-catalytic process

Standard experiments are carried out in the photo-reactor and dual-cell, as described in Sections 4.1.1 and 4.1.2. In each case, a certain amount of zinc sulfide powder is dispersed in an electrolyte solution at 55-60 °C, and exposed to light using the solar simulator. Catalyst concentration and light intensity are the main parameters that affect photo-catalytic performance and they are varied for each experiment. The concentration of sodium sulfide as a sacrificial agent is kept constant with a molarity ratio of 4.8 with respect to zinc sulfide. The aqueous solution is alkalized to pH 13.2 using sodium hydroxide in both the photo-

reactor and dual-cell. The aqueous solution is well agitated to provide a uniform distribution of catalyst concentration inside the reactor volume, and to facilitate mass transfer.

Hydrogen and oxygen evolution in the dual-cell reactor are measured by pressure sensors that are calibrated in a 0 to 210 kPa range with a resolution of 0.05 kPa. Hydrogen evolution in the photo-reactor is measured in a constant pressure system as explained in Section 4.1.1. The volume of produced gas is calculated using a digital calliper that measures the incremental displacement of the stroke with 0.01 mm resolution. The measurements are also carried out without any catalyst to quantify the water surface evaporation rate under solar irradiation. The pressure change in the dual-cell and photo-reactor in one hour illumination of aqueous solution was measured as 0.06 kPa, which indicates the negligible effect of vapour pressure.

4.11. Experimental apparatus and method for oxygen production process

Electro-catalytic water splitting experiments are performed to study the design parameters for the oxygen production reactor. The information extracted from these experiments is used to design an integrated system, where hydrogen production is being produced in one half-cell and oxygen is evolved in the other half-cell. The water electrolysis of a KOH aqueous solution is conducted under atmospheric pressure using Ni and graphite as electrodes. In order to investigate the OER overpotential, the controlling parameters consist of current density, electrolyte temperature, concentration gradient between two half cells, space between the electrode and membrane, and electrode height. From hydrodynamic and electrochemistry considerations, the void fraction increases at a higher current density, higher temperature, narrower space between electrodes, and larger height. Subsequently, ohmic and concentration losses increase and a higher overpotential is required to dissociate hydroxide ions.

Figure 4.9 shows the apparatus used in the experimental measurements in the laboratory. Inside each half cell (350 mL capacity) made of quartz, the electrodes are assembled vertically and fixed in parallel. The height of the electrodes is varied between 10 mm to 50 mm, while the diameter of the electrodes is fixed at 6 mm. A separator membrane is set at the middle position between electrodes to conduct hydroxide ions. The separator sheet is an anion exchange membrane sheet of 4 mm thickness based on chloride form. A DC power supplier enables DC current up to 60 A and DC voltage up to 6 V between the electrodes, while the current density ranges from 50 to 300 mA cm⁻². Hydrogen and oxygen gas are collected in gas collectors and measured by gas pressure sensors. The temperature of

the KOH aqueous solution is controlled at 20 °C, 40 °C, or 60 °C, while being agitated by a hot plate stirrer. The over-potential of OER is measured by a calomel reference electrode for each operating condition. The surface of the electrodes is polished after several experiments to keep the same overvoltage on electrodes.

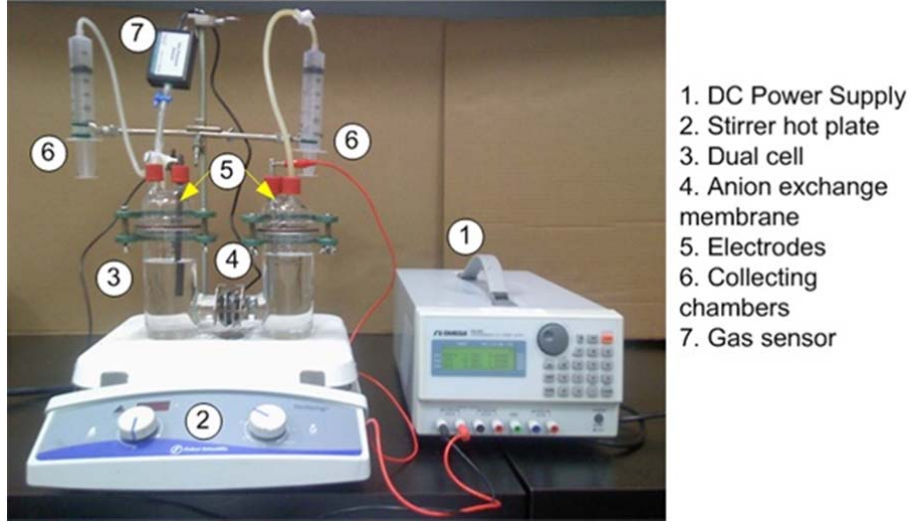


Figure 4.9: Experimental apparatus for electro-catalytic water splitting.

4.12. Uncertainty analysis of experimental data

The uncertainties associated with measurements acquired from three different setups, as described in Section 4.1.1, 4.1.2, and 4.1.11, are outlined in this section. Kline and McClintock's [197] method is used for estimating the uncertainties. The uncertainty evaluation is based on precision and bias limits. The precision error for each set of measured data is estimated based on its standard deviation as follows [198]:

$$U_{P,measurement} = \frac{S_D}{\sqrt{N}} \quad (4.1)$$

The bias error is an estimate of the fixed error magnitude, and remains constant for all the experiments. The mode of deviation from the mean is assigned as the bias error. The bias errors are associated with the pressure sensor, data acquisition system, and digital calliper for the photo-reactor, pressure sensors, and multimeter for the dual-cell experimental setup. The precision and bias errors for the devices are obtained from the equipment manufacturers as listed in Table 4.3. The total precision and bias errors are calculated by

$$U_P = \sqrt{U_{P,measurement}^2 + U_{P,device}^2} \quad (4.2)$$

$$U_B = \sqrt{U_{B,measurement}^2 + U_{B,device}^2} \quad (4.3)$$

The overall uncertainty in the determination of measurement range of each parameter (X) is then obtained from

$$\frac{U_N}{X} = \sqrt{\left(\frac{U_B}{X}\right)^2 + \left(\frac{U_P}{X}\right)^2} \quad (4.4)$$

The uncertainty associated with each experiment is mentioned in results section.

Table 4.3: Precision and bias errors of measurement devices.

Device/ Model	Precision Error	Bias Error
Pressure sensor / PX409-USB	0.001 kPa	0.005 kPa
Pressure sensor / Vernier	0.0015 kPa	0.005 kPa
Digital calliper/ iGAGING (IP54)	0.01 mm	0.012 mm
Multimeter (electric current and voltage measurement)	0.1 mA	0.155 mA
pH meter/ Omega (PHH-103A)	0.08 pH	0.15 pH

Other sources of error in the measurement process for both photo-reactor and dual-cell include positioning of sensors, non-steady state operation, spatial variations of temperature and pressure, time scales, and impurities of aqueous solution. Furthermore, measurement of over-potential and pH of the anolyte in oxygen production analysis is engaged with similar error sources.

Prior to experiments, several measurement tests are performed to find the best location for installing the pressure, temperature, and pH sensors. The spatial variation of temperature and pressure are almost negligible since the reactor accommodates less than 300 mL of solution which has been well agitated during the measurements. The photo-catalytic hydrogen production experiments in the dual-cell reactor are performed in a quasi-steady operation mode. The operation is paused at specific time intervals to purge the reactor and replenish fresh chemicals. The truncated data between each time interval are integrated and post-processed to minimize the non-steady state measurement effect. The precision error related to possible impurities and other inevitable factors are also estimated by a comparison of each set of data with a bench-mark. The bench mark is chosen among the measured values, during a repeatability test, which has the least uncertainty value. The cumulative effects of

the non-steady state operation, impurities, and other intervening factors are summarized in Table 4.4.

Table 4.4: Cumulative precision errors of measurements.

Parameter	Precision Error
Pressure	0.001 kPa
Temperature	0.5 K
Voltage	0.1 V
pH	0.1 pH

Chapter 5

Conceptual Design and Scale-up Study

5.1. Conceptual designs

In this section, the proposed systems including hybrid photo-catalytic water splitting system, electro-catalytic seawater splitting system, and large scale continuous flow photo-reactors are described in detail. The related results extracted from mathematical modeling, energy, exergy, and environmental analysis are presented in Section 7.

5.1.1. Water splitting reactor with hybrid photochemical conversion of solar energy

A photochemical reactor comprises a radiation source, a reactor transparent for the light, a gas product outlet and a photocatalytic reactor. As shown in Figure 5.1, the vessel comprises two photochemical reactors separated by a light driven proton pump membrane. Similar to natural photo-systems, an artificial water-splitting photo-system requires a number of essential molecular components that must be organized in supramolecular complexes such that the photo-generated electron-hole pair is quickly and efficiently separated and the potential energy is delivered to functional co-catalysts. The system contains a minimum number of necessary components such as a photo-sensitizer, oxygen and hydrogen evolution reaction catalysts. An efficient and robust sensitizer absorbs photons and generates long-lived electron-hole pairs that are coupled to appropriate multi-electron co-catalysts for oxygen and hydrogen evolution.

Photolysis solutions consist of $[\{(bpy)_2Ru(dpp)\}_2 2RhBr_2](PF_6)_5$ ($65\mu M$), water ($0.62 M$) acidified to $pH = 2$ with triflic acid, and dimethylaniline ($1.5 M$) in a solution of acetonitrile ($4.46 mL$) [9]. In the water photo-oxidation reactor, on the left, selected supramolecular photo-catalysts are used to capture light energy and generate electrical charges at reaction sites to oxidize water and produce oxygen gas and protons. Fresh water is continuously supplied to this reactor, and the flow rate of fresh water is adjusted such that the water level in the vessel remains constant.

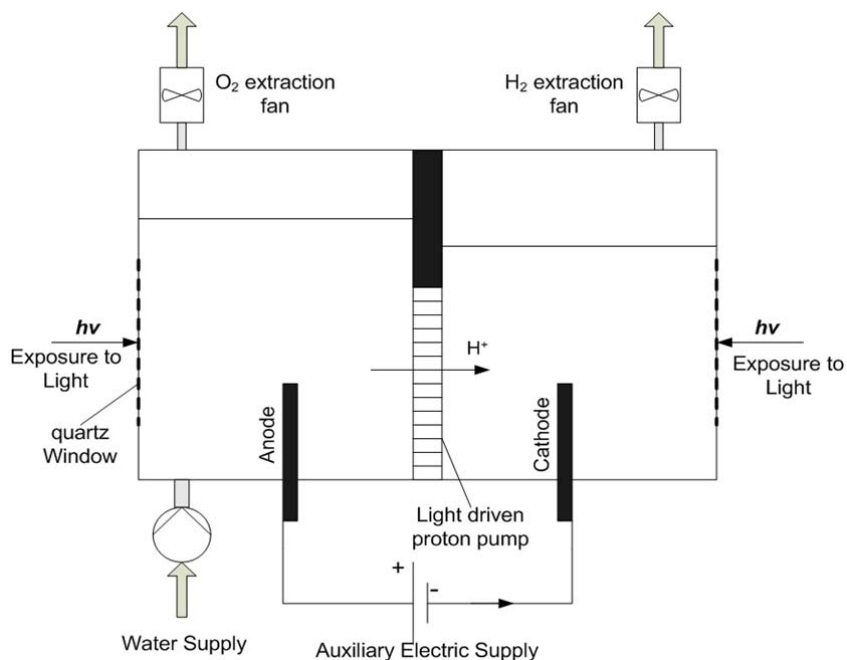


Figure 5.1: Schematic of water splitting photochemical reactor with external power source.

In the water reduction reactor, selected supramolecular complexes for photocatalytic reduction of water to hydrogen are dissolved in a proper concentration. These catalysts generate photoelectrons, which makes hydrogen evolution reactions occur. An auxiliary electric circuit is established to provide an external electric potential and improve the photocatalytic reaction performance. Negative charges, generated by a power supply, are donated at the electrode surface to the supramolecular devices, and these are transmitted to the reaction sites under the influence of photonic radiation. Two extraction fans are used above the liquid level, to extract oxygen and hydrogen, continuously.

In this study, the Ru(II)- bipyridyl complexes are considered as sensitizers to drive the water-splitting reaction. As seen in the modified Latimer diagram, shown in Figure 5.2, each cycle starts with photoreactions to capture the light energy (at ~ 450 nm or 2.75 eV) to form the excited single molecule $[\text{Ru}(\text{bpy})_3]^{2+*}$. This molecule rapidly loses some energy with an intersystem crossing to the triplet state, $[\text{Ru}(\text{bpy})_3]^{2+*}$. The photo-excited complex, denoted $[\text{Ru}(\text{bpy})_3]^{2+*}$ or more simply Ru^{2+*} , is both a good oxidant and a good reductant. Electron transfer either to or from the excited state complex traps the ruthenium complex as $[\text{Ru}(\text{bpy})_3]^+$ or $[\text{Ru}(\text{bpy})_3]^{3+}$, respectively.

These photoproducts are potent reductants ($[\text{Ru}(\text{bpy})_3]^+$) and oxidants ($[\text{Ru}(\text{bpy})_3]^{3+}$) which can drive subsequent redox reactions. These various species can be

used to drive a catalytic reaction by either an oxidative or reductive quenching pathway. The steps of the water-splitting reaction within these two manifolds are also shown in Figure 5.2. The reactions are normalized to a 4-photon, 4-electron process, and a pH of 7.0 is assumed. EA and ED refer to generic electron acceptor and donor molecules.

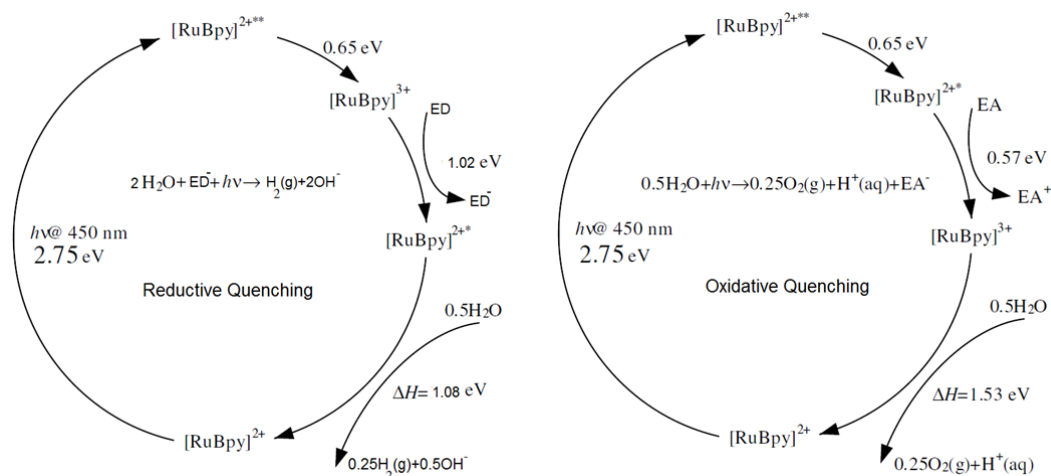


Figure 5.2: Photoreactions based on reductive and oxidative quenching of the photo-excited [Ru(bpy)₃]²⁺.

5.1.2. Dual-cell reactor for seawater electro-catalysis

Although hydrogen production occurs at high coulombic efficiency, it causes a localized pH change. It leads to a higher cell voltage and solid deposition as significant challenges of seawater electrolysis. In this regard, the anolyte feed after oxygen evolution to the cathode compartment for hydrogen production is examined.

Two different configurations for the electro-catalytic cell are designed to evaluate the effectiveness of a seawater feeding system. The conceptual design of the cells is shown in Figure 5.3. The dual-cell is composed of an anode, a cathode, and a membrane to separate the electrodes. The molybdenum-oxo catalyst dissociates the seawater to produce hydrogen. A nickel electrode is used as the anode. For a conventional configuration (Figure 5.3a), an anion exchange membrane enables monovalent anion transport, but a cation exchange membrane is suggested in the new conceptual design (Figure 5.3b).

The feeding system in this design differentiates it from ordinary dual-cells for seawater electrolysis. The neutral solution is fed to the inlet of the anode compartment, and the pH of the solution decreases due to oxygen and chlorine evolution in the anode compartment. The low pH solution is flowed into the cathode compartment. The pH values of

the catholyte and anolyte are measured, and the feed flow rate can be adjusted at the inlet of the cathode compartment. The applied potential for electrolysis and pH values of the electrolyte volume are considered for industrial electrolyzers. The variation of three parameters including pH, potential of cathode compartment, and flow rate of the feeding system are estimated and controlled by the anodic reaction duration.

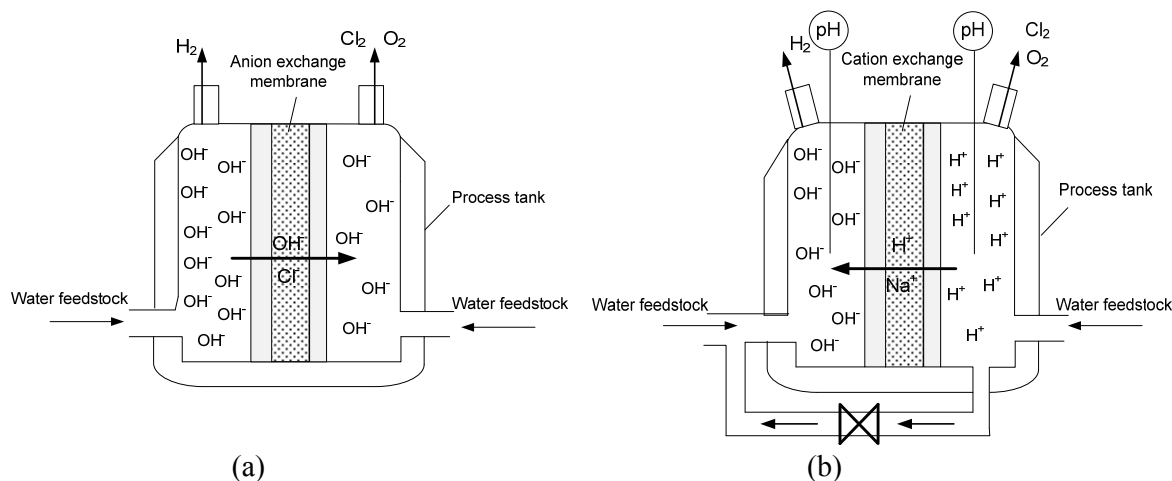


Figure 5.3: (a) Seawater electro-catalysis system and (b) modified seawater electro-catalysis system.

5.1.3. Conceptual design for large-scale continuous flow photo-reactor

A photo-catalytic reactor activated by sunlight and UV-visible lamps capable of continuous operation under real process conditions is considered for scale-up purposes. Figure 5.4 shows an assembly of a hybridized photo-catalysis reactor that utilizes the light energy from both the sun and a lamp, in conjunction with electrodes to substitute sacrificial electron donors that consume photo-generated holes or transfer charge to a metallic active center of catalyst that leads to hydrogen evolution. More details are shown in Figure 5.5. Utilization of UV-visible lamps inside a sunlight concentrator provides the capability of performing photoreactions during night or cloudy periods.

This design addresses one of the challenges regarding oxidation and reduction mechanisms in photo-catalysis that involves replenishment of electron acceptors and donors. Continues consumption of electron donors requires replenishment of the material either by a sustainable reforming process of electron donors, or by extraction and replacement of the electron donors. The proposed approach applies an external power source and two electrodes immersed in the catalyst solution to supply and transfer electrons inside two reactors. The presence of an ionic molecular device at the electrode interface, where it exchange electrons

(donate or accept) with high activity, eliminate the need for coating the electrode surface by expensive catalysts such as platinum group materials.

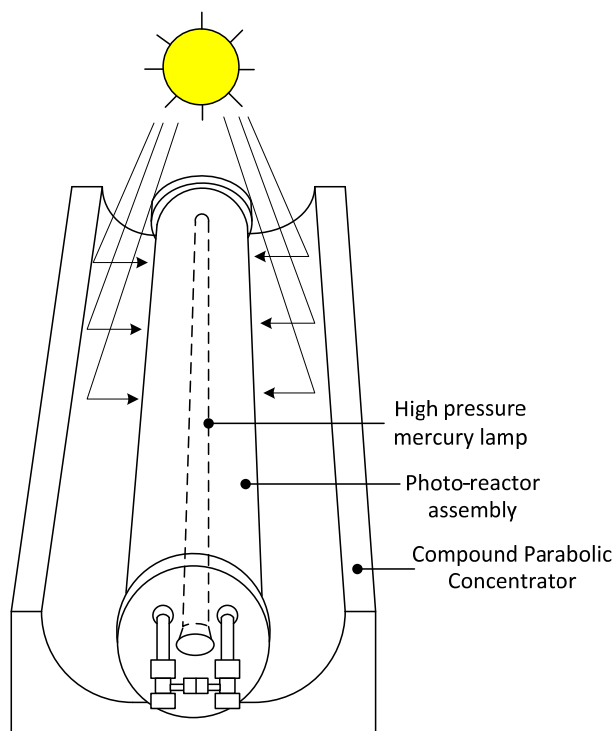


Figure 5.4: Pilot plant scale hybrid photo-reactor for continuous operation, under sunlight and artificial illumination.

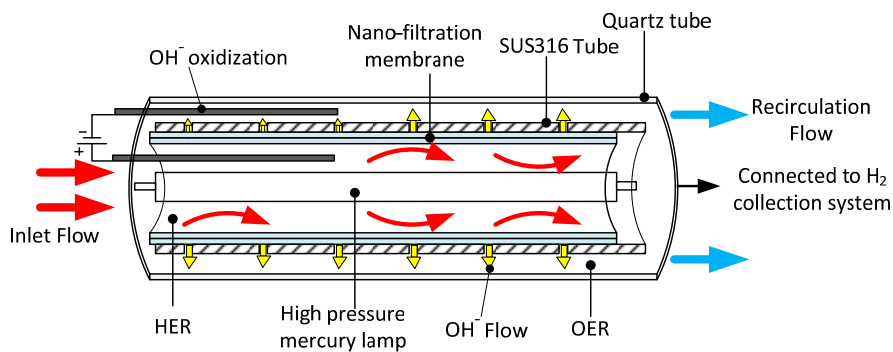


Figure 5.5: Schematic of hybrid photo-reactor.

A nano-filtration membrane is utilized to separate hydrogen and oxygen in the reactor. This membrane retains the catalyst while allowing passage of the solvent, water, and produced ions (H^+ or OH^-) into a second reactor. The neutralized solution will be recirculating to the inlet flow in order to maintain the species concentration constant. Prior to

the photocatalytic reaction, a constant-flow pump is used. After the system has reached a steady state, the light source is turned on and the photocatalytic reaction for water splitting is initiated.

While photocatalytic hydrogen production under visible light irradiation ($\lambda \geq 430$ nm) is more desired, efficient utilization of the UV portion of solar light by CPC is also an important consideration. The photons in the UV range are much more efficient in driving the photocatalytic hydrogen production. In the process of reactor design, very low flow velocities are avoided to prevent a decrease in the hydrogen production rate. Also, if the flow velocity is too high, this would lead to a significantly reduced exposure time of the photocatalyst to solar light, which is not beneficial considering that sufficient radiation time is essential for the photocatalytic reaction to proceed efficiently [199]. Thus an optimal flow velocity is needed for such systems.

It is necessary that uniform flow be maintained at all times in the reactor, since non-uniform flow causes non-uniform residence times that can lower the efficiency compared to ideal conditions. In the case of a heterogeneous process with photocatalyst powder in suspension, sedimentation and depositing of the catalyst along the hydraulic loop must be avoided, so that turbulent flow in the reactor is maintained. As reported by Malato et al. [199], the Reynolds number between about 10,000-50,000 assures fully turbulent flow and avoids the settlement of TiO_2 particles in the tubes. The requirement for turbulent flow makes the pressure loss an important parameter, especially in the case of an industrial plant with long reactor tube lengths. Furthermore, every photo reactor design must guarantee that the useful incoming photons are mostly used and do not escape without having intercepted a particle in the reactor.

5.1.4. Exergo-environmental study of large-scale solar reactors

In this section, a continuous flow photo-catalytic system is introduced, where photocatalytic hydrogen production occurs by water splitting. Figure 5.6 shows a schematic of a hybridized photo-catalysis system for water splitting that utilizes the photo-reactor described in the previous section. In order to compare the exergetic performance and greenhouse gas emissions reduction of this system, the method of solar-thermal steam reforming of methanol is also analyzed. Both methods use medium operating temperatures for solar hydrogen production, but with different CO_2 emissions and productivities. Photo-catalytic hydrogen

production has lower energy conversion rates than methanol reforming processes, but without emissions.

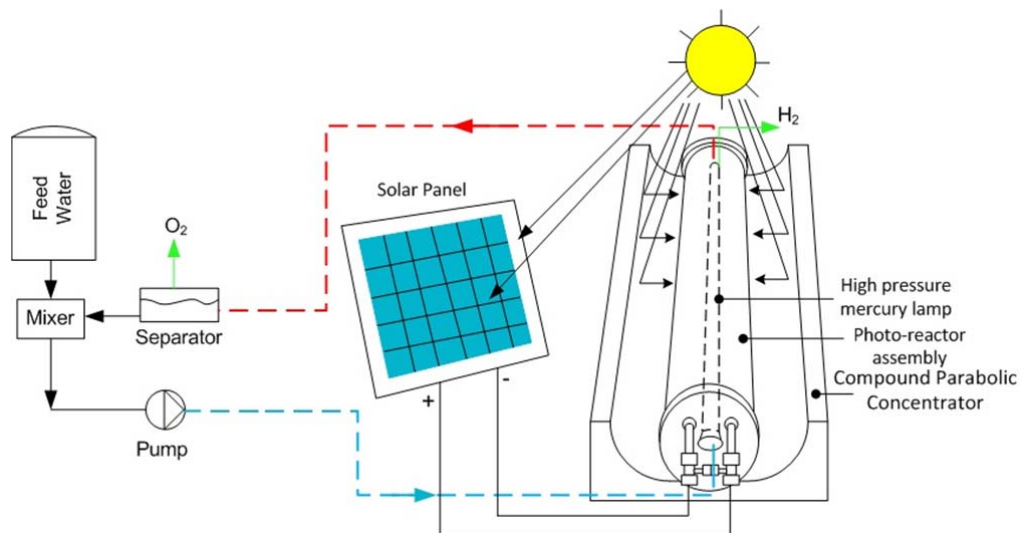
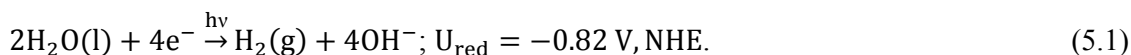
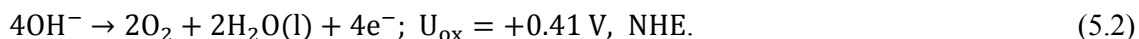


Figure 5.6: Pilot plant scale hybrid photo-catalytic system for continuous operation, under sunlight and artificial illumination.

An anion exchange membrane is utilized to separate hydrogen and oxygen in the reactor. This membrane retains the catalyst while allowing passage of the negative ions such as hydroxide ion by-products into a second reactor. The water photo-reduction reaction occurs as follows:



Hydrogen is separated from water in the hydrogen evolution chamber and used for measurement and storage. The transfer of hydroxide ions from the hydrogen evolving reactor to the oxygen evolving reactor and decomposition of these ions to constituent molecules are necessary processes to avoid any rate limiting effects. Subsequently, the pH of the aqueous solution is balanced and the excess charge is neutralized. The hydroxide ion decomposition at the anode occurs based on the following reaction:



The neutralized solution recirculates to the inlet flow to maintain constant concentration of species. Oxygen is then separated from water in a gas-liquid separation unit after the reactor bed. In conjunction with a solar light source, a 500 W high pressure mercury lamp is utilized to enhance the light intensity and operation at night. Prior to the photocatalytic reaction, a 10 kW constant-flow pump is used. After the system has reached a steady state, the mercury lamp can be turned on and the photocatalytic reaction for water splitting is boosted due to a higher light intensity.

As mentioned in the previous section, the Reynolds number in range of 10,000-50,000 is selected to avoid settlement of catalyst particles in the tubes and ensure fully turbulent flow [199]. In order to prevent non-uniform residence times the reactor flow should be kept uniform. Also for efficient capturing the incoming photons and maximizing the interception of catalyst particles in the reactor a Compound Parabolic Concentrator (CPC) is utilized. For the maximum absorbance of solar radiation, the aperture of the CPC should be perpendicular to the incident light as far as possible.

For photocatalytic hydrogen production, the total volume of recirculating water in the hydraulic loop is 10 L. In this analysis, the catalyst concentration effect on hydrogen production is investigated in the range of 0.3 g L⁻¹ to 2 g L⁻¹ and the flow rate from 1 L min⁻¹ to 8 L min⁻¹. The concentration of Na₂S as a sacrificial agent is kept at 0.05 mole L⁻¹ during the operation. Photocatalytic hydrogen production is considered under visible-light irradiation ($\lambda \geq 430$ nm). The reaction temperature is 60 °C. The reactor temperature is controlled to avoid water boiling.

Figure 5.7 shows a general schematic of a system for solar thermal hydrogen production using methanol steam reforming (MSR), which consists of a heat exchanger, solar receiver/ reactor, separator, and solar parabolic trough concentrator. During this process, the fresh methanol liquid fuel and the feeding water were initially mixed and fed to the evaporator. The mole ratio of water to liquid methanol was investigated in the range of 1 to 2.5. The solar flux is also varied from 350 to 850 W m⁻², and it affects the conversion rate from 20% to 100%, respectively [200]. The superheated vapour of methanol and steam generated in an evaporator heat exchanger, as shown in Figure 5.7, were made to flow into the middle-temperature solar receiver/reactor. The following reaction takes places at relatively low reforming temperatures (150 °C – 300 °C):



In the solar receiver/reactor, methanol steam reforming was conducted, driven by solar thermal energy at 150 °C – 300 °C. The gas products included H₂, CO₂, non-reacted CH₃OH, and H₂O, which left the reactor and were cooled in a plate-fin condenser by a water-cooling system, where the non-reacted methanol fuel and water were separated from one another. The non-reacted mixture can enter the next loop using a 10 kW constant-flow pump. Production of CO gas is neglected in this analysis.

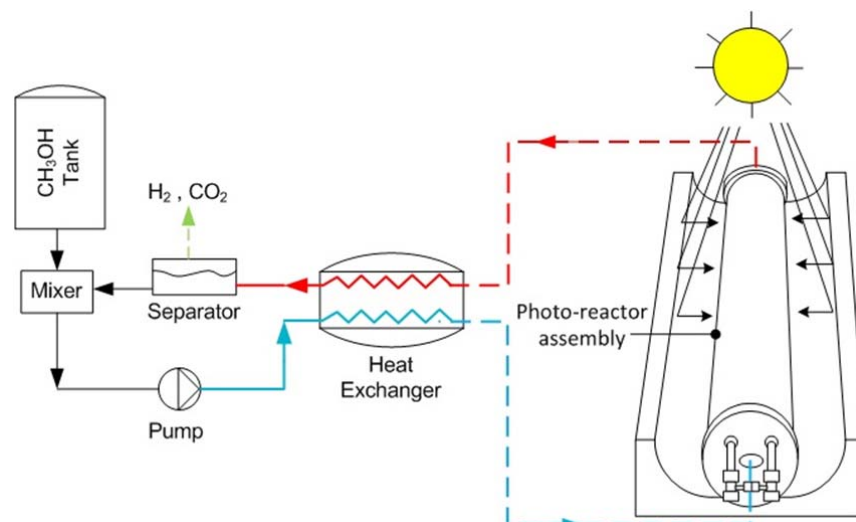


Figure 5.7: Schematic of solar thermal hydrogen production by methanol steam reforming.

For both photocatalytic water splitting and solar-thermal methanol reforming systems, a solar receiver/reactor is considered to consist of a parabolic trough concentrator and a tubular bed receiver/reactor. The parabolic trough concentrator is composed of glass mirrors with 4 m length. The aperture area is 10 m^2 and it delivers up to 6 kW at a peak solar flux. The solar reactor dimensions are designed as 30 mm in outer diameter and 4.5 m in length. A transparent glass with an outer diameter of 50 mm and 0.9 transmissivity level is considered as the receiver/reactor insulation. The catalyst for methanol steam reforming is immobilized in a packed tubular bed, whereas the photo-catalyst for water splitting is suspended in aqueous solution and flows through the hydraulic loop.

5.2. Scaling-up study

5.2.1. Methodology

The design of a large photo-catalytic reactor requires the prediction of the reactant's conversion on a macroscopic scale. A kinetic model with parameters based on a phenomenological or mechanistic basis should be developed to evaluate the reaction rate under operational conditions of a photo-reactor. Some equations such as the Langmuir-Hinshelwood kinetic model may be utilized to consider the effect of radiation flux, concentration of the reactants and products, and catalyst concentration.

The experimental features of the reactor should not dominate the kinetic models for the design of photo-catalytic reactors. The reaction mechanism of the process, including the light induced steps and electron-hole formation rate, should be modeled in detail.

Consequently the derived kinetic expressions which have been developed are not only valid for the experimental setup but can also be extrapolated to the scaled-up reactor. Figure 2 summarizes the proposed methodology.

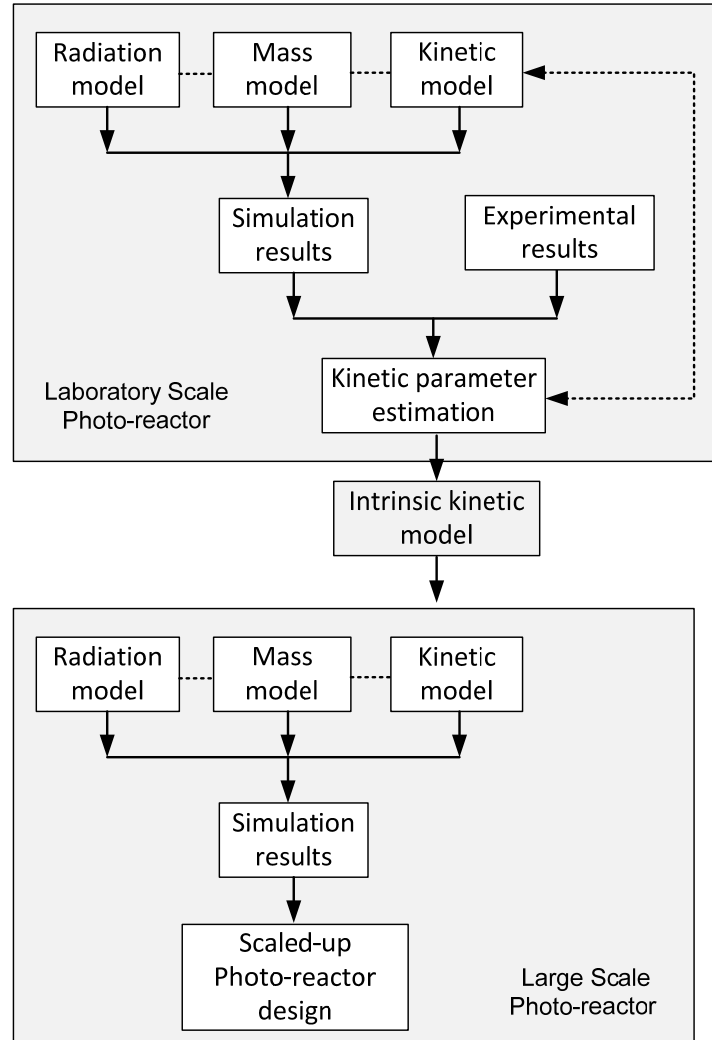


Figure 5.8: Scale-up methodology.

An algorithm that minimizes the error between the experimental results and the predicted values can be utilized to validate the proposed kinetic equation and the related constant values. The design of the large-scale photo-reactor can be initiated after the intrinsic kinetic model of the process is obtained using laboratory data. The complete scale-up procedure can be validated by construction of the designed photo-reactor and comparison of its performance with the predicted values.

5.2.2. Modeling of photo-reactor

In this section a general mathematical model for the steady-state continuous flow and externally illuminated photo-reactor is presented. This model applies to cuboidal and cylindrical reactors with external irradiation. It consists of a mathematical model for light absorption, intrinsic kinetics, and mass balance as the main considerations in the scale-up analysis. Predictive models for photo-catalytic reactors involve uncertainties due to the radiation diffraction that causes non-uniform distribution of the local radiation absorption and reaction rates.

5.2.2.1. Light absorption model

For a photo-reactor that is uniformly illuminated from one side, the Lambert-Beer law is applied to consider light absorption by the solvent medium that lead to light attenuation inside the photo-reactor. Thus, the light intensity (I) at a distance (L) from the illumination surface is given by

$$I = I_0 \exp(-\Psi C_{solvent} L) \quad (5.4)$$

where I is the light intensity (W m^{-2}) that reaches the illumination surface, Ψ is the solvent medium mass attenuation coefficient ($\text{cm}^2 \text{g}^{-1}$), and $C_{solvent}$ is the solvent concentration, e.g. water in this study. As shown in Figure (5.9a), the distance (L) is from the illumination surface to a point inside the photo-reactor where the light penetration is almost zero.

Figure (5.9b) shows a schematic diagram for an externally illuminated cylindrical photo-reactor. Assuming that the photo-reactor is composed of two concentric cylindrical compartments of equal volume, the radius of the inner cylinder would be $D/2 - D_0$. Equation (5.5) expresses the total volume of the photo-reactor in terms of the volume of the inner cylinder.

$$\pi h \left(\frac{D}{2}\right)^2 = 2\pi h \left(\frac{D}{2} - D_0\right)^2 \quad (5.5)$$

where h is the liquid level in the photo-reactor. Subsequently, the distance (D_0) from the surface of the photo-reactor to the surface of the inner cylinder is $D_0 = 0.1464D$.

The total amount of light energy that reaches the illumination surface is equal to the total amount of light energy on the surface of the concentric inner cylinder, as written in Equation (5.6). Thus, the light intensity (I) received by the surface of the concentric inner cylinder is given by

$$I_0 \pi D_0 h = I \pi (D - 2D_0) h \quad (5.6)$$

$$I = \frac{I_0 D_0}{D - 2D_0} \quad (5.7)$$

Considering the light attenuation due to absorption by the solvent, Equation (5.7) is replaced by the following equation:

$$I = \frac{I_0 D_0}{D - 2D_0} \exp(-\Psi C_{solvent} D_0) \quad (5.8)$$

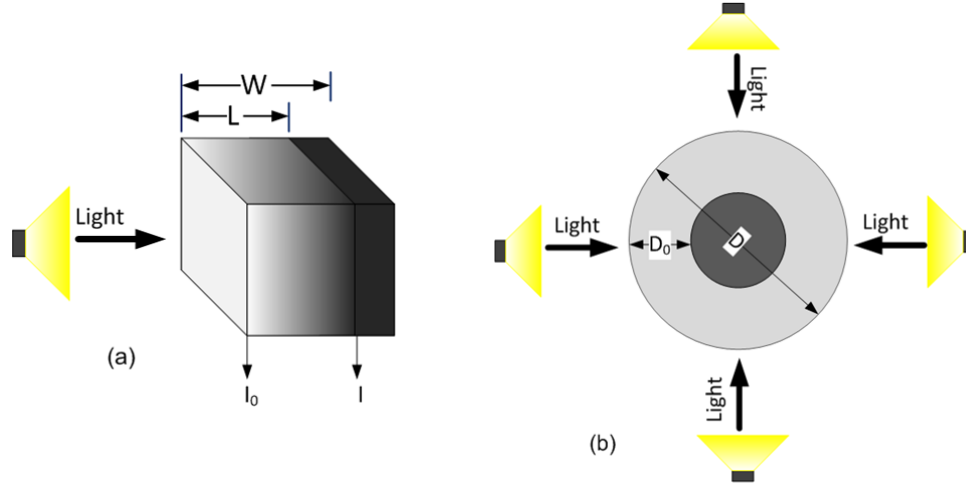


Figure 5.9: Schematic representation of light distribution in (a) externally illuminated cuboidal photo-reactor, (b) externally illuminated cylindrical photo-reactor; I_0 : incident light intensity, I : light intensity inside the photo-reactor, L : Length of photo-reactor, D : diameter of the cylindrical photo-reactor.

The useful photons with energy beyond the band-gap limit of the photo-catalyst are only absorbed by the solid photo-catalyst particles. If the scattering albedo of the catalyst is smaller than approximately 0.3, the light scattering effect can be safely neglected [158]. This coefficient is defined as

$$\omega = \frac{\sigma}{\sigma + \alpha} \quad (5.8)$$

where σ is specific mass scattering coefficient averaged over the spectrum of the incident radiation, and α is specific mass absorption coefficient averaged over the spectrum of the incident radiation. In the reaction space, it is assumed that the useful photons enter the reactor liquid volume in an orthogonal direction to the radiated surface.

In this study, the Equation (5.9) is used to calculate the attenuated light intensity that reaches the catalyst particles and it is absorbed. The modeling assumptions are based on the experimental apparatus configuration, and the existing tubular photo-catalytic reactor which is illuminated from one side. Therefore the average absorbed light by the catalyst can be expressed as

$$I = \Lambda I_0 \exp(-\Psi C_{solvent} L) \quad (5.9)$$

where $\Lambda = \alpha C_{cat}$ is the absorption coefficient averaged over the spectrum of the incident radiation.

5.2.2.2. Fluid dynamics model

In this study, a steady-state, continuous flow condition is assumed. The liquid phase is a Newtonian fluid with constant physical properties. The distribution of the catalyst particles is assumed to be uniform within the liquid volume; however, the concentration of solids does not cause substantial changes in the physical properties of the fluid.

5.2.2.3. Intrinsic kinetic model

The rate of water splitting, at each point in the reaction domain, is considered to be proportional to the average volumetric rate of energy absorption raised to the m^{th} power and to the n^{th} power of water concentration C_{H_2O} as follows:

$$r = K(\Lambda I_0 \exp(-\Psi C_{Solvent} L))^m C_{H_2O}^n \quad (5.10)$$

where K is a constant that takes into account all other factors that may affect the overall quantum yield, with the exception of the water concentration and absorbed light. The coefficients m and n should be estimated by linear regression of experimental data, and the K coefficient has to be determined by least-squares fitting of the modeling equations to the experimental results. This power law model is preferred to the Langmuirian rate equation for the sake of simplicity. The Langmuir type of kinetic model does not offer significantly better representation of these phenomena [201].

The objective is not to involve complicated representation of the reaction mechanism but to provide a satisfactory model of the rate data. The present kinetic rate equation does not include the effect of reaction intermediates, but the K coefficient this effect to some extent.

5.2.2.4. Mass balance

In photo-catalytic reactor design, the mass species transform into another through chemical reactions. Considering the rate of formation of each component within the control volume a material balance can be proposed [202]. The component balance for a substance A is

$$\text{Flow rate of component A into the volume} + \text{net rate at which component A is consumed during reaction} = \text{Flow rate of component A out of the volume} + \text{net rate at which component A accumulates within the volume} \quad (5.11)$$

A component balance can be expressed in mass units; however, component A will be a distinct molecular species. It is more convenient to use molar units. For the water component in the case of photo-catalytic water splitting, the mass balance would be

$$Q_{in}C_{H_2O,in} + \bar{R}_{H_2O}V = Q_{out}C_{H_2O,out} + \frac{d(V\bar{C}_{H_2O})}{dt} \quad (5.12)$$

where \bar{R}_{H_2O} is the volume-average rate of consumption of water in moles per volume per time, and \bar{C}_{H_2O} is the spatial average of the molar concentration of water. Since water is consumed to evolve the hydrogen evolution, the \bar{R}_{H_2O} value is negative.

In this study, the photo-catalytic water splitting is performed in a quasi-steady mode. In other words, the water and other chemicals, e.g. sacrificial agents, are supplied to the photo-reactor at specific time intervals to maintain a constant reaction rate. Therefore the last term of Equation (5.12) is neglected.

5.3. Scale-up relationships and methods

The scale-up relationships and strategies for tubular reactors are examined. Results are restricted to tubes with a constant cross-sectional area. Scale-up factors are specialized for a non-isothermal reactor that operates in turbulent flow and a continuously stirred condition [202-203].

5.3.1. Scaling factors

The scaling factor (S) with respect to Y , as any design or operating variable of a chemical reactor, is defined as the ratio of Y in the full-scale plant to that of the laboratory scale.

$$S_Y = \frac{Y_{full\ scale}}{Y_{pilot\ scale}} = \frac{Y_2}{Y_1} \quad (5.13)$$

Scaling factors may vary depending on the specific type of reactor. For tubular reactors, a combination of radius and length gives the scaling factor for volume,

$$S_V = \frac{V_2}{V_1} = \frac{\pi R_2^2 L_2}{\pi R_1^2 L_1} = \left(\frac{R_2}{R_1}\right)^2 \left(\frac{L_2}{L_1}\right) = S_R^2 S_L \quad (5.14)$$

where $S_R = R_2 / R_1$ and $S_L = L_2 / L_1$. The scaling factors for volumetric flow rate and radius can be expressed as a ratio of linear velocities, \bar{u}_2 / \bar{u}_1 :

$$S_{\bar{u}} = \frac{\bar{u}_2}{\bar{u}_1} = \frac{(Q/\pi R^2)_1}{(Q/\pi R^2)_2} = S_Q S_R^{-2} \quad (5.15)$$

The Reynolds number can be written as

$$S_{Re} = \frac{Re_2}{Re_1} = \frac{R_2 \rho_2 \bar{u}_2 / \mu_2}{R_1 \rho_1 \bar{u}_1 / \mu_1} = \left(\frac{R_2}{R_1} \right)^{-1} \left[\frac{\pi R_2^2 \rho_2 \bar{u}_2}{\pi R_1^2 \rho_1 \bar{u}_1} \right] = S_R^{-1} S_{mass\ flow} \quad (5.16)$$

where

$$S_{mass\ flow} = \frac{\text{mass flow through full-scale unit}}{\text{mass flow through pilot unit}} = \frac{(\rho Q)_{full\ scale}}{(\rho Q)_{pilot\ scale}} \quad (5.17)$$

If the small and large reactors have the same density, then $S_Q = S_{mass\ flow}$. Since the product $\rho \bar{u}$ appears in some equations, the constant density assumption is not required.

Table 5.1 presents scale-up factors for a tubular reactor that operates with turbulent flow. In this study, the Reynolds number for the bench scale apparatus is more than 3000 due to a high agitation speed. Therefore, scale-up analysis is performed based on turbulent flow in a stirred tank. The information in the Table is sorted based on a residence time dependence. The general scale-up factors in Table 5.1 consider $S_{mass\ flow}$, S_R , and S_L as independent variables. These factors can be used regardless of reaction characteristics.

Table 5.1: Scale-up factors for tubular reactor operating with constant properties.

Fully turbulent flow	Unconstrained with arbitrary \bar{t}	Scale-ups with constant \bar{t} $S_{mass\ flow} = S = S_R^2 S_L$		Scale-ups with constant \bar{t}
	General scale-up factors	S and S_R specified	S and S_L specified	Geometric Similarity
Diameter scaling factor	S_R	S_R	$S^{1/2} S_L^{-1/2}$	$S^{1/3}$
Length scaling factor	S_L	$S S_R^{-2}$	S_L	$S^{1/3}$
Length to diameter ratio	$S_L S_R^{-1}$	$S S_R^3$	$S^{1/2} S_L^{-1/2}$	1
Velocity, \bar{u}	$S_{mass\ flow} S_R^{-2}$	$S S_R^{-2}$	S_L	$S^{1/3}$
Pressure scaling factor ΔP	$S_{mass\ flow} S_R^{-4} S_L$	$S^2 S_R^{-6}$	$S^{-1} S_L^3$	$S^{1/2}$

5.3.2. Scale-up methods

The mean residence time (\bar{t}) is one of the main constraints in scale-up analysis. A constant mean residence time as the main constraining scale-up factor is preferred in this study. The general scale-up factors are then subject to the constraints that $S_{mass\ flow} = S$ and $S = S_R^2 S_L$. By imposing a constant value for \bar{t} , only two independent variables remain. S is

selected as one of them, and then either S_R or S_L can be chosen as the other. Table 5.1 gives both options. Depending on the scale-up method a specific value for either of S_R or S_L can be chosen.

The different paths to increase the capacity of a tubular reactor can be taken.

- 1) Parallel addition of identical reactors. This sets $S_R = S_L = 1$ for each reactor. The approach is widely used in the water treatment industry.
- 2) Increase of length. For a constant-density fluid, this strategy makes $S_R = 1$ and $S_L = S$. Increase of tube length to enlarge the capacity is not a common way, but it is viable.
- 3) Increase of tube diameter at constant length, $S_R = S^{1/2}$ and $S_L = 1$. This method is usually applied for gas phase and adiabatic reactors.
- 4) Increase both the length and diameter. This sets $S_R > 1$ and $S_L > 1$ subject to a fixed total volume constraint. The scale-up strategy based on geometric similarity utilizes this approach. It requires the same or close length to diameter ratio, L/D , for tubular reactors.

A scale-up method based on a constant Reynolds number is not recommended. If one sets $S_{Re} = S_R^{-1} S = 1$, this gives $S_R = S$ for the constant-density case. Applying the constraint that $S = S_R^2 S_L$ gives $S_L = S^{-1}$. Therefore, upon scale-up, the reactor becomes wider but shorter. In practical observation, scale-up leads to increase of the Reynolds number. In case of small reactor, turbulent flow is beneficial because the scaled-up model for the larger reactor will more closely approximate actual practice.

The use of geometric similarity in the scale-up of stirred tanks is common. Geometric similarity requires that the production-scale reactor has the same shape as the pilot-scale reactor. The same factor of $S^{1/3}$ applies to change all linear dimensions such as liquid height, reactor diameter, and impeller diameter. Surface areas will scale as $S^{2/3}$. Norwood and Metzner [204] proposed a classic correlation for turbine impellers in baffled vessels that can be applied to estimate the mixing time t_{mix} .

The mixing time in a stirred batch tank is the time taken for the contents of the vessel to become uniform. If the reactor mixing time, t_{mix} , is substantially shorter than the other characteristic times, e.g. residence time, the stirred reactors can be safely treated as a perfect mixer. The full correlation of t_{mix} is a complex function of the tank to impeller diameter ratio, the ratio of tank diameter to liquid level, the Reynolds number, and the Froude number. However, a first order approximation for geometrically similar vessels that operate at high Reynolds numbers can be reasonably used as $\omega t_{mix} = const.$ where ω is the rotational velocity of the impeller.

For agitated vessels, an additional scaling factor, S_N , which is the ratio of impeller speeds in a large rather than small vessel should be considered. Normally, the impeller speed decreases upon scale-up so $S_N < 1$ is usual. Table 5.2 is used to estimate the operational parameters.

Table 5.2: Scale-up factors for tubular reactor operating with constant properties.

	General scaling factor	Scaling factor for constant power per unit volume
Vessel diameter	$S^{1/3}$	$S^{1/3}$
Impeller diameter	$S^{1/3}$	$S^{1/3}$
Vessel volume	S	S
Residence time	1	1
Reynolds number	$S_N S^{2/3}$	$S^{4/9}$
Agitator speed	S_N	$S^{-2/9}$
Power	$S_N^3 S^{5/3}$	S
Mixing time	S_N^{-1}	$S^{2/9}$

Chapter 6

Analysis and Optimization

In this chapter, the analyses of photo-catalytic hydrogen production and electro-catalytic oxygen production processes are presented through mathematical and electrochemical modeling. Energy and exergy analyses of these processes are also presented and discussed. At the end of the chapter, an exergo-economic analysis of the photo-catalytic water splitting reactor is performed. The main assumptions that are considered in modeling and post-processing the experimental data are as follows:

- 1- The useful photons enter the reactor liquid volume in an orthogonal direction to the radiated surface.
- 2- The experimental results from the existing tubular photo-catalytic reactor are implemented in modeling the photo-reactor.
- 3- A steady-state, and continuous flow condition is assumed for the scale-up study.
- 4- The density and viscosity of the aqueous solution in the photo-catalysis are equal to those of water.
- 5- The dissociation of hydroxyl ions only occurs at the electrode interface.
- 6- The photo-reactor exergy loss and destruction result from chemical reaction, physical changes in water flow, radiation, and convective heat transfer from the reactor surface.
- 7- For the scale-up study, the reactor is assumed to be tubular and the flow is fully turbulent.
- 8- The mean residence time (\bar{t}) is constant.
- 9- In the exergo-economic study, all sacrificial agents for the photochemical process are recycled and electricity for internal use is provided.

6.1. Photo-catalytic hydrogen production

This section addresses the modeling of the photo-catalytic hydrogen production process by water reduction. The simulation of photo-catalytic water splitting is required for

better understanding of the light-induced hydrogen production mechanism, and design of an efficient photo-reactor.

Kinetic modeling based on molecular charge transfer, activation energies, and light intensities provides valuable information to explore the effects of bulk and surface processes on photo-catalytic reaction rate. The rate-determining steps have a strong effect on activation energies, and they consist of bulk processes related to carrier dynamics and surface reactions involving cleavage and formation of bonds, both of which should be studied concurrently. Hydrogen evolution in catalytic centers and extraction at the surface of a liquid solution involves molecular diffusion and mass transfer resistance. The influence of hydrogen pressure, in a gaseous phase, on reaction rate is also a key factor. This study develops a model to consider the aforementioned mechanisms. The results are also validated with experiments, as reported in Section 7.1.3.

6.1.1. Photo-catalysis and quantum efficiency models

The photo-catalytic reactions have a complicated sequence of competing processes. The water reduction by zinc sulfide photo-catalyst in an alkaline solution and sodium sulfide sacrificial agents is considered. The main possible reactions are shown in Figure 6.1. Following the incidence of a photon to the ZnS catalytic site, 1 pair of electron and hole is generated inside the photo-catalyst particles due to band gap excitation. The photo-excited carriers are diffused to surface active sites, where sodium sulfide scavenges the hole and a water molecule undergoes a surface redox reaction using the electron. The mass diffusion of reactants and products, and recombination of photo-excited carriers, occur simultaneously. A recombination of electrons and holes leads to losses in heat or light. Therefore, it is difficult to identify the dominant reaction during the photo-catalytic activity.

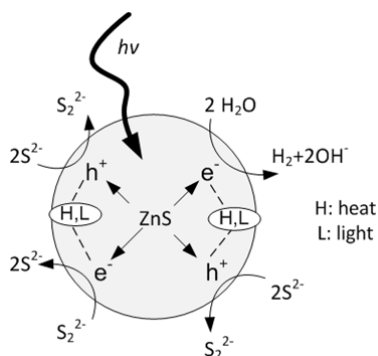


Figure 6.1: Schematic illustration of the possible reactions resulting from the irradiation of zinc sulfide in a sodium sulfide solution.

The photo-catalytic hydrogen production by water reduction undergoes the following reactions [7]:



The role of sulfide ions as hole scavengers is crucial to prevent the photo-corrosion of the catalyst. Photo-catalytic hydrogen formation occurs as a result of several competing events following absorption of a photon by a catalyst. These interactions can be explained as follows [205]:

- Excited state formation due to photon absorption and electron transition from the ground state to the vibronic energy level.
- Vibrational relaxation of the molecule by either vibrational transfer of energy to the surrounding medium or by individual rearrangement of energy levels.
- Fluorescence, which is a spontaneous emission of photonic radiation by relaxation of the energy.
- Phosphorescence, which is a relaxation to the ground state through spontaneous radiation of an excited molecule.
- Water molecular diffusion to the vicinity of the excited catalyst and effective encounter.
- Molecular desorption of hydrogen atoms from the catalyst active site.
- Hydrogen molecule formation.

The quantum efficiency of photo-catalytic hydrogen production can be expressed as the probability that a pair of incident photons could accomplish a sequence of aforementioned interactions that eventually lead to the formation of a hydrogen molecule. Each molecular event occurs at a specific rate. Therefore, the quantum efficiency can be expressed as follows:

$$\eta_\phi = k_{\text{H}_2} / \sum k_i \quad (6.3)$$

where k_{H_2} is the quantum rate at which a molecule of hydrogen is formed and $\sum k_i$ is the summation of the rates of all required events from photon absorption to hydrogen molecule desorption at a catalytic active site.

The quantum efficiency of light-induced hydrogen production is also defined as the ratio of the hydrogen production rate to incident absorbed photons;

$$\eta_\phi = \dot{n}_{\text{H}_2} / \dot{n}_{\text{ph}} \quad (6.4)$$

where \dot{n}_{H_2} represents the molar rate of hydrogen production and \dot{n}_{ph} is the photon rate, providing that each hydrogen molecule requires energy of 2 photons to evolve [206].

Considering that the quantum rate of hydrogen formation represents the inverse of the summation of time factors of all subsequent events to reduce a water molecule, then

$$k_{\text{H}_2} = (\sum \tau_j)^{-1} \quad (6.5)$$

Depending on the photo-catalytic system structure, some specific events should be taken into account. For the case of this study the following time factors are considered:

- Excited state formation (τ_{ex}), which is the time factor of catalyst activation, is estimated by the time factor in which an electron moves from valence to conduction band and has the order of $\tau_{\text{ex}} \cong 10^{-10}$ s.
- Hole scavenger encounter (τ_{HS}) is the time factor associated with sulfide ion encounter to the catalyst. This depends on the rate of molecular diffusion and can be calculated as [207]:

$$k_{\text{enc},\text{S}^{2-}} = 8/3 (RT/\mu) C_{\text{S}^{2-}} \quad (6.6)$$

where $k_{\text{enc},\text{S}^{2-}}$ is the constant rate at which the S^{2-} ion encounters the reaction site through a diffusion-controlled reaction. This depends on the solvent's dynamic viscosity (μ) and Na_2S molar concentration $C_{\text{S}^{2-}}$. The concentration of sulfide ions for the subsequent experiments in this study is between 0.24 to 1 M and the solvent is water. Therefore the encounter rate of the hole scavenger is in range of $1.8 \times 10^6 \text{ s}^{-1}$ to $7.5 \times 10^6 \text{ s}^{-1}$ which corresponds to a time factor of $\tau_{\text{HS}} \cong 5.5 \times 10^{-7}$ to 1.3×10^{-6} s.

- Intermolecular electron transfer (τ_{et}) is in the order of $10^{-9} - 10^{-7}$ s [208].
- The encounter time factor of a water molecule ($\tau_{\text{enc},\text{H}_2\text{O}}$) can be derived based on Equation (6.6). The rate of catalyst water encounter is almost $\tau_{\text{H}_2\text{O}} \cong 2 \times 10^{-6}$ s.
- The time factor of hydrogen atom formation (τ_{Hf}) includes the time for hydrogen atoms formation and desorption from the catalytic site. It has the typical order of $\tau_{\text{f}} \cong 10^{-6}$ s [208].

Therefore, the time factor of hydrogen evolution would be: $\tau_{\text{H}_2} = \tau_{\text{ex}} + \tau_{\text{HS}} + \tau_{\text{enc},\text{H}_2\text{O}} + \tau_{\text{Hf}} \cong 10^{-10} + 5.5 \times 10^{-7} + 5 \times 10^{-8} + 2 \times 10^{-6} + 10^{-6} \cong 3.6 \times 10^{-6}$ s; and the quantum rate of hydrogen evolution is $k_{\text{H}_2} \cong 2.78 \times 10^5 \text{ s}^{-1}$.

The main processes related to the events included in the dominator of Equation (6.3) consist of the following parts:

- Rate Constant of catalyst relaxation to the ground state (k_{GS}) through various possible mechanisms includes vibrational relaxation, fluorescence, phosphorescence, and electron-hole recombination. The excited state decay to ground state has typical

maximum value of $10^{-5} - 10^{-4}$ s.

- Rate constant of hydrogen evolution (k_{H_2}), as previously calculated.
- Rate constant of catalyst encounter with non-favorable ions and molecules ($k_{enc,i}$). The non-favorable ions and molecules refer to species which are present in the solution other than sacrificial agents and water molecules. Therefore, $k_{enc,i} = 8/3 (RT/\mu) (C_{H_2} + C_{Na_2S} + C_{NaOH})$.

The hydrogen evolved in solution is present in two forms of dissolved and dispersed phases. The concentration of dissolved hydrogen depends on the solubility limit of the aqueous solution. The rest of the produced hydrogen is in the form of rising bubbles of a relatively small diameter. The concentration of bubbles depends on the process boundary conditions and rate of hydrogen generation. The agitation of the aqueous solution enhances bubble bursting at the interface, and avoids hydrogen molecular diffusion back into liquid.

The molar concentration of dissolved hydrogen can be calculated using Henry's law

$$C_{H_2,dissolved} = P_{H_2}/\xi \quad (6.7)$$

where ξ is Henry constant with a value of $1,265.3 \text{ dm}^3 \text{ bar mol}^{-1}$ for dissolution of hydrogen in water, and P_{H_2} is the partial pressure of hydrogen above the liquid interface. Equation (6.3) can be expanded as follows:

$$\eta_\phi = k_{H_2}/[k_{H_2} + k_{GS} + 8/3 (RT/\mu)(C_{H_2,dissolved} + C_{H_2,bubble} + C_{Na_2S} + C_{NaOH})] \quad (6.8)$$

An expression of Equations (6.4) and (6.8) yields the expression for hydrogen production rate in terms of evolved hydrogen concentration

$$\dot{n}_{H_2} = \dot{n}_{ph} \times k_{H_2}/[k_{H_2} + k_{GS} + 8/3 (RT/\mu)(C_{H_2} + C_{Na_2S} + C_{NaOH})] \quad (5.9)$$

By substitution of constant values and rate of incident photons within the absorption spectra of the photo-catalyst for a specific timeframe, the Equation (6.9) can be solved analytically. The ratio of $C_{H_2,dissolved} / C_{H_2,bubble}$ has an order of 10^{-4} according to the experimental results reported in Section 7.1.

6.2. Fitting rate data and thermodynamics

The main goal in this section is to show how reaction rate expressions $r(a, b, \dots, T)$ are obtained from experimental data needed for the design of the chemical reactor. Model development begins by postulating a mathematical model that contains one or more parameters. An optimization routine is then used to adjust the parameters to obtain a good fit

to a set of experimental measurements. The usual approach is to minimize a sum of squares (SS) [202].

$$SS^2 = \sum_{Data} [experiments - model]^2 \quad (6.10)$$

where “experiment” refers to a measurement, typically of a concentration or reaction rate, made in a laboratory, at a pilot scale. The “model” refers to predictions of the concentrations or rates calculated from an assumed kinetic model. The simplest case occurs when the experiments are performed in a constant-density continuous flow stirred tank reactor (CSTR). Then the measured inlet and outlet concentration, $C(t)$, gives the reaction rate directly.

$$\left[\frac{C_{out}-C_{in}}{\bar{t}}\right]_{data} = [r_A]_{data} \quad (6.11)$$

For a reaction like $A \rightarrow B$, the postulated rate equation is

$$[r_A]_{model} = k_0 I^m C^n \quad (6.12)$$

The sum of squares has the form

$$SS^2 = \sum_{j=1}^J [r_{data} - r_{model}]^2 = \sum_{j=1}^J \left[\left(\frac{C_{out}-C_{in}}{\bar{t}} \right)_{data} - k_0 I^m C^n \right]^2 \quad (6.13)$$

where J is the number of data points and k_0 , m , and n are model parameters to be determined by the fitting routine. The situation is a more complex when the experiments are done in a batch reactor. Here, typical data consists of concentrations, $C(t)$, for various times within a run and for various temperatures between runs. Equation (5.10) takes the form

$$SS^2 = \sum_{j=1}^J [[C(t)]_{data} - [C(t)]_{model}]^2 \quad (6.14)$$

For $A \rightarrow B$, the model equation is

$$\frac{C}{C_0} = e^{-kt} \quad (6.15)$$

Subsequently Equation (6.14) becomes

$$SS^2 = \sum_{j=1}^J [C(t)_{data} - C_0 \exp[-k_0 t \exp(-\frac{T_{act}}{T})]]^2 \quad (6.16)$$

Thus, the procedure contains a functional form for the rate equation, substituted into the batch design equation and integration. The integration may be numerical. The result will be a prediction of $C(t)$ that can be compared directly to the experimental results.

6.2.1. Fitting CSTR data

In order to determine a function $r(C_a, C_b, \dots, T)$ for the reaction $A \rightarrow B$ and considering that the CSTR measurements are all performed at the same temperature, here are some options that contain no more than three adjustable constants:

$$r = k C_{out}^n \quad \text{or} \quad r = \frac{k C_{out}^n}{1 + k_A C_{out}} \quad \text{or} \quad r = k C_{a,out}^n C_{b,out}^r \quad \text{or} \quad r = \frac{k C_{out}^n}{1 + k_B C_{out}} \quad (6.17)$$

where C is concentration and n and k are model constants to be determined. The choice of a model that contains one, two, or more adjustable constants is a matter of physical judgment combined with mathematics. The mathematical portion is the minimization of the sum of squares

$$SS^2 = \sum_{Data} [r_{data} - r_{model}]^2 \quad (6.18)$$

where R_{data} is the set of J experimental rate measurements. For a variable-density CSTR, the experimental rate is calculated from

$$[r_A]_{data} = \left[\frac{Q_{out}C_{out} - Q_{in}C_{in}}{V} \right]_{data} \quad (6.19)$$

The predicted rate r_{model} is calculated by substituting the measured concentrations for $C_{a,out}$ and $C_{b,out}$ into one of equations (6.17) with assumed values for the model parameters, for example, k , n , and k_A . An optimization method then should be used to adjust the parameter values in order to minimize SS^2 . There will be some residual error as

$$s = \sqrt{\frac{SS^2_{residual}}{J}} \quad (6.20)$$

which is a root mean error that combines experimental error and fitting error. The root mean error is a reasonable estimate of experimental error. The introduction of additional constants would reduce the root mean square error but would be over-fitting.

6.2.2. Fitting batch reactor data

When kinetic measurements are made in batch reactors, the reaction rate is not directly determined. Instead, an integral of the rate is measured, and the rate itself must be inferred. All the parameters of the model must be specified, for example r_{model} (k , m , n , r , s, \dots , k_0 , I), but this is performed by the optimization routine. The integration can be done analytically in simple cases or numerically in more complicated cases. For a batch reactor

$$\left[\frac{d(VC)}{dt} = Vr_A \right] \quad (6.21)$$

6.3. Hybridization approach

6.3.1. Utilization of electrodes instead of electron donors

One of the main challenges regarding oxidation and reduction mechanisms involves replenishment of electron acceptors and donors. Consumption of electron donors will require replenishment of this material either by a sustainable process reaction that causes the electron donor to reform, or by extraction and replacement of the electron donor. Our new proposed approach applies an external power source and two electrodes immersed in the catalyst

solution to supply and transfer electrons inside two reactors. The presence of ionic molecular devices at the electrode interface, where they exchange electrons (donate or accept) with high activity, dispels the need for coating the electrode surface by expensive catalysts such as platinum group materials. Various electrode materials are examined and their electron exchange effectiveness is compared.

6.3.2. Use of multiple catalysts to utilize wide range of spectrum

There exist various photo-catalysts that are functional under UV light and require high energy photons. However, UV light constitutes less than 10 percent of the total solar spectrum. Some semiconductors such as WO_3 are functional for photo-catalytic O_2 evolution under visible light irradiation but are not active for H_2 evolution because of their low conduction band level. The band gap of a photo-catalyst should be narrower than 3.0 eV ($\lambda \geq 415$ nm) to be functional in visible-light. Therefore, suitable band engineering is required in order to develop new photo-catalysts for water splitting under visible light irradiation. Band gap engineering is the process of controlling or altering the band gap of a material by controlling the composition of certain semiconductor alloys, such as GaAlAs, InGaAs, and InAlAs. It is also possible to construct layered materials with alternating compositions by techniques such as molecular beam epitaxy.

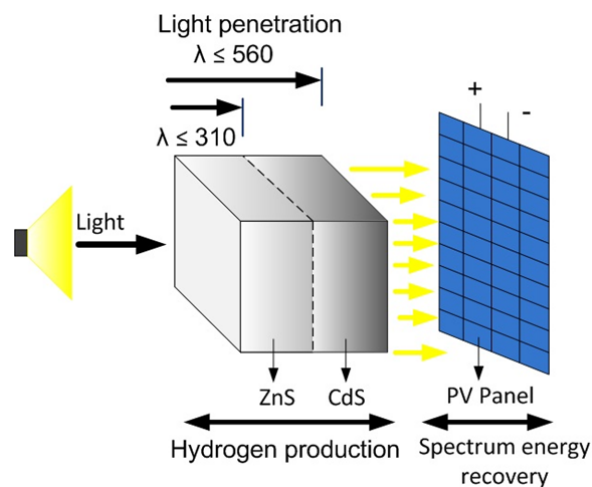


Figure 6.2: Hybridization method for photo-catalytic hydrogen production.

In this study, however, an alternative approach is utilized to enhance the productivity of photo-catalytic hydrogen production system without any synthetic process. As shown in Figure 6.2, zinc sulfide catalyst is irradiated as the first receiver of solar light. This photo-

catalyst absorbs the UV light within the range of $\lambda \leq 310$ nm. The penetrated light is supplied to the second reactor where cadmium sulfide suspensions can absorb up to 2.2 eV (560 nm) energy level of photons. The cooperation of these two catalysts can enhance hydrogen production rates significantly. The rest of the spectrum can be captured by solar cells to generate the required electric current for oxygen evolution reaction.

6.4. Oxygen production reactor design

6.4.1. Electrochemical cell model

The mechanism of the oxygen evolution reaction is more complex compared to the pathways suggested for the hydrogen evolution reaction. There are a number of theories presented and discussed in past literature. The most generally accepted mechanism involves the following steps:



The electrochemical cell performance of the oxygen evolving reactor, including individual ohmic, activation, and concentration overpotentials, can be expressed in terms of mathematical functions. In the water splitting system, the required voltage E is larger than the reversible voltage because of the irreversibilities resulting from the water splitting reactions. The following relation can be derived from energy balance:

$$E = E_{rev} + U_{act} + U_{con} + U_{ohm} \quad (6.25)$$

where $U_{act} = \frac{RT}{\alpha n_e F} \ln\left(\frac{j}{j_0}\right)$ is the activation overpotential loss related to the electrochemical kinetics [209], j_0 is the exchange current density specified for an electrode, and n_e is the number of electrons, $U_{con} = \frac{RT}{\alpha n_e F} \ln\left(\frac{j_L}{j_L - j}\right)$ is the concentration overpotential loss caused by mass transfer [209], j_L is the limiting current density, $U_{ohm} = j \frac{t_{el}}{k}$ is the ohmic overpotential loss caused by the resistance of electrolyte as the resistance of electrodes are negligible compared with the electrolyte [210], t_{el} is the thickness of the KOH electrolyte, and k is the specific conductivity of the KOH solution. All constant values are shown in Table 6.3.

Based on the following correlation, developed by Gilliam et al. [215], the relationship between the specific conductivity of aqueous KOH solution and electrolyte concentration C , can be expressed as follows:

$$k = -2.041C - 0.0028C^2 + 0.005332 CT + 207.2 C/T + 0.001043 C^3 - 0.0000003C^2T^2 \quad (6.26)$$

which is valid over a range of temperatures from 0 °C to 100 °C and KOH concentrations from 0 to 12 M.

Table 6.3: Inputs and fitting parameters used in this study.

Parameter	Value	Reference
α	0.5	[164]
D_{OH^-}	$5.26 \times 10^{-5} \text{ cm}^2 \text{ s}^{-1}$	[211]
$j_{o(Ni)}$	$6 \times 10^{-6} \text{ A cm}^2$	[212]
$j_{o(G)}$	$4.6 \times 10^{-5} \text{ A cm}^2$	[213]
$j_{L(Ni)}$	400 mA cm ²	[211]
$j_{L(G)}$	150 mA cm ²	[212]
$n_{OH^-}^{init}$	1M	NA
$\mu_{o(OH^-)}$	$20.5 \times 10^{-4} \text{ cm}^2 \text{ V}^{-1} \text{ s}^{-1}$	[214]

The reaction rate decreases with increasing activation energy, so reducing the activation energy is always favored for more efficient water electrolysis. Furthermore, the activation energy rises with increasing current density and it can be lowered by using appropriate electro-catalysts. The over-potential of oxygen evolution is more difficult to reduce than hydrogen evolution, owing to the complex mechanism and irreversibility.

6.4.2. Mathematical modelling of mass transport

The mass transfer in electrolyte solutions is determined by the driving forces acting on the individual components of the solution and by friction. The driving forces acting on the components of a system can be expressed by gradients in their electrochemical potential. The friction or the resistance that must be overcome by the driving force to achieve the transport of the component is generally expressed by a hydrodynamic permeability, a diffusion coefficient, or in an electrolyte solution, also by the electrical resistance of the electrolyte. To describe the mass transport in a system, the thermodynamic and kinetic parameters must be mathematically related. To describe mass transport phenomena in electrolyte solutions, the Nernst-Planck equation is used. This equation considers three modes of mass transport in ion-exchange membranes:

- Diffusion, meaning the movement of molecular components due to a local gradient in the chemical potential;

- Migration, which is the movement of ions due to an electrical potential gradient;
- Convection, which is the movement of mass due to a mechanical force, i.e., in general a hydrostatic pressure difference.

A suitable approach to describe the mass transport in an electrolyte solution is provided by the Nernst-Planck flux equation in differential form in direction x as follows:

$$\frac{d\eta_i}{dx} = \frac{RT}{C_i} \left(1 + C_i \frac{d \ln \gamma_i}{dC_i}\right) \frac{dC_i}{dx} + z_i F \frac{dE}{dx} \quad (6.25)$$

where η is the electrochemical potential, p is hydrostatic pressure, z is the valence, F is the Faraday constant, R is the universal gas constant, T is the absolute temperature, the subscript i refers to a component, C represents concentration, γ is the activity coefficient, E is electric potential, i and k refer to individual components.

Replacing the Stefan-Maxwell diffusion coefficient by Fick's diffusion coefficient, the anion and cation flux of a completely dissociated salt is

$$J_i = -D_i \frac{dC_i}{dx} - D_i \frac{z_i F C_i}{RT} \frac{d\phi}{dx} + v_k C_i \quad (6.26)$$

where D_i is the Fick's diffusion coefficient of the component i in reference to the water in the membrane, and v is linear velocity. In this equation, the first term represents the diffusion, the second term the migration, and the third term is the convection.

6.4.3. Hydroxide ion transfer

Hydroxyl ions are formed by the reduction of water to hydrogen gas, either during the photochemical or electro-catalytic reaction. Then OH⁻ ions diffuse into the anode surface where they are oxidized to produce oxygen gas. The transport of hydroxyl ions occurs in two different regions of the complete cell: through the membrane, and within the free volume between the membrane-electrolyte interface and the OER-electrode (as shown in Figure 6.5).

It is assumed that dissociation of hydroxyl ions only occurs at the electrode interface. The bulk electrolyte layer (with thickness t_{el}) is considered only for ionic transport. Thus, the mass flux of hydroxide ions at the membrane interface is based on a boundary condition for mass transport within the bulk electrolyte. The continuity equation is given as follows [216]:

$$D_{OH^-} \frac{\partial^2 C_{OH^-}}{\partial x^2} + \mu_{OH^-} E \frac{\partial C_{OH^-}}{\partial x} + \mu_{OH^-} n_{OH^-} \frac{dE}{dx} = \frac{\partial C_{OH^-}}{\partial t} \quad (6.27)$$

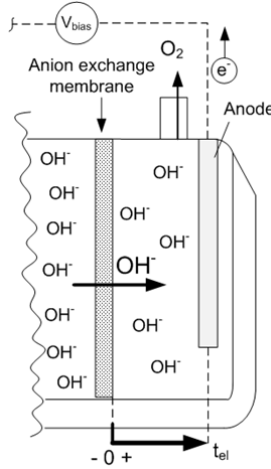


Figure 6.3: Schematic representation of the oxygen evolving half-cell.

Equation (6.28) relates the hydroxide ion flux at any position x to the gradient of OH^- concentration across the electrolyte layer (n_{OH^-}) by means of the OH^- diffusion coefficient (D_{OH^-}), the OH^- mobility (μ_{OH^-}), and the macroscopic electric field (E). For the initial condition, at instant $t = 0$, the initial concentration of the electrolyte species is assumed as follows:

$$\text{At } t = 0 \quad C_{\text{OH}^-}(x, 0) = C_{\text{OH}^-}^{\text{init}} \quad (6.28)$$

With respect to boundary conditions, at $x = 0$, corresponding to the transition between the porous membrane and the bulk liquid, the concentrations (n_{OH^-}) and flux of OH^- ions (J_{OH^-}) in the bulk liquid and membrane interface are identical

$$\text{At } x = 0 \quad C_{\text{OH}^-}^{0-} = C_{\text{OH}^-}^{0+} \quad (6.29)$$

$$J_{\text{OH}^-}^{0-} = J_{\text{OH}^-}^{0+} \quad (6.30)$$

$$\text{where } J_{\text{OH}^-}^{0+} = -D_{\text{OH}^-} \frac{\partial C_{\text{OH}^-}}{\partial x} + \mu_{\text{OH}^-} C_{\text{OH}^-} E.$$

At $x = t_{el}$, which is the electrode-electrolyte interface, only the electrons are able to flow. Thus, the net flux of OH^- is zero.

$$\text{At } x = t_{el} \quad \frac{\partial C_{\text{OH}^-}(L,t)}{\partial x} = 0 \quad (5.31)$$

The thickness of the membrane is negligible compared with the distance between the membrane interface and anode electrode. The OH^- flux through the membrane can be calculated by the following equation:

$$J_{\text{OH}^-}^{0-} = J_{\text{OH}^-}^{0+} = \frac{j \times t_n}{Fz} \quad (6.32)$$

where j is the current density, t_n is transport number of the ion exchange membrane, and z is the valence of OH^- ion which is 1.

6.4.4. Effects of pH change

The performance and durability of any catalyst that facilitate the water splitting under solar irradiation or electro-catalytic reaction is restricted with the pH of the aqueous solution. The performance of the catalyst should be evaluated to quantify the side effects of possible changes in solution pH during experiments or real practice.

The electrolyte has a key role in charge transfer from the membrane to the electrode. Any imperfection of electrolyte or membrane performance leads to hydroxide accumulation in the hydrogen evolving half-cell, which increases the pH of the system and becomes rate limiting. Although electrolyte replenishment is considered, due to resistances against charge transfer, unexpected changes of solution pH are inevitable and very accurate monitoring and control of pH is not always possible. Therefore the effect of pH change of the HER solution on the required energy of water dissociation should be calculated and considered in practice.

The Nernst equation expresses the reduction reaction in terms of the electrochemical potential (V) using the following relationship with Gibbs free energy (G):

$$\Delta G = -nEF \quad (6.33)$$

$$E_{Cell} = E_{Cell}^0 - \left(\frac{RT}{nF}\right)\ln Q \quad (6.34)$$

where E_{Cell} = cell potential under nonstandard conditions (V), E_{Cell}^0 = cell potential under standard conditions; R = gas constant, which is $8.31 \text{ (V C mol}^{-1} \text{ K}^{-1})$; T = temperature (K); n = number of moles of electrons exchanged in the electrochemical reaction (mol); F = Faraday's constant, which is $96,500 \text{ C mol}^{-1}$; and Q = reaction quotient, which is the equilibrium expression with initial concentrations rather than equilibrium concentrations.

6.5. Electrochemical analysis of seawater electro-catalysis

The theoretical potential for seawater electrolysis is 1.229 V. However, the pH of the anode compartment decreases to about 2 due to oxygen formation because the permeation fraction of hydroxide ions is lower than 100%. Also the pH of the cathode compartment increases to about 12 due to hydrogen formation. As a result, the electrolysis voltage will exceed 1.8 V. For energy savings, it is desirable to avoid the pH difference between solutions at the anode and cathode.

The only major cathodic reaction in seawater is hydrogen evolution. Although hydrogen evolution occurs at a high coulombic efficiency, it also causes a localized pH change, resulting in a higher cell voltage and causing deposition. As the cathode surface

becomes more basic during electrolysis, the thermodynamic voltage for hydrogen evolution becomes more cathodic according to the following equation [217]:

$$E_{H_2} = \frac{RT}{F} \log(C_{H^+})_{cathode} - \frac{RT}{2F} \log(p_{H_2}) \quad (6.35)$$

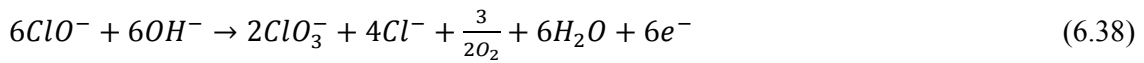
As with the anode reaction, the actual pH of the solution adjacent to the cathode, and hence the voltage at which the electrode operates during electrolysis, is dependent on conditions of flow rate, current density, and temperature. The effective cathode pH usually ranges from 11 to 14.

The basic nature of the solution at the cathode surface results in a surface deposit which is the most difficult operational problem encountered with the electrolysis of seawater. A chemical precipitation of magnesium hydroxide occurs at a pH of 10.7 - 11.0. This deposit tends to adhere to the cathode surface and later grow onto neutral surfaces. If such a deposit is allowed to continue, it causes an even higher pH at the cathode interface and will eventually clog the electrode gap. Such deposits cannot be eliminated entirely, but they can be effectively minimized by high seawater turbulence and a proper choice of current density and cathode surface.

In addition to the increase in precipitate with electrolyte concentration, the composition of the electrolyte also affects the change of pH. The increase in pH is likely the result of chlorine escape from the solution. The overall reaction becomes



which causes the pH to rise. However, secondary reactions involving chlorine or the formation of oxygen tend to lower the pH by consuming hydroxide ions (or releasing hydrogen ions in acid solutions). Three such reactions are



Without the loss of chlorine, these reactions would neutralize the hydroxide formation at the cathode according to the following reaction:



Here, the precipitate formation during seawater electrolysis is mainly based on the following reactions:



The cation composition of the precipitate was found to be predominantly magnesium (~95%) with some calcium (~5%).

It is instructive to examine the precipitation process more closely. The evolution of hydrogen at the cathode results in a local pH gradient because of the loss of hydrogen ions in acid conditions or the liberation of hydroxide ions in alkaline solutions. To estimate pH values near the surface, an empirical equation for the Sherwood number was used. The relationship based on van Shaw et al. [218] for the Sherwood number has been supported by data presented by Schütz [219]. The relationship for short electrodes in turbulent flow is

$$Sh_{av} = 0.276Re^{0.58}Sc^{1/3} \left(\frac{De}{D}\right)^{1/3} \quad (6.43)$$

where Sh_{av} = average Sherwood number, Re = Reynolds number, Sc = Schmidt number, which is the ratio of momentum diffusivity (viscosity) and mass diffusivity and takes the value of 0.118 in this study, De = reactor equivalent diameter, and D = diffusion coefficient.

A mass transfer model is used to estimate the magnesium hydroxide formation due to the magnesium flux near the electrode surface in the following form:

$$\frac{Mg_{flux}}{c_{bMg^{2+}}} = Sh_{av} \times \frac{D}{De} \quad (6.44)$$

The rate of precipitation depends primarily on several factors. If the rate of reaction for the magnesium hydroxide is slow, then the magnesium ion concentration will rise near the surface because of migration forces. If, on the other hand, magnesium hydroxide formation is rapid, then the rate of transport will become the controlling factor. Movement to the surface would occur by diffusion, migration and convection. In this case, increasing convection and turbulence near the electrode surface would increase the precipitation rate, but not necessarily the adhered precipitate. The effective diffusion layer region (δ_{eff}) can be determined by the forced convection and the effect of gas bubble evolution. The relationship proposed and verified by Kelsall [138] is

$$\frac{1}{\delta_{eff}} = \frac{1}{\delta_f} + \frac{1}{\delta_{bubble}} \quad (6.45)$$

where δ_f = diffusion layer from forced convection and δ_{bubble} = diffusion layer from gas evolution.

The two components of the effective diffusion layer can be considered individually. The convective component can be treated as a function of the Reynolds number. Although there is agreement in the archival literature concerning the decrease in boundary layer thickness with gas evolution, there is some uncertainty over the precise mechanism.

However, it is apparent that mass transport can be increased by either increasing fluid turbulence near the electrode surface, or by increasing the gas evolution rate.

6.6. Energy and exergy analyses

The analyses of energy, exergy of the photo-catalytic hydrogen production systems is presented in this section. Exergy analysis is a useful tool to develop strategies and guidelines to enhance the use of energy quality, and recently the method has been successfully applied to hydrogen production systems.

The mass balance of water splitting reactor is written as

$$\frac{dm_{system}}{dt} = \sum_{input} \dot{m}_i - \sum_{output} \dot{m}_j \quad (6.46)$$

Considering the concentration of species in aqueous solution $C(t)$ and for steady state operation of reactor, the above equation can be re-written as

$$C_{H_2O,in} = C_{H_2O,out} + C_{H_2} + C_{O_2} \quad (6.47)$$

The energy balance of a photocatalytic water splitting reactor would be

$$\Delta \dot{E}n_{system} = \sum_{input} \dot{m}_i \left(h_i + \frac{V_i^2}{2} \right) - \sum_{output} \dot{m}_j \left(h_j + \frac{V_j^2}{2} \right) + \dot{E}n_S - \dot{E}n_{loss} \quad (6.48)$$

The exergy balance for the photocatalytic process involves chemical reactions, and can be written as [220]

$$\Delta \dot{E}x_{system} = \sum_{input} \dot{m}_i \left(ex_i + \frac{V_i^2}{2} \right) - \sum_{output} \dot{m}_j \left(ex_j + \frac{V_j^2}{2} \right) + \dot{E}x_S - \dot{E}x_{loss} - \dot{E}x_{destruction} \quad (6.49)$$

The entropy balance of the water splitting reactor is also written as

$$\frac{dS_{system}}{dt} = \sum_{input} \dot{m}_i s_i - \sum_{output} \dot{m}_j s_j + \frac{\dot{Q}}{T_{reaction}} - \dot{S}_{gen} \quad (6.50)$$

For a steady-state system, the terms $\Delta \dot{E}n_{system}$, $\Delta \dot{E}x_{system}$, and $\frac{dS_{system}}{dt}$ are zero. The exergy associated with a process at a specified state involves physical and chemical contributions. Thus, the specific exergy of a stream associated with the process is

$$\bar{ex} = \bar{ex}^{ph} + \bar{ex}^{ch} = (\bar{h} - \bar{h}_0) - T_0(\bar{s} - \bar{s}_0) + \frac{V^2}{2} + gz + \bar{ex}^{ch} \quad (6.51)$$

Using Equation (6.51), exergy destruction can be written as

$$\begin{aligned} \bar{ex}_{destruction} = & \sum \left[(\bar{h} - \bar{h}_0) - T_0(\bar{s} - \bar{s}_0) + \frac{V^2}{2} + gz + \bar{ex}^{ch} \right]_{in} \\ & - \sum \left[(\bar{h} - \bar{h}_0) - T_0(\bar{s} - \bar{s}_0) + \frac{V^2}{2} + gz + \bar{ex}^{ch} \right]_{out} + \left(1 - \frac{T_0}{T_{reaction}} \right) \bar{q} \end{aligned} \quad (6.52)$$

where \bar{q} is molar specific reaction heat that interacts with the system (negative for exothermic reactions).

The standard chemical exergy is defined as the chemical exergy of any exergy reference environment with standard values of the environmental temperature T_0 and pressure P_0 , such as 298.15 K and 1 atm. In order to determine the standard chemical exergy of any substance, the reaction of the substance with other substances with known standard chemical exergies can be utilized as follows [180]:

$$\bar{ex}^{ch} = -\Delta g + \sum_P \bar{n} \bar{ex}^{ch} - \sum_R \bar{n} \bar{ex}^{ch} \quad (6.53)$$

where Δg is the change in the Gibbs function for the reaction, for each separate substance at the temperature T_0 and pressure P_0 . The other two terms on the right side of Equation (6.53) are calculated together with n values, which represent the moles of these reactants and products per mole of the substance with a known chemical exergy value.

Energy and exergy efficiencies for a photocatalytic water splitting process can be defined as

$$\eta_{en} = \frac{\dot{n}_{H_2} HHV_{H_2}}{\dot{E}_{inS} + \dot{n}_{H_2O} (\bar{h}_{H_2O} + \frac{V_{H_2O, in}^2}{2})} \quad (6.54)$$

$$\eta_{ex} = \frac{\dot{n}_{H_2} \Delta G_{H_2O \rightarrow H_2 + 1/2 O_2}}{\dot{E}_{inS} + \dot{n}_{H_2O} (\bar{e}x_{H_2O} + \frac{V_{H_2O, in}^2}{2})} \quad (6.55)$$

Exergy destruction ratio can be introduced based on ratio of exergy destruction/loss rate in each component of a system to total input exergy

$$\delta_k = \frac{\delta \dot{E}x}{\dot{E}x_{input}} \quad (6.56)$$

where $\delta \dot{E}x$ denotes the exergy destruction or loss rate.

6.6.1. Energy of solar radiation

In general cases, the temperature and properties (e.g. emissivity) of the source, from where the radiation arrives, may be unknown. Energy of such radiation is considered as arbitrary radiation (i.e. radiation of any irregular spectrum not known, e.g. ideal black or grey model). This can be determined by the radiosity based on results of the spectrum measurements. In this paper, the radiation arriving at the reactor surface is considered to be radiation arriving from the sun or a UV-visible lamp.

The radiosity, ζ_s , in kW m⁻², of solar radiation of the real spectrum is determined in numerical form as follows:

$$\zeta_s = 4.329 \times 10^{-5} \pi \sum_n (K_\lambda \Delta \lambda)_n \quad (6.57)$$

where K_λ is the measured monochromatic intensity of radiation, $\text{kW m}^{-3} \text{sr}^{-1}$, depending on the wavelength, λ . The factor ‘n’ is the successive number of the wavelength intervals within the wavelength range.

The monochromatic intensity values K_λ given by Kondratiew [221] are used. For the 0 to 1 wavelength range, the sum in Equation (5.67) has been modeled by Petela [183] and the respective radiosity is $\zeta_s = 1.3678 \text{ kW m}^{-2}$. The ζ_s value is slightly larger than the value of 1.3661 kW m^{-2} determined by Gueymard [222]. For the visible spectrum arriving from the sun in the highest layer of the atmosphere within the wavelength range of 400-700 nm: $\sum_n (K_\lambda \Delta\lambda)_n = 4013.105 \text{ kW m}^{-2} \text{sr}^{-1}$. Thus the radiosity of the visible spectrum calculated from Equation (5.67) is $\zeta_v = 0.5446 \text{ kW m}^{-2}$.

6.6.2. Energy radiation exchange at the reactor surface

The radiation emitted by the reactor surface entails the radiation subject to its surface properties. The radiative emission propagates in all directions of a hemisphere as well as the radiation from the environment arriving at the reactor surface from all directions of the hemisphere. Therefore, the energy rate \dot{q}_e exchanged between the reactor and the environment is written as

$$\dot{q}_e = \alpha_s \varepsilon_b (T^4 - T_0^4) \quad (6.58)$$

where α_s is the average absorptivity of the reactor surface, and ε_b is the Stefan–Boltzmann radiation constant ($\varepsilon_b = 5.667 \times 10^{-8} \text{ Wm}^{-2} \text{K}^{-4}$). At small temperatures (T and T_0), the energy of visible spectrum is relatively small, in comparison to the case of radiation at the sun’s temperature. Therefore, it can be assumed that the average absorptivity equals the reactor absorptivity for the non-visible wavelengths range.

6.6.3. Exergy of solar radiation exchange

The following formula for uniform and direct solar radiation exergy rate, $\dot{E}x_s$, arriving in the Earth’s atmosphere can be derived as follows [183]:

$$\dot{E}x_s = 4.329 \times 10^{-5} \pi \left(\frac{9.445 \times 10^{-12}}{\pi} T_0^4 + \sum_n (K_\lambda \Delta\lambda)_n - T_0 \sum_n (S_\lambda \Delta\lambda)_n \right) \quad (6.59)$$

By substituting $T_0 = 293 \text{ K}$, and related values for entropy and intensity of each wavelength interval in Equation (6.59), the exergy of total solar radiation $\dot{E}x_s = 1.2835 \text{ kW m}^{-2}$ and the exergy of visible portion, $\dot{E}x_v = 0.5155 \text{ kW m}^{-2}$, are calculated.

6.6.4. Exergy of radiation exchange at a surface

The exergy of radiative emission for any surface at the temperature of the local environment, T_0 , is zero. Therefore, the exergy of environmental radiation arriving at the reactor surface is zero. Exergy rate $\dot{E}x_s$ of emissions from the surface at a temperature T can be determined by the formula given by Petela [183].

$$\dot{E}x_s = \alpha_s \frac{\epsilon_b}{3} (3T_s^4 + T_0^4 - 4T_0T_s^3) \quad (6.60)$$

6.6.5. Energy balance for photo-reactor system

The energy conservation equation is formulated for continuous flow photo-catalytic water splitting system. The delivered energy consists of absorbed solar radiation and the enthalpy of liquid water. The energy increase of the system is determined by the rates of hydrogen evolution and liquid water physical changes in the solution. The extracted energy consists of the enthalpies of oxygen and hydrogen gas as well as convective and radiative heat exchange with the reactor surface

$$\gamma[\alpha_V \zeta_V + \alpha_{nV}(\zeta_S - \zeta_V)] + \dot{n}_{H_2O,in} \bar{h}_{H_2O,in} = \dot{n}_{H_2} \bar{h}_{H_2} + \dot{n}_{O_2} \bar{h}_{O_2} + \dot{n}_{H_2O,out} \bar{h}_{H_2O,out} + \dot{q}_{conv} + \dot{q}_{em} \quad (6.61)$$

where γ is the radiation weakening factor and α_V and α_L are the absorptivities of the catalyst within and beyond the visible wavelength range, respectively. The heat transfer by convection from the reactor surface to the environment is $\dot{q}_{conv} = h_{conv} A(T - T_0)$, where h is the heat transfer coefficient.

6.6.6. Exergy balance for photo-reactor system

The irreversibility of photocatalysis processes can be evaluated using an exergy balance which comprises the entropy changes occurring as a consequence of the process. As the sun or source of light emits radiation regardless of the presence of the catalyst, the space is filled with this radiation exchange and its respective entropy transfer.

When the reactor becomes exposed, then a portion of the incident solar radiation is absorbed by the catalyst. Other effects are the convective and radiation heat transfer from the reactor surface to the environment of temperature T_0 . The following exergy balance equation can be written for the photo-reactor system:

$$\gamma[\alpha_V \dot{E}x_V + \alpha_{nV}(\dot{E}x_S - \dot{E}x_V)] + \dot{n}_{H_2O,in} \bar{e}x_{H_2O,in} = \dot{n}_{H_2} \bar{e}x_{H_2} + \dot{n}_{O_2} \bar{e}x_{O_2} + \dot{n}_{H_2O,out} \bar{e}x_{H_2O,out} + \dot{E}x_{conv} + \dot{E}x_{em} + \delta \dot{E}x \quad (6.62)$$

where $\delta\dot{E}x$ is the total exergy destruction due to all irreversible processes occurring within the system.

6.6.7. Analyses of continuous flow photo-catalysis process

The following input values are used in the computations for the model:

- The environment temperature is $T_0 = 293$ K.
- The environment pressure p_0 equals the standard pressure 101.325 kPa.
- The weakening radiation factor is $\gamma = 0.8$.
- The reactor surface absorptivity within visible wavelength range is $\alpha_V = 0.31$.
- The reactor surface absorptivity beyond the visible range is $\alpha_{nV} = 1.8$.
- The convective heat transfer coefficient is $h_{conv} = 0.003$ kW m⁻² K⁻¹.

The value of α_{nV} is more than 1 because it represents the absorptivity of the reactor surface only within the non-visible wavelength range. The energy and exergy efficiencies reflect the degree of thermodynamic losses in the photo-catalytic hydrogen production process. All terms of the energy and exergy balance equations are categorized either as useful products, or process input, or losses. The denominator of the efficiencies represents the input terms, whereas the numerator expresses the useful products. Energy and exergy efficiencies for this process can be defined as

$$\eta_{en} = \frac{\dot{n}_{H_2} HHV_{H_2}}{\gamma[\alpha_V j_V + \alpha_{nV}(\zeta_S - \zeta_V)] + \dot{n}_{H_2O}(\bar{h}_{H_2O} + \frac{V_{H_2O,in}^2}{2})} \quad (6.63)$$

$$\eta_{ex} = \frac{\dot{n}_{H_2} \Delta G_{H_2O \rightarrow H_2 + 1/2 O_2}}{\gamma[\alpha_V Ex_V + \alpha_{nV}(Ex_S - Ex_V)] + \dot{n}_{H_2O}(\bar{e}x_{H_2O} + \frac{V_{H_2O,in}^2}{2})} \quad (6.64)$$

where \dot{n}_{H_2} is the molar flow rate of H₂ produced and ΔG is the standard Gibbs free energy change of the reaction at 298 K (237 kJ mol⁻¹), i.e., maximum possible amount of work that may be extracted from H₂ at 298 K, when both H₂ and O₂ are available at 1 bar. Care should be taken to not overlap the losses of component processes. Although hydrogen and oxygen are produced in a photo-catalytic process, only hydrogen is considered in the energy efficiency since oxygen is not a fuel. Oxygen is then taken into account in the exergy efficiency as a useful output. In the present approach, the total exergy loss is assumed to be the sum of four components arising from: chemical reaction, physical changes in water flow, radiation, and convective heat transfer from the reactor surface.

However, the solar radiation absorbed at the catalyst active sites is expended only on three processes: chemical reaction, physical changes, and heat exchange in the reactor. To

calculate the three respective exergy destructions and losses, the entropy of the absorbed radiation is split appropriately in accordance with the energy exchange. Based on the energy balance Equation (6.61), each of the respective fractions is a ratio of each specific energy term over total energy of absorbed solar radiation. Therefore the incident radiation energy is distributed according to the following three fractions

$$\varphi_{ch} = \frac{n_{H_2}h_{H_2} + n_{O_2}h_{O_2}}{\gamma[\alpha_V\zeta_V + \alpha_{nV}(\zeta_S - \zeta_V)]} \quad (6.65)$$

$$\varphi_{ph} = \frac{n_{H_2O,in}h_{H_2O,in} - n_{H_2O,out}h_{H_2O,out}}{\gamma[\alpha_V\zeta_V + \alpha_{nV}(\zeta_S - \zeta_V)]} \quad (6.66)$$

$$\varphi_{heat\ transfer} = \frac{q_{conv} + q_e}{\gamma[\alpha_V\zeta_V + \alpha_{nV}(\zeta_S - \zeta_V)]} \quad (6.67)$$

It is assumed that the entropy of the absorbed incident solar radiation is split according to the above fractions. The following statements can be written for the rate of exergy destructions and loss:

$$\delta\dot{E}x_{ch} = \dot{n}_{H_2}Ex_{H_2} + \dot{n}_{O_2}Ex_{O_2} - (\dot{n}_{H_2O,in}Ex_{H_2O,in} - \dot{n}_{H_2O,out}Ex_{H_2O,out})_{@T_0,P_0} \quad (6.68)$$

$$\delta\dot{E}x_{ph} = \dot{n}_{H_2O,in}Ex_{H_2O,in} - \dot{n}_{H_2O,out}Ex_{H_2O,out} \quad (6.69)$$

$$\delta\dot{E}x_{heat\ transfer} = T_0q_{conv} \left(\frac{1}{T_0} - \frac{1}{T_f} \right) + \alpha_L \frac{\varepsilon_b}{3} (3T_s^4 + T_0^4 - 4T_0T_s^3) \quad (6.70)$$

where $T_f = (T_0 + T_s)/2$.

6.7. Environmental impact assessment

To improve environmental sustainability, it is important to minimize environmental damage while using sustainable or renewable sources of energy. This leads to a reduction in the use of limited resources and extended lifetimes. Accordingly, a sustainability index SI is used to connect exergy and environmental impact [223]

$$SI = \frac{1}{D_p} \quad (6.71)$$

where D_p is a depletion number, which is defined as the exergy destruction / input exergy [224]. This relation characterizes the ability to reduce a system's environmental impact by decreasing its exergy destruction.

The emissions of CO_2 are defined in $kg\ kWh^{-1}$. The mitigation of CO_2 emissions from photo-catalytic water splitting and CO_2 emissions from solar thermal methanol reforming are normalized based on the incident irradiation as follows:

$$Emi_{CO_2} = \frac{\dot{m}_{CO_2}}{\zeta_S \times A} \times 3600 \quad (6.72)$$

In order to calculate the amount of prevented CO₂ by the photo-catalytic water splitting method, the electricity consumed by the lamp and pump is assumed to be provided by methane gas combustion in a gas turbine.

6.8. Exergo-economic analysis

The effective techniques for analysis and design of energy systems are mainly combined with thermodynamics and economic disciplines to achieve optimum designs. The traditional cost analysis based on energy does not reflect the irreversibilities associated with the second law of thermodynamics. Costs can be better characterized when cost accounting is based on exergy. Exergy-based economic analysis and methodologies have been extensively reported [225-230].

This methodology is applied to the water splitting system, in order to identify the effects of the design variables on the costs and suggest modifications to the design variables that can make the system more cost effective.

In an economic analysis of production systems, the annual values of chemicals, fuel costs, raw water costs, and operating and maintenance expenses \dot{Z} supplied to the overall system are necessary inputs. However, these cost components may vary significantly over their economic lives. Therefore, levelized (annualized) values for all cost components are typically used in the economic analysis and evaluations of the overall system.

The total cost to produce the exiting streams (hydrogen, oxygen, and losses) equals to the total cost of the entering streams plus the cost of owning and operating the cycle. Here we have oxygen as an output, although it is also a potential marketable by-product. The following cost rate balance can be expressed for the system:

$$\dot{C}_{H_2} + \dot{C}_{O_2} + \dot{C}_{Losses} = \dot{C}_{Solar} + \dot{C}_{Electricity} + \dot{Z} \quad (6.73)$$

where \dot{C} denotes the cost rate of the respective stream and \dot{Z} is the cost rate associated with owning and operating the cycle. The cost rates are expressed in unit \$/hour. Equation (6.73) states that the total cost of the exiting exergy streams equals the total expenditure to obtain them: the cost of the entering exergy streams plus the capital and other costs. Since the heat losses from the cycle are considered as waste, we can assume the unit cost \dot{C}_{Losses} is zero.

Oxygen and hydrogen unit costs are treated the same as they are both marketable products.

Thus, Equation (6.73) simplifies to

$$\dot{C}_{H_2} + \dot{C}_{O_2} = \dot{C}_{solar} + \dot{C}_{Electricity} + \dot{Z} \quad (6.74)$$

In the present discussion, the cost rate \dot{Z} is presumed known from an economic analysis, as presented in Table 7.14. Although the cost rates denoted in Equation (6.74) are evaluated by various means in practice, the present discussion features the use of exergy for this purpose. Since exergy measures the true thermodynamic values of the work, heat, and other interactions between a system and its surroundings, as well as the effect of irreversibilities within the system, exergy is a solid basis for assigning costs. With exergy costing, each of the cost rates is evaluated in terms of the associated rate of exergy transfer and unit cost. Thus, for an entering or exiting stream

$$\dot{C} = c\dot{E}x \quad (6.75)$$

where c denotes the cost per unit of exergy (for example in cents per kWh) and $\dot{E}x$ is the associated exergy transfer rate. In exergy costing, a cost is associated with each exergy stream. Exergy cost rates associated with fluid flow, electricity, and solar energy input may be written respectively as

$$\dot{C}_{matter} = (c\dot{E}x)_{matter} \quad (6.76)$$

$$\dot{C}_{electricity} = (c\dot{E}x)_{electricity} \quad (6.77)$$

$$\dot{C}_{solar} = (c\dot{E}x)_{solar} = [c\dot{E}]_{incident-photons} \quad (6.78)$$

Thus Equation (6.74) can be expressed as follows:

$$c_{H_2} (\dot{E}x_{H_2} + \dot{E}x_{O_2}) = (c\dot{E}x)_{incident-photons} + (c\dot{E}x)_{Electricity} + \dot{Z}^T \quad (6.79)$$

Solving for the unit cost of hydrogen c_{H_2} yields

$$c_{H_2} = \frac{c_{in}(\dot{E}x_{Solar} + \dot{E}x_{Electricity}) + \dot{Z}^T}{\dot{E}x_{H_2} + \dot{E}x_{O_2}} \quad (6.80)$$

where

$$\dot{Z}^T = \dot{Z}^C + \dot{Z}^M \quad (6.81)$$

Here, \dot{Z}^T , \dot{Z}^C , and \dot{Z}^M are the hourly annualized costs of capital investment, operation and maintenance, and the total cost of the whole system. C_w is the cost of the generated or consumed power by the equipment.

In order to calculate \dot{Z}^T , an annualized cost method is used. A four step algorithm of Kwak et al. [225] is utilized as follows: first, the present worth (PW) of the proposed system is calculated by substituting the salvage value, S_n , into Equation (6.82). In this study, the salvage values are taken as 10% of the capital cost. Using the CRF (capital recovery factor), a

function of the lifetime (n years), interest rate (ir), and annual capital cost is found, which is used for the calculation of the capital cost flow of the present system (\dot{Z}^T)

$$PW = C - S_n PWF(ir, n) \quad (6.82)$$

$$AC = PW \times CRF(ir, n) \quad (6.83)$$

$$\dot{Z}^T = \frac{\varphi AC}{3600 \text{ s h}^{-1} \times 8200 \text{ h yr}^{-1}} \quad (6.84)$$

$$CRF = \frac{ir(1+ir)^n}{(1+ir)^n - 1} \quad (6.85)$$

where PWF (ir, n) is the present worth factor, and φ is the factor for the operating and maintenance costs. In this case, PWF is taken as 7.0236 [226], φ is taken as 1.068 of the AC [225], and the lifetime of the system is taken as 25 years. The capital costs are often the most significant component of the total cost generation. Cost generation components, e.g. interest rates, component lifetimes, and salvage values, are often proportional to capital costs [229].

The economic assessment of solar hydrogen production plants may include the calculation of capital costs with specified government intervention related aspects of the system lifecycle. This includes carbon tax, incentives, and in particular feed-in-tariff programs. Some policies have been passed in countries such as Canada to provide funding or loans for green energy investments as well as attractive sale prices for electricity being fed into grid systems [227]. Implementing incentives is another method for clean energy alternatives as carbon emission-based taxation.

Carbon taxation is another promoting opportunity which has been implemented with the aim of limiting CO₂ emission, and also facilitating economic advantages for clean power technologies. Relatively high tax levels are applied to gasoline in Ontario. Specific carbon tax regulations in some European countries such as the UK and France considerably affect automobile taxes. Carbon taxes may have a significant impact on the large-scale production of electricity. The minimum required CO₂ tax level to equalize the cost of fossil fuel power production with that of renewables is US \$200 per tonne of CO₂ [227].

Feed-in-Tariff (FIT) program is another beneficial opportunity outlined by the Ontario Power Authority (2009). This program is based on integration of de-centralized production of energy using renewable energy sources with the grid. The price of generated electricity is standardized for various project types and sizes. The rooftop solar PV assemblies with a capacity under 10 kW are considered an incentive of 0.802 \$ kWh⁻¹ plus financial compensation for the installation of clean power systems.

Chapter 7

Results and Discussion

In this chapter, the results of experimental analysis of a photo-catalytic water splitting system are presented. The hybridization of the system is investigated, and a scale-up analysis is performed based on experimental data and a modelling scheme. An oxygen production reactor is designed and analyzed through experimentations and mathematical modeling. The performance of a complete water splitting reactor is also studied for photo-catalytic and electro-catalytic hydrogen and oxygen production. An electrochemical performance analysis of seawater electrolysis, as an alternative method of hydrogen production is then conducted. Large scale continuous flow photo-reactors are investigated from radiative heat transfer and catalytic performance views. The results of exergy analysis and greenhouse gas emission assessment of these reactors are also presented and discussed. Exergo-economic analysis of different scale photo-catalytic hydrogen production plants are performed and compared at the end of this chapter.

7.1. Experimental results of photo-catalytic water splitting

7.1.1. Photo-reactor operation

Photo-catalytic hydrogen production is performed by illuminating zinc sulfide suspended in basic solutions which contain sulfide ions under a solar simulator. The initial pH of the solution is adjusted to 13.2 using NaOH salt. The experiments are performed under constant pressure in the photo-reactor, as described in Section 4.1.1. The evolved hydrogen is continuously stored in a variable volume cylinder that automatically keeps the pressure above the liquid constant. The incremental increase of collected hydrogen is measured by a digital calliper. The gas headspace is initially purged with nitrogen for 30 minutes to prevent oxygen reduction. The overall water splitting reaction by photonic energy occurs as follows:



Figure 7.1 shows hydrogen production over a 1 hour experiment for different catalyst

concentrations. During hydrogen formation, the simultaneous oxidation of sulfide to disulfide ions occurs according to:



During the experiments, only disulfide ions are formed and no sulphur precipitation is observed. The reaction initiates with a higher rate of hydrogen formation; however, it decreases during the course of the reaction, due to the increasing concentration of disulfide ions which competes with the reduction of water molecules according to:



The production rate is reduced from 0.4 mL min^{-1} to almost 0.12 mL min^{-1} for a catalyst concentration of 2% w/v. In addition, the opaque colour of disulfides acts as an optical filter, and reduces the light absorption of ZnS. An increase of catalyst concentration from 1% to 3% w/v enhances the hydrogen production rate by almost 15%.

Although the sulfide ions act as hole scavengers which stabilize the ZnS surface against anodic photo-corrosion, they should be replenished over time to maintain the constant productivity of the catalyst. Due to the limited volume of the reactor, the aqueous solution is saturated at a ZnS concentration of 3% w/v.

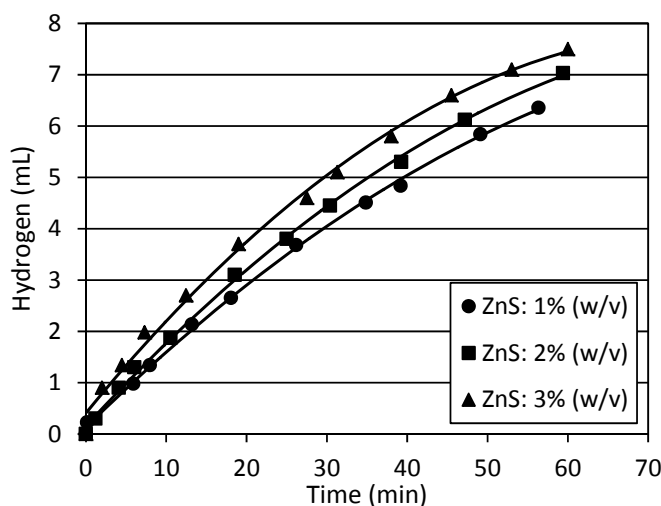


Figure 7.1: Effect of ZnS concentration on hydrogen production (Uncertainty $\pm 3.1\%$).

The performance of the ZnS catalyst is examined with three different light intensities, as shown in Figure 7.2. At higher light intensities, more photons within the band gap energy of ZnS are available per unit time, which leads to a higher electron concentration and a higher

reaction rate. More than a 20% increase in productivity of the catalyst is observed by increasing light intensity from 900 to 1000 W m^{-2} . This improvement is not repeated by increasing light intensity to 1100 W m^{-2} . Following the higher photon incidence rate the concentration of electron-hole pair increases, which in turn enhances the electron-hole recombination probability. In fact, diffusion rate limitation and rapid electron-hole recombination may negate the effect of light intensity enhancement. Higher concentration of sacrificial reagent and some additives such as carbonate salt can diminish the electron-hole recombination effect.

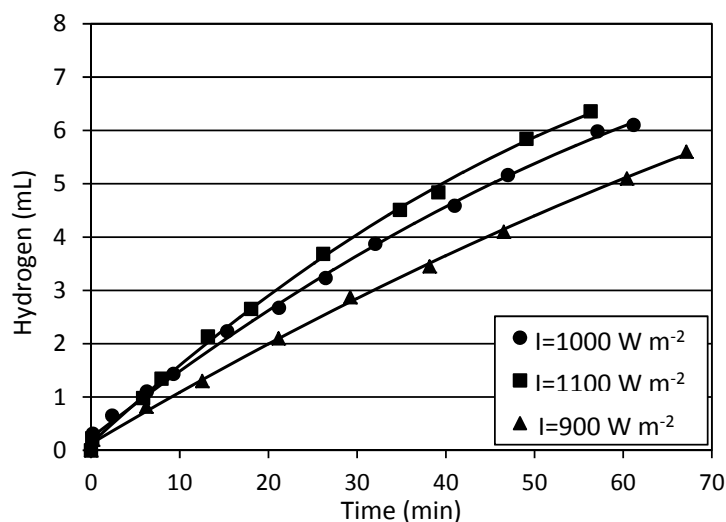


Figure 7.2: Effect of light intensity on hydrogen production (Uncertainty $\pm 3.5\%$).

In the presence of sulfide ions, the hydrogen evolution rate is not constant due to the formation of disulfide ions from oxidation of S^{2-} ions by photo-holes that compete with the reduction of water molecules. Therefore, the rate of hydrogen production in a batch reactor depends on the concentration of both sulfide and disulfide ions. The hydrogen production by irradiation of ZnS suspensions in Na_2S solutions of two different concentrations is represented in Figure 7.3. The results indicate a significant increase of the hydrogen production rate due to a higher molarity of sacrificial agents at the beginning of the reaction. However, the production rate is limited after a few time intervals and the positive effect of higher Na_2S concentration is enervated. Furthermore, as sulfide ions absorb light in a part of the absorption range of ZnS, the flux of photons reaching the ZnS surface is smaller at a higher Na_2S concentration. It is concluded that the addition of sacrificial agents more than a specific limit is not beneficial. The rest of the experiments are performed at a minimum

required Na_2S concentration. It is experimentally found that concentrations of hole scavengers below 1.0 M are not sufficient for efficiently competing with the electron-hole recombination.

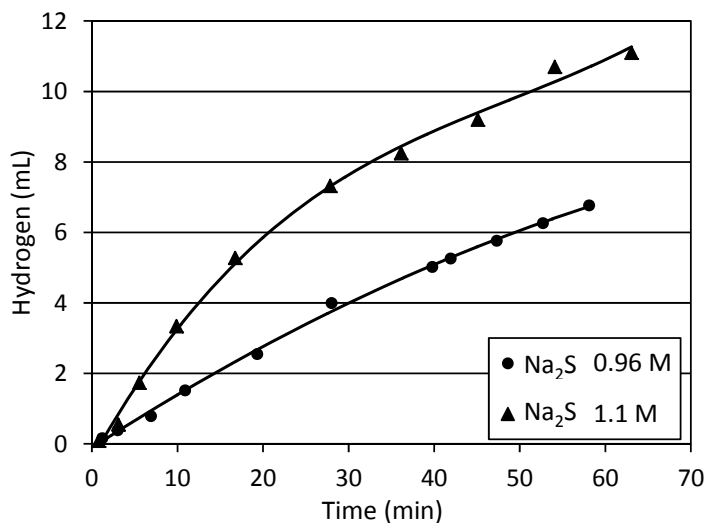


Figure 7.3: Effect of sacrificial agent concentration on hydrogen production for ZnS 2% w/v- $I=1000 \text{ W m}^{-2}$ (Uncertainty $\pm 3.4\%$).

7.1.2. Dual-cell operation

The photo-activity of the zinc sulfide catalyst is determined in a quasi-steady flow dual-cell reactor. The concentration of sulfide ions is compensated during the operation to maintain the constant productivity of the catalyst. The alkaline aqueous solution is injected into the system gradually. The main objective is to perform photo-catalysis of water to produce hydrogen on one half cell and electro-catalytic decomposition of hydroxide ions in the other half cell to produce oxygen. The complete system apparatus is described in Section 4.1.2. The hydrogen formation, due to illumination of zinc sulfide suspensions, follows reaction 7.3 and oxygen evolution, due to hydroxide ion decomposition, takes place according to:



Hydroxide and disulfide ions migrate from the hydrogen evolution reactor to the oxygen evolution reactor through the anion exchange membrane. Diffusion of disulfide ions from the hydrogen evolution reaction site to the other half cell suppresses the competitive reaction (7.4) and benefits the photo-activity of the catalyst. Over the course of experiments, no catalyst degradation has been observed, as the production rate remained constant and the amounts of replenished sacrificial reagents at each time interval were equal.

Since the latest reaction is derived by electrical energy, the polarization curve of the aqueous solution is provided by experiments, as shown in Figure 7.4. Using these data, the required over-potential for the oxygen evolution reaction is adjusted to perform hydroxide ion decomposition with the least interference in the hydrogen evolution reaction. A correlation is extracted from Figure 7.4 to calculate the electric current value corresponding to a specific voltage that is supplied to the system as follows:

$$i = 0.0145 \times U^2 - 0.0014 \times U + 0.0005, R^2 = 0.9942 \quad (7.6)$$

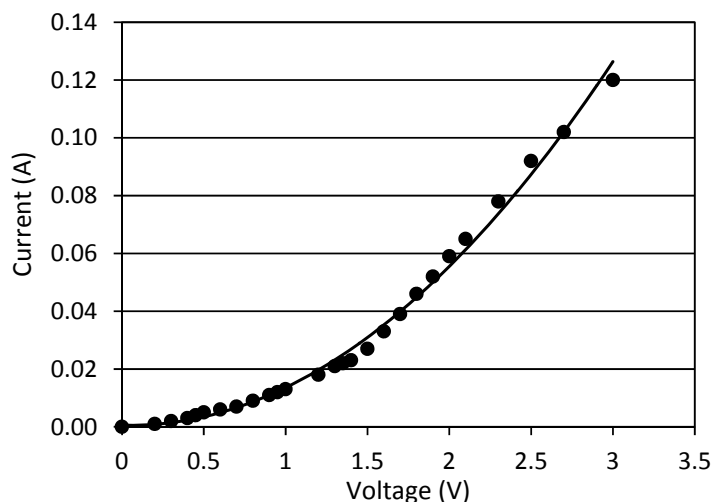


Figure 7.4: Polarization curve for catalyst aqueous solution (Uncertainty $\pm 2\%$).

Since the delivered electrons to the reaction site are supplied by both photons and power supply, hydrogen evolution takes place in a hybrid manner. All of the following experiments are performed in a current density range of $0.4 \text{ mA cm}^{-2} < J < 0.8 \text{ mA cm}^{-2}$. All of the experiments are verified for repeatability and uncertainty issues. Both hydrogen and oxygen reactions initiate with higher rate constants, but the production rate becomes steady after almost 20 minutes of operation and the production rate decreases to almost constant value.

Figure 7.5 shows the hydrogen and oxygen evolution over a 3 hour period of water splitting in the dual-cell. The produced hydrogen during the irradiation of suspensions of zinc sulfide in the electrolyte solutions is measured. Since the process is hybridized with an electricity source of energy, the hydrogen generated by solar energy is calculated after deduction of the amount of evolved hydrogen by electro-catalysis. The rate of hydrogen production with 1.5% w/v ZnS concentration and under 1 sun is about 0.0042 g h^{-1} . The

volume of generated oxygen is measured as almost half of the hydrogen amount which confirms the accomplishment of hydroxide ion decomposition by electro-catalysis.

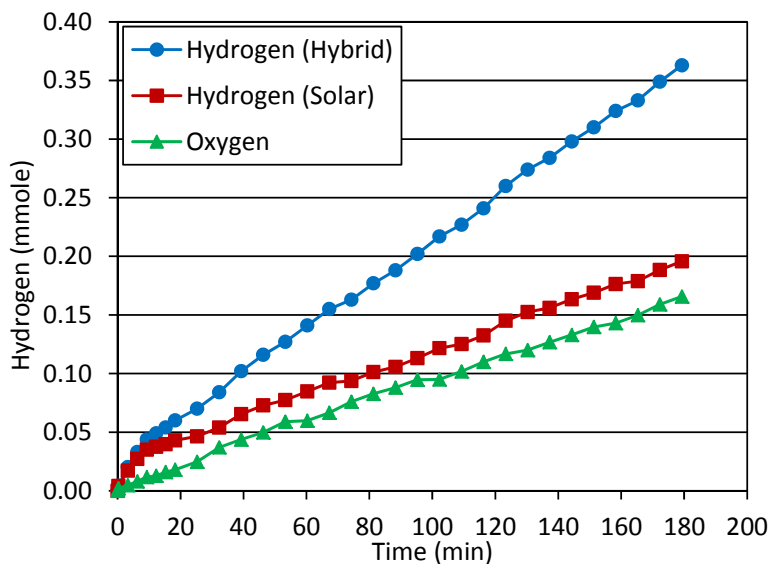


Figure 7.5: Amount of hydrogen and oxygen evolved versus illumination time for ZnS concentration 1.5% w/v and light intensity 1000 W m^{-2} (Uncertainty $\pm 3.6\%$).

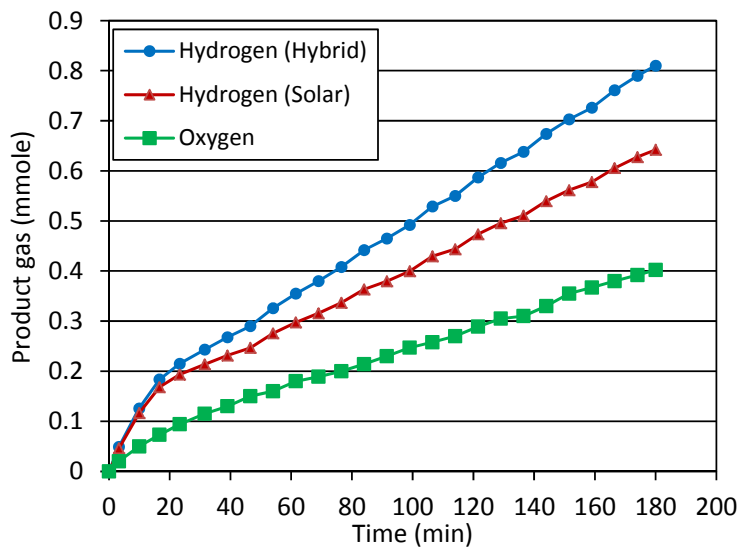


Figure 7.6: Amount of hydrogen and oxygen evolved versus illumination time for ZnS concentration 3% w/v and light intensity 1000 W m^{-2} (Uncertainty $\pm 4.1\%$).

Several experiments are carried out for various catalyst concentration and light intensities. As shown in Figure 7.6, a two-fold increase of the catalyst concentration leads to

a two-fold enhancement of the production rate. The oxygen production rate is also increased due to a higher rate of hydroxide ion generation. The rate of oxygen formation is increased by almost three times.

The effect of a lower catalyst concentration and light intensity is examined, as presented in Figure 7.7. A comparison of results in Figure 7.5 indicates that simultaneous reduction of the catalyst concentration and light intensity does not lead to a significant degradation of the conversion rate. In other words, if the rate of high energy photons is diminished, a lower catalyst concentration should be taken to maintain the same productivity and avoid chemical waste.

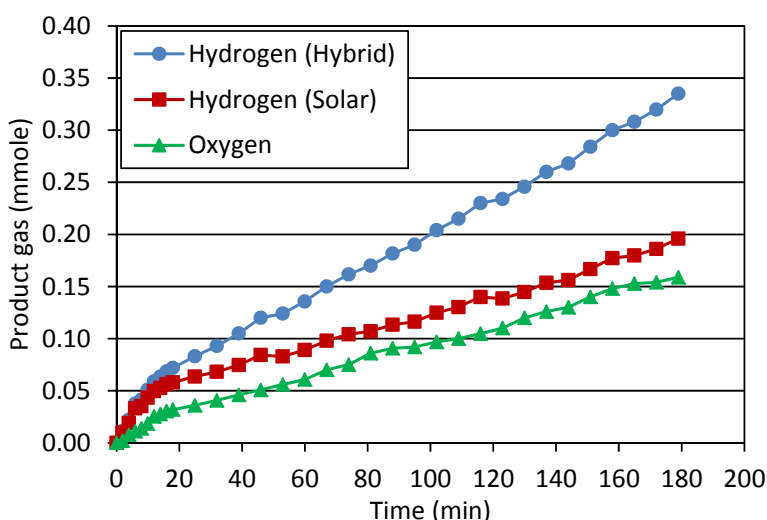


Figure 7.7: Amount of hydrogen and oxygen evolved versus illumination time for ZnS concentration 1% w/v and light intensity 900 W m^{-2} (Uncertainty $\pm 4.3\%$).

The evolved hydrogen during three hours of photo-catalytic water splitting with different catalyst concentrations is shown in Figure 7.8. Hydrogen evolution initiates at higher rate constants during almost 20 minutes of operation; it slows down due to competing reactions and electron-hole recombination effects. It can be concluded that almost 2.5 times enhancement is achieved by using a triple catalyst concentration.

The same experiments are performed by illuminating ZnS suspensions with less light intensity e.g. 900 W m^{-2} . The results in Figure 7.9 indicate that the hydrogen production rate is 25% less than the same experiment with 1000 W m^{-2} light intensity. It is also observed that higher light intensity is more effective at higher catalyst concentrations as the water

molecules have a higher chance to encounter catalytic active sites, and the ionic diffusion rates are higher.

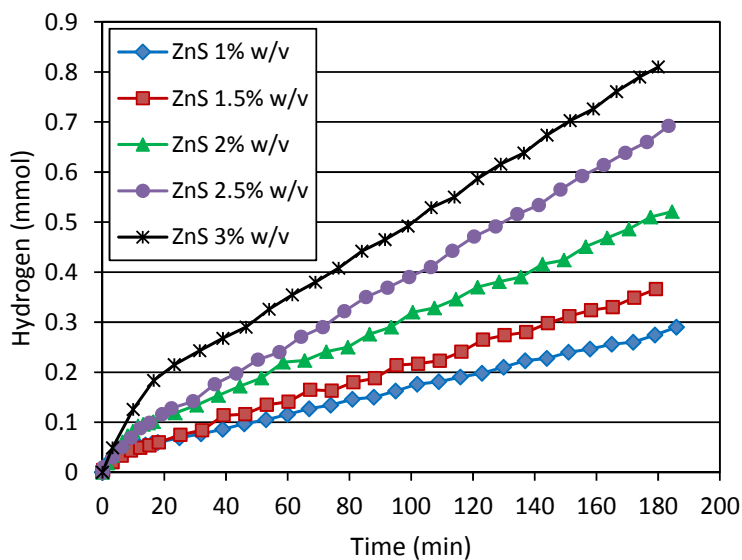


Figure 7.8: Amount of hydrogen evolved versus illumination time for light intensity of 1000 W m^{-2} and different catalyst concentrations (Uncertainty $\pm 4.3\%$).

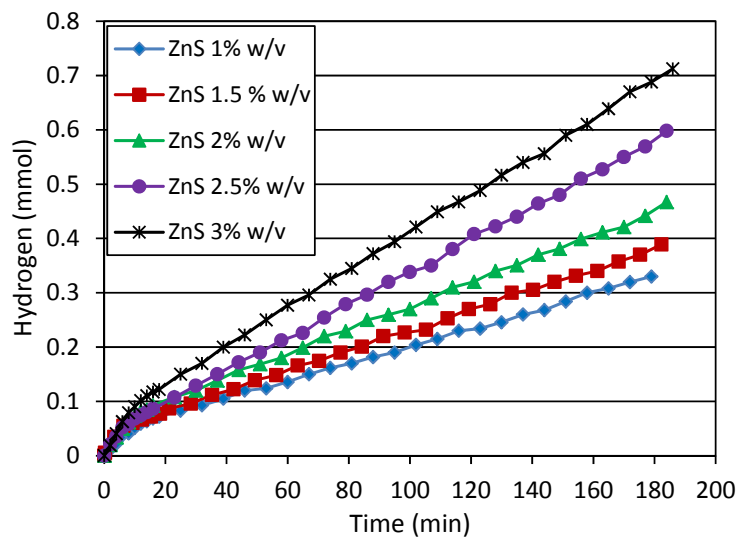


Figure 7.9: Amount of hydrogen evolved versus illumination time for light intensity of 900 W m^{-2} and different catalyst concentrations (Uncertainty $\pm 4.8\%$).

Since the hydrogen and oxygen pressure build-up in the reactor headspace may cause rate limiting effects, the concentration of dissolved gas during the time period of experiments is calculated using Henry's law and real-time partial pressure of gas above the liquid surface.

The results in Figure 7.10 show the ratio of dissolved gas to extracted gas, i.e. dissolve ratio, that is measured for both hydrogen and oxygen over time. It can be concluded that the amount of dissolved hydrogen and oxygen is almost negligible and the reported values of evolved gas can be safely counted to analyze the photo-catalytic activity of ZnS catalyst.

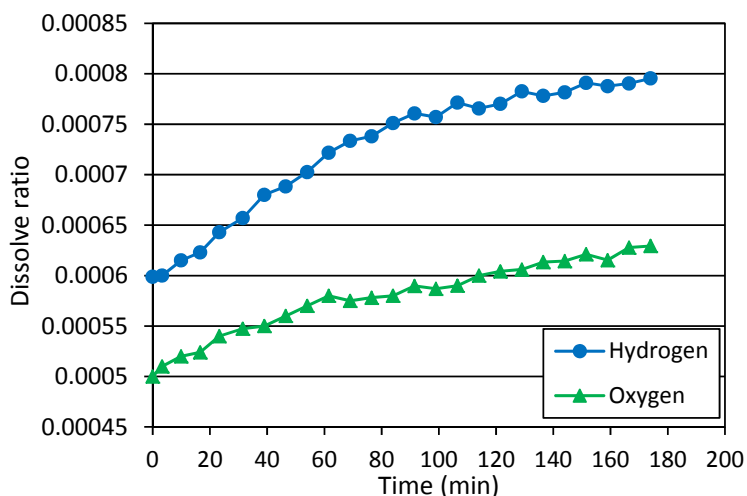


Figure 7.10: Dissolved gas ratio versus time for ZnS concentration 3% w/v and light intensity 1000 W m^{-2} (Uncertainty $\pm 4.9\%$).

The effect of catalyst concentration on hydrogen and oxygen production rates is presented in Figure 7.11. The collected data are related to illumination of ZnS suspensions under 1 sun. An increase in the number of moles of catalyst per unit volume of solution enhances the rate of electron donor encounter, electron transfer, and water molecules encountered within the catalytic active site. The hydrogen production rate is significantly increased by almost 4 times due to an increase of catalyst concentration from 1 to 2.5% w/v. However, the increase of suspended particles magnifies the opaque colour of the aqueous solution and prevents the light penetration inside the reactor. Therefore, the increasing trend of the hydrogen production rate is expected to slow down for higher concentrations. The experiments for higher concentrations are not performed due to limited solubility of water and reactor volume. The oxygen evolution rate is a function of hydrogen production rate, and it follows almost the same trend. The results in Figure 7.11 confirm the functionality of the anion exchange membrane and the fact that the reaction rate is diffusion controlled. The following correlations are extracted for hydrogen and oxygen production rates, respectively:

$$\dot{n}_{H_2} = -0.0259C_{cat}^2 + 0.2596C_{cat} - 0.107, R^2 = 0.989 \quad (7.7)$$

$$\dot{n}_{O_2} = -0.0099C_{cat}^2 + 0.1167C_{cat} - 0.0504, R^2 = 0.978 \quad (7.8)$$

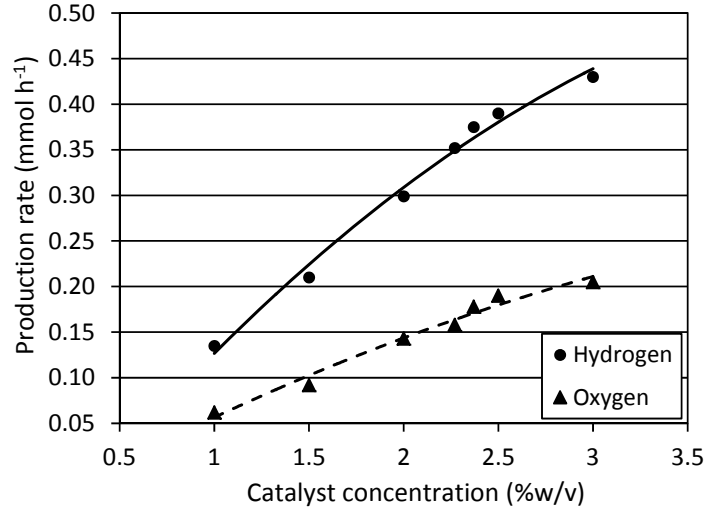


Figure 7.11: Effect of ZnS concentration on Hydrogen production rate (Uncertainty $\pm 3.5\%$).

The effect of light intensity on hydrogen and oxygen production rates is also investigated, as shown in Figure 7.12. The tilt angle of the reflecting mirror and the power input of the solar simulator are adjusted to vary the light intensity that reaches the reactor area. A 3% w/v suspended solution of ZnS is examined in a wide range of light intensities from 800 to 1200 W m⁻². At higher light intensities, more photons per second arrive at the catalytic active site to form the excited states of the zinc sulfide. Subsequently, catalyst relaxation to a ground state is compensated to some extent and the hydrogen production rate is enhanced. The productivity of the catalyst is increased five-fold by increasing the light intensity from 800 W m⁻² to 1200 W m⁻². This information helps to simulate the practical conditions that are encountered in different solar incidence angles. The radiation incident on a tilted surface may vary due to different geographic attitudes or seasonal changes between the earth and solar axis angle. The following correlations are extracted for hydrogen and oxygen production rates, respectively:

$$\dot{n}_{H_2} = -1E(-6)I^2 + 0.0032I - 1.86, R^2 = 0.984 \quad (7.9)$$

$$\dot{n}_{O_2} = -8E(-7)I^2 + 0.002I - 1.132, R^2 = 0.967 \quad (7.10)$$

The quantum efficiency of photo-catalytic hydrogen is calculated based on experimental data to quantify the photo-catalytic activity of the water splitting process. The incident flux of photons for the quantum yield determination is considered based on a frequency of $\lambda \geq 310$ nm ($3.44337E-05$ photon moles m⁻² s⁻¹), which is the absorption threshold of the zinc sulfide. Figure 7.13 shows the effect of catalyst concentration on quantum efficiency. The quantum efficiency is almost doubled for twice the concentration of

the catalyst, but it reaches a saturation point which in this reactor is confined to almost 3% w/v. Quantum efficiency is the measure of effectiveness of a catalyst in absorbing the photonic energy to form the excited states and reduction of water molecules to hydrogen. It is concluded that a higher catalyst concentration might not necessarily act in favour of a higher production rate as it causes a higher catalyst encounter with species other than electron donors and water molecules, and also negates the light penetration through the aqueous solution. The following correlation is extracted for quantum efficiency:

$$\eta_{\phi} = -3.79C_{Cat}^4 + 26.8C_{Cat}^3 - 64.99C_{Cat}^2 + 84.66C_{Cat} - 25.32, R^2 = 0.99 \quad (7.11)$$

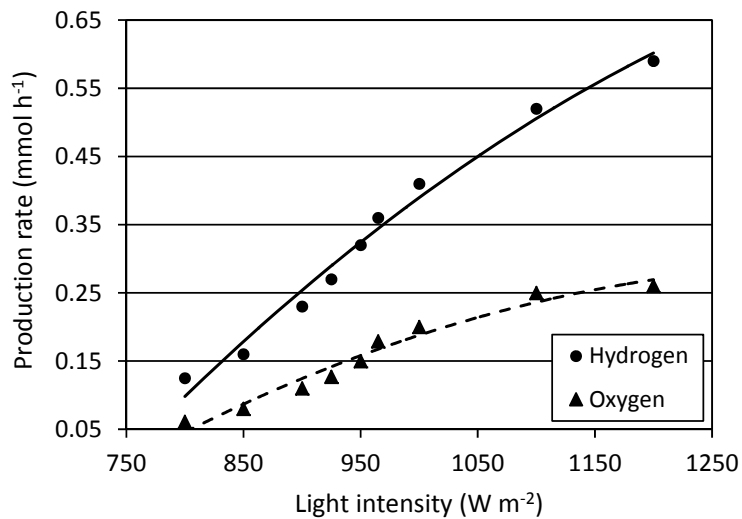


Figure 7.12: Effect of light intensity on hydrogen production rate (Uncertainty $\pm 3.6\%$).

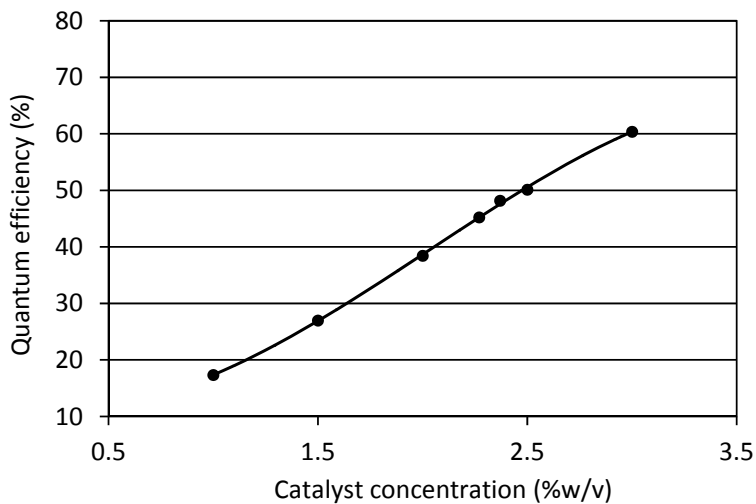


Figure 7.13: Effect of ZnS concentration on quantum efficiency.

Energy and exergy efficiencies of catalytic hydrogen and oxygen production in the dual-cell are calculated based on measured data. The agitator energy consumption is almost 1 percent of the input solar energy, and can be safely neglected. The energy efficiency represents the conversion ratio of solar to hydrogen energy. Exergy efficiency accounts for chemical and physical exergy content of the output product. The results in Figure 7.14 show the exergy efficiency of the hydrogen evolution reaction and the complete system, denoted as H₂ and H₂+O₂ respectively, to compare the efficiency enhancement due to utilization of a complete system of water splitting. The results indicate that energy and exergy efficiencies of hydrogen production are improved up to three times by increasing the catalyst concentration from 1% to 3% w/v. The exergy efficiency of the overall system is almost 25% more than the exergy efficiency of the hydrogen production half reaction, which emphasises the beneficial contribution of oxygen production in a photo-catalytic water splitting process. The energy and exergy efficiencies are increased drastically for lower concentrations of catalyst as opposed to high concentrations, which can be interpreted as a lower conversion rate of input energy and exergy of light to hydrogen and oxygen. The following correlations are extracted for the energy and exergy efficiencies of the complete system:

$$\eta_{en} = -0.21C_{Cat}^3 + 1.42C_{Cat}^2 - 1.64C_{Cat} + 1.18, R^2 = 0.99 \quad (7.12)$$

$$\eta_{ex} = 0.0415C_{Cat}^3 + 0.059C_{Cat}^2 + 0.83C_{Cat} + 0.155, R^2 = 0.99 \quad (7.13)$$

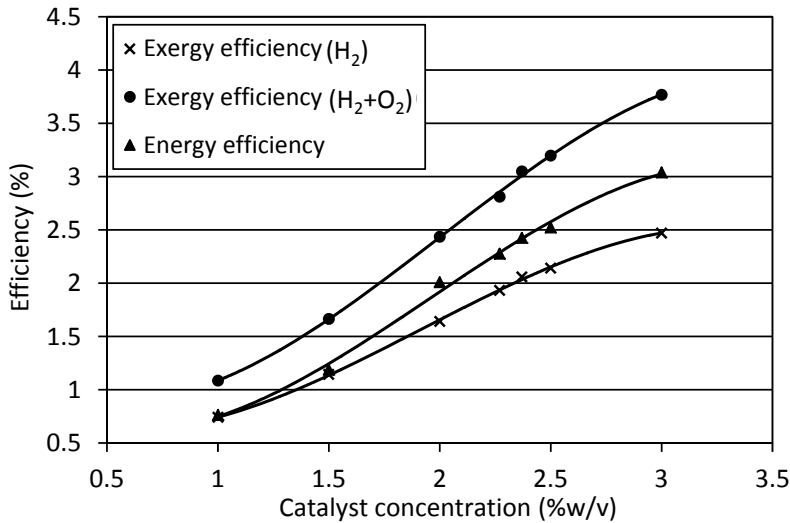


Figure 7.14: Effect of ZnS concentration on energy and exergy efficiency.

The effect of light intensity on quantum efficiency is shown in Figure 7.15. The efficiency calculations are based on experimental data for ZnS suspension with 3% w/v

concentration. The quantum efficiency is increased 2.5 times when the light intensity is increased from 800 to 1200 W m^{-2} . The increasing trend suggests that light intensities above 1 sun, e.g. 1000 W m^{-2} , is less beneficial to enhance the productivity of the catalyst. This is related to the limited diffusion rate of ions and contributing species, and light penetration restrictions at high concentrations of the catalyst. The following correlation is extracted for quantum efficiency:

$$\eta_{\phi} = -0.0001I^2 + 0.416I - 239.01, R^2 = 0.98 \quad (7.11)$$

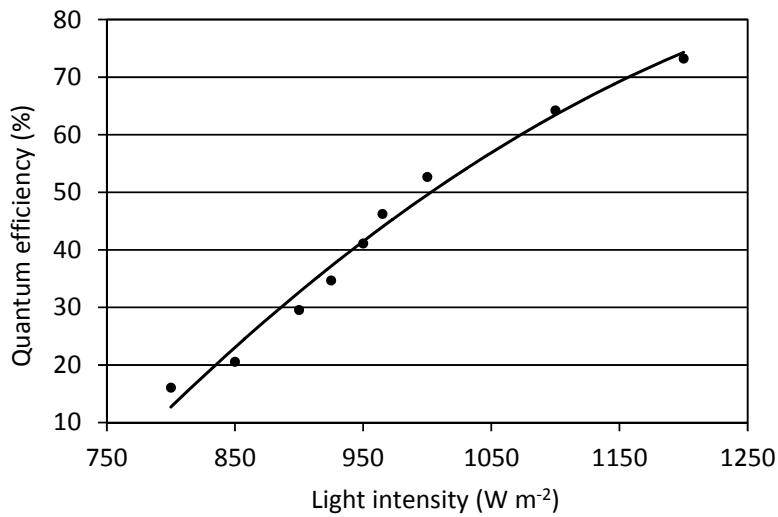


Figure 7.15: Effect of light intensity on quantum efficiency.

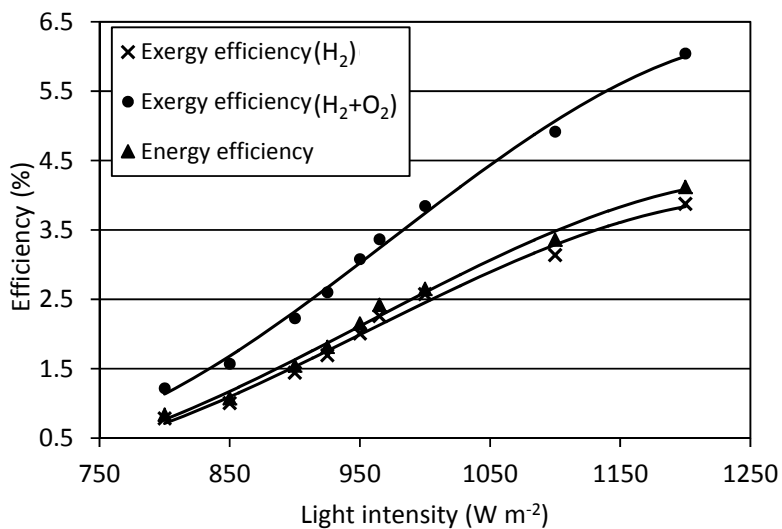


Figure 7.16: Effect of light intensity on energy and exergy efficiencies.

An evaluation of energy and exergy efficiencies versus light intensity explores the capability of zinc sulfide to utilize the incident light in favour of hydrogen production. The results in Figure 7.16 indicate the rapid increase of efficiency due to light intensity increase to 1000 W m^{-2} and fewer enhancements for higher values. The exergy efficiency of the complete system can be upgraded up to six fold if the light intensity increases 50%. The efficiency results are based on experimental data for the ZnS suspension with 3% w/v concentration. The following correlations are extracted for energy and exergy efficiencies of the complete system:

$$\eta_{en} = -7E - 8I^3 + 0.0002I^2 - 0.181I + 53.36, R^2 = 0.995 \quad (7.12)$$

$$\eta_{ex} = -9E - 8I^3 + 0.0003I^2 - 0.24I + 70.5, R^2 = 0.993 \quad (7.13)$$

7.1.3. Model validation

The experimental data are compared with the predictive model, as developed in Section 6.1.1, to validate the accuracy of the model and the feasibility of production rate measurements. Figure 7.17 shows the hydrogen production rate versus catalyst concentration at light intensity of 1000 W m^{-2} . The measured and predicted values show close agreement as the maximum difference between the two results is about 3.5%. Also, the experimental results are compared with the predictive model for variation of the hydrogen production rate as a function of light intensity. As shown in Figure 7.18, the results are in acceptable agreement with a maximum deviation of 3.1%. These results confirm that photo-catalytic reaction is correctly modeled based on the sequence of molecular reactions.

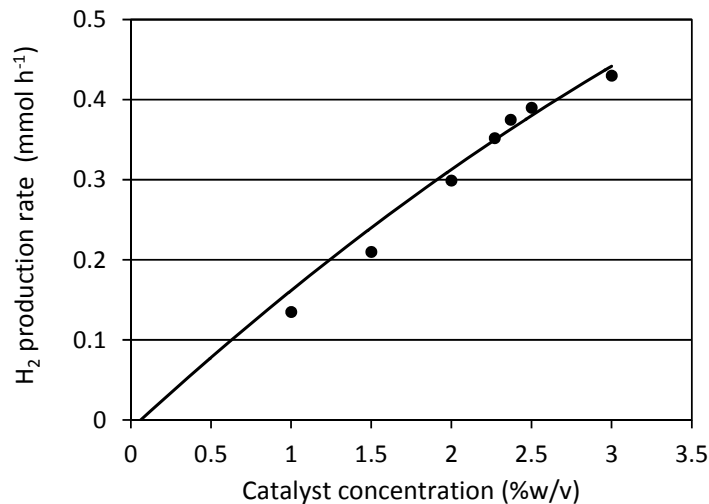


Figure 7.17: Measured (solid dots) and predicted (solid line) values of hydrogen production rate versus catalyst concentration.

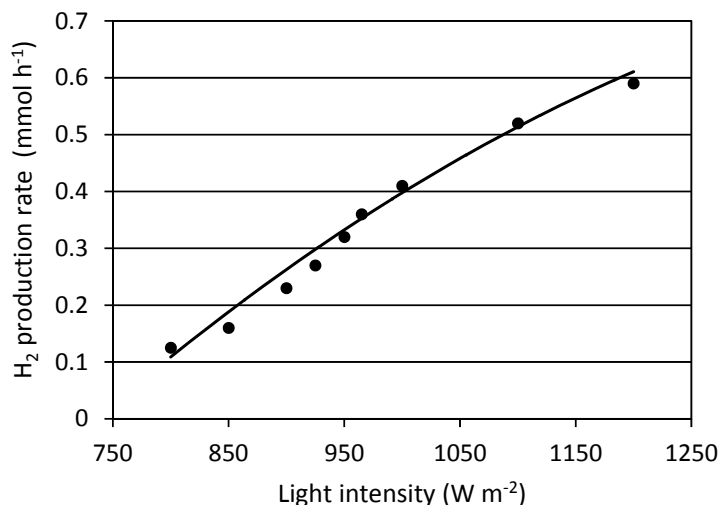


Figure 7.18: Measured (solid dots) and predicted (solid line) values of hydrogen production rate versus light intensity.

The experimental results are also qualitatively compared with past literature data [7]. A close agreement between the conclusions is observed. Rober et al. [7] performed some experiments with 1% w/v concentration of zinc sulfide suspension under illumination with a high-pressure mercury lamp. The source of light in their experiments supplied only high energy photons in the UV spectrum. Therefore, the productivity of the catalyst is almost 2 times higher. By adjusting the hydrogen production rate from reference [7] with respect to the light intensity used in this research, e.g. 1000 W m⁻² solar spectrum, the result would be about 0.157, which is close to the data presented in Figure 7.17.

The increasing trend of hydrogen production rate with light intensity is qualitatively verified with available data in the literature [230], and a good agreement is obtained. The increase of incident photons to the catalytic centre enhances the photo-excitation of more catalyst molecules that lead to a higher electron injection rate and subsequently higher water reduction rate. However, an increase of light intensity is followed by unfavourable mechanisms such as electron-hole recombination that results in a gradual decaying trend. This effect will be intensified if the catalyst concentration is not high enough to capture the incident photons.

7.1.4. Dual-cell experiments with CdS catalyst

The band gap of zinc sulfide is 3.6 eV, which categorizes it as an ultraviolet-light-driven photo-catalyst. This characteristic limits the catalyst absorption to less than 5% of the

solar spectrum. Therefore, more than 95% of the spectrum remains unused. Cadmium sulfide is an alternative photo-catalyst with band gap of 2.4 eV, which is able to absorb the light from the UV to part of the visible spectrum with $\lambda \leq 520$ nm. Although the CdS catalyst seems to have a suitable band gap with visible light response, it incorporates photo-corrosion during water splitting as follows:



Consequently, the disulfide ion in CdS is oxidized by photo-generated holes rather than H_2O . However, this issue can be addressed by the addition of hole scavenger materials such as sodium sulfide (Na_2S).

Several experiments are performed with the CdS photo-catalyst in the same conditions as ZnS experiments. The main objective is to evaluate the performance of CdS in a wider range of light spectrum and to utilize this catalyst with the accompanying of ZnS in a hybrid manner. Figure 7.19 shows the amount of hydrogen and oxygen that evolved during a 3 hour illumination of CdS suspensions in a basic solution of sodium sulfide under the solar simulator. The hydrogen evolution is driven by light and electrical energy, as denoted by the hybrid hydrogen. The hydrogen produced by the solar driven water splitting reaction is calculated based on measured values of evolved hydrogen and the current density of electrodes.

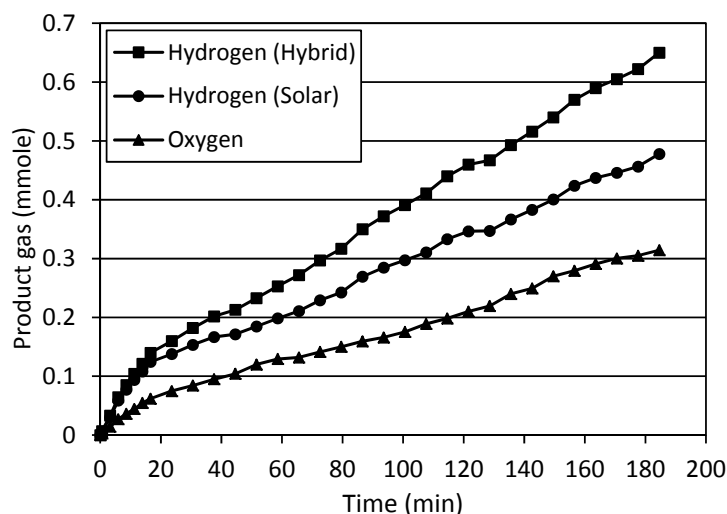


Figure 7.19: Amount of hydrogen and oxygen evolved versus illumination time for CdS concentration 1% w/v, and light intensity 1000 W m^{-2} (Uncertainty $\pm 4.9\%$).

The effect of CdS catalyst concentration on hydrogen production is presented in Figure 7.20. The data are recorded during illumination of CdS suspensions under 1 sun. For concentrations higher than 1.5% w/v, the productivity of the catalyst is considerably degraded. The photo-catalytic activity of CdS mesh powders depends on their specific surface area. At higher catalyst concentrations, particle agglomerates avoid effective absorption of light, and also cause light diffraction and scattering. Increasing the catalyst concentration from 1% to 1.5% w/v enhances the reactor productivity by almost 6%; this drops about 15% by the further addition of the catalyst to 2% w/v.

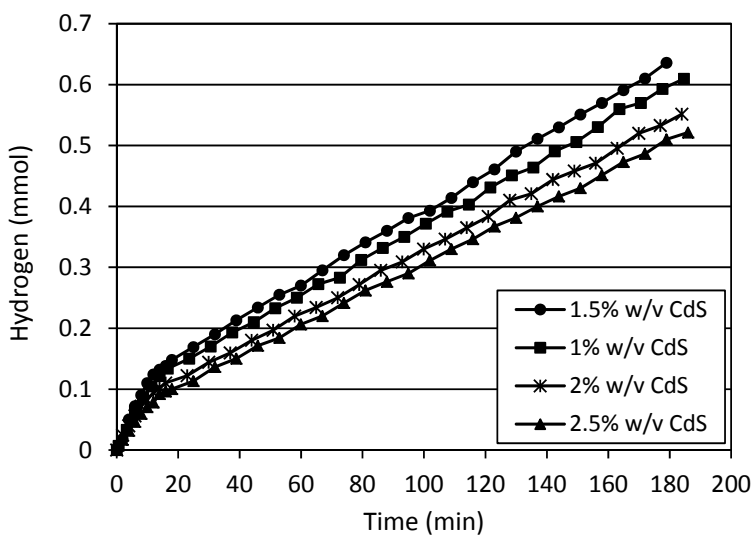


Figure 7.20: Effect of CdS concentration on hydrogen production (Uncertainty $\pm 3.9\%$).

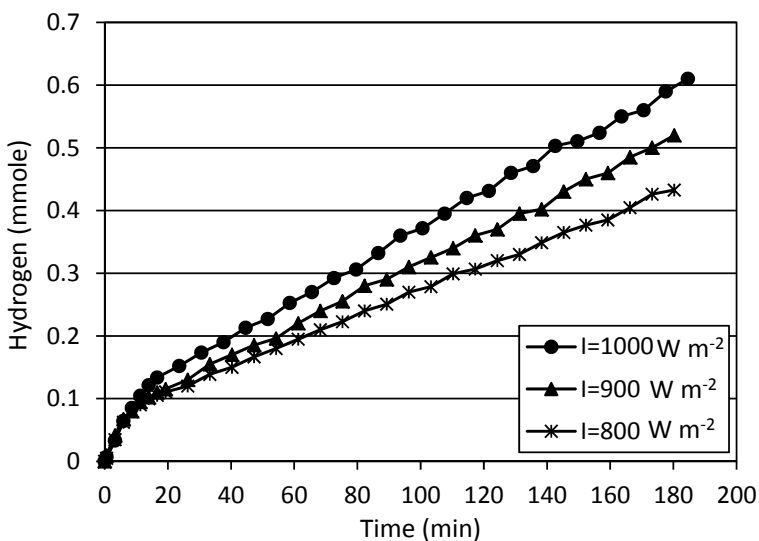


Figure 7.21: Effect of light intensity on hydrogen production, (Uncertainty $\pm 4.1\%$).

The hydrogen production in 1% w/v CdS suspensions is measured under 3 different light intensities to analyze the photo-catalytic response of this catalyst to the rate of high energy photons in UV and visible spectra. As shown in Figure 7.21, the rate of hydrogen production decreases by almost 12% for every 100 W m⁻² reduction in light intensity.

Different efficiencies are calculated to measure the effectiveness of the CdS catalyst to convert UV and visible light energy to hydrogen energy in a complete system. Table 7.1 presents the efficiency data for two different catalyst concentrations. The results show low quantum efficiency for CdS compared with ZnS (Figure 7.13), which indicates the higher effectiveness of ZnS catalyst in absorbing the photon energies within the band gap spectra. However, the values of energy and exergy efficiencies are almost 50% higher for CdS catalyst. This indicates that cadmium sulfide is not an effective absorbent of light energy, but that it utilizes the partially absorbed energy and exergy more effectively than zinc sulfide. This conclusion confirms the possibility of using ZnS and CdS in a hybrid manner. More details are provided in Section 7.1.5.

Table 7.1: Efficiencies of photo-catalytic water splitting using CdS catalyst.

[CdS] %w/v	H ₂ (mmol h ⁻¹)	O ₂ (mmol h ⁻¹)	η_{ϕ}	η_{en}	η_{ex,H_2}	η_{ex,H_2+O_2}
1	0.34	0.15	0.013	0.023	0.022	0.032
1.5	0.39	0.153	0.015	0.027	0.026	0.036

7.1.5. Hybridization of photo-catalytic water splitting

Hybridization of the water splitting process is accomplished in two ways. The first step is utilization of electric power supply to deliver negative charges at catalytic active sites for reduction of water molecules to hydrogen and decomposition of hydroxide ions to oxygen. This technique enhances the hydrogen production rate in a complete system through water electrolysis. Secondly, another photo catalyst is utilized to recover the visible portion of the solar spectrum.

The dual-cell may consist of two tandem units that are installed back to back. The first chamber is exposed to solar radiation at the cathodic side through a transparent window, and contains zinc sulfide suspensions to capture the solar energy in the UV spectrum. The rest of the photons, with lower energies, penetrate the second chamber, where cadmium sulfide suspensions can interact with the upper visible light spectrum and dislocate multiple electrons

at the active centre. The remaining un-absorbed portion of radiation (mainly in the lower visible and infrared range) crosses the second tandem and reaches a PV array or a solar thermal collector. The unused portion of the spectrum is hypothetically used for co-generating low-grade heat or generating the electricity needed for the oxygen evolution reaction. Figure 7.22 shows the approximate cut-off wavelength for each unit of the hybrid photocatalytic water splitting system.

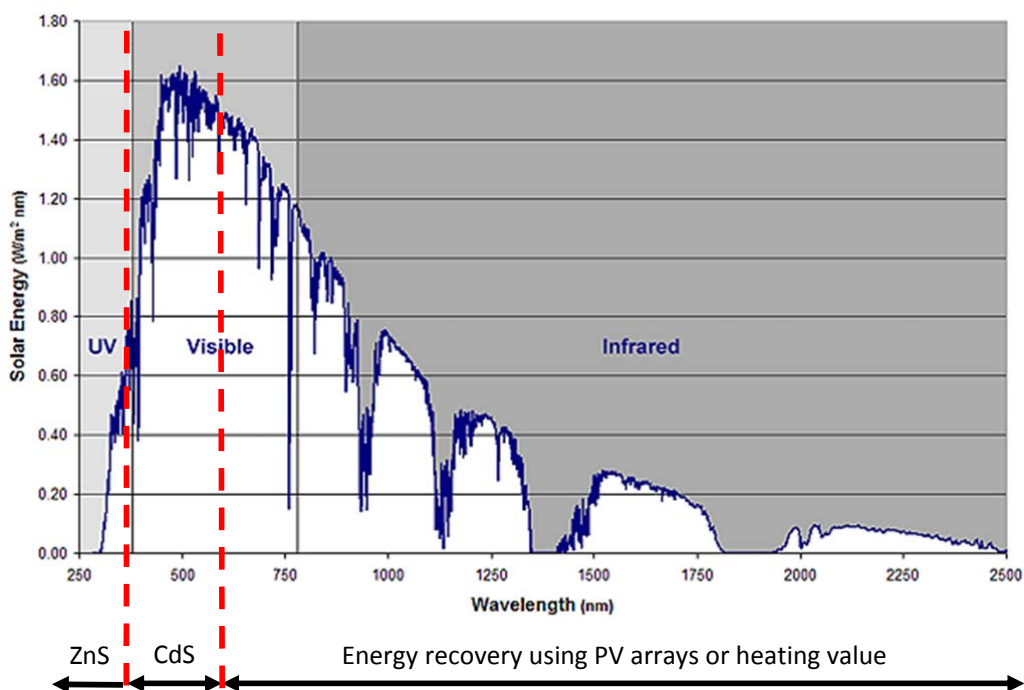


Figure 7.22: Hybrid utilization of solar spectrum.

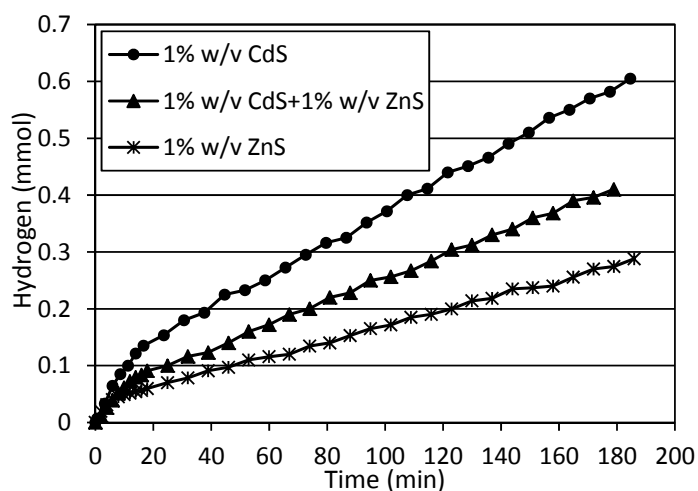


Figure 7.23: Productivity of ZnS and CdS catalysts in stand-alone and mixture operation (Uncertainty $\pm 3.9\%$).

The CdS and ZnS photo-catalyst powders are mixed in an aqueous solution to examine the possibility of the hydrogen production rate enhancement by utilizing more of the portion of the solar spectrum. As shown in Figure 7.23, the production rate in the case of mixing CdS and ZnS is increased by almost 30% compared with ZnS performance. However, the CdS catalyst has a higher productivity in a standalone operation. Cadmium sulfide provides a higher conversion rate even with a lower molar concentration (0.07 M CdS compared to 0.1 M ZnS), and CdS atoms have less chance of receiving high energy photons in the presence of ZnS catalyst molecules. On the other hand, the CdS catalyst is more expensive than twice the ZnS market price, and requires higher amounts of sacrificial agents during the experiments to avoid degradation. Therefore, the utilization of cadmium sulfide in favour of enhancing the productivity of zinc sulfide has to be determined by the production rate scale.

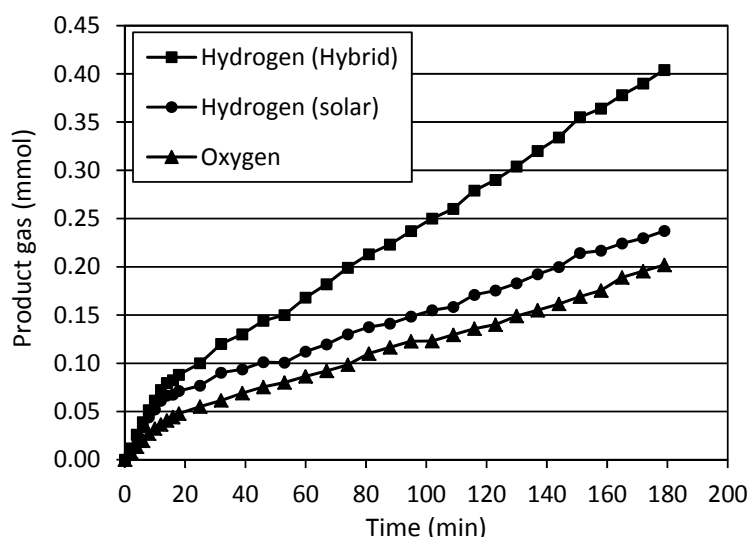


Figure 7.24: Amount of hydrogen and oxygen evolved versus illumination time for ZnS 1% w/v mixed with CdS 1% w/v at light intensity of 1000 W m^{-2} (Uncertainty $\pm 4.9\%$).

As concluded from previous results, cadmium sulfide is an alternative photo-reactor to recover a portion of solar light that falls in the visible spectra. Hydrogen and oxygen evolution during 3 hours of photocatalytic water splitting, using a mixture of CdS and ZnS photo-catalyst powders, is shown in Figure 7.24. The data points denoted as hydrogen (hybrid) are related to generated hydrogen with two sources of light and electrical energy. The amount of sodium sulfide which is consumed, in order to maintain the catalyst mixture

activated during the operation, is almost 40% more than the case of utilizing 2% w/v ZnS catalyst.

The effect of catalytic hybridization on hydrogen production is investigated from a catalyst concentration point of view. The results in Figure 7.25 are calculated based on experimental data for each catalyst in a standalone and mixture operation. The results indicate that a mixture of ZnS and CdS catalysts can enhance the productivity of the photo-catalytic process by about 45%. However, the addition of the CdS catalyst from 1% to 1.5% w/v does not make a significant difference. Also, as concluded from previous results in Figure (7.20), CdS concentrations of more than 1.5% w/v make a negative effect due to light scattering and agglomeration of catalyst particles.

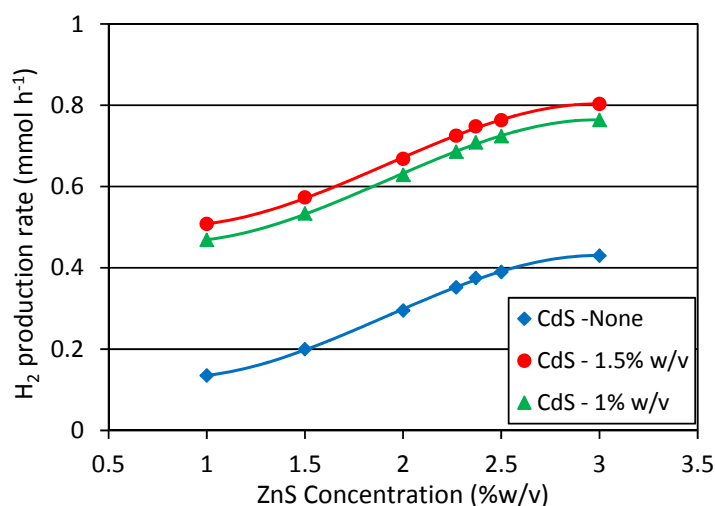


Figure 7.25: Effect of catalytic hybridization on hydrogen production for different ZnS concentrations.

The catalytic hybridization experiments are also performed by exposing the dual-cell reactor to different light intensities and ZnS catalyst concentration of 3% w/v. As shown in Figure 7.26, an increase of light intensity to more than 1,000 W m⁻² leads to more enhancements in the productivity of catalyst mixtures than pure ZnS suspension. At light intensities above 1,000 W m⁻², more photons with enough energy reach the catalytic centres and compensate the scattering and diffraction of light due to accumulation of catalyst particles. The productivity of the catalyst is improved by almost 30% due to a 20% increase in reference light intensity.

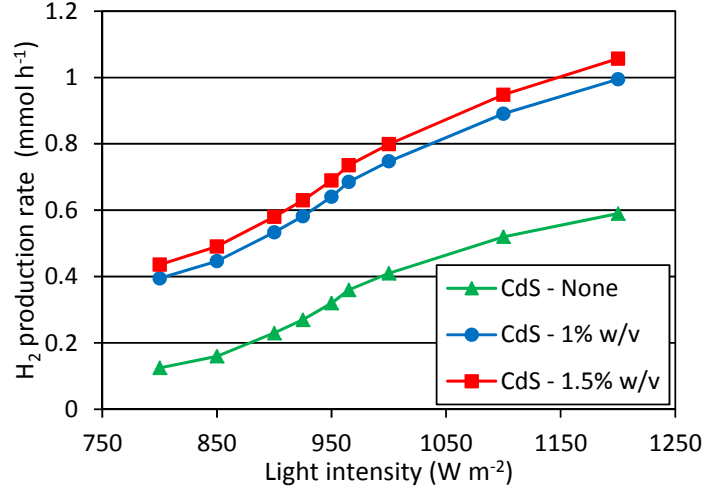


Figure 7.26: Effect of catalytic hybridization on hydrogen production for different light intensities.

7.1.6. Scale up results for photo-catalytic reactor

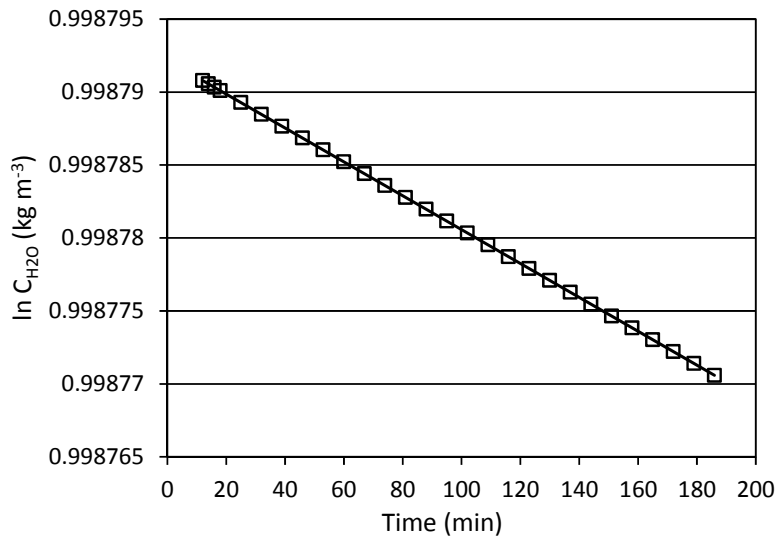
As stated in Section 5.2, a kinetic model for the photo-reactor should be developed as utilized for a scale-up analysis. The rate of the hydrogen production reaction is considered to be proportional to the n^{th} power of the water concentration and the volumetric rate of energy absorption raised to the m^{th} power. The parameter m is related to the rate of excited state formation, electron-hole formation and recombination at the surface of the catalyst. It normally takes a value between 0.5 and 1.

The coefficients n and m in the kinetic rate equation are obtained from linear regression of a plot of $\ln C_{H_2O}$ versus time and $\ln(-dC_{H_2}/dt)$ versus $\ln(I)$, as shown in Figure 7.27. The only adjustable parameter of the model (K) is estimated by least-squares fitting of the fitted equation to the experimental results of the photo-catalytic hydrogen production under different experimental conditions. The plot of $\ln C_{H_2O}$ versus time in Figure 7.27 (a) is linear, therefore the photo-catalytic water splitting is a 1st order reaction and the “ n ” coefficient is set to 1. A linear curve fitting of experimental data in Figure 7.27 (b) derives the coefficient “ m ” as 0.729. A MATLAB code is developed to find the parameter K based on least-squares fitting of the modeling equation as $3.606E-10$ ($3.49E-10$, $3.71E-10$) $\text{kg}^{(1-n)} \text{s}^{-1} \text{m}^{3m+3n-3} \text{W}^{-m}$. Therefore, the kinetic model equation takes the following form:

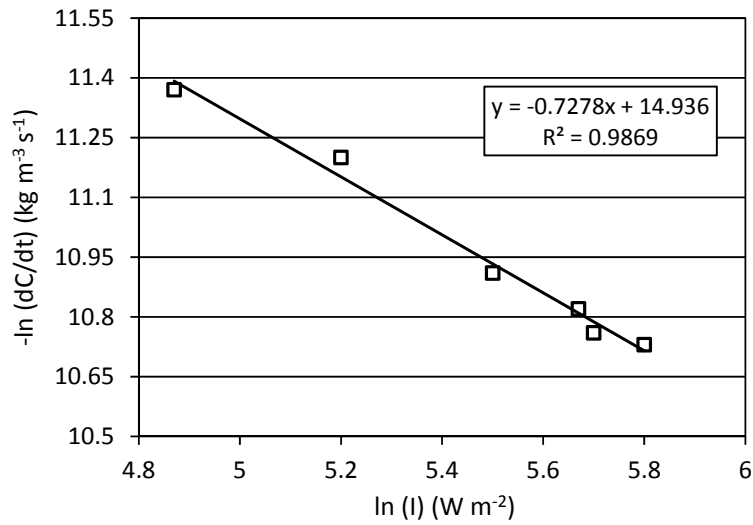
$$r_{H_2} = 3.606E - 10(I_{ave})^{0.729} C_{H_2O} \quad (7.15)$$

A scale-up analysis of the photo-reactor is performed by following the procedure that is described in Section 5.2.1. The reactor is assumed to be tubular and the flow is fully turbulent. Among several ways of increasing the capacity of a tubular reactor, geometric

similarity is selected for simultaneous scaling up of reactor diameter and length. The length-to-diameter ratio of the scaled-up reactor is kept at less than 5.5 to avoid interruptions in the photo-catalytic activity of catalyst. Very long tubular reactors cause mixing problems and settlement of catalyst suspensions. In addition, reactors with very large diameters do not have enough penetration of light.



(a)



(b)

Figure 7.27: Estimation of kinetic parameters n (a) and m (b) for photo-catalytic hydrogen production.

The mean residence time (\bar{t}) is also assumed to be constant. Implementation of scale-up factors with constant mean residence time is commonly used. The general scale-up factors are then subject to the constraints that $S = S_R^2 S_L$. Imposing a constant value for \bar{t} means that

only two independent variables should be upgraded for each design. The parameter S is taken as one of them. Either S_R or S_L is then chosen as the other. The rest of the variables are calculated based on Table 5.2. Depending on the scale-up method, a specific value for either of S_R or S_L can be selected.

Tables 7.2 and 7.3 list the results of a scale-up study for the photo-reactor under 1 sun irradiation. The calculations are performed for 6 different scale-up ratios with three different constraints in every case considered as follows:

- 1) The length scale factor is known.
- 2) The diameter scale factor is known.
- 3) The length to diameter ratio factor is known.

Table 7.2: Geometry characteristics of Scaled up photo-reactor.

Design constraint	Scale-up ratio	\dot{n}_{H_2} (mmol h ⁻¹)	S_R	S_L	S	R_2 (m)	L_2 (m)	V_2 (L)
1	2	0.6	1.155	1.500	2	0.029	0.195	0.357
2	2	0.6	1.200	1.389	2	0.030	0.181	0.357
3	2	0.6	1.260	1.260	2	0.031	0.164	0.357
1	5	1.5	1.414	2.000	4	0.035	0.260	0.714
2	5	1.5	1.400	2.041	4	0.035	0.265	0.714
3	5	1.5	1.587	1.587	4	0.040	0.206	0.714
1	10	3	1.528	3.000	7	0.038	0.390	1.250
2	10	3	1.800	2.160	7	0.045	0.281	1.250
3	10	3	1.913	1.913	7	0.048	0.249	1.250
1	50	15	2.449	5.000	30	0.061	0.650	5.358
2	50	15	2.700	4.115	30	0.068	0.535	5.358
3	50	15	3.107	3.107	30	0.078	0.404	5.358
1	100	30	3.162	7.000	70	0.079	0.910	12.501
2	100	30	3.300	7.428	70	0.083	0.836	12.501
3	100	30	4.121	4.121	70	0.103	0.536	12.501
1	1000	300	5.774	12.000	400	0.144	1.560	71.435
2	1000	300	7.200	10.406	400	0.155	1.353	71.435
3	1000	300	7.368	7.368	400	0.184	0.958	71.435

The reference geometry is the same as the dual-cell experimental apparatus that is described in Section 4.1.2. For the scale-up ratios from 2 to 50, all three constraints have the same result for kinetic and physical characteristics. It should be noted that detailed calculations are required to confirm any design. The scaling exponents are approximations for conceptual studies and approach the most promising option for scale-up.

As confirmed in previous results, the productivity of each photo-reactor is increased by enhancing the light intensity at which the catalytic sites are illuminated. This can be implemented by concentrating the light or using several light sources. Scale-up analysis is conducted to analyze the effect of higher light intensities on the productivity rate. The geometric characteristics are kept the same as the previous case with $1,000 \text{ W m}^{-2}$ light intensity, and calculations are performed to determine how much improvement in hydrogen production can be achieved with each scaled-up design and similar amounts of catalyst. The results in Tables 7.4, 7.5, and 7.6 present the output values for the upgraded production rates at light intensities of $2,000 \text{ W m}^{-2}$, $5,000 \text{ W m}^{-2}$, and $10,000 \text{ W m}^{-2}$ respectively.

Table 7.3: Kinetic and physical characteristics of scaled-up photo-reactor.

Design Constraint	Scale-up ratio	\dot{n}_{H_2} (mmol h ⁻¹)	ZnS (kg)	[Na ₂ S] (M)	[H ₂ O] (kg m ⁻³)	Impeller diameter (m)	Agitator speed (rev/s)	Power (W)	Mixing time (min)
1,2,3	2	0.6	0.003	1.440	909.09	0.0420	1.714	0.4	11.67
1,2,3	5	1.5	0.009	4.128	892.86	0.0529	1.470	0.8	13.61
1,2,3	10	3	0.019	9.120	869.57	0.0637	1.298	1.4	15.41
1,2,3	50	15	0.107	51.120	847.46	0.1035	0.939	6	21.29
1	100	30	0.204	97.920	847.46	0.1372	0.778	14	25.71
2	100	30	0.205	98.256	847.46	0.1372	0.778	14	25.71
3	100	30	0.209	100.512	847.46	0.1372	0.778	14	25.71
1	1000	300	3.740	1795.20	833.33	0.2451	0.528	80	37.86
2	1000	300	4.000	1920.0	833.33	0.2451	0.528	80	37.86
3	1000	300	4.200	2017.0	833.33	0.2451	0.528	80	37.86

Table 7.4: Productivity enhancement of scaled-up reactor with $2,000 \text{ W m}^{-2}$ light intensity.

Design constraint	ZnS (kg)	Scale-up ratio	\dot{n}_{H_2} (mmol h ⁻¹)
1,2,3	0.003	3.28	0.98
1,2,3	0.0086	8.28	2.48
1,2,3	0.019	17.55	4.96
1,2,3	0.1088	82.26	24.68
1,2,3	0.204	165.73	49.72
1	3.74	1657.10	497.83
2	4	1655.94	497.78
3	4.2	1561.83	468.55

It is observed that the third constraint leads to lower enhancement in productivity at higher light intensities. A 10-fold increase of light intensity leads to 5 times higher hydrogen production rate without any necessary change in geometry or dimensions of the photo-reactor. Since the capital cost of light concentration is a challenging engineering issue, the

economic feasibility of very large scale-up ratios requires further research and studies to be conducted in detail. Parallel arrangement of smaller photo-reactor scales may be more beneficial. Utilization of a large scale photo reactor is also limited by catalyst concentration, as it causes optical blockage and saturation of water due to excess sacrificial reagent.

Table 7.5: Productivity enhancement of scaled-up reactor with 5,000 W m⁻² light intensity.

Design constrain	ZnS (kg)	Scale-up ratio	\dot{n}_{H_2} (mmol h⁻¹)
1,2,3	0.003	7.39	1.92
1,2,3	0.0086	17.19	4.86
1,2,3	0.019	32.24	9.67
1,2,3	0.1065	160.46	48.14
1,2,3	0.204	323.21	97.96
1	3.74	3229.87	968.96
2	4	3229.55	968.86
3	4.2	3047.01	913.80

Table 7.6: Productivity enhancement of scaled-up reactor with 10,000 W m⁻² light intensity.

Design constraint	ZnS (kg)	Scale-up ratio	\dot{n}_{H_2} (mmol h⁻¹)
1,2,3	0.003	10.59	3.18
1,2,3	0.0086	27.83	8.05
1,2,3	0.019	53.44	17.03
1,2,3	0.1065	265.96	79.79
1,2,3	0.204	535.72	160.72
1	3.74	5353.47	1607.04
2	4	5352.94	1605.88
3	4.2	5048.73	1514.62

In conclusion, the following scale-up criteria should be considered for design and fabrication of large scale photo-catalytic hydrogen production plants:

1) Hydrogen production capacity:

The target capacity for annual hydrogen production should be identified as the first constraint. This, in turn, determines the energy demand and operational working conditions. Subsequently, the feasibility of energy recovery options can be investigated.

2) Availability of resources:

The annual average insolation at the geographical attitude of the hydrogen production plant determines the potential light harvesting systems that can implemented with the most cost effectiveness and efficiency. It also implies a number required production

units that should be installed in parallel. In addition, water as the main source of hydrogen should be available in the purest form. Any impurity or water shortage in arid areas incorporates some limitations.

3) Technology constraint:

The conversion efficiency of water splitting technology has a direct effect on the capital cost. The plant capital cost, as the major contributor to the hydrogen price, limits the potential choices in terms of construction materials, technology complexity and subsequently the design approach.

7.2. Oxygen production reactor

7.2.1. Experimental results

In this section, the effects of current density and concentration difference between two half cells on the OER-overpotential of water electrolysis are discussed. In general, the voltage qualitatively represents the electric power that is required to produce a certain mass flux of hydrogen. In other words, a lower voltage means higher efficiency of water decomposition. The experimental results show that the current density, space between electrodes, electrode height, and concentration difference between two half cells have significant effects on the efficiency of water electrolysis. In this section, the experimental results are presented for the effects of these parameters. Following these results, the time dependent concentration of ions is modeled.

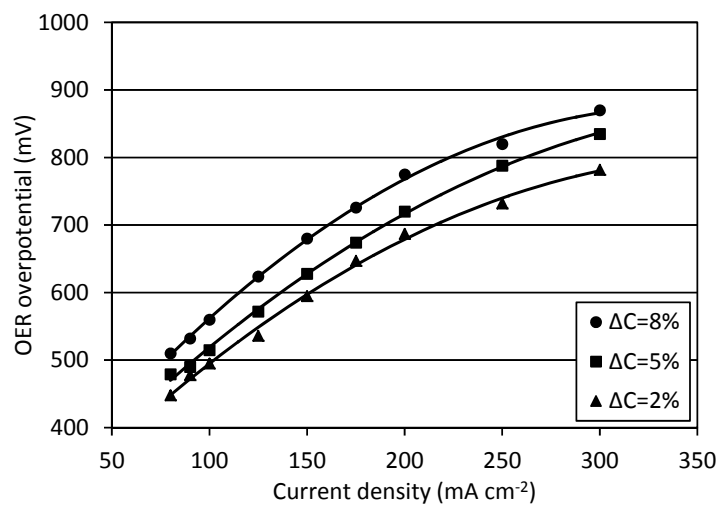


Figure 7.28: OER over-potential versus current density for H = 1.5 cm, S = 1 cm.

Experimental apparatus for OER experiments is described in Section 4.1.11. Figure 7.28 illustrates the relation between OER over-potential, $E(\text{mV})$, and electrolyte concentration difference between two half cells, at electrode height of $H = 1.5 \text{ cm}$, electrodes spacing of $S = 1 \text{ cm}$, and room temperature $T = 20 \text{ }^\circ\text{C}$. The following correlations are extracted for the minimum overpotential corresponding to concentration gradient of 2%, at $S = 1 \text{ cm}$ and $S = 1.5 \text{ cm}$ respectively:

$$U = -0.0041j^2 + 3.078j + 228.26, R^2 = 0.997 \quad (7.16)$$

$$U = -0.0041j^2 + 3.25j + 242.14, R^2 = 0.994 \quad (7.17)$$

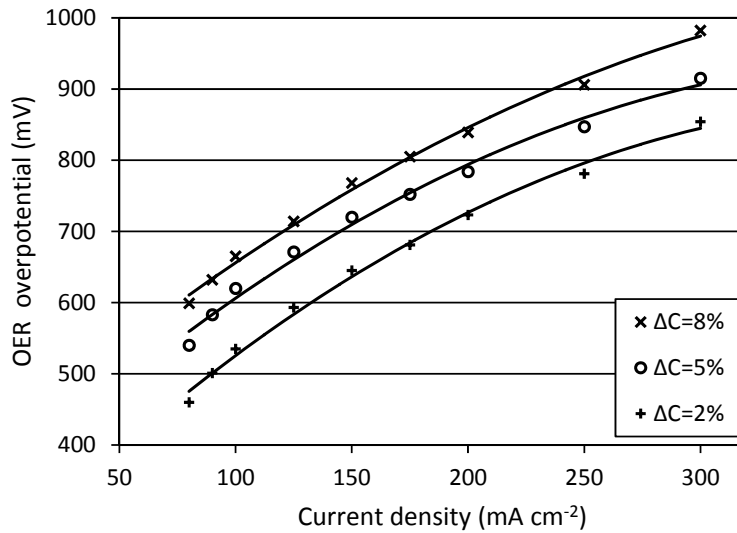


Figure 7.29: OER over-potential versus current density for $H = 1.5 \text{ cm}$ and $S = 1.5 \text{ cm}$.

Figure 7.29 illustrates this relation for electrode spacing of $S = 1.5 \text{ cm}$. A comparison of results shows the voltage decreases as the space becomes smaller. It is observed from this trend that the electric resistance between electrodes becomes smaller as the space gets closer. It is also shown that the electrolyte concentration difference between half cells has a negative effect on OER over-potential. However, a minimum current density is required to facilitate the diffusion of hydroxide ions. A concentration difference of 2% is selected as the minimum requirement.

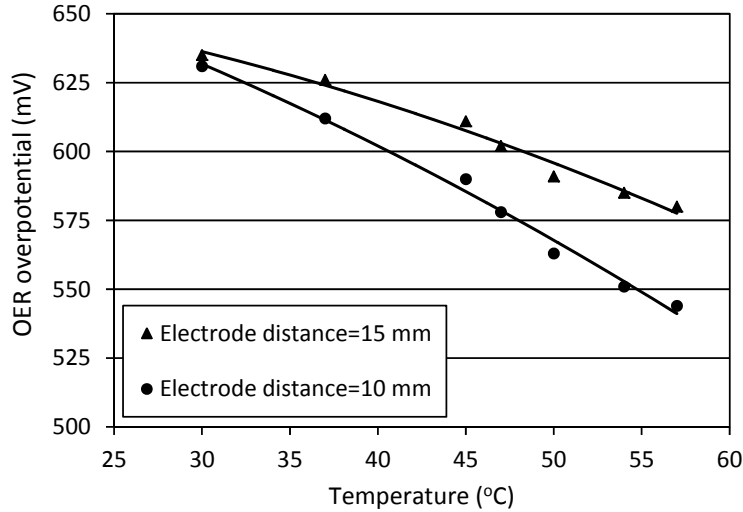


Figure 7.30: OER over-potential versus temperature for different electrode distances.

Figure 7.30 shows the effect of temperature on overpotential for two different electrode spaces. It can be concluded that the OER overpotential and subsequently the electro-catalysis efficiency become higher as the system temperature increases, especially in the region of smaller space between electrodes. A higher system temperature causes the increase of bubble volume and decrease of reversible potential. The increase of bubble volume is related to an increase of void fraction between electrodes, and subsequently, the efficiency is higher as the temperature increases. The following correlation is derived for the minimum overpotential corresponding to electrode distance of 10 mm:

$$U = -0.0225T^2 - 1.4T + 694.07, R^2 = 0.99 \quad (7.18)$$

Figure 7.31 illustrates the experimental result when the height of electrodes, H , was 50 and 15 mm, for different concentration gradients. Comparing the results, it is concluded that a lower OER overpotential can arise either with a smaller height of electrodes or lower concentration gradient. This result can be explained because the average void fraction between electrodes of a larger height is higher than that of a smaller height, assuming the mass flux of gas is uniform on both electrodes, but the result is affected differently by a concentration gradient of 5%. The effect of a shorter height is compensated by a lower concentration gradient. It is also worth noticing that there is no clear optimum space in the result of a 15 mm height. This implies the existence of an optimum space, depending on not only the current density but also the height of electrodes.

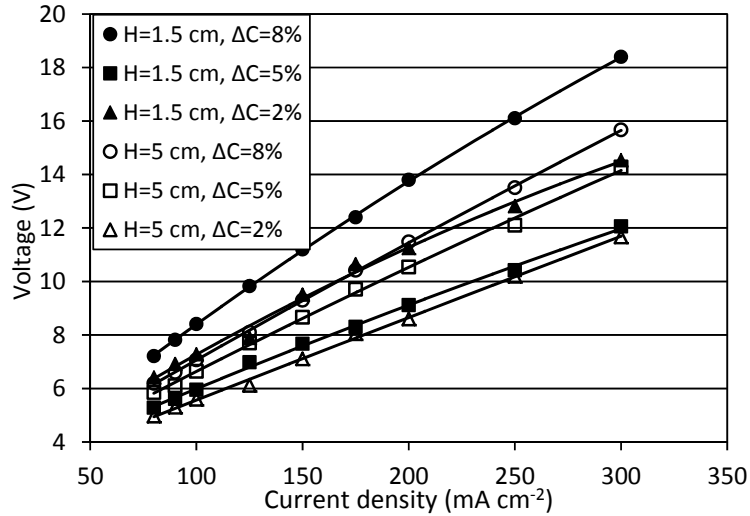


Figure 7.31: Effect of concentration gradient and electrode height on electrochemical performance (at working conditions $T = 300 \text{ K}$, $S = 1 \text{ cm}$, $J = 250 \text{ mA cm}^{-2}$).

7.2.2. Predictive model

The experimental data have been post-processed to derive a predictive model using commercial software called *Design-Expert 8.0.7.1 Trial*. A quadratic equation is fitted to the data as follows:

$$\begin{aligned}
 U = & 647.84 + 283.42 \times J + 288.13 \times T + 92.36 \times \Delta C + 67.53 \times H + 411.52 \times S + 51.31 \times J \times \Delta C + \\
 & 70.64 \times J \times H + 1288.59 \times J \times S - 1252.13 \times T \times S + 40.26 \times \Delta C \times H + 77.29 \times \Delta C \times S - 51.95 \times H \times S - \\
 & 353.24 \times J^2 + 444.97 \times T^2 + 149.32 \times \Delta C^2, R^2 = 0.93
 \end{aligned}
 \tag{7.19}$$

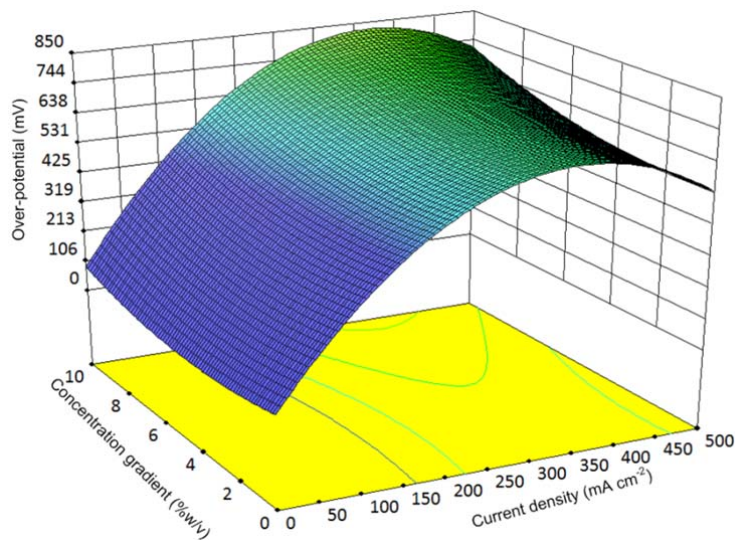


Figure 7.32: OER overpotential contours at different concentration gradients and current densities (at working conditions $T = 350 \text{ K}$, $H = 5 \text{ cm}$, $S = 10 \text{ mm}$).

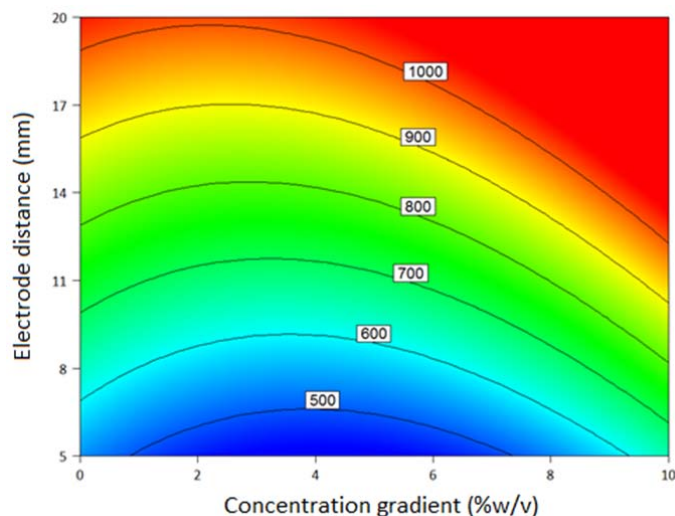


Figure 7.33: OER overpotential contours at different electrode distances and current densities (at working conditions $J = 250 \text{ mA cm}^{-2}$, $T = 350 \text{ K}$, $H = 5 \text{ cm}$).

The results of the predictive model are shown in Figures 7.32, 7.33 and 7.34. It can be concluded that the concentration gradient between two half cells in the range of $2\% < \Delta C < 4\%$ leads to an optimum over-potential in a practical range of current density. It is also observed that in a range of concentration gradient, the overpotential has an optimum point at a certain distance between electrodes. Figure 7.33 provides useful information to adjust the electrode distance depending on the concentration gradient to minimize the over-potential. The electrode height and distance affect the overpotential in a linear manner as shown in Figure 7.34.

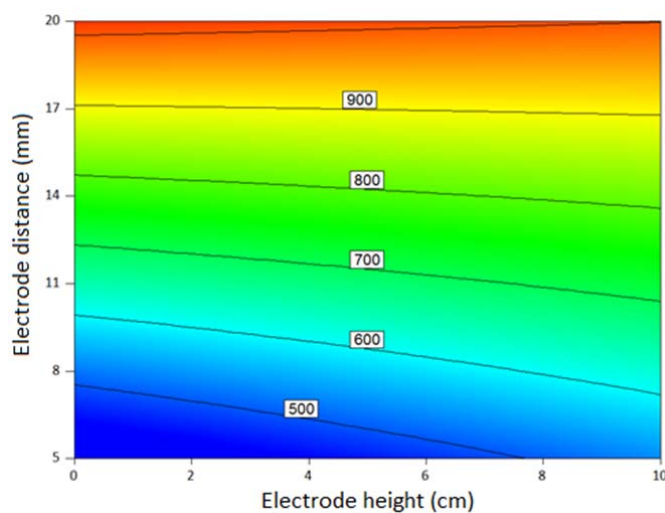


Figure 7.34: OER overpotential contours at different electrode distances and electrode heights (at working conditions $J = 250 \text{ mA cm}^{-2}$, $T = 350 \text{ K}$, $\Delta C = 2\% \text{ w/v}$).

7.2.3. Optimization of OER overpotential

The experimental study shows the importance of optimization to find a suitable range of physical parameters that minimize the OER overpotential. In this regard, a MATLAB code is developed based on the Nelder-Mead optimization algorithm (Appendix I) to find the minimum values of OER overpotential in a range of temperature, electrode height, and electrode distance at two different current densities and concentration differences of 2% (w/v). Values of $J = 150 \text{ mA cm}^{-2}$ and $J = 300 \text{ mA cm}^{-2}$ have been selected as two practical current densities and concentration differences between two half cells and minimized to 2% to avoid excess over-potential. The optimization results are shown in Tables 7.7 and 7.8 to include a necessary set of operational parameters that lead to an OER overpotential lower than 600 mV.

Table 7.7: Optimization results for $J = 150 \text{ mA cm}^{-2}$, $\Delta C = 2\%$ (w/v).

Number	T (K)	H (cm)	S (mm)	V (V)	U (mV)
1	300	1.5	10.0	8.4	594.0
2	358	3.9	13.7	7.2	499.2
3	309	2.1	7.8	5.7	453.1
4	348	3.9	14.4	7.6	575.7
5	336	4.4	10.4	5.1	451.4
6	330	3.6	11.1	7.4	507.6
7	360	2.3	11.7	4.8	397.9
8	358	2.8	14.9	7.5	554.0
9	325	3.8	10.0	5.8	482.5
10	315	1.6	11.6	8.5	597.6
11	341	4.0	11.5	5.8	481.9
12	304	4.5	9.9	7.3	577.9
13	354	4.5	14.5	7.1	557.7
14	308	2.9	9.0	7.6	513.2
15	356	1.8	11.6	5.0	402.6

The “fminsearch” function is utilized in MATLAB code that finds the minimum of a scalar function of several variables, starting at an initial estimate. This is generally referred to as unconstrained nonlinear optimization. The Nelder-Mead algorithm requires an initial set of data points that represent solution estimates. These data are supplied by experiments. The number of points supplied is greater than the spatial dimension to form a "simplex" in 2D. Subsequently, the algorithm evaluates the function at each point on the simplex, and then considers various ways of seeking a minimized estimate through replacement of one the vertexes of the simplex by its reflected image, or by shrinking or expanding the simplex.

Table 7.8: Optimization results for $J = 300 \text{ mA cm}^{-2}$, $\Delta C = 2\%$ (w/v).

Number	T (K)	H (cm)	S (mm)	V (V)	U (mV)
1	327.41	1.73	7.89	9.66806	593.347
3	340.8	4.06	5.55	7.93119	475.224
4	359.59	3.44	7.35	7.18096	422.543
5	308.39	4.87	4.05	8.17091	559.448
6	349.18	4.79	4.72	5.37408	399.371
7	332.87	1.9	7.07	8.48273	530.348
8	339.44	4.98	2.52	4.27686	344.009
9	300.09	4.98	2.43	7.46377	523.754
10	327.21	1.73	2.34	5.91033	389.013
11	319.73	2.85	3.53	7.21634	477
12	314.5	1.78	4.35	8.56978	537.432
13	353.12	4.16	4.36	4.87613	362.783
14	323.24	2.82	4.28	7.5655	495.091
15	305.69	4.51	4.25	8.63791	580.164
16	358.68	4.97	5.68	5.36709	400.014
17	357.07	1.57	7.27	7.71498	425.582

7.2.4. Reaction-diffusion formulation

In modeling of electrocatalysis at the vicinity of electrodes, it is assumed that a flat surface of the electrode is covered with a uniform layer of electrolyte of a specified thickness d that surrounds the supramolecular complexes. The selected supramolecular complex $[\{(bpy)_2Ru(dpp)\}_2 2RhBr_2](PF_6)_5$, is used to capture light energy and generate electrical charges at reaction sites to reduce water and produce hydrogen gas and hydroxide ions. Negative charges, generated by a power supply, are donated at the electrode surface to the supramolecular devices, and these are transmitted to the reaction sites under the influence of photonic radiation. The schematic representation of the electrode and electro-catalytic active site is given in Figure 7.35.

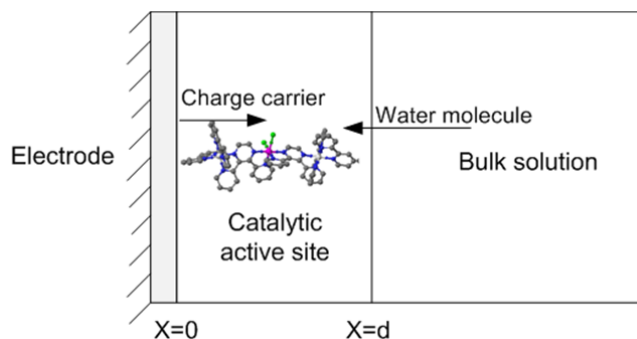


Figure 7.35: Schematic representation of electrode surface processes.

The electrochemical charge transfer process was analyzed based on the following reduction [231]:



where R and P are the reactant and reaction product, respectively, and n is a charge carrier, i.e., an electron for the cathodic reduction, and k is a second-order rate constant for the chemical reaction. The water molecule (H_2O) is referred to R as the reactant and the hydroxide ion (OH^-) is referred to P as the product. The transient reaction-diffusion equations governing the transport of electro-active species for the reaction (7.9) are given as follows:

$$\frac{\partial[H_2O(x,t)]}{\partial t} = D \frac{\partial[H_2O(x,t)]}{\partial x^2} - k[H_2O(x,t)][n(x,t)] \quad (7.10)$$

$$\frac{\partial[OH^-(x,t)]}{\partial t} = D \frac{\partial[OH^-(x,t)]}{\partial x^2} - k[H_2O(x,t)][n(x,t)] \quad (7.11)$$

$$\frac{\partial[n(x,t)]}{\partial t} = D_n \frac{\partial[n(x,t)]}{\partial x^2} - k[H_2O][n(x,t)] \quad (7.12)$$

Here, x and t refer to space and time, respectively. Also, $[H_2O(x,t)]$, $[OH^-(x,t)]$, and $[n(x,t)]$ denote the concentrations of water, hydroxide ions and charge carrier. D is the diffusion coefficient for the reactant/product and D_n is the diffusion coefficient for the charge carrier within catalytically active sites. The initial and boundary conditions are given as follows:

Initial conditions:

$$\text{At } t = 0: [H_2O(x, t = 0)] = 0.62 \text{ M}, [OH^-(x, t = 0)] = 0, [n(x, t = 0)] = 1 \text{ M} \quad (7.13)$$

Boundary conditions:

$$\text{At } x=0: \frac{\partial[H_2O(x,t)]}{\partial x} = 0; \frac{\partial[OH^-(x,t)]}{\partial x} = 0; [n(x,t)] = 1 \text{ M} \quad (7.14)$$

$$\text{At } x=d: [H_2O(x, t)] = 0.62 \text{ M}; [OH^-(x, t)] = 0; \frac{\partial n(x,t)}{\partial x} = 0 \quad (7.15)$$

The MATLAB software is utilized to solve the non-linear equations. The objective of this study is to investigate the charge and mass transfer in the vicinity of the electrode within the catalytically active site. This objective can be achieved explicitly by studying the effects of the second-order rate constant. Table 7.9 summarizes the values of parameters in the study.

Table 7.9: Input values and parameters.

Parameter	Dimension	Value
d	m	1×10^{-4}
D	$\text{m}^2 \text{s}^{-1}$	1×10^{-8}
D_n	$\text{m}^2 \text{s}^{-1}$	1×10^{-9}
k	$\text{M}^{-1} \text{s}^{-1}$	0.001-0.01
$\text{H}_2\text{O}(t = 0)$	M	0.62
$n(t = 0)$	M	1

Figure 7.36 shows the transient change of the hydroxide ion concentration in the alkali electrolyte of the OER at 3 V and under standard conditions. The initial concentration of hydroxide ions is assumed to be 1 M. The electrode-electrolyte interface, as the left boundary condition, is $x = 0$ cm and the catalytically active center thickness, as the other boundary, is located at $x = 0.01$ cm. The hydroxide ion density profiles in the first millimetres from the electrode are characterized by a steady increase that decreases over time. The variation of hydroxide ions concentration towards $x = 0.01$ cm decreases as the catalytic active center becomes farther from the electrode surface.

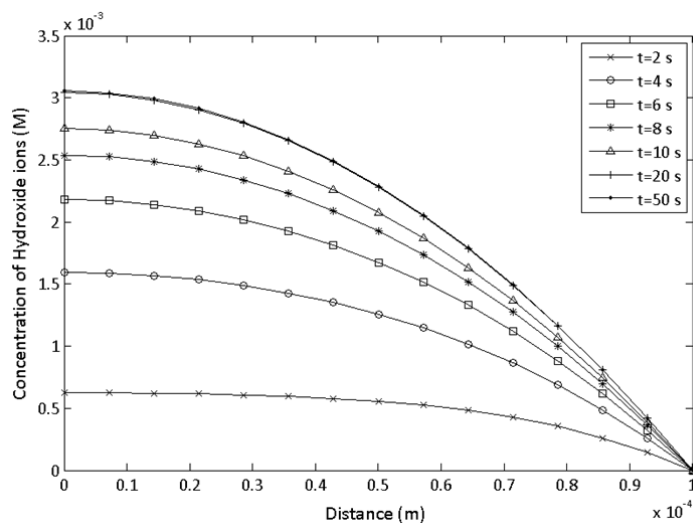


Figure 7.36: Time dependent spatial variation of hydroxide ion concentration ($k = 0.01 \text{ M}^{-1} \text{s}^{-1}$).

A second-order rate constant is defined as the dimensional rate constant for the chemical reaction. In this analysis, the value is varied from 0.01 to $0.001 \text{ M}^{-1} \text{s}^{-1}$. A comparison of Figures 7.37 and 7.40 shows that when the process is reaction rate controlled a

constant current can be predicted for a higher time. However, the hydroxide ion concentration increases when the value of the rate constant increases to $0.01 \text{ M}^{-1} \text{ s}^{-1}$.

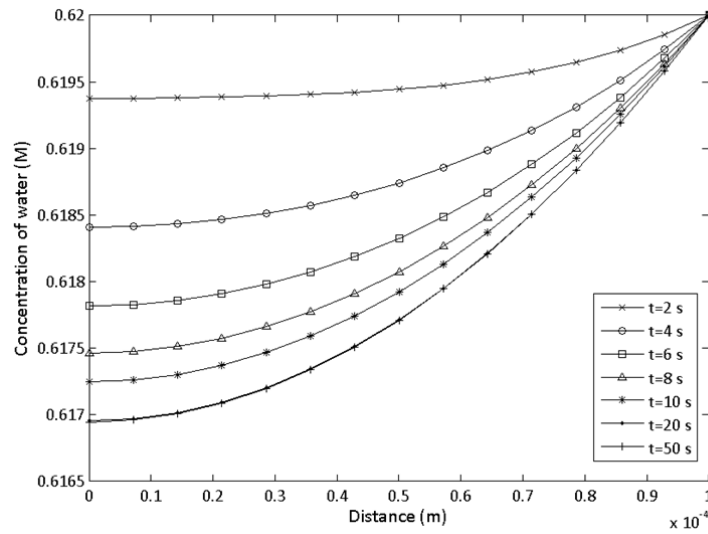


Figure 7.37: Time dependent spatial variation of water concentration ($k = 0.01 \text{ M}^{-1} \text{ s}^{-1}$).

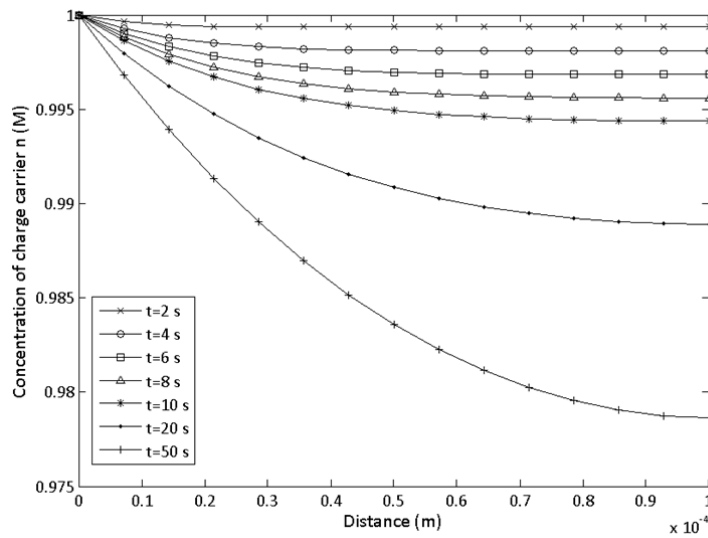


Figure 7.38: Time dependent spatial variation of charge carrier concentration ($k = 0.01 \text{ M}^{-1} \text{ s}^{-1}$).

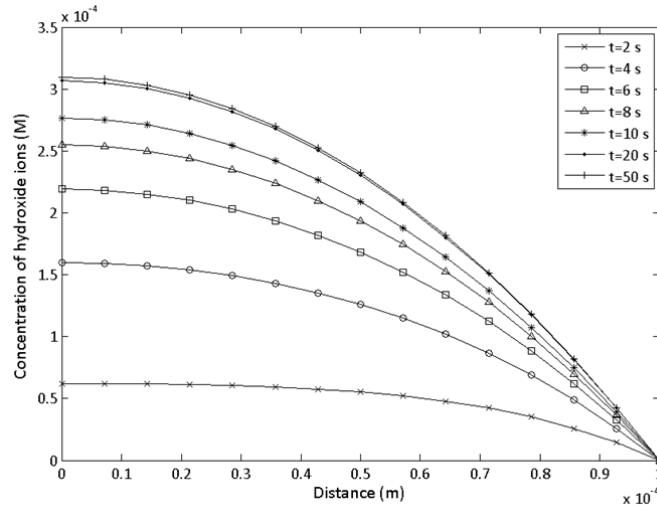


Figure 7.39: Time dependent spatial variation of hydroxide ion concentration ($k = 0.001 \text{ M}^{-1} \text{ s}^{-1}$).

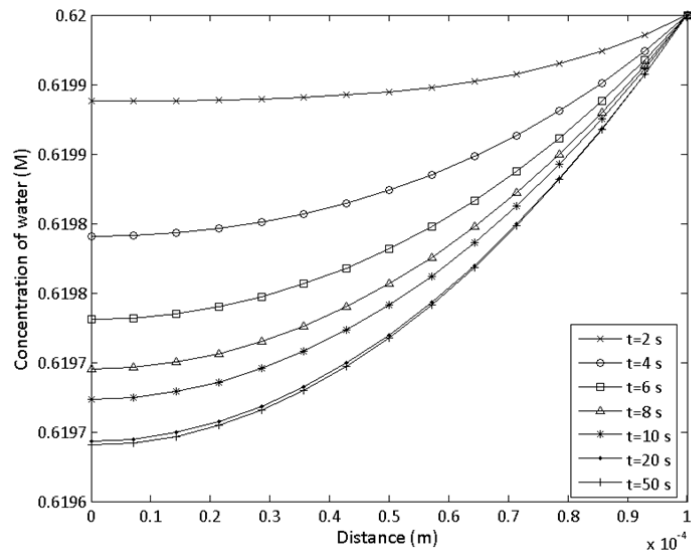


Figure 7.40: Time dependent spatial variation of water concentration ($k = 0.001 \text{ M}^{-1} \text{ s}^{-1}$).

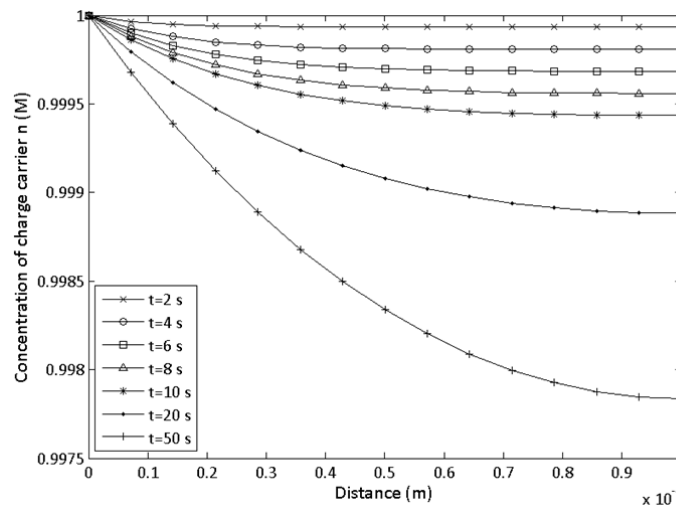


Figure 7.41: Time dependent spatial variation of charge carrier concentration ($k = 0.001 \text{ M}^{-1} \text{ s}^{-1}$).

7.2.5. Oxygen evolving reactor overpotentials and ion diffusion

In this section, a comprehensive analysis is conducted to investigate the thermodynamic and electrochemical performance of an oxygen evolving reactor that is integrated with a catalytic hydrogen production reactor. An electrochemical model is developed to quantify the over-potential requirements of the OER under various conditions. Also, a transient phenomenological model for ion transfer in the OER is presented. This model aims to develop a better understanding of the ion transfer phenomena occurring in a complete system and how it contributes to electrochemical cell performance.

The activation over-potential is a measure of the activity of the electrodes. It represents the over-potential required for the electrochemical reaction. The exchange current density is an important parameter in calculating the activation over-potential. It represents the electrode's ability to proceed with the electrochemical reaction. A high exchange current density means high reactivity of the electrode. As shown in Figure 7.42, the anode activation over-potential increases abruptly over low current densities, but gradually for values close to $J = 200 \text{ mA cm}^{-2}$. The modeling results are presented for two electrode types: nickel and graphite as the most widely used options in practical applications. A nickel electrode contributes almost 40% less activation over-potential than graphite.

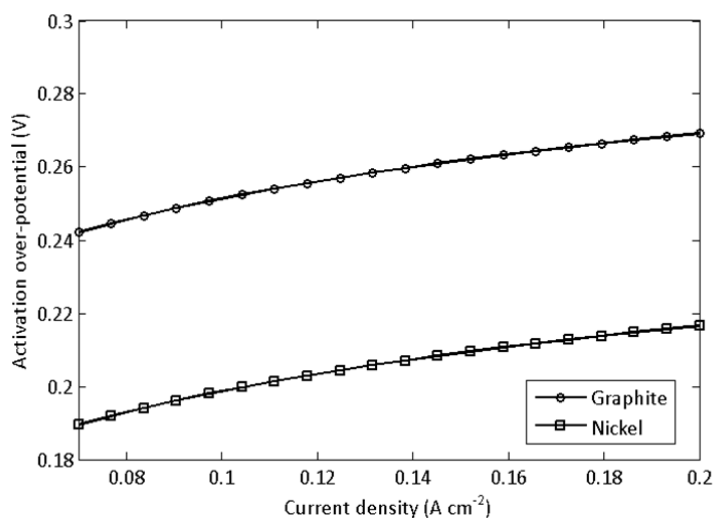


Figure 7.42: Activation over-potential versus current density for graphite and nickel electrodes.

For the results in Figure 7.43, the cell potential is found to decrease with increasing temperature. At a higher operating temperature, the electrochemical reaction is faster, thus the exchange current density is higher, leading to lower activation overpotential. In addition,

the electrolyte ionic conductivity increases with temperature, leading to a lower ohmic overpotential. The combined effects of the temperature increase result in a decrease in cell potential. It also can be concluded that the effect of temperature increase becomes less beneficial at higher temperatures. The results are then related to nickel electrode.

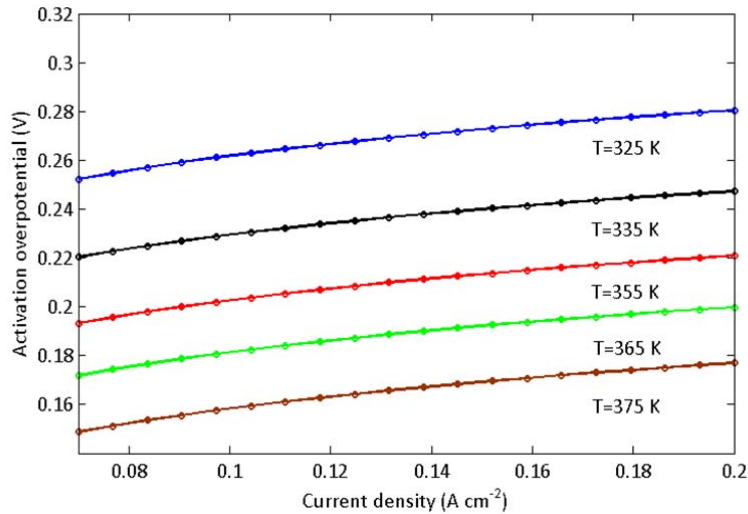


Figure 7.43: Activation over-potential versus current density at different temperatures.

One of the major resistances at high current densities is the ohmic loss in the electrolyte, which includes resistances from the bubbles, membrane and ionic transfer. Figure 7.44 indicates that the ohmic overpotential increases steadily with current density. It is also shown that at higher temperatures, the ohmic overpotential decreases by almost 50% for a 40 K temperature difference.

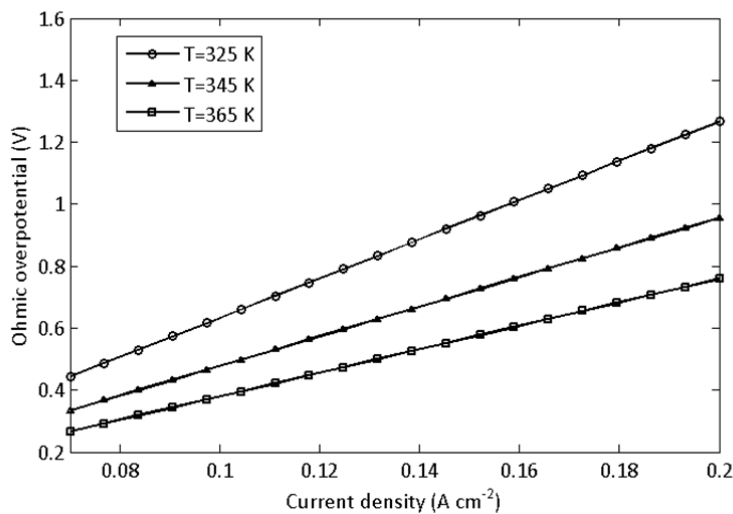


Figure 7.44: Ohmic over-potential versus current density at different temperatures.

Figure 7.45 presents the effect of temperature on concentration over-potential which involves the depletion of charge-carriers at the electrode surface. It can be concluded that temperature has almost a negligible effect on the concentration of charge-carriers, which are depleted by the physical formation of a bubble. It is also observed that the concentration over-potential has the least significance compared with other overpotentials.

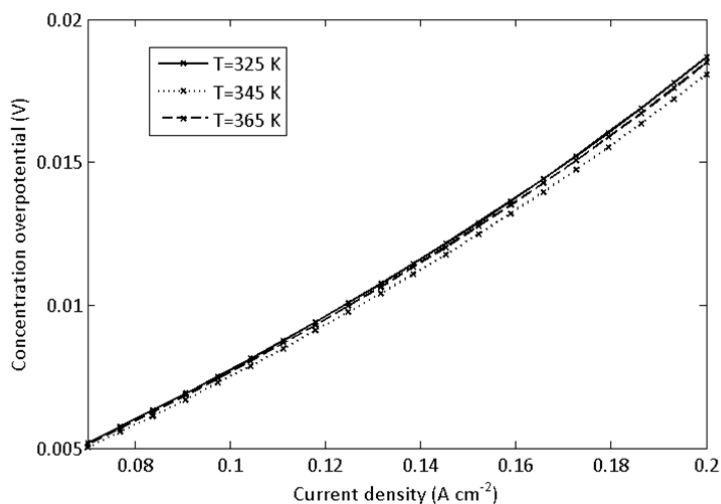


Figure 7.45: Concentration over-potential versus current density at different temperatures.

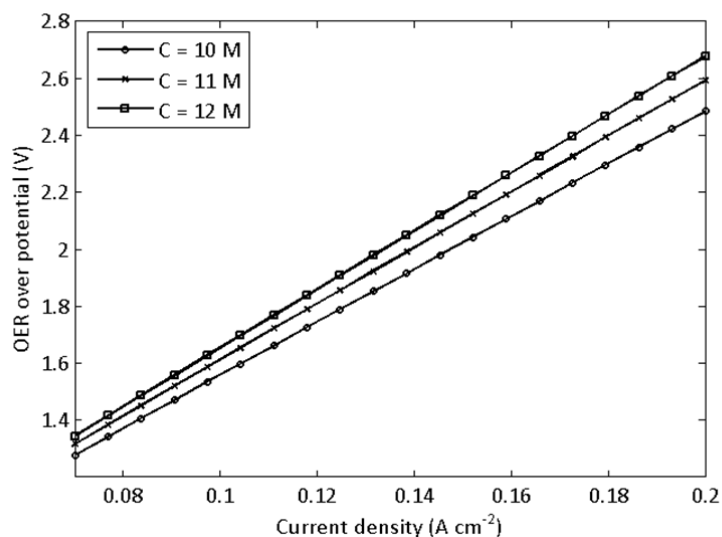


Figure 7.46: OER over-potential versus current density for different electrolyte concentrations.

In a concentrated solution of a highly ionized strong electrolyte, the ions are close enough to one another so that any one of them is influenced by the electrical field across the electrodes and the surrounding ions. The ionic velocities are dependent upon both forces. The

increase of the equivalent conductance of solutions of strong electrolytes in the low-concentration range is not due to an increase in dissociation, because the dissociation is already complete, but rather to an increased mobility of the ions. The effect of electrolyte concentration on OER overpotential is shown in Figure 7.46. It can be concluded that at the environment temperature, the total over-potential of the OER can be decreased by the use of a lower concentration of electrolyte such as potassium hydroxide.

The effect of electrolyte concentration on OER over-potential for different electrolyte thicknesses (distance between electrolyte and membrane) is shown in Figure 7.47 when the current density is relatively high and the space between the membrane and electrode is relatively small. Therefore, the void fraction between the electrodes, which is the fraction of the fluid volume between the electrode and membrane that is occupied by gas bubbles, becomes larger. It results in a higher electric resistance between the electrodes, and then lower efficiency of water electrolysis. Therefore, there is an optimum concentration for the electric potential needed for water electrolysis, which depends on the membrane-electrode distance. The results in Figure 7.47 indicate that the optimum concentration at $j = 0.15 \text{ A cm}^{-2}$ is about 12.7 M, which is more effective at higher distances between the electrode and membrane.

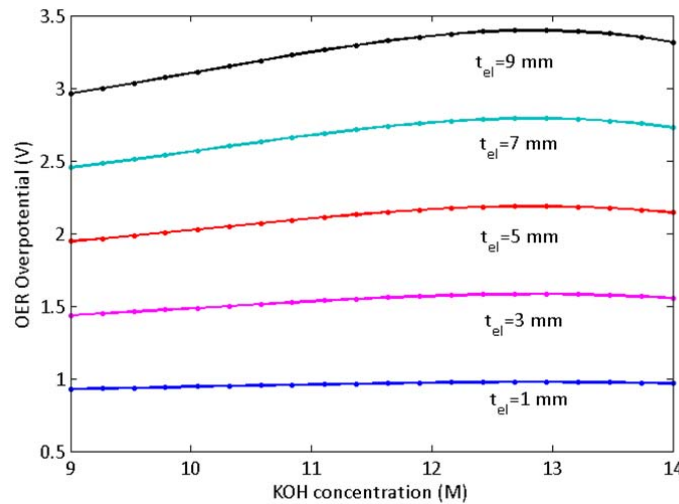


Figure 7.47: OER over-potential versus electrolyte concentrations for different electrode-membrane distances.

Figure 7.48 shows the transient change of the hydroxide ions in the alkali electrolyte of the OER at 3 V and under assumed conditions. The initial concentration of hydroxide ions is assumed to be 1 M. The membrane-electrolyte interface, as the left boundary condition, is

$x = 0$ cm and the electrode-electrolyte interface, as the other boundary, is located at $x = 1$ cm. The hydroxide density profiles in the first millimetres from the membrane are characterized by a steady increase, becoming a nearly flat profile towards $x = 1$ cm.

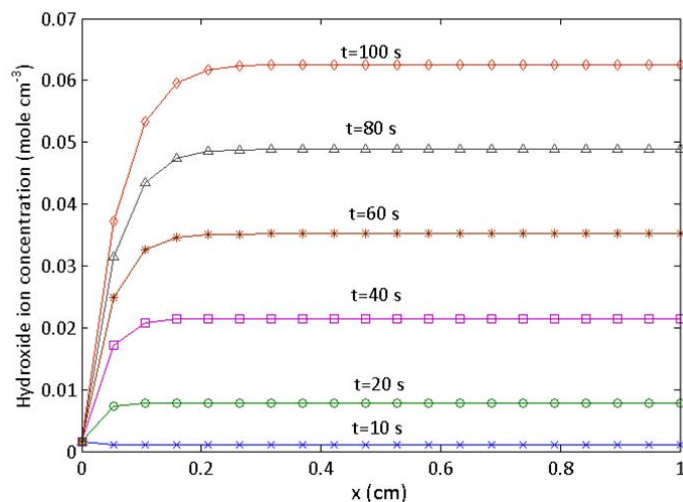


Figure 7.48: Hydroxide ion diffusion between membrane and anode.

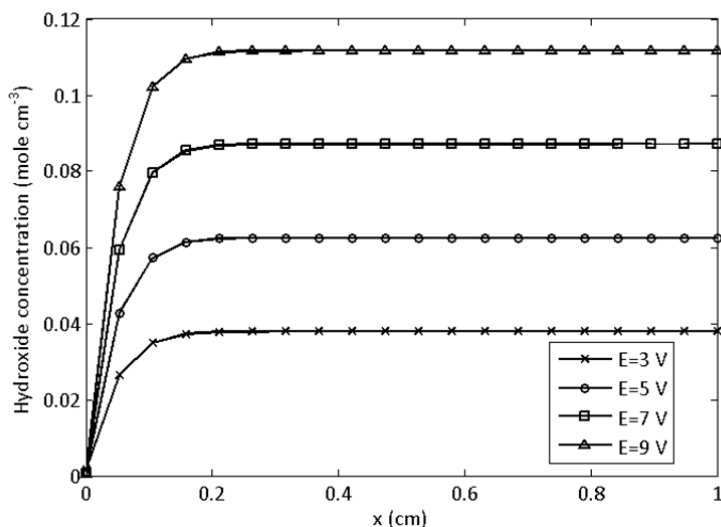


Figure 7.49: Hydroxide ion concentration at $t = 60$ s for different electric potentials.

The hydroxide ion density profiles at $t = 60$ s under various electric potentials are shown in Figure 7.49. The electric potential as a driving force can enhance the rate of ion diffusion from the hydrogen evolving half-cell to the oxygen evolving reactor. The rate of decomposition of hydroxide ions at the anode depends on the rate at which these ions move through the bulk solution and reach the electrode. This type of analysis can help to predict the

maximum possible enhancement of hydroxide ion diffusion inside the bulk solution, which correlates to the oxygen evolution rate. It should be noted that the decomposition rate of hydroxide ions is equal to its production rate, and OH^- accumulation is neglected. The OER half-cell is designed based on the Faradic efficiency to decompose all of the hydroxide ions that are migrated through the membrane and avoid rate limiting effects.

The transient concentration of hydroxide ions at a 5 mm distance from the membrane interface for different current densities is shown in Figure 7.50. As expected, an increase in the current density does not affect the hydroxide ion migration significantly. It can be concluded from the Nernst-Planck equation that at a constant voltage and similar concentration gradients, the current density does not provide a sufficient driving force for ion movement. A minor change that occurs over time is possibly due to higher mobility of ions and more flow rate of electrons through the solution. This indicates that more conductive electrolytes and electrodes can enhance the performance of the oxygen evolution half-cell to prevent hydroxide ion accumulation and rate limiting consequences.

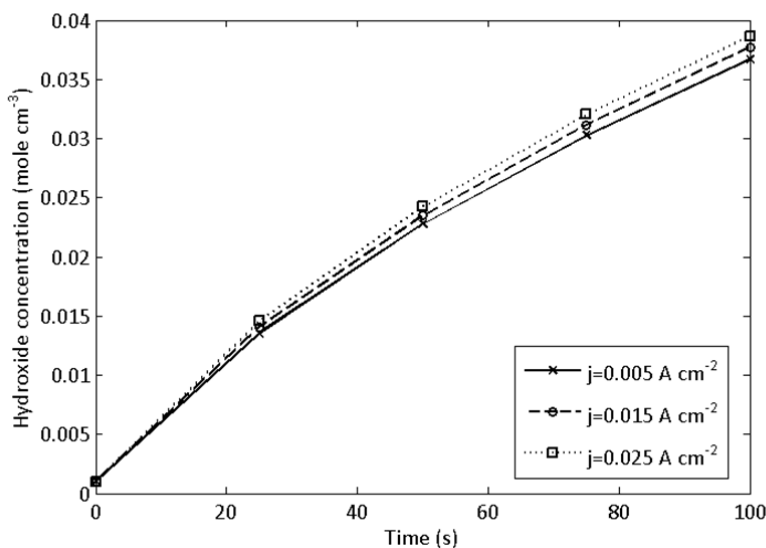


Figure 7.50: Hydroxide ion concentration at $t = 60 \text{ s}$ for different current densities.

Figure 7.51 shows the energy efficiency of a complete system based on photocatalytic hydrogen production versus applied current density of the oxygen evolving reaction (OER). Three different mixed-metal supramolecular complexes are examined. The variation of complexes is based on terminal ligands (bpy, phen or Ph_2phen), and the halide is Bromine. The efficiency calculations are based on the productivity of each catalyst at a $120 \mu\text{M}$ concentration and 7.27×10^{19} photons/minute light intensity. A Higher productivity of

supramolecular complexes with Ph₂phen ligand makes it superior by almost 3 times at low current densities of OER.

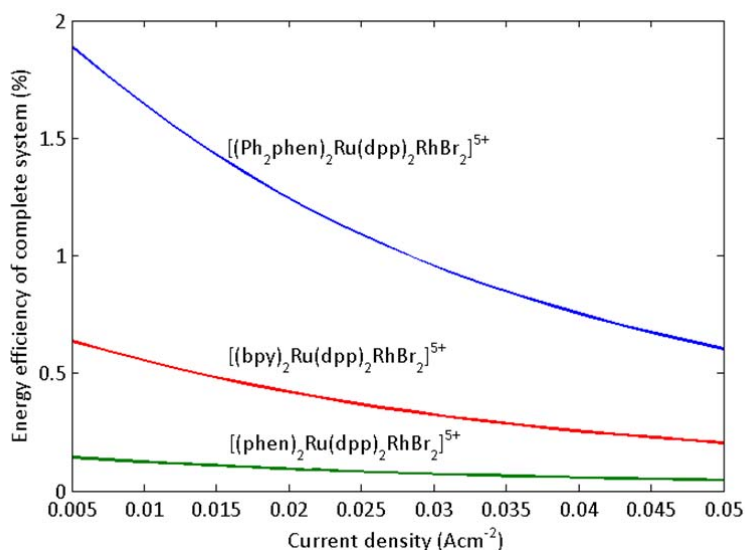


Figure 7.51: Energy efficiency of complete photo-catalytic system.

The energy efficiency of a complete system based on the molybdenum-oxo catalyst is demonstrated in Figure 7.52. It is shown that higher over-potentials for electro-catalysis of water and lower current densities for the oxygen evolving reaction increase the energy efficiency significantly. In order to operate the system at practical current densities, some efficiency losses are expected.

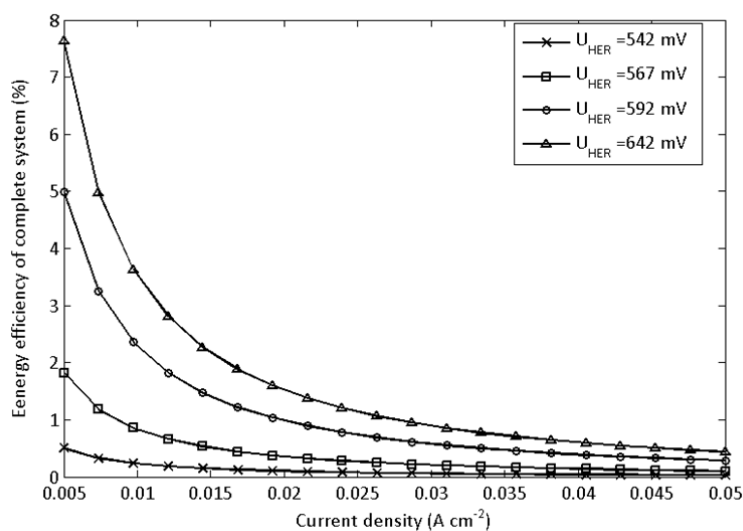


Figure 7.52: Energy efficiency of complete electro-catalytic system.

7.3. Performance of a water splitting reactor

In this section, results are presented based on an extended analysis of a new photochemical water splitting system by Zamfirescu et al. [232] with modifications to improve the system performance. The proposed system is described in Section 4.3.1. These modifications mainly consist of hybridization of a photocatalytic system by an external electric source, implementation of a light driven proton pump, and efficient photo-sensitizers. This research investigates the performance of a photochemical hydrogen generation reactor through energy and exergy methods, and also comparisons with other water splitting methods.

Also, the assessment of electrochemical performance of electro-catalytic water splitting system is based on the molybdenum-oxo catalyst [10], in comparison with other water electro-catalysis technologies, and also the main characteristics of an oxygen evolving reactor, required for neutralizing hydroxide ions as the by-product of the hydrogen evolving reaction.

7.3.1. Hybrid photochemical water splitting reactor

As described in Section 6.3.1, an external power source and two electrodes immersed in the catalyst solution are utilized to supply and transfer electrons inside two reactors. This can dispel the need for replenishment of electron acceptors and donors. The equivalent circuit of the scheme shown in Figure 7.53 should correspond to that of the schematic in Figure 5.1. The presence of ionic molecular devices at the electrode interface, where they exchange electrons (donate or accept) with high activity, dispel the need for coating the electrode surface with expensive catalysts such as platinum group materials. This research uses porous graphite electrodes [233].

The calculated cell potential (1.23 V) is the minimum voltage needed for electrolysis. In practice, however, electrolysis generally starts at a somewhat higher potential to overcome the overpotential and ohmic losses needed to form hydrogen and oxygen [234]. In past experimental data [233], a stream of fine gas bubbles started to form at the anode and the size of these oxygen bubbles gradually increased with potential until ~1.8 V. The first activity at the cathode was a stream of fine bubbles (formed at ~2.3 V). Although the decomposition potential for oxygen and hydrogen are slightly different, the practical decomposition potential is nearly the same (~2.3 V), regardless of the immersed area of the electrodes.

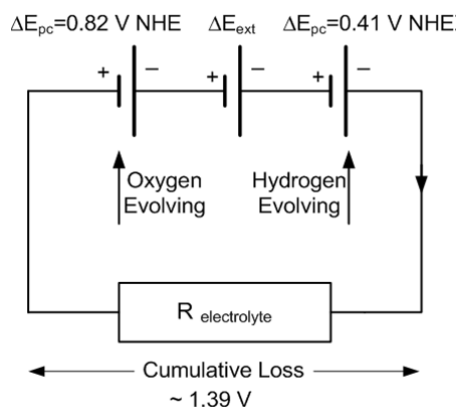


Figure 7.53: Equivalent schematic diagram of the electric circuit for water splitting reactors.

Another approach to extend the conceptual design in Ref. [235] is the use of light driven proton pumps instead of conventional proton exchange membranes. This study uses a slightly modified version of the system, as shown in Figure 7.54. The proposed proton pump comprises a reaction center, which is a molecular triad containing an electron donor and an electron acceptor, both linked to a photosensitive porphyrin group. The triad molecule is inside the bilayer of a liposome. The molecular triad absorbs a photon and trans-locates a negative charge near the outer surface and a positive charge near the inner surface of the liposome by generating charge separated species. Following these interactions, protons will be transported across the membrane from the lower proton potential to the higher proton potential side of the membrane, e.g. oxygen and hydrogen production reactors, respectively.

The transport of protons in this system is mainly due to combined effects of photo-induced energy transduction within the molecular structure of the membrane and electro-osmotic forces applied at the two porous electrodes. The anode acts as a proton source and the cathode as a proton sink. The conversion of light energy into the electrochemical gradient of protons across the membrane can be quantitatively characterized by the quantum yield (or quantum efficiency) Φ of proton translocation. This parameter is defined as follows:

$$\Phi = \frac{\text{number of protons pumped}}{\text{number of photons absorbed}} \quad (7.16)$$

Based on a case study in Ref. [235], in 1 ms, the shuttle makes nearly 16 trips and transfers ten protons through the membrane, provided that the light intensity is $I = 0.133 \text{ mWcm}^{-2}$. Considering the number of photons absorbed in 1ms is ~ 18 , the approximate quantum yield of the pumping process is $\sim 55\%$. The effect of this module on system performance is discussed as following.

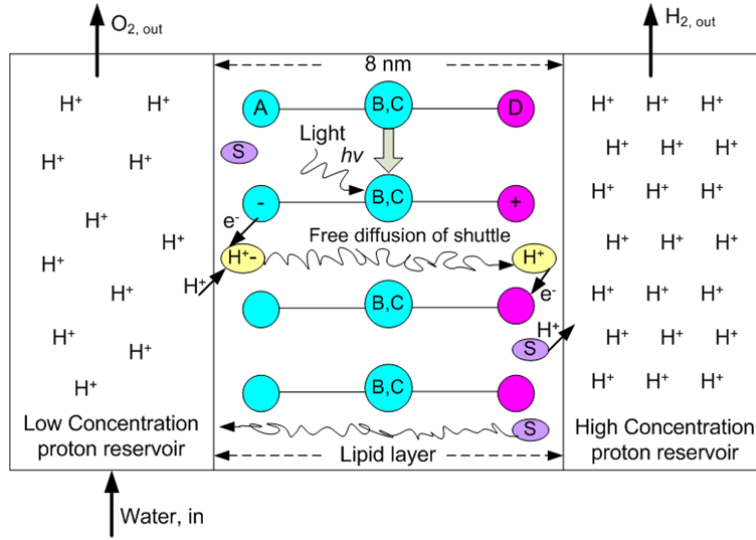


Figure 7.54: Schematic diagram of the light-induced proton pump across the lipid bilayer in a liposomic membrane. A molecular triad $A-BC-D$ is symmetrically inserted in the lipid bilayer. A refers to acceptor, D for donor, and S for shuttle.

As shown in Figure 4.11, only part of the energy captured by light will be used by an excited singlet molecule $[Ru(bpy)_3]^{2+*}$ to form hydrogen or oxygen. This translates to two important efficiencies regarding photochemical and electrochemical performances of both water oxidation and reduction reactors. Define the photochemical efficiency (η_{PC}) of quenching pathways as the energy efficiency of this process, which is part of the transmitted irradiation contributed to the water oxidation/reduction reaction divided by the photonic energy. Referring to Figure 4.11, the efficiencies of the catalytic cycle for water oxidation and reduction at 450 nm are calculated as follows:

$$\eta_{PC} = \frac{1.53\text{eV}}{2.75\text{eV}} = 55.5\% \quad (7.17)$$

$$\eta_{EC} = \frac{1.08\text{eV}}{2.75\text{eV}} = 39.3\% \quad (7.18)$$

The electrochemical efficiency (η_{EC}) of water reduction has a similar definition, as the input energy is supplied by external electric power. There are several uncertainties related to over-potential values, or in other words, an effective contribution of the external electric potential in the decomposition potential. Therefore, this study conducted the energy and exergy analysis for different electrochemical efficiencies.

The maximum energy conversion efficiency of the hybrid photochemical water splitting system is defined as follows:

$$\eta_{\max, H_2} = \frac{HHV_{H_2} \times \dot{n}_{H_2}}{\dot{W}_S + \dot{W}_{EL}} \quad (7.19)$$

where \dot{n}_{H_2} is the maximum possible molar flow rate of produced H_2 ,

$$\dot{n}_{H_2} = \left(\frac{\dot{W}_S \eta_{pc} + \dot{W}_{EL} \eta_{EC}}{\Delta E_{H_2}} \right) \quad (7.20)$$

and $\Delta E_{H_2} = 1060 \text{ kJ / mol}$, equivalent to the minimum required energy captured from light (\dot{W}_S at $\sim 450 \text{ nm}$ or 2.75 eV) or the external electric power (\dot{W}_{EL}) to form the excited singlet molecule $[Ru(bpy)_3]^{2+**}$.

Figure 7.55 shows the effect of the delivered potential at the electrode interface to the electrolyte on the maximum energy conversion efficiency. The photochemical efficiency is assumed to be $\eta_{pc} = 0.55$ and this study considered different electrochemical efficiencies. The photolysis is conducted with 5W LED having an excitation wavelength of 470 nm. It is observed that a hybrid configuration of a water splitting system may improve the efficiency if the electrochemical efficiency is higher than the photochemical efficiency. The reason is a very low quantum efficiency of LEDs, which was taken as 1.3% in this analysis. In other words, the auxiliary power supply will be helpful if it delivers excitation energy more efficiently than the photonic source. A maximum 30% solar conversion efficiency improvement is estimated by applying 5 volts of electric potential.

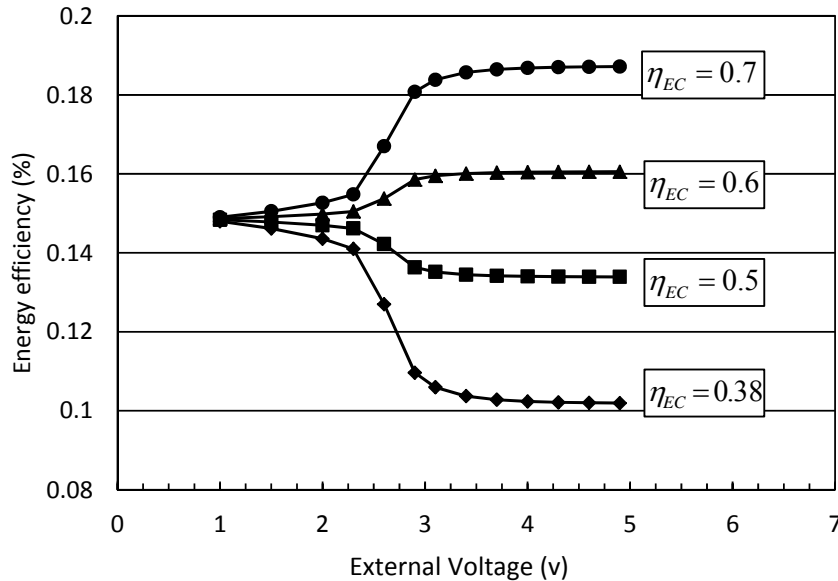


Figure 7.55: Effect of external electric potential on maximum energy conversion efficiency.

Evaluating the energy and exergy efficiencies of the hydrogen production reactor requires the hydrogen production rate from a correlation ($\dot{n}_{H_2} = 2.725 \frac{\mu\text{mol}}{\text{h}}, 0 < t < 5 \text{ h}$) based on a recent study by Brewer et al. [9] on a new photo-catalyst

$[(bpy)_2Ru(dpp)]_2RhBr_2(PF_6)_5$. Our investigation involved the determination of the energy and exergy efficiency by varying the DC current density at a low voltage (0-6 V) using graphite electrodes and an electrolyte concentration of 65 μ M of the aforementioned molecular complexes in 0.62 M water. The definition of energy efficiency is similar to the maximum energy conversion efficiency, Equation (7.19), but the molar production rate of hydrogen is substituted by the value according to the aforementioned correlation.

Figure 7.56 shows the effect of external voltage on the energy efficiency. Compared to the electrolytic load, the resistive load of the cell is relatively high, yielding a very small current density which slowly changes linearly with increasing potentials (< 2 V). Its effect on input electric power is shown in Figure 7.57. At voltages higher than 2.3 V, the current density increases very rapidly due to the redox reactions. Thus, above the decomposition potential, the current density consists of the ohmic current density plus the current density produced by the redox reaction.

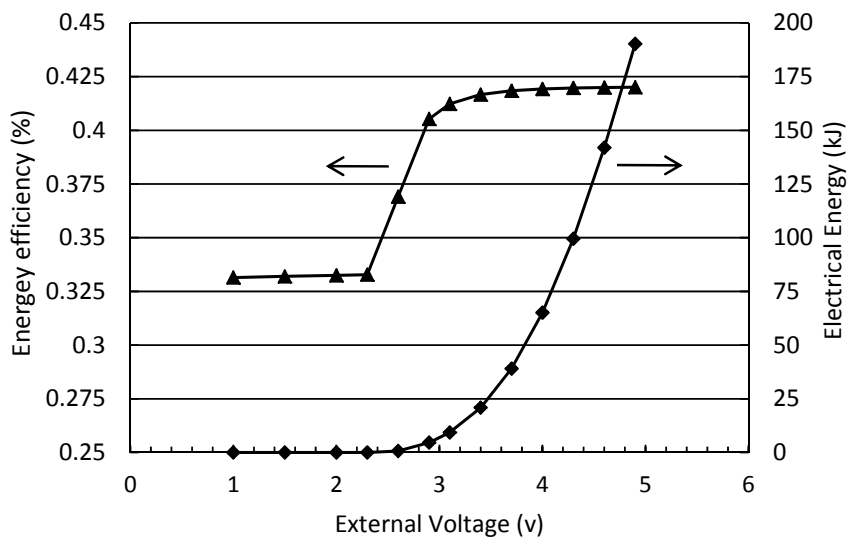


Figure 7.56: Energy efficiency and supplied electric energy versus external voltage.

Up to a certain energy efficiency it does not differ, but as the applied potential rises above 2.3 volts, the efficiency increases rapidly and then decreases following higher concentration and ohmic losses. Almost a 27% improvement in energy efficiency is achieved over 6 volts of external electric potential. The energy efficiency of photochemical water splitting reactors without any external power is about 0.33%.

The absorbed photonic radiation plus electric energy drives an endothermic chemical reaction. The measure of how these sources of energy are converted to chemical energy stored in H₂ for a given process is the exergy efficiency defined as:

$$\eta_{\text{exergy}} = \frac{\dot{n}_{\text{H}_2} \times \Delta G_{\text{H}_2 + 0.5\text{O}_2 \rightarrow \text{H}_2\text{O}}}{\dot{W}_S + \dot{W}_{\text{EL}}} \quad (7.21)$$

where \dot{n}_{H_2} is the actual molar flow rate of produced H₂, based on a correlation extracted from experimental data [9], and ΔG is the standard Gibbs free energy change of the reaction at 298 K (237 kJ mol⁻¹), i.e., maximum possible amount of work that may be extracted from H₂ at 298 K, when both H₂ and O₂ are available at 1 bar.

Figure 7.57 shows the calculated exergy efficiencies over a range of applied electric potential, and it shows similar trends to energy efficiency. About 30% enhancement in exergy efficiency is calculated. If the auxiliary power supply is unplugged, this efficiency will be about 0.55%.

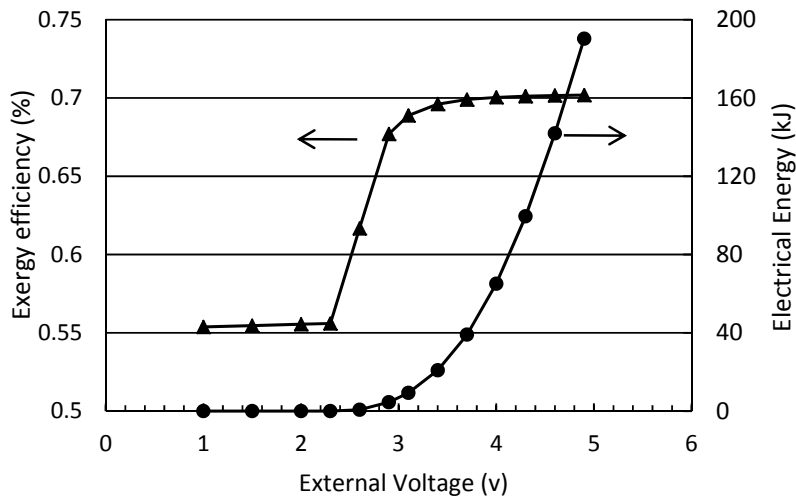


Figure 7.57: Exergy efficiency and supplied electric energy versus external voltage.

The solution pH should be a major factor that can be tuned to favour hydrogen reduction or water oxidation. Applying the Nernst equation for the two manifolds yields

Reductive quenching pathway:

$$\Delta G_{\text{OER}} = 84 - 22.85 \times (\text{pH}) \quad (\text{kJ mol}^{-1}) \quad (7.22)$$

$$\Delta G_{\text{HER}} = -420 + 22.85 \times (\text{pH}) \quad (\text{kJ mol}^{-1}) \quad (7.23)$$

Oxidative quenching pathway:

$$\Delta G_{\text{OER}} = -116 - 22.85 \times (\text{pH}) \quad (\text{kJ mol}^{-1}) \quad (7.24)$$

$$\Delta G_{\text{HER}} = -220 + 22.85 \times (\text{pH}) \quad (\text{kJ mol}^{-1}) \quad (7.25)$$

From these expressions, an acidic solution oxidative quenching pathway is more exothermic during the hydrogen evolution process than a reductive pathway, which implies a higher photochemical efficiency according to Equation (7.17). Similarly, the oxygen evolution energy in the oxidative pathway is higher in a basic solution. Hence, the oxidative quenching pathway is selected in the design in order to take advantage of the light driven proton pump. Also, the pH range in which water splitting can occur should be determined, assuming the two half-reactions are not energetically coupled. The free energy of the Hydrogen Evolution Reaction (HER) is not used to help drive the Oxygen Evolution Reaction (OER) or vice versa. These energies and pH ranges are specific for $[\text{Ru}(\text{bpy})_3]^{2+}$, assuming a 4 photon process. They are tuneable by modifying the complex structure.

Figures 7.58 and 7.59 represent the maximum energy conversion and exergy efficiencies of oxygen and hydrogen production reactors versus electrical potential at the electrode interface, considering the effect of the solution pH difference between reactors. The case $\Delta\text{pH} = 0$ implies that a photolysis solution with $\text{pH}=7$ and increasing the pH difference makes hydrogen and oxygen quenches acidic and basic, respectively. It was found that the hydrogen production volume in the acidic medium exceeds the basic medium. At an acidic pH, more H^+ ions would be absorbed by the $[\text{Ru}(\text{bpy})_3]^{2+*}$, and hence the possibility for reduction of H^+ to H_2 increases.

Increasing the proton concentration in the catalyst solution of the hydrogen evolution manifold could lead to about 10% improvement in maximum energy conversion efficiency, and 13% in exergy efficiency. All graphs meet at a point corresponding to 2.65 volts where efficiencies have an opposite trend before and afterwards. In other words, increasing the external voltage up to about 2.65 volts does not make any difference, and a higher pH difference leads to an efficiency reduction with an opposite trend after the coincidence point.

Due to high ohmic losses at low voltages that makes a poor current density, the input electrical power decreases and it coincides with the photochemical deficiency due to a low proton concentration in the oxygen evolution manifold. This subsequently makes the light energy absorption deficient. This provides completely the opposite trend for voltages over 2.65 V and the current density at the electrode interface increases exponentially. Also, the electrochemical efficiency of hydrogen production quench rises with higher proton concentration, for a more acidic catalytic solution.

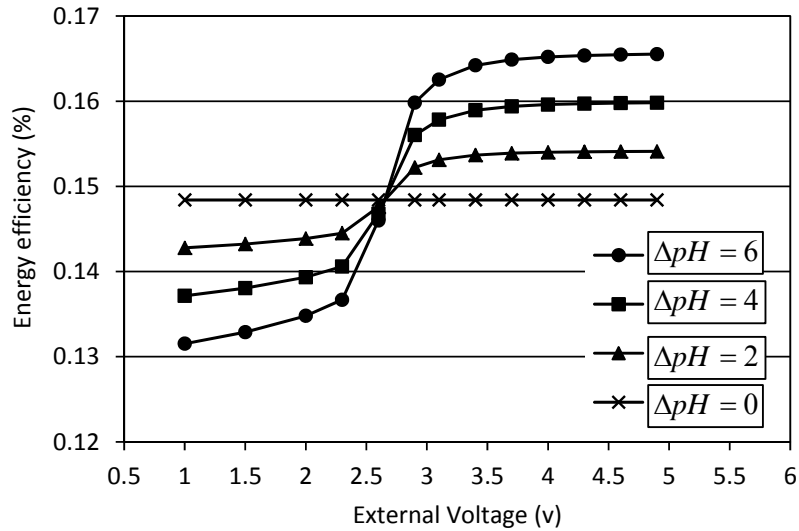


Figure 7.58: Effect of external power supply on maximum energy efficiency.

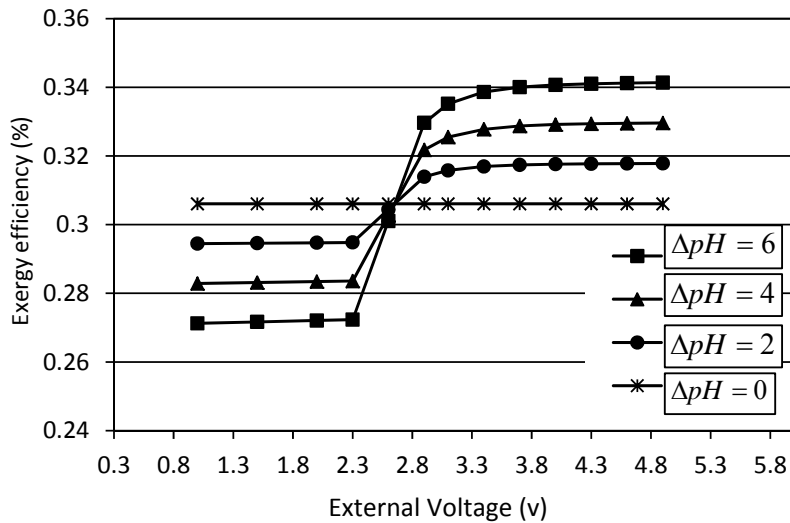


Figure 7.59: Effect of external power supply on exergy efficiency.

This research compared the proposed hybrid photochemical method with three other water splitting techniques in Figure 7.60. This is helpful for better understanding of the current status of the state-of-the-art hydrogen production scenarios from energy and exergy aspects of view. Consider photochemical (PC), photoelectrochemical (PEC), and conventional electrocatalysis (EC) methods for comparison, based on experimental data published in references [3, 234, 121], respectively. The input energy for all four cases is assumed to be equal and working conditions are consistent. Although it couldn't reach the efficiency of a photoelectrochemical system, hybridization of photochemical processes is promising. The hybridization made an improvement in the photochemical performance, and it

shows almost a 30% increase in efficiencies. Compared to conventional electrolysis, solar based methods are relatively deficient, and they need more efforts for commercialization purposes. Low quantum efficiency of current photo-catalysts is a crucial challenge to be addressed in order to decrease exergy destructions and losses.

The effects of $[\text{Ru}(\text{bpy})_3]^{2+}$, Eosin Y, and Cu-phthalocyanine, as different photosensitizer types for hydrogen production photoreactions, on energy and exergy efficiencies, are shown in Figure 7.61. Their effectiveness occurs in the following order: Cu-phthalocyanine > $[\text{Ru}(\text{bpy})_3]^{2+}$ > Eosin Y. The difference in the hydrogen production rate is based on the structures and properties of these dyes and the differences in their electron injection characteristics.

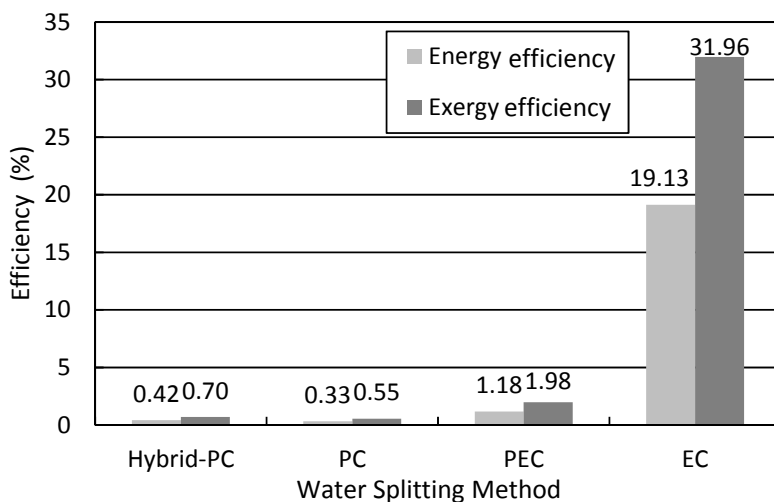


Figure 7.60: Comparison between energy and exergy efficiencies for different water splitting methods

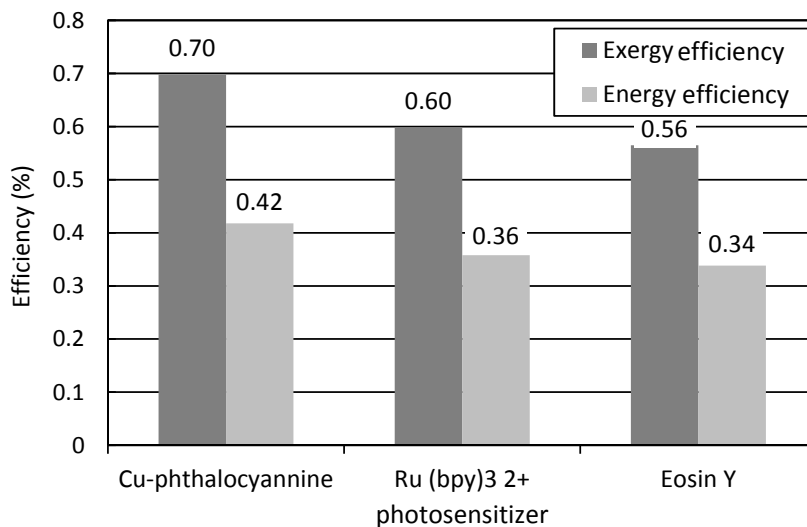


Figure 7.61: Comparison between energy and exergy efficiencies for different photo-sensitizers.

The energy conversion efficiency calculated for the proposed system is compared and qualitatively validated with some experimental data on photo- or solar-electrolysis efficiencies, as contained in Table 7.10. Although some of the numbers claimed have been questioned by others, independent verification is warranted, and the losses associated with process scale-up are still unknown. The energy efficiencies calculated in this study have almost the same order of magnitude with respect to similar systems, whereas photoelectrochemical water splitting systems [236-237] with higher efficiencies are not utilizing the same phenomenological approach as a photo-catalytic method of this study.

Table 7.10: Comparison between experimentally and theoretically obtained efficiencies for the photo-catalysis of water.

Entry Number	Efficiency (%)	Remarks	Reference
1	0.6-2.2	A tandem monolithic configuration used with WO ₃ films biased by a PV junction.	[236]
2	1-2.8	Bipolar CdSe/CdS panels used under 52 mW/cm ² effective solar flux. Upper limit after correction for light absorption by the electrolyte.	[237-238]
3	1.84	Measured for a cell with n-Fe ₂ O ₃ photoanode under 50.0 mW/cm ² Xe arc lamp irradiation and at a bias potential of 0.2 V/SCE at pH 14.	[239]
4	0.05	Measured for a polycrystalline p/n diode assembly based on Fe ₂ O ₃ . Poor efficiency attributed to the non-optimal charge transfer properties of the oxide.	[240]
5	0.33-0.43	Calculated for a hybrid system based on supramolecular complexes [(bpy) ₂ Ru(dpp)] ₂ 2RhBr ₂ (PF ₆) ₅ as the photo-catalysts, and an external electric power supply to enhance the photochemical reaction.	Present study

7.3.2. Conversion efficiency of light energy based on energy balance

The conversion efficiency of light energy is defined as the conversion efficiency of light energy when the hydrogen energy output is equal to an equivalent energy input of the system, which is marked as “ η_c ”. Figure 7.62 shows the energy flow of the hydrogen production system, proposed in this study for hybrid photo-catalytic water decomposition. Assume the energy input comprises only the solar energy, and operation energy. The former can be considered as free energy. The latter is consumed to drive the supply pump, extraction fans and stirrer, which is usually electricity. The energy output of the system is the chemical energy of hydrogen output flow.

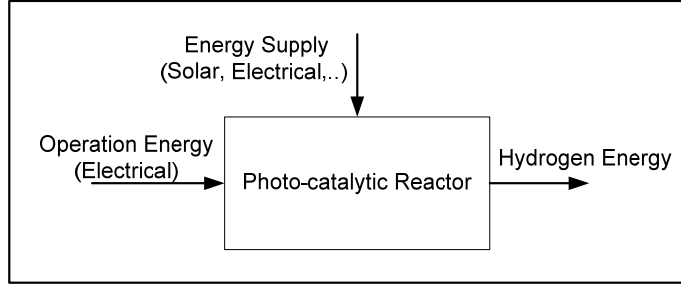


Figure 7.62: Energy flow of the photo-catalytic system.

The minimum conversion efficiency of light energy of a certain system would be the case when the hydrogen energy output of the system will be equal to the equivalent input energy, so as to compensate the expenditure of the system. Therefore, only if the conversion efficiency of light energy is greater than this minimum value, an energy benefit can be achieved. The concept of conversion efficiency of light energy, by the aforementioned definition, sets a target of commercial-scale production for the current experiments of the hydrogen production from photo-catalytic water decomposition. It can be concluded that if the energy efficiency of light energy for an experimental system is greater than this value, the system could be considered for a commercial-scale production.

Neglecting the factors such as dissolvability, viscosity, and pressure loss in pipelines, the energy balance of the system is

$$\dot{W}_S + \dot{W}_{Pump} + \dot{W}_{Fan} + \dot{W}_{Stirrer} = HHV_{H_2} \times \dot{n}_{H_2} + \dot{W}_L \quad (7.26)$$

where \dot{W}_L denotes energy loss. In order to find the minimum value for the conversion efficiency of light energy, the equation of the energy balance of the system could be written as

$$\dot{W}_{Pump} + \dot{W}_{Fan} + \dot{W}_{Stirrer} = HHV_{H_2} \times \dot{n}_{H_2} \quad (7.27)$$

Assuming a range of 100 to 500 ton of annual hydrogen production capacity, and 3,000 hr annual duration of sunshine in Canada, the conversion efficiency of light based on an energy balance is calculated as follows.

Considering the conversion efficiency of light energy “ η_c ”, the minimum imposed area of the reactor needed for solar energy harvesting is

$$S_R = \left(\frac{HHV_{H_2} \times \dot{n}_{H_2}}{\dot{W}_S \times \eta_c} \right) = 351.19 \times \eta_c^{-1} \quad (7.28)$$

Selecting the tri-lamina propeller standard formant stirrer, and assuming the diameter of the impeller is one third of the reactor diameter, then

$$D = \frac{d}{3} = 21.15 \times \eta_c^{-0.5} (\text{m}) \quad (7.29)$$

where D is the diameter of the impeller and d is the reactor diameter. The rotational speed is set to $n = 10$ rpm.

Assuming that the density and viscosity of the solution are equal to those of water, so $\rho_{\text{H}_2\text{O}} = 997.9 \text{ kg m}^{-3}$, $\mu_{\text{H}_2\text{O}} = 0.8973 \text{ cp}$, at 298 K. Therefore, the Reynolds number of the flow based on the stirrer diameter is

$$\text{Re} = \frac{D^2 \times n \times \rho_{\text{H}_2\text{O}}}{\mu_{\text{H}_2\text{O}}} = \frac{(21.15 \times \eta_c^{-0.5})^2 \times 10 \times 997.9}{60 \times 0.8973 \times 10^{-3}} = (8.3 \times 10^7) \times \eta_c^{-1} \quad (7.30)$$

Knowing that $0 < \eta_c < 1$, the Reynolds number is greater than 100,000, and hence, the solution in the reactor has turbulence; therefore, the power factor of the stirrer, ϕ , can be set as 7.1.

The power consumption of the stirrer would be

$$\dot{W}_{\text{stirrer}} = \frac{7.1 \rho_{\text{H}_2\text{O}} n^3 D^5}{0.8} = (7.14 \times 10^5) \times \eta_c^{-2.5} (\text{kW}) \quad (7.31)$$

The annual energy consumption of the stirrer is

$$W_{\text{stirrer}} = (7.14 \times 10^5) \times \eta_c^{-2.5} \times 3000 \times 360 = (7.63 \times 10^{12}) \times \eta_c^{-2.5} (\text{kJ}) \quad (7.32)$$

Assuming the theoretical water decomposition rate, the maximum energy consumption of the pump and extraction fans are calculated. Substituting the energy consumption values for each utility into Equation (5.27), the conversion efficiency calculation for 100 tons of annual hydrogen production is given as follows:

$$12893.5 + 6130 \times 10^5 \times \eta_c^{-2.5} = 142915 \times 10^5 \quad (7.33)$$

therefore, $\eta_c = 1.79\%$.

Figure 7.63 shows the conversion efficiency of light energy for the range of 100 to 500 tons of annual hydrogen production capacity. A correlation for conversion efficiency of such a system could be developed by curve fitting of these data with a power function, as follows:

$$\eta_c = 0.113 \text{ AT}^{0.6} \quad (7.34)$$

where AT is the annual hydrogen production capacity of the photo-catalytic system.

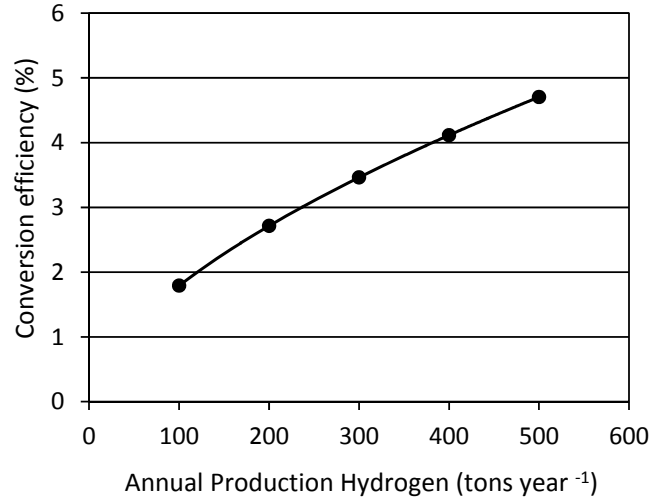


Figure 7.63: Energy efficiency of light based energy balance.

According to the definition, it can be concluded that by doubling the production capacity, the minimum desired conversion efficiency of the system should be improved by almost 50% to be commercially justifiable. Satisfaction of this requirement is quite difficult in practice, and utilizing parallel units with the same capacities is recommended instead of a large scaled system. Another approach to address this issue would be exergy efficiency evaluation of this system.

The following definition is applied to find the exergy efficiency of such systems:

$$\eta_{\text{ex}} = \frac{\dot{E}_{x\text{out}}}{\dot{E}_{x\text{in}}} = 1 - \dot{I}_{\text{total}}/\dot{E}_{x\text{in}} \quad (7.35)$$

where \dot{I}_{total} and \dot{E}_{in} are the irreversibility, and input exergy rate of the hydrogen production system, respectively.

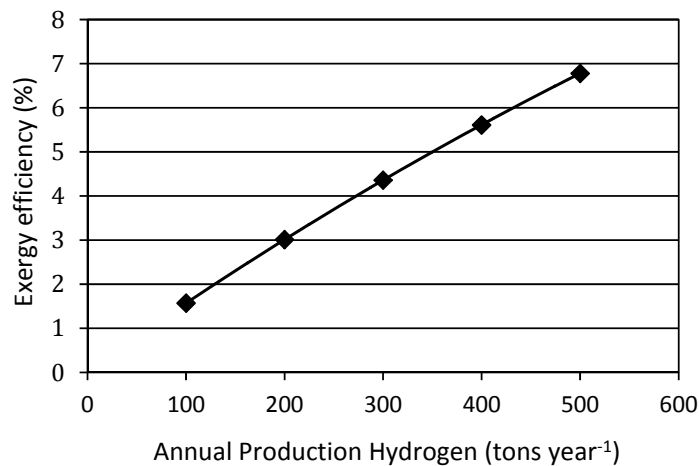


Figure 7.64: The exergy efficiency of photo-catalytic system.

Figure 7.64 shows the exergy efficiency of this system for 100 to 500 tons of hydrogen production capacities. These results imply that the exergy efficiency at higher capacities improves significantly. This matter together with the previous result implies a trade-off between scaled up and parallelized production units. A detailed optimization is required to distinguish the most beneficial option. Due to the production rate limiting nature of photo-catalytic systems, the results of Figure 7.63 or 7.64 cannot be extended to very high capacity ranges.

7.3.3. Hydrogen production via molecular molybdenum-oxo catalyst

The catalyst developed by Karunadasa et al. [10] simulates the process of an alkaline cell, where the water is introduced at the cathode and it is decomposed into hydrogen and hydroxide ion. The main difference is that instead of hydrogen evolution on the electrode surface, the heterogeneous solution of molybdenum-oxo complexes dissociates the water molecules to hydrogen and hydroxide ions. The OH^- ions migrate through the electrolytic material to the anode where oxygen is formed. The hydrogen remains in the catalyst solution. The hydrogen is then separated from the water in a gas-liquid separation unit outside of the electrolyser.

The results presented in Sections 7.3.3.1 to 7.3.3.6 are related to design and analysis of a dual-cell reactor based on a molybdenum-oxo metal complex. The experimental results presented in reference [10] are adopted for theoretical analysis and the oxygen evolving reactor is designed to match the production rate of this catalyst.

7.3.3.1. Post-processing of controlled potential electrolysis (CPE) experiments

The CPE experiments are performed in a double-compartment cell to assess the efficiency of the catalyst. It has been shown that every electron is used for the reduction of protons. The turnover frequency for the catalyst is calculated. The maximum turnover frequency is 1,600 moles of H_2 per mole of catalyst per hour [10].

One method for evaluating this technology is by use of the Tafel diagram (polarization curve) from the experimental data. The Tafel equation is a useful model of electrode kinetics. Although the UCal technology [10] does not involve any catalytic activation on the electrodes, the catalyst itself can be assessed by electrochemical benchmarks such as the Tafel diagram or thermodynamic efficiency.

Figure 7.65 shows the Tafel diagram of the catalyst $[(PY5Me_2)MoO](PF_6)_2$ based on CPE experiments performed and reported in Ref. [10]. The over-potential value increases with increasing current density and follows a logarithmic trend that is confirmed by the Tafel equation. One of the challenges regarding this catalyst is the high value of over-potential at fairly low current densities. The following correlation is extracted for over-potential of molybdenum-oxo catalyst for water splitting:

$$U = -333.2 \ln j + 1056.9, R^2 = 0.97 \quad (7.36)$$

Figure 7.66 presents the energy efficiency for a hydrogen production half-cell with the molybdenum-oxo catalyst. The efficiency values are in accordance with data points of Figure 7.65. As observed in Figure 7.65, small increments of over-potential rapidly increase the charge build-up, which means the cumulative effect of ohmic and concentration losses will be lowered at higher current densities. Therefore, higher energy efficiency at higher current densities is obtained.

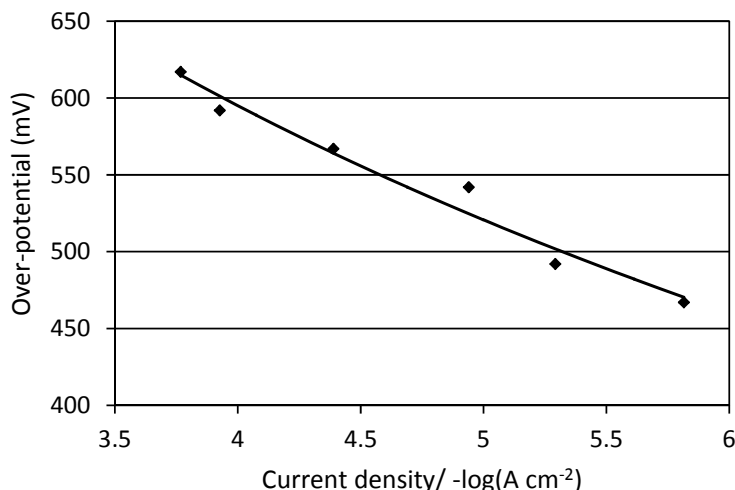


Figure 7.65: Over-potential versus current density for water electro-catalysis with $7.7\mu M$ solution of $[(PY5Me_2)MoO](PF_6)_2$.

By comparison, the electrochemical performance of the molybdenum-oxo catalyst is evaluated in Table 7.11. Among the most efficient cathode electrodes for a hydrogen evolving reaction (HER) cell, Pt and Rh have the lowest over-potential (U) values. Ni and Ni alloys are very promising from both economic and effectiveness aspects. The over-potential required by the molybdenum-oxo catalyst, as shown in the last row of Table 7.11, is much higher than other accepted cathode electrodes. This over-potential occurs at a low current density. It should be noted that the working temperature of electrodes, in Table 7.11, is higher

than experiments reported in Ref. [10] and decreases the over-potential to some extent, while the catalyst over-potential is still not competitive. The following correlation is extracted for energy efficiency of molybdenum-oxo catalyst for water splitting:

$$\eta_{en} = -11.67 \ln j + 91.93, R^2 = 0.97 \quad (7.37)$$

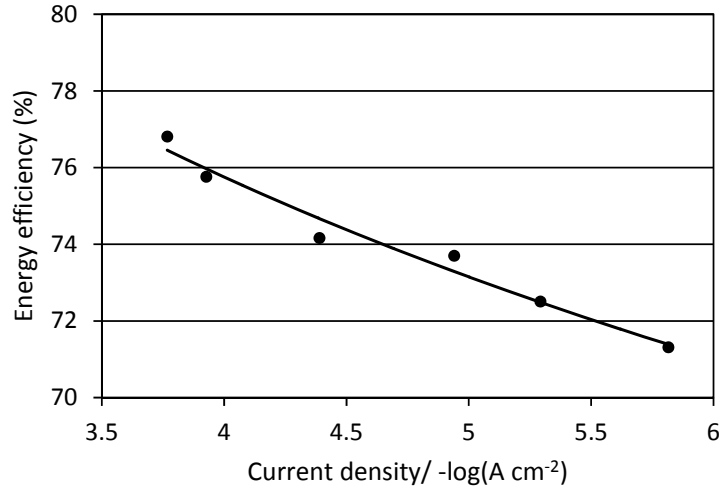


Figure 7.66: System energy efficiency based on molybdenum-oxo function in HER.

Table 7.11: Comparison of HER over-potentials of different metal electrodes and catalysts.

Composition formula	T (°C)	Electrolyte	C (mol dm ⁻³)	J(A m ⁻²)	U (mv)
Pt	80	KOH	30 wt%	1000	46
Rh	N/A	NAOH	1	1000	42
Ni	90	KOH	50 wt%	1000	95
Co	80	KOH	30 wt%	1000	126
Fe	80	KOH	30 wt%	1000	191
Ni-Fe-Mo-Zn	80	KOH	6	1000	83
Ni-S-Co	80	NAOH	28 wt%	1350	70
Ti ₂ Ni	70	KOH	30 wt%	1500	16
Ni75%Mo25%	80	KOH	6	3000	185
[(PY ₅ Me ₂)MoO](PF ₆) ₂	25	phosphate buffer	1.8	91	~ 550

7.3.3.2. Electrical circuit analogy

A number of barriers must be overcome during the water electro-catalysis reaction process, which requires a sufficient electrical energy supply. These barriers include electrical resistance of the circuit, activation energies of the electrochemical reactions occurring on the surfaces of the electrodes, availability of electrode surfaces due to partial coverage by gas

bubbles, and the resistances to ionic transfer within the electrolyte solution. It is important to examine whether or not the technology based on the molybdenum-oxo catalyst can decrease or eliminate these resistances.

Figure 7.67 presents the resistances of the water electro-catalysis system, using the molybdenum-oxo catalyst for hydrogen production. The first resistance from the left-hand side, R_1 , is the external electrical circuit resistance, including the wiring and connections at the anode. R_{anode} originates from the over-potential of the oxygen evolution reaction on the surface of the anode. $R_{\text{bubble,O}_2}$ is the resistance due to partial coverage of the anode by the oxygen bubbles, hindering contact between the anode and the electrolyte. Similarly, R_{cathode} and R_1' have reference to the cathode side. The resistances from the electrolyte and membrane are noted as R_{ions} and R_{membrane} , respectively. Thus, the total resistance can be expressed as follows:

$$R_{\text{Total}} = R_1 + R_{\text{anode}} + R_{\text{bubble,O}_2} + R_{\text{ions}} + R_{\text{membrane}} + R_{\text{cathode}} + R_1' \quad (7.38)$$

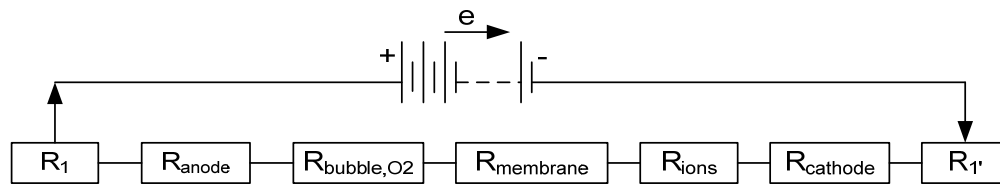


Figure 7.67: Electrical circuit analogy of water electrolysis system.

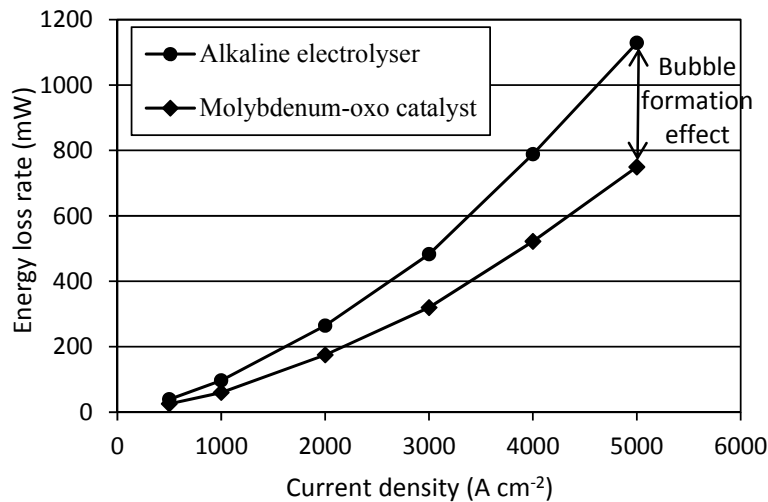


Figure 7.68: Qualitative comparison of energy losses between MoO catalyst and alkaline electrolyser.

Transport-related resistances are the physical resistances experienced in a typical electrolysis process, such as gas bubbles covering the electrode surfaces. Transport resistances such as electrical resistances lead to heat generation according to Joule's law and

transport phenomena [241], thereby causing deficiency of the electro-catalysis system. The molybdenum-oxo catalyst has the advantage of eliminating bubble formation at the cathode surface, because the catalytic reaction will occur inside the solution. Figure 7.68 shows a promising contribution of molybdenum-oxo catalysts to one of the water electrolysis barriers. The current densities are theoretical, but they lie in a potentially commercial range. Energy losses due to bubble formation can be reduced by almost 20% at high current densities using the molybdenum-oxo catalyst.

7.3.3.3. Seawater electrolysis

Direct sea water electrolysis has been used at a commercial level for disinfecting sewage streams, and for sterilizing water used in pressure injection in oil and gas formations. In these cases, only the anodic reactions are a focus. There has also been interest in the cathodic production of hydrogen for onsite use as a reducing agent, or as part of the overall hydrogen economy [141].

Molybdenum-oxo catalyst performance has been evaluated on a sample of California sea water with no added electrolyte [10]. Short time CPE experiments display a maximum turn-over frequency of 1,200 moles of H₂ per mole of catalyst per hour for a 7.7 μM catalyst concentration in a 5 mL solution. The polarization curve, Figure 7.69, indicates that over-potential values of the HER half-cell of sea water electrolysis are within an acceptable range of commercialized technologies. In comparison, at similar current densities, the over-potential required for Ni and Ni-Fe-C cathodes is reported to be 0.7-0.8 V to split sea water [242]. The following correlation is extracted for over-potential of the molybdenum-oxo catalyst in seawater catalysis:

$$U = -959.1 \ln j + 2116.1, R^2 = 0.97 \quad (7.39)$$

The energy efficiency of seawater dissociation with the molybdenum-oxo catalyst is shown in Figure 7.70. The minimum point at about 1.1E-5 A cm⁻² indicates the optimum over-potential to overcome the charge transfer resistances of the cell, namely the minimum activation energy required to enhance the hydrogen production rate. Better performance of this organometallic complex in seawater is observed, compared with other widely used metal catalysts. In other words, the energy efficiency and over-potential values of CPE experimental data reveals more beneficial application of the molybdenum-oxo catalyst in seawater instead of neutral water.

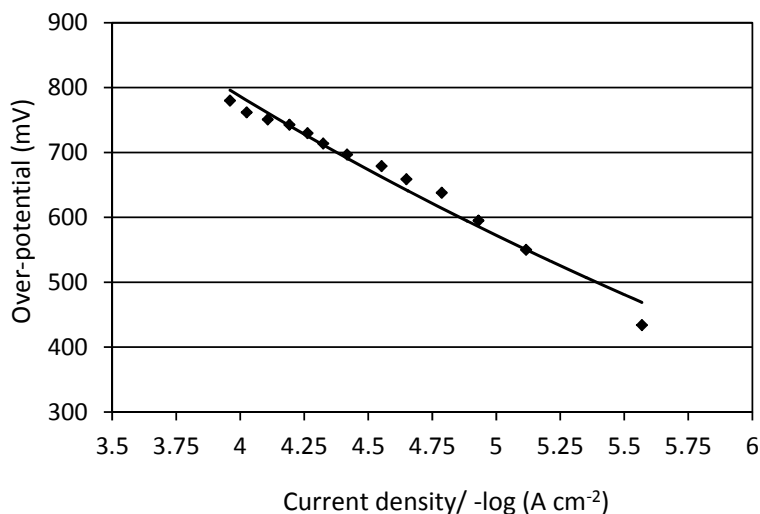


Figure 7.69: Over-potential versus current density for electrocatalysis of seawater in $7.7\mu\text{M}$ solution of $[(\text{PY5Me}_2)\text{MoO}](\text{PF}_6)_2$.

A difficulty in using sea water, whether intended for hypochlorite, chlorine or hydrogen production, is the gradual build-up of insoluble precipitates on the cathode surface. These precipitates result in increased power costs or reduced production, because of increased hydrogen over-potentials and lower active surface areas at the cathode. Periodic cleaning of the cathode surfaces is required to maintain efficiency. This matter has not been evaluated by for molybdenum-oxo catalyst before, which is one of the most challenging issues that should be addressed to ensure the high capability of seawater electrolysis using this catalyst.

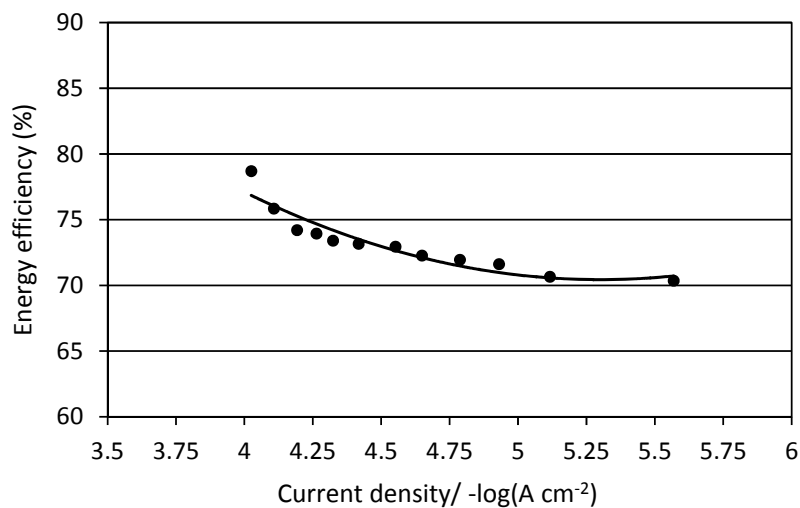


Figure 7.70: System energy efficiency based on molybdenum-oxo function in HER of seawater.

7.3.3.4. Effects of pH change

It has been demonstrated that molybdenum-oxo catalyst is effective for long durations at close to neutral pH, but its durability is limited by the strength of the buffer [10]. The performance of the catalyst should be evaluated to quantify the side effects of possible changes in solution pH during experiments or real practice.

The role of electrolyte in charge transfer from the membrane to the electrode is crucial. The electrolyte and membrane should function well to avoid hydroxide accumulation in the hydrogen evolving half-cell. Otherwise, pH increase of the system limits the reaction rate. The resistances against charge transfer lead to unexpected changes of solution pH that affect the accuracy of monitoring and control of pH. Therefore the effect of pH change of the anolyte solution on the required energy of water splitting should be calculated and considered in practice.

The Nernst equation expresses the reduction reaction in terms of the electrochemical potential using the following relationship with Gibbs free energy. Substituting for the oxygen evolving reaction, it yields

$$E_{Cell} = -0.83 - 0.0295 \times \log(p(H_2)[OH^-]^2) \quad (7.40)$$

$$E_{Cell} = -0.83 - 0.059 \times \log[OH^-] \quad (7.41)$$

$$E_{Cell} = -0.83 + 0.059 \times (14 - pH) \quad (7.42)$$

Figure 7.71 shows the effect of pH change on HER over-potential differentiation from neutral pH and also the energy efficiency of the electrolysis cell as a consequence. This type of quantification provides useful benchmarks of energy loss during the experiments.

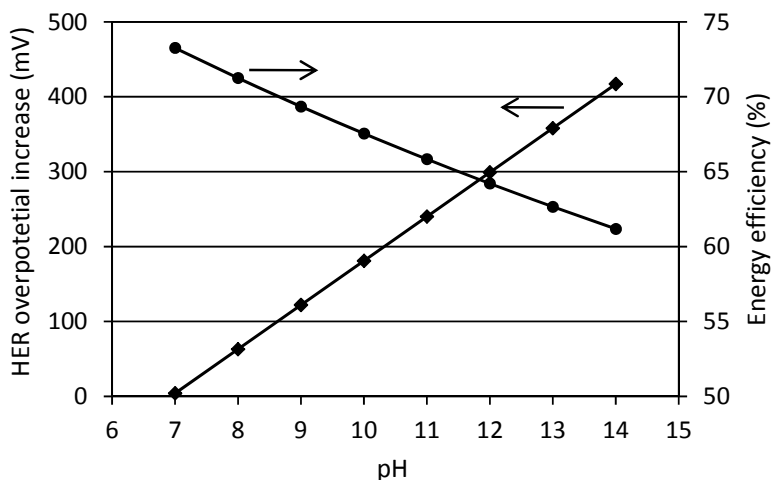


Figure 7.71: Effects of pH change on HER over-potential and energy efficiency of the electrolysis cell

7.3.3.5. Oxygen evolving reactor

The reactor design for water electrolysis experiments typically includes batch or semi-batch type reactors, but it should be modified to a continuous-flow type for scaled-up applications. The rate constant for the main reaction in an oxygen evolving reactor ($2\text{OH}^- \rightarrow \frac{1}{2}\text{O}_2 + \text{H}_2\text{O}$) is within the range of $7.05 \times 10^{11} < k < 1.51 \times 10^{12}$. Therefore, even water is reproduced during oxygen evolving reactions, and for the cases of experimental design, both hydrogen and oxygen evolving reactors can have the same size.

In practice, the efficiency of water electrolysis is limited by the large anodic over-potential of the oxygen evolution reaction (OER). Over decades, considerable research has been devoted to the design, synthesis and characterization of anode materials, with the aim of achieving useful rates of OER at the lowest possible over-potential, in order to optimize the overall electrolysis process.

Figure 7.72 also shows a comparison of energy and exergy efficiencies of the complete system (two half reactions) based on extended electrolysis data of Ref. [10]. A comparison of efficiency values confirms the suitability of Ni electrodes to be selected for the oxygen half-cell.

The amount of hydrogen generated using the molybdenum-oxo catalyst in 71 hours can be estimated from the amount of charge transferred as 0.245 moles [10]. This assumes 100% Faradic efficiency; if the efficiency is less than 100%, the amount of hydrogen produced would also be less. The HHV of hydrogen is $141.9 \text{ MJ kg}^{-1} = 141.9 \text{ kJ g}^{-1} = 287.1 \text{ kJ mole}^{-1}$. This yields a total energy availability of the produced hydrogen of 70.1 kJ.

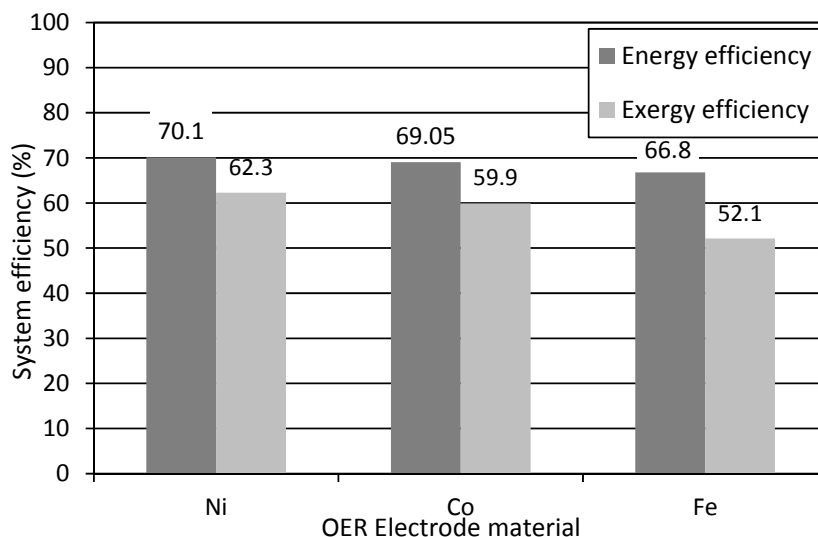


Figure 7.72: Energy and exergy efficiency of electrolysis cell with different OER electrodes.

Table 7.12 compares the relative activities of the three electrodes for the OER in terms of the real current density at a potential in the lower Tafel region. The values of $i_{(E=0.57 \text{ V})}$ suggest that catalytic performance decreases in the order $\text{Ni} > \text{Co} > \text{Fe}$. Caution is however required since there is a greater electrical contribution to the current density at a given potential for the Ni and Fe electrodes, owing to the higher transfer coefficient of $\alpha = 3/2$ for these systems, compared to the value of $\alpha = 5/4$ that prevails for Co.

Table 7.12: Comparison of electrochemical properties of three OER electrodes.

Electrode	$b \text{ (mV dec}^{-1}\text{)}$	$i_{(E=0.57 \text{ V})} \text{ (A m}^{-2}\text{)}$
Co	47.1	1.05×10^{-5}
Fe	37.9	9.1×10^{-7}
Ni	38.2	2.78×10^{-5}

7.3.3.6. Electrolyte concentration

In the next step, choosing an appropriate electrolyte for the oxygen evolving reactor, an investigation of the effects of electrolyte concentration on electrochemical performance of the electrode is essential. Most commercial electrolyzers have adopted alkali (potassium or sodium hydroxide) solutions as the electrolyte. Aqueous alkaline electrolytes of approximately 30-50 wt% KOH or NaOH are widely used. The liquid electrolyte is not consumed in the reaction, but must be replenished over time because of other system losses primarily during hydrogen recovery.

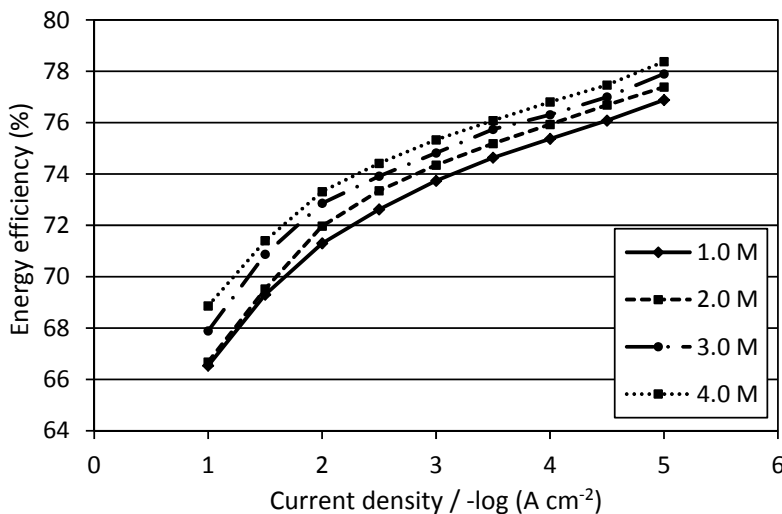


Figure 7.73: Effect of electrolyte concentration on energy efficiency versus current density.

The concentration of the electrolyte may be tuned to favour the energy requirements of the oxygen evolving reaction. As shown in Figure 7.73, almost a 4% increase in energy efficiency of the electro-catalytic system can be achieved by 5 times increasing the electrolyte concentration. Higher electrolyte concentration improves the charge transfer capacity of the solution and decreases the required over-potential at the anode. The efficiency values are calculated for extended electro-catalysis based on the molybdenum-oxo catalyst by considering both OER and HER half cells. The calculations are based on the pre-reduced Ni electrode in various NaOH solutions for the OER half-cell.

7.4. Electrochemical performance of seawater electrolysis

In this section the cathodic polarization behaviour of a molybdenum-oxo catalyst is studied in detail. The relations between the bulk solution pH and the change in polarization potential due to pH changes in the anode and cathode compartments are examined. Also, the possibility of utilizing a new configuration for a seawater feeding system is analysed from an energy savings aspect of view. The system is described in Section 5.1.2. Finally, studies are undertaken to evaluate the parameters which affect cathodic fouling and precipitate formation for a re-circulating seawater electrolysis cell.

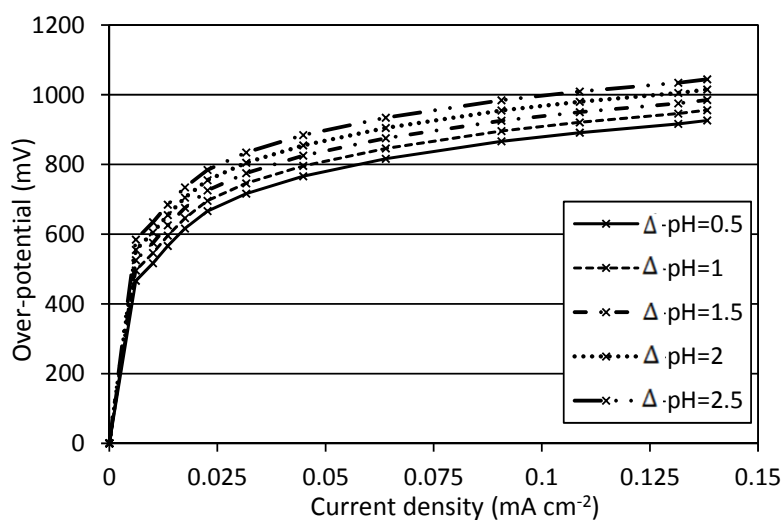


Figure 7.74: Polarization curve for the molybdenum-oxo catalyst at different pH differences.

The polarization curve given in Figure 7.74 indicates that over-potential values of the HER half-cell of sea water electrolysis are within an acceptable range of commercialized technologies. Mass spectrometry studies indicate a reduced stability for $[(PY5Me_2)MoO]^{2+}$ at high pH, with a significant dissociation of the molybdenum centre from the PY5Me₂ ligand

to generate $[\text{MoO}_4]^{2-}$ occurring above pH 12. Also, the energy consumption of the system increases with accumulation of hydroxide ions due to higher over-potentials.

Figure 7.64 shows the variation of the catalyst over-potential at different alkali concentrations in terms of the pH difference between natural seawater and an alkali seawater solution that is created during catalysis. Also, this result indicates the positive effect of anolyte mixing with the catholyte to bring the pH of the system closer to natural seawater. The solid line in this figure corresponds to natural seawater at pH = 7.5 and the others are hypothetical pH values of a seawater solution during catalysis. At high current densities, the cathodic over-potential can be decreased by almost 15 percent for pH reduction from 9.5 to 7.5. The data in Figure 7.74 indicate the importance of neutralizing the hydroxide ions during the course of catalysis to prevent excess energy demand and also preserving the functionality of the catalyst. In comparison, at similar current densities, the over-potential required for Ni and Ni–Fe–C cathodes are reported to be 0.7–0.8 V to split seawater [243].

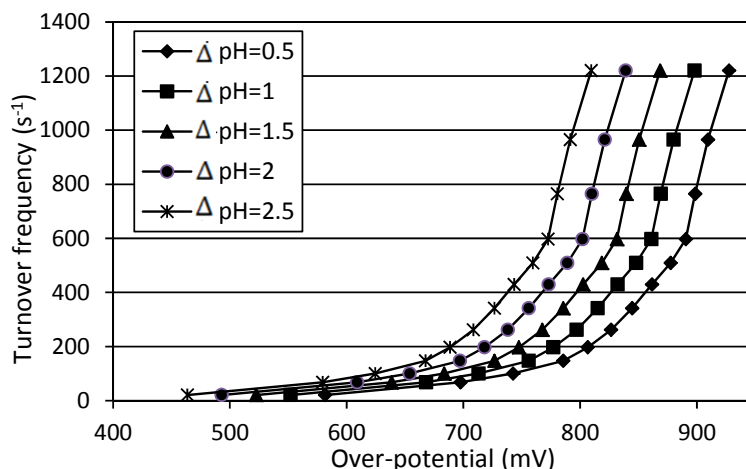


Figure 7.75: Turnover frequency of molybdenum-oxo catalyst at different pH differences (ΔpH).

Figure 7.75 shows the effect of pH of seawater on the turnover frequency, which is defined as the number of evolved H_2 moles per mole of catalyst per hour. The results are based on experimental data for a $7.7 \mu\text{M}$ solution of $[(\text{PY5Me}_2)\text{MoO}](\text{PF}_6)_2$ (7) [10]. Accumulation of hydroxide ions will resist the deprotonating of the Mo–O bond near water molecules to produce the reactive intermediate $[(\text{PY5Me}_2)\text{Mo}(\text{H}_2\text{O})]^{2+}$ and release two OH^- anions. The effect of the new design in refreshing the seawater by decreasing the pH from 9.5 to 7.5 can enhance the turnover frequency by almost 3 times. The lower pH difference between two half-cells enhances the mass and ion transfer. This leads to a decrease of concentration loss and overpotential of water splitting using the same amount of energy.

The irreversibilities associated with seawater electrolysis are modeled using Equation (6.25). The constant values are provided in Table 7.13. Since the over-potential values from experimental data [10] are related to the cathode reaction where the molybdenum-oxo catalyst is functioning instead of an electrode in conventional electrolysis, the activation loss is neglected on the cathode side. The concentration overpotentials are also assumed to be negligible. This is reasonable if the current density is not too high (i.e. $j < 10,000 \text{ A m}^{-2}$). Therefore the total over-potential of the hydrogen evolving reactor is almost equal to the ohmic losses and proportional with the inverse of electrolyte conductivity. The effect of seawater TDS (Total Dissolved Solids) on turnover frequency is presented in Figure 7.76. The results are based on a variation of seawater conductivity versus TDS, taken from experimental data [242].

Table 7.13: Inputs and fitting parameters used in this study.

Parameter	Value	Reference
α	0.5	[164]
$j_o(\text{Graphite})$	$4.6 \times 10^{-5} \text{ A cm}^{-2}$	[213]
$j_L(\text{Graphite})$	150 mA cm^{-2}	[213]
k	$0.42\text{-}0.5 \text{ } \mu\text{s cm}^{-1}$	Present study
t_{ele}	1 mm	Present study

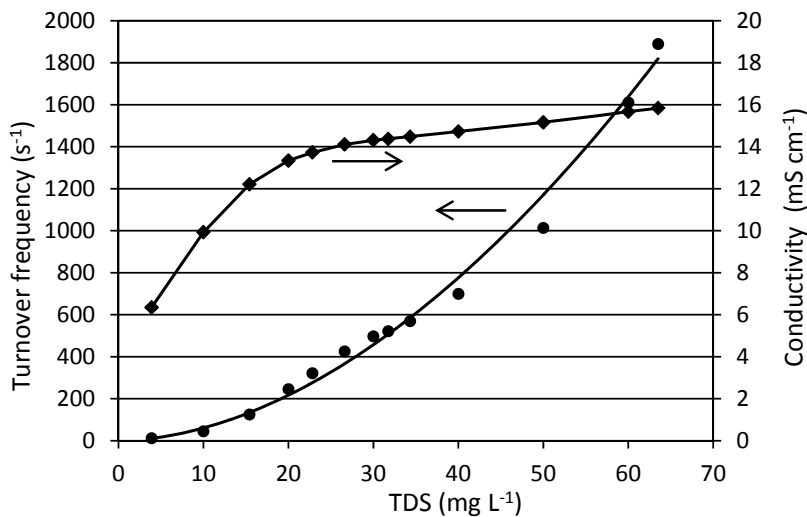


Figure 7.76: Turnover frequency of molybdenum-oxo catalyst at different salinities.

As shown in Figure 7.76, the sharp increasing trend of the hydrogen production rate with TDS implies the importance of dissolved salt in seawater as a charge carrier from the

bulk solution to the active center of the catalyst. The following correlation is extracted for turnover frequency as a function of TDS:

$$TOF = 0.865 \times TDS^{1.84}, R^2 = 0.99 \quad (7.43)$$

A detailed design of the proposed system requires the calculation of the anolyte circulation rate in terms of seawater flow rate. The anolyte is meant to be transferred from the anode side where the pH is decreased due to evolution of chlorine and oxygen to the cathode compartment. Figure 7.77 shows the necessary flow rate that should be circulated from the anode to the cathode in order to maintain the pH of the catholyte constant. The model data are based on a hydrogen production rate using the molybdenum-oxo catalyst by applying 780 mV over-potential.

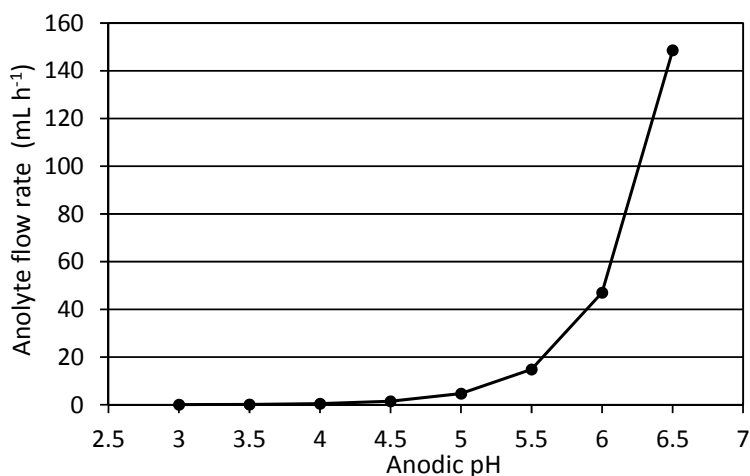


Figure 7.77: Anolyte flow rate required at different anodic pH values.

It is apparent that mass transport can be increased by either increasing the fluid turbulence near the electrode surface, or by increasing the gas evolution rate. Increasing the current density and hence the hydrogen evolution rate decreases the effective diffusion layer thickness as well as increase the migration transport and also increase the pH near the surface. In the bulk fluid, the hydroxide concentration is essentially constant and $\text{pH} \ll 9$, hence no magnesium hydroxide precipitation occurs. The increase in hydroxide levels is confined to the boundary layer near the surface. Utilization of molybdenum-oxo catalyst instead of an active cathode delocalizes the salt formation and makes the bulk solution pH much more important. Figure 7.78 shows the effect of the new design to reduce the magnesium hydroxide formation by decreasing the catholyte pH. It also shows the slight increase in salt precipitation by increasing the reactor equivalent diameter, which leads to decrease in electrolyte circulation flow rate.

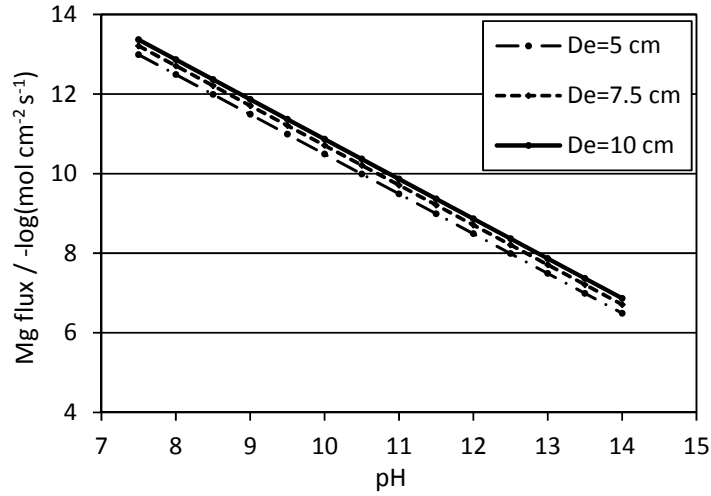


Figure 7.78: Magnesium hydroxide formation rate versus catholyte pH for different diameters.

The rate of precipitation depends on several factors. If the rate of reaction for the magnesium hydroxide is slow, then the magnesium ion concentration will rise near the surface because of migration forces. If, on the other hand, magnesium hydroxide formation is rapid, then the rate of transport will become the controlling factor. Movement to the surface would occur by diffusion, migration and convection. In this case, increasing the convection and turbulence near the electrode surface would increase the precipitation rate, but not necessarily the adhered precipitate. The effect of flow rate in Figure 7.79 indicates an improved mass transport in the bulk fluid increases the total precipitate formation. The results are based on salinity of 30 g kg^{-1} . The effect of improved mass transport can be offset by the decrease in pH at the catholyte active centers. This makes the functionality of the new design in mixing the anolyte and catholyte more advantageous.

The evolution of gas bubbles contributes to the thickness of the effective diffusion layer, via Equation (6.45) so that

$$\frac{1}{\delta_{\text{eff}}} = \frac{\delta_{\text{bubble}} + \delta_f}{\delta_{\text{bubble}} \times \delta_f} \quad (7.44)$$

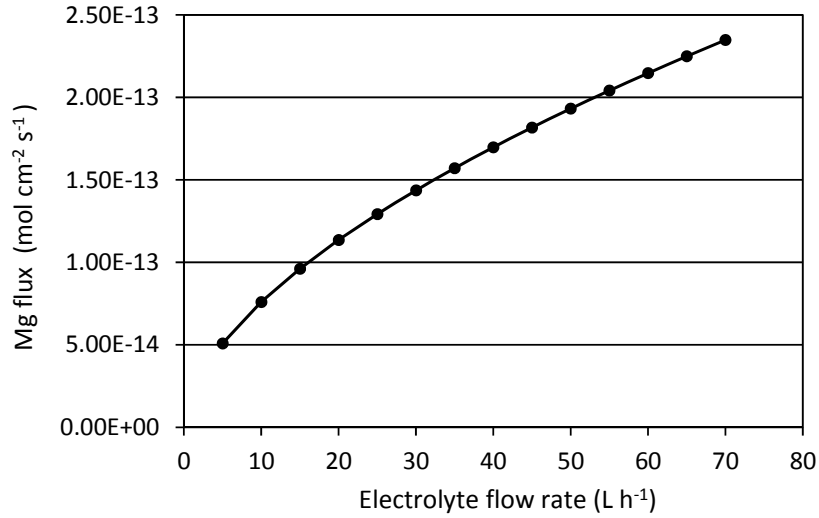


Figure 7.79: Effect of electrolyte flow rate on total precipitate formation.

If the gas evolution effect is large relative to the fluid flow effect, then $\delta_{\text{eff}} \approx \delta_{\text{bubble}}$. In this regard, the effect of current density and concentration gradient between the bulk fluid and surface on the effective diffusion layer is observed in Figure 7.80. It can be concluded that the decreasing effect of gas evolution on minimizing the diffusion layer becomes negligible at high current densities. The pH difference between the bulk solution and near the electrode surface is also found to be an important factor to increase the diffusion layer thickness. Hydroxide ion concentration is the diffusion driving force that accelerates the total precipitate formation. Therefore, as observed in Figure 7.80, working conditions at low current densities and higher concentration gradients become disadvantageous.

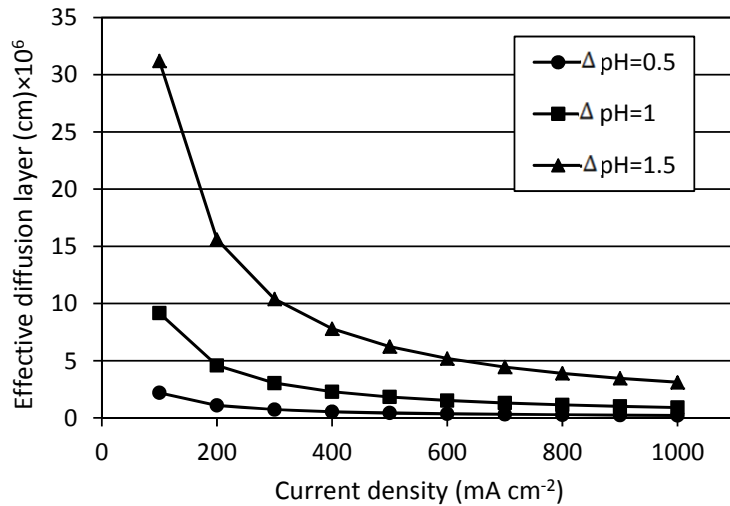


Figure 7.80: Effect of current density and concentration gradient on effective diffusion layer.

7.5. Radiative heat transfer and catalyst performance

This section examines the design of a solar photocatalytic hydrogen production in large-scale continuous flow photo-reactor, and the results based on energy and exergy efficiency are presented. The reactor is described in Section 5.1.3. The efficiency analysis is based on experimental data of $\text{Cd}_{1-x}\text{Zn}_x\text{S}$ solid solution photocatalyst [244] and supramolecular complexes $\{[(\text{bpy})_2\text{Ru}(\text{dpp})]_2\text{RhBr}_2\}(\text{PF}_6)_5$ [70].

Energy and exergy efficiencies are evaluated as effective methods to provide the necessary information to establish the optimal system design, and provide the necessary insight to move from small scale to larger scale systems, and longer term operation. The main parameters to be considered in this study are the catalyst concentration, flow velocity, light intensity, reactor surface absorptivity, and ambient temperature.

The effect of catalyst concentration on energy and exergy efficiency of the catalytic water splitting system is presented in Figure 7.81. The results indicate a rapid increase of efficiencies by increasing the catalyst concentration, but the rate of increase falls after a certain point which is related to the illuminated light intensity and absorptivity of catalyst. It can be concluded that energy and exergy efficiencies of the system can be increased more than 1.5 times by doubling the catalyst concentration.

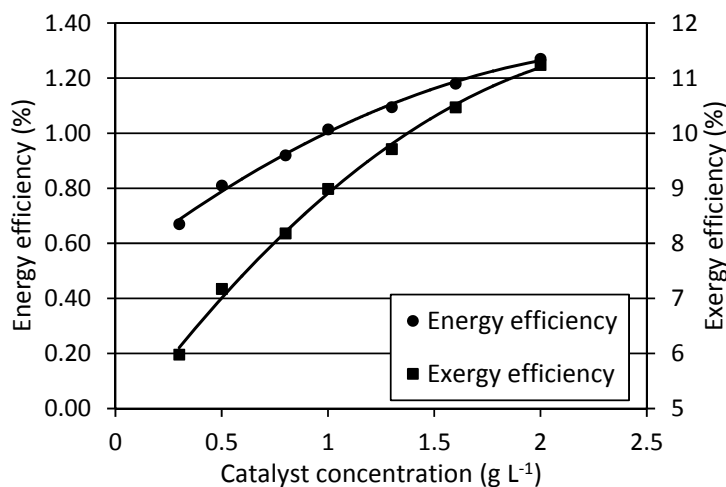


Figure 7.81: Energy and exergy efficiencies versus catalyst concentration.

The effect of water flow rate in continuous operation of the reactor is investigated in terms of energy and exergy efficiency, as shown in Figure 7.82. An increase of water flow rate can enhance the hydrogen production within a certain range. In this design, an increase of flow rate is provided by an increase of velocity, and the reactor radius is fixed. Higher

kinetic energy of the solution increases the photochemical interactions between active sites of the catalyst and water molecules to exchange electrons and hydroxide ions. The optimum flow rate inside the reactor is found to be 6 L min^{-1} , since exergy efficiency starts decreasing afterwards. This is due to an increase of physical exergy destruction compared with the hydrogen production rate at high flow rates.

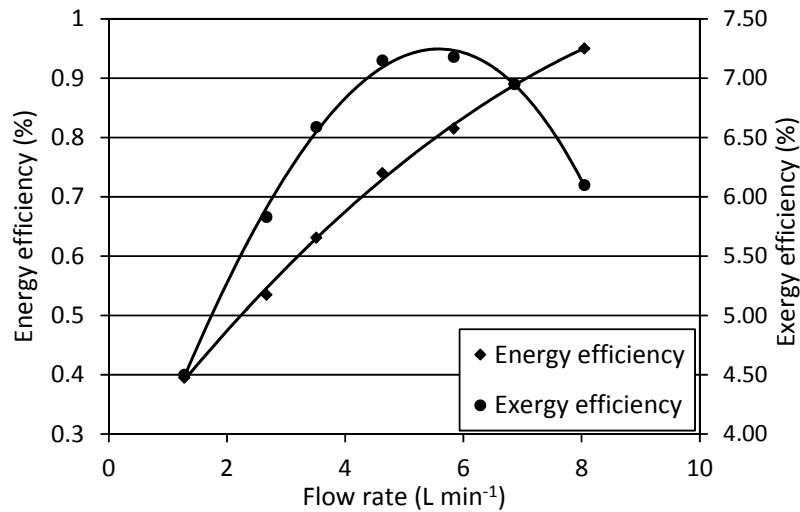


Figure 7.82: Energy and exergy efficiencies of photo-reactor at different flow rates.

Figure 7.83 shows the distribution of exergy loss and destruction for the photo-initiated water splitting reactor. The results are based on 1 g L^{-1} catalyst concentration, 6 L min^{-1} flow rate, and 490 W m^{-2} light intensity. The largest loss occurs during radiation from the reactor surface (50.6%) due to reflection and scattering. The next largest loss (24.9%) is due to physical destructions involved with flow and continuous operation of the reactor. The chemical exergy destruction (24.4%) contribution is almost the same as the physical destruction. This latter loss includes the lost exergy due to water reduction to hydrogen and hydroxide ions and also the oxygen evolution reaction. Convection from the reactor surface at temperature T has the least effect on the exergy loss. It should be noted that only natural convection is considered and surface temperature is calculated based on the light intensity and r absorptivity.

Figure 7.84 shows the effect of reactor surface absorptivity of light within the visible wavelength range on the exergy efficiency for different average absorptivity coefficients of wavelengths beyond the visible range (400-700 nm). It can be concluded that exergy efficiency has the highest value when the visible light absorptivity is minimum. This was also

verified for the absorptivity of wavelengths beyond the visible range. At $\alpha_{nV} = 1.3$ and $\alpha_V = 0.2$, the transmitted light through the reactor surface is at maximum and the absorbed light by the catalyst is high enough to provide the optimum hydrogen rate. Any increase in the absorbed photon energy causes further energy loss by convection and radiation.

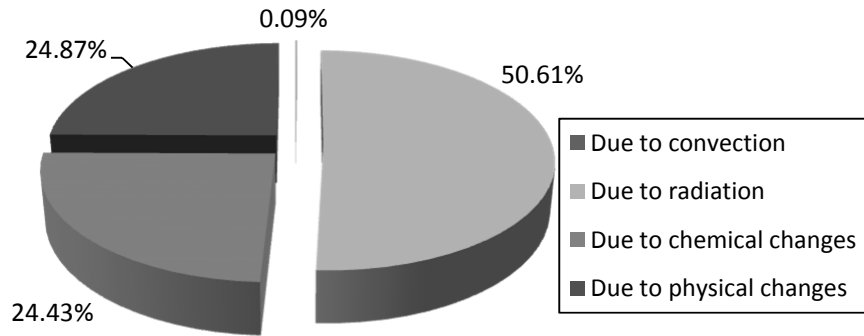


Figure 7.83: Distribution of exergy loss and destruction in the photo-reactor system.

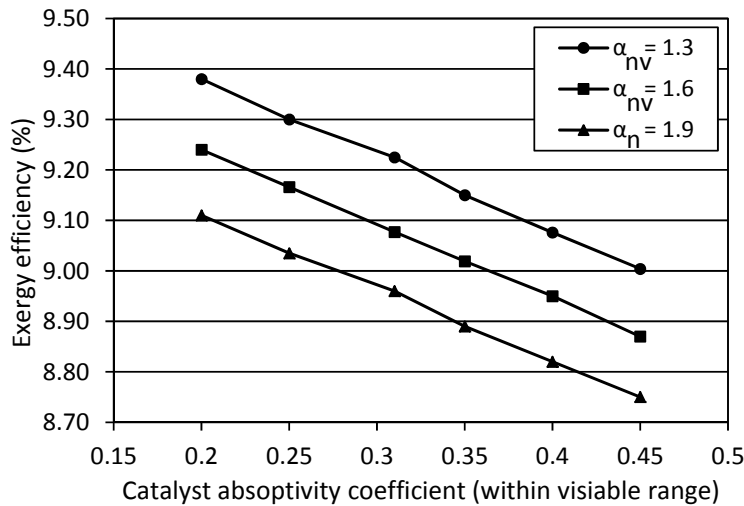


Figure 7.84: Exergy efficiency variations for light absorptivity of catalyst.

Although light absorptivity of the catalyst over irradiated wavelengths of the light source determines the hydrogen productivity of the photo-catalytic water splitting system, the light intensity can be recognized as one of the key parameters in design and optimization of photo-reactors. Figure 7.85 shows an increase in energy and exergy efficiencies due to an increase in light intensity. This effect is gradually lowered after 600 W m^{-2} light intensity by the light absorptivity limitation of the catalyst.

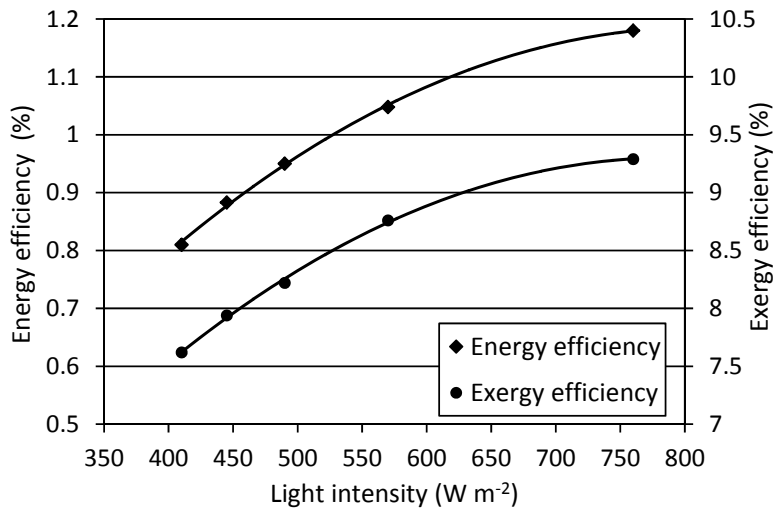


Figure 7.85: Energy and exergy efficiencies of photo-reactor for different light intensities.

Although the environment temperature is not an operating parameter in the photo-catalytic water splitting, it has a major effect on the energy and exergy efficiencies. The irreversibility's due to heat transfer, chemical reactions, and physical variations in the system are affected by the environment temperature. As shown in Figure 7.86, both the energy and exergy efficiencies decrease by almost 30% over a 15 degree increase in the ambient temperature. Increases in ambient temperature cause lower heat transfer by radiation and convection from the reactor, but increases the physical and chemical exergy losses due to higher available exergy at the dead state. The inlet exergy of the system also increases at higher environment temperatures.

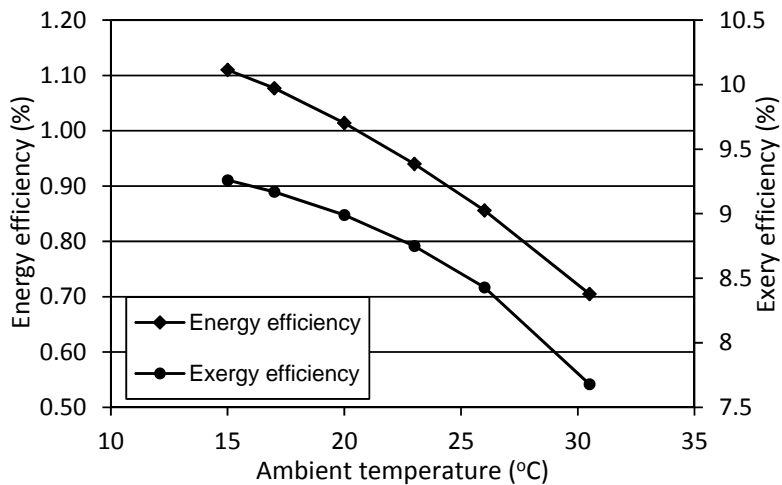


Figure 7.86: Energy and exergy efficiencies of photo-reactor for different ambient temperatures.

Figure 7.87 shows the effect of ambient temperature on exergy loss of the system in terms of the exergy destruction ratio due to heat transfer, chemical and physical reactions. It can be concluded that a higher environment temperature reduces the exergy destruction due to heat transfer from the reactor surface area whereas chemical and physical exergy losses are increased by almost 35% over a 15 degree temperature increase. These results indicate the advantage of lower ambient temperature conditions for photo-catalytic hydrogen production systems. An optimized heat transfer design of the reactor should be considered to maintain the solution at a certain temperature and avoid excess heat losses to environment.

In order to determine the optimal region of operation, the exergy destruction ratio of the reactor should be investigated at different operating parameters. The variation of the exergy destruction by flow rate, and light intensity is demonstrated in Figures 7.88, and 7.89, respectively. An increase of these parameters enhances the hydrogen production rate with the cost of lower exergy efficiency. A decrease in exergy destruction ratio is mostly due to an increase in inlet exergy of the system. The decreasing rate of the exergy destruction ratio over the flow rates between 3 and 6 L min⁻¹ and light intensity of 450 to 600 W m⁻² is significant. Comparison of results in these two figures with those of which presented in Figures 7.82, 7.83, and 7.85 indicate the beneficial effect of higher catalyst concentrations at higher light intensity and optimum flow rate of 6 L min⁻¹.

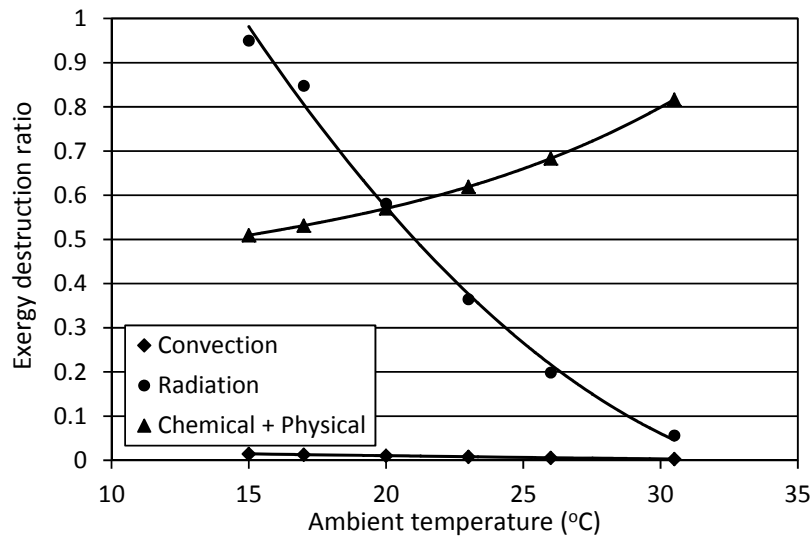


Figure 7.87: Exergy destruction ratios of photo-reactor at different ambient temperatures.

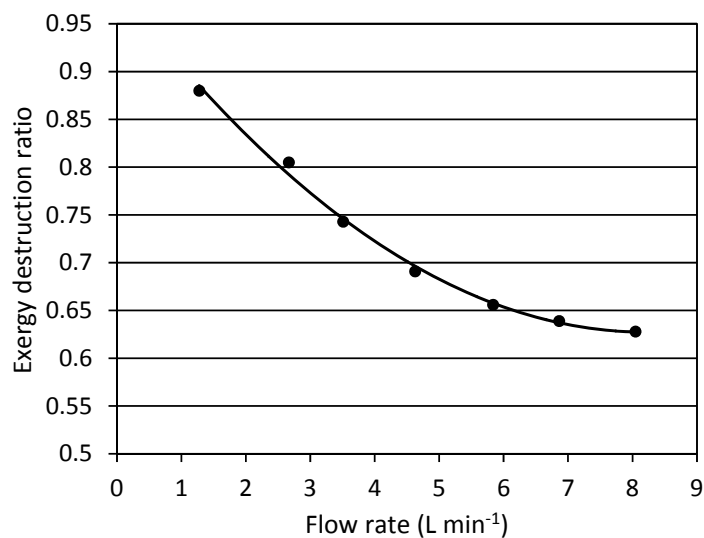


Figure 7.88: Variation of exergy destruction ratio by flow rate.

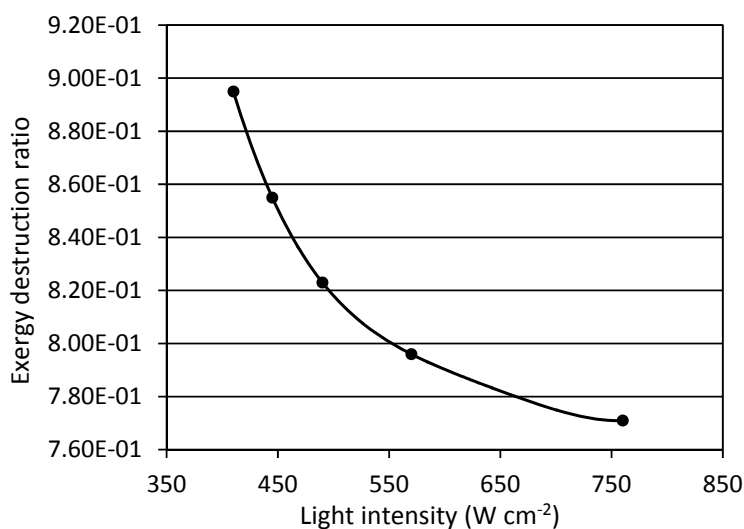


Figure 7.89: Variation of exergy destruction ratio by light intensity.

Three different mixed-metal supramolecular complexes are examined from energy and exergy efficiency aspect of view, as shown in Figure 7.90. The variation of complexes is based on the terminal ligands (bpy, phen or Ph₂phen) and the halide is Bromine. The efficiency calculations are based on the productivity of each catalyst at a 120 μM concentration and 7.27×10^{19} photons per minute light intensity. A higher productivity of supramolecular complexes with the Ph₂phen ligand makes it superior by at least 3 times in comparison with the bpy ligand.

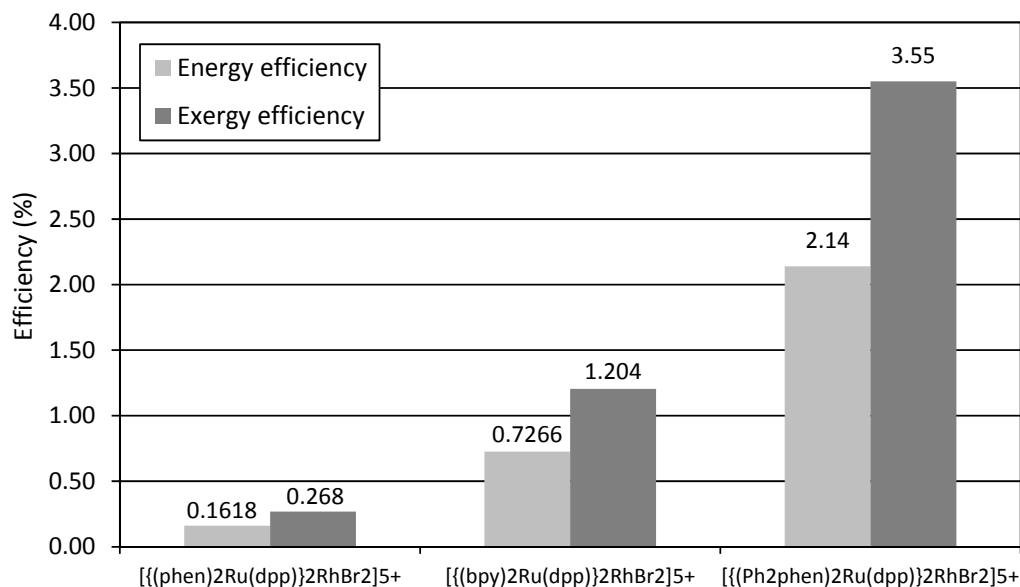


Figure 7.90: Energy and exergy efficiencies of photo-reactor for different mixed-metal supramolecular complexes.

7.6. Exergo-environmental assessment results of continuous flow photoreactor

In this section, a new photo-catalytic energy conversion system is analyzed for continuous production of hydrogen at a pilot-plant scale. The system is described in section 5.1.4. Two methods of photo-catalytic water splitting and solar methanol steam reforming are investigated as two potential solar-based methods of catalytic hydrogen production. The exergy efficiency, exergy destruction, environmental impact and sustainability index are investigated for these systems. This study elucidates the advantages of each hydrogen production method by thermodynamics and environmental analyses. The equations are developed and programmed using Engineering Equation Solver (EES).

This analysis evaluates different output parameters that include exergy efficiency and exergy destruction rates of photo-catalytic hydrogen production, as well as the carbon dioxide emissions. These parameters are examined under the variation of the catalyst concentration, flow velocity, light intensity, and ambient temperature. The exergy efficiency and carbon dioxide emissions are examined for two photo-catalytic hydrogen production systems, namely, water splitting and methanol steam reforming. Exergy efficiency analysis is an effective method to establish the optimal system design that provides the necessary insight to move from small scale to larger scale systems and longer term operation.

The effect of catalyst concentration on exergy efficiency of the catalytic water splitting system is presented in Figure 7.91. The results show a rapid increase of efficiencies by increasing the catalyst concentration, while the rate of increase falls after a certain point which is related to the absorptivity limits of the catalyst. It can be concluded that the exergy efficiency of the system can be increased by more than 15% by performing the photo-catalytic process at 15 °C ambient temperature compared with 25 °C.

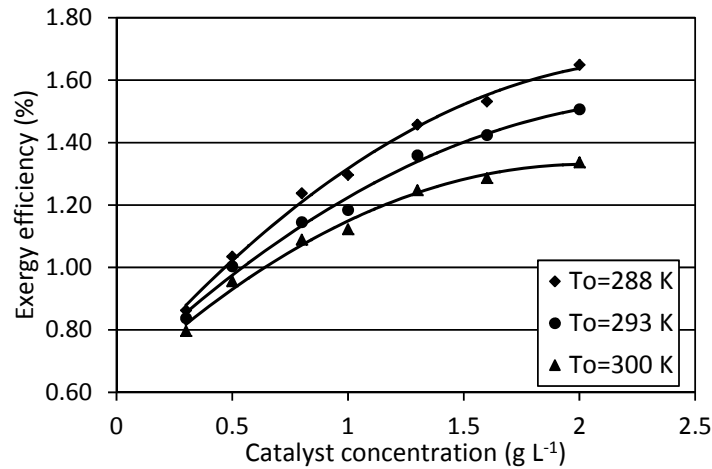


Figure 7.91: Exergy efficiency versus catalyst concentration at different ambient temperatures.

The effect of water flow rate on continuous operation of the reactor is investigated in terms of exergy efficiency and CO₂ emissions, as shown in Figure 7.92. An increase of water flow rate can enhance the hydrogen production within a certain range. In this design, an increase of flow rate is provided by an increase of velocity and the reactor radius is fixed. Higher kinetic energy of the solution increases the photochemical interactions between active sites of the catalyst and water molecules to exchange electrons and hydroxyl ions. The optimum flow rate inside the reactor is found to be 6 L min⁻¹, since exergy efficiency starts decreasing afterwards. This is due to an increase of physical exergy loss compared with the hydrogen production rate at high flow rates. The CO₂ emissions that are reduced by this process increase at higher flow rates. CO₂ emissions reduction is calculated based on the assumption that the energy to derive the photo-catalytic water splitting system is substituted by fossil fuel combustion. Since the rate of hydrogen production increases at higher water flow rates, the system performance will be better environmentally.

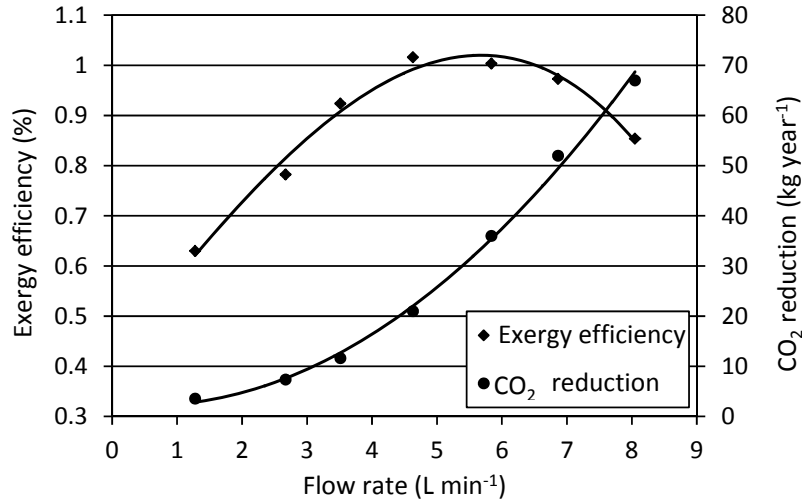


Figure 7.92: Exergy efficiency and CO₂ emissions reduction of water splitting photo-reactor.

Figure 7.93 shows the exergy destruction rate and sustainability index variation at various flow rates. The total exergy destruction rate increases with a higher flow rate as the physical and chemical losses increase accordingly. The sustainability index increases up to same point, which is associated with the optimum flow rate of the system. Exergy depletion of the water splitting system is optimized at an inlet flow rate of about 6 L min⁻¹ corresponding to 2 L h⁻¹ of hydrogen production capacity.

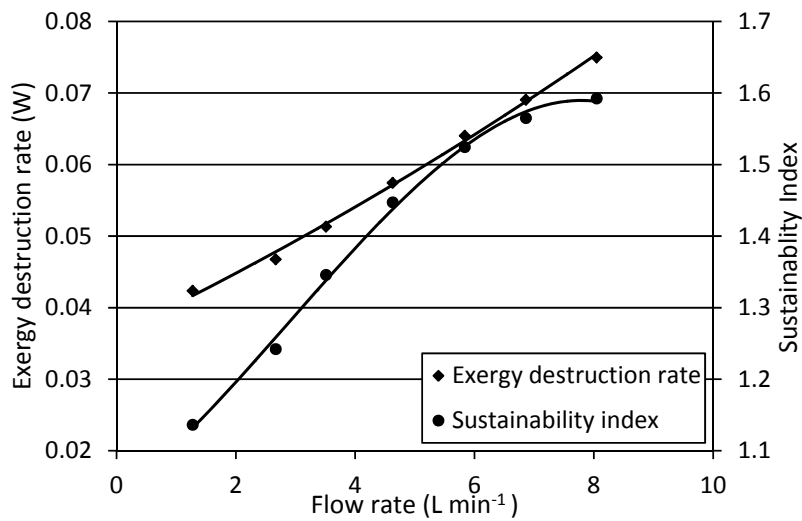


Figure 7.93: Exergy destruction rate and sustainability index of water splitting photo-reactor.

7.7.1. Solar thermal methanol reforming

The results in this section pertain to solar thermal hydrogen production via methanol steam reforming. The greenhouse gas emissions of this process can be compared with CO₂ reduction of which presented for photo-catalytic water splitting process in the previous section. Figure 7.94 illustrates the mass flow rate and exergy flow rate of each stream for all chemical constituents. The values of mass flow and exergy flow rate are calculated based on 600 W m⁻² solar intensity, and a water/methanol mole ratio of 2. The exergy of the stream at the inlet and output of each component contains the physical and chemical exergy contents.

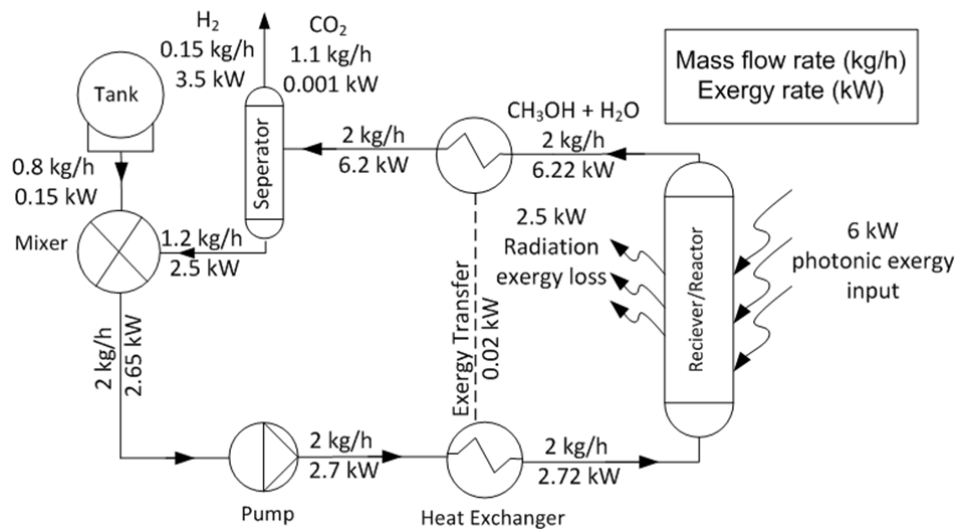


Figure 7.94: Mass flow and exergy rate of solar-thermal methanol reforming for hydrogen production.

Figure 7.95 shows the effect of the mole ratio of water and methanol on exergy efficiency of the methanol steam reforming system. This effect is evaluated for various light intensities. The light intensity is one of the key parameters in optimization of photo-reactor design, which should be considered in conjunction with light absorptivity of the catalyst over irradiated wavelengths of the light source to determine the hydrogen production of the system. At higher light intensities, there is a significant improvement in exergy efficiency of the methanol reforming system, mainly due to higher hydrogen production. However, at higher light intensities, an increase of feed flow rate causes rapid degradation of the inlet exergy utilization. The exergy efficiency at 600 W m⁻² light intensity decreases by almost 45% when the flow rate is increased 2.5 times, whereas it decreases less than 5% at light intensity of 320 W m⁻².

The CO₂ emissions of solar thermal methanol steam reforming are shown in Figure 7.96. The results are calculated for different light intensities. Similar to conclusions drawn from the exergy efficiency analysis, the emissions of greenhouse gases are more affected at higher light intensities. A comparison of the results in Figures 7.95 and 7.96 indicates that a trade-off exists in terms of exergy efficiency improvement and CO₂ emissions of the solar thermal hydrogen production system. The light intensity range of $530 \text{ W m}^{-2} < I < 600 \text{ W m}^{-2}$ and water-methanol mole ratio of 1.5 to 2 are found to be optimal criteria from exergy-environmental point of view.

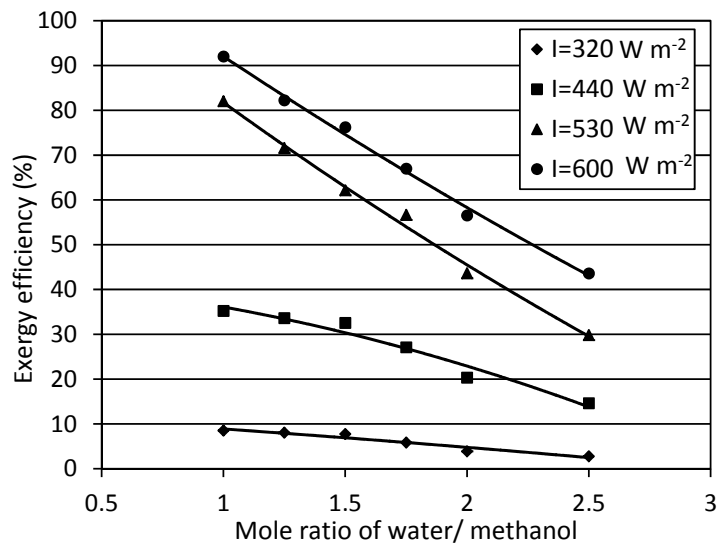


Figure 7.95: Exergy efficiency variations versus mole ratio of water and methanol.

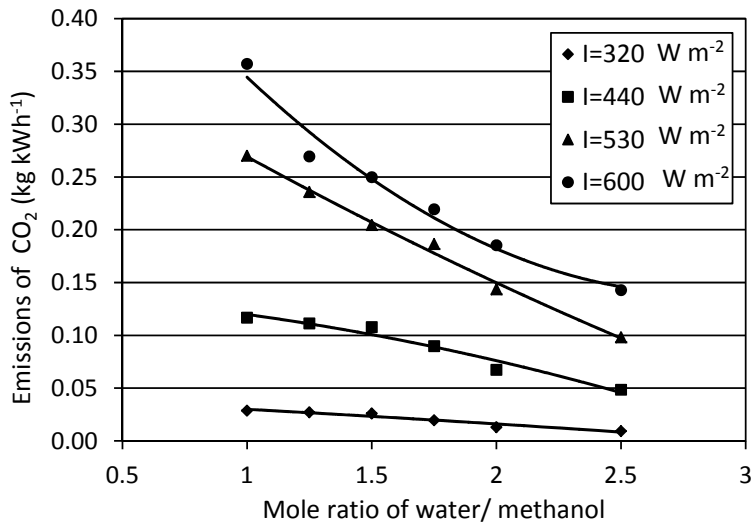


Figure 7.96: CO₂ emissions variations versus mole ratio of water and methanol.

The irreversibilities due to heat transfer, chemical reactions, and physical variations in the system are affected by the solar irradiation into the system. As shown in Figure 7.97, both the exergy efficiency and emissions of greenhouse gases increase with higher irradiated solar energy. The rates of exergy efficiency and CO₂ emissions decrease at higher solar energy inputs. Solar input of more than 3,000 W involves high environmental pollution while it does not improve the exergy efficiency significantly. The effect of solar flux on CO₂ emissions at two different feed flow rates is shown in Figure 7.98.

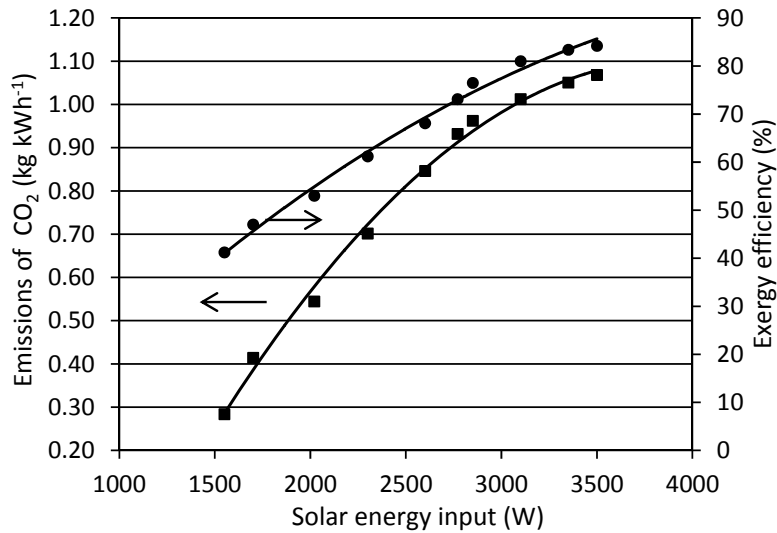


Figure 7.97: Exergy efficiency and CO₂ emissions of photo-catalytic methanol steam reforming.

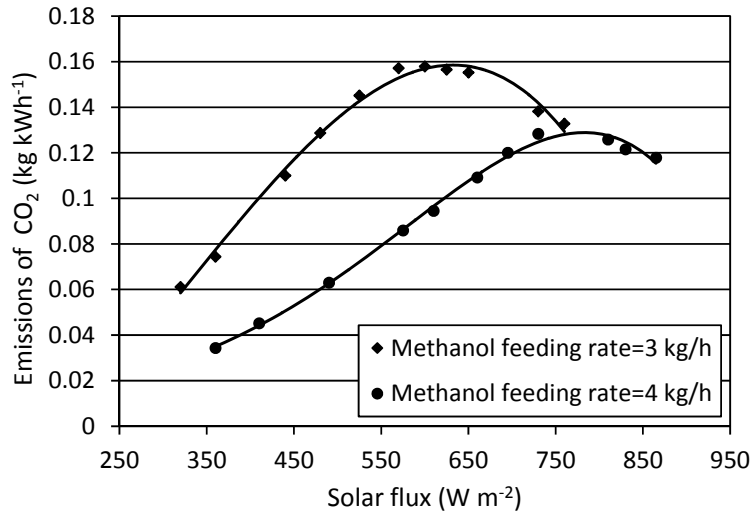


Figure 7.98: CO₂ emissions of photo-catalytic methanol steam reforming at different feeding rates.

It should be mentioned that a reactor temperature corresponds to a fixed methanol conversion rate for the two feed rates of the reactants. It occurs because methanol conversion is usually a monotone function of reactor temperature, $X_{\text{CH}_3\text{OH}} = f(T_{\text{reactor}})$. Therefore, an increase of feed rate causes lower reactor temperatures by improving the potential energy of the flow stream and subsequently lower conversion of methanol which decreases the CO_2 emissions of the system. It is also found that CO_2 emissions are maximized at an optimum feed rate, which indicates the amount of solar flux that drives the conversion of methanol to hydrogen.

7.7. Exergo-economic analysis of photo-catalytic water splitting plants

Following the exergo-economic study guidelines for photo-catalytic hydrogen production system, presented in Section 6.8, two case scenarios for economic evaluation of a hydrogen production plant with three different production capacities is performed as follows:

Case 1: Hydrogen production (Single product).

Case 2: Hydrogen and oxygen production (Two products).

In both cases a heliostat field with upper solar spectrum is used for photochemical process and lower spectrum for additional hydrogen production method which works synergistically with photo-catalysis. Also the calculations are extended to consider three insolation values of 4, 8, and 12 $\text{kWh m}^{-2} \text{day}^{-1}$ to conform different irradiation patterns at different geographical zones.

A hybrid catalysis configuration is applied. It is assumed that double or triple gap absorption system based on a combination of catalysts including ZnS and CdS suspensions are utilized. The low energy photons are captured by a solar thermal collector for additional H_2 production infrastructure such as Cu-Cl with efficiency between 30% and 50% as for years 2015-2025 [247]. It is assumed that all sacrificial agents for photochemical process are recycled and electricity for internal use is provided.

The reference capacity of hydrogen production plant e.g. thermochemical plant plus photochemical plant is assumed 100 tons per day and solar plant capital cost is 50% of all capital cost. The capital cost calculation are, then, based on scaling up or down of the reference values by appropriate cost scaling laws adopted by Kromer et al. [247] in average for year 2025.

The Life time of plant is assumed 30 years with minor maintenances. The cost of photo-chemically produced hydrogen essentially depends on spectral splitting system of

which cost is proportional with heliostat field cost and the ratio between upper and lower portion of solar radiation. Therefore, the following relation is proposed to estimate the cost of photochemical hydrogen portion of the reference capacity:

$$c_{H_2,pc} = f \frac{Ex''_{h,h}}{Ex''_{h,l}} c_{H_2,thc} \quad (7.45)$$

where f is proportionality factors with variable values of $f = 0.3$ (worst), 0.2 (average), 0.1 (best) estimates. Cost of chemicals and materials for photochemical is included in the proportionality factors. The main calculation steps including intermediate steps, assumptions, and remarks are presented in Table 7.14. The carbon taxation value is adopted from [228], and assumed to have greater magnitude for the average and best case scenarios.

Table 7.14: Cost assessment assumptions and intermediate results.

Item	Symbol	Worst	Average	Best	Units	Remarks
Insolation	I	4	8	12	kWh/m ² day	Assume 1 sun light intensity 1,000 W m ⁻²
Exergy rate of insolation	Ex''	3.8	7.6	11.4	kWh/m ² day	Exergy factor 0.95 [246]
Land occupancy factor	LOF	0.75	0.85	0.95	NA	Fraction occupied with light harvesting units
Optical losses	OL	20	10	5	%	Photons energy loses due to optical system
Harvested light exergy	Ex''_h	2.28	5.8	10.3	kWh/m ² day	Light that reaches H ₂ production unit
High energy photons	$Ex''_{h,h}$	0.75	1.9	3.39	kWh/m ² day	Photons fraction with $\lambda < 560$ nm is $w_h = 35\%$ of solar radiation
Low energy photons	$Ex''_{h,l}$	1.53	3.89	7.89	kWh/m ² day	Photons fraction with $\lambda > 560$ nm is $1 - w_h = 65\%$
Exergy efficiency of photocatalytic system	η_{pc}	10	15	20	%	Hybrid catalysis is applied.
H ₂ produced from photocatalysis	m''_{pc}	2	8.7	20	g H ₂ /m ² day	Uses only the exergy of the harvested high energy photons. $m''_{pc} ex^{ch} = \eta_{pc} Ex''_{h,h}$
Efficiency of additional H ₂ production method	η_{thc}	30	40	40	%	using lower spectrum

H ₂ produced by thermochemical method	m''_{thc}	14	47.5	84	g H ₂ /m ² day	
Total H ₂ produced per day and ha	m''_{H_2}	163	563	1048	kg/ha.day	$m''_{H_2} = m''_{pc} + m''_{thc}$
Life time of plant	LT	30	30	30	Years	
Total H ₂ photochemically	$m''_{pc,t}$	25	96	226	kg H ₂ /m ²	$m''_{pc,t} = LT m''_{pc}$
additional H ₂ production	$m''_{thc,t}$	153	520	921	kg H ₂ /m ²	$m''_{thc,t} = LT m''_{thc}$
Total H ₂ produced per m ² per day	$m''_{H_2,t}$	178	616	1148	kg H ₂ /m ²	$m''_{H_2,t} = m''_{pc,t} + m''_{thc,t}$
Hydrogen cost for additional H ₂ production method only	$C_{H_2,thc}$	3	3	3	\$/kg	Assumed 100 tons per day production of hydrogen; data taken in average for year 2025 from [247].
Hydrogen cost photochemical portion	$C_{H_2,pc}$	0.17	0.12	0.059	\$/kg	$C_{H_2,pc} = f \frac{Ex''_{h,h}}{Ex''_{h,l}} C_{H_2,thc}$
Compounded hydrogen cost, additional H ₂ production method	C_{H_2}	2.1	2	2	\$/kg	$C_{H_2} = w_h C_{H_2,pc} + (1 - w_h) C_{H_2,thc}$
Total land area for 100 tons per day plant	TLA_{ref}	614	177	96	ha	$TLA_{ref} m''_{H_2} = m_{day}$ here $m_{day} = 100,000$ kg H ₂ /day.
Total capital cost for 100 t/day plant	C_{ref}	276	273	271	M\$	$C_{ref} = C_{H_2} m_{day} / C_f$; where $C_f = 0.75$ is capacity factor as in [245] where $m_{day} = 100$ tons H ₂ /day
Equivalent electricity from produced H ₂ for lifetime in the reference case	W_{eqv}	21	21	21	TWh	$W_{eqv} = m_{H_2,ref} HHV \eta_{ref}$ where $m_{H_2,ref} = 365 LT m_{day}$ $HHV = 141$ MJ/kg, and $\eta_{ref} = 0.5$ average efficiency at power generation with fuel cells.
Feed-in-tariff factor	FIT	0.2	0.4	0.6	\$/kWh	As in Ontario Feed-In-Tariff type program according to [227]

Capital recovery applicable	CR_{FIT}	43	8.6	10.7	M\$	$CR_{FIT} = W_{eqv} FIT$
Carbon mitigation due to renewable hydrogen generation	\mathcal{M}_{GHG}	21	21	21	Mt GHG	Carbon GHG mitigation factor is taken 1 kg CO ₂ per kWh electricity (or 1 Mt CO ₂ per TWh electricity) as in reference [248]
Carbon taxation	CT	1	5	6	\$/t GHG	Assumed conservatively from [227]
Capital recovery from carbon tax	CR_{CT}	21	107	129	M\$	$CR_{CT} = \mathcal{M}_{GHG} CT$
Renewable energy incentive factor	IF	1	5	8	¢/kg H ₂	Assumed conservatively from [245]
Capital recovery from incentives	CR_{IF}	11	54.7	87.6	M\$	$CR_{IF} = m_{H_2,ref} IF$
Amended capital cost	$C_{ref,a}$	200	102	44	M\$	Accounting for FIT, CT, and IF; $C_{ref,a} = C_{ref} - (CR_{FIT} + CR_{CT} + CR_{IF})$
Amended hydrogen cost	$C_{H_2,a}$	1.5	0.76	0.33	\$/kg	For reference case; $C_{H_2,a} = C_{ref} C_f / m_{day}$
Scaling factor	SF	0.8	0.7	0.7		
Total amount of O ₂ produced for large scale per day	m_{ls,O_2}	21912	21912	21912	t/day	$m_{O_2} = m_{ls} * 8$
Cost of O ₂	m_{O_2}	0.2	0.3	0.4	\$/kg	[247]
Revenue generated due to O ₂ per day for large scale	Rv_{ls,O_2}	4.4	7.57	8.76	M\$/day	$R_{O_2} = m_{O_2} \times m_{ls,O_2} \times 1000$
Capital for large production scale	C_{ls}	2,200	830	358	M\$	$m_{ls} = 2,000$ t/day, $C_{ls} = C_{ref,a} \left(\frac{m_{ls}}{m_{ref,a}} \right)^{SF}$
Capital for small production scale	C_{ss}	5	4.1	1.736	M\$	$m_{ss} = 1$ t/day, $C_{ss} = C_{ref,a} \left(\frac{m_{ss}}{m_{ref,a}} \right)^{SF}$

The hydrogen production costs are calculated based on the practically reasonable assumptions for the above given case scenarios with different production capacities. A summary of the hydrogen cost projected by the photochemical hydrogen production analysis is shown in Table 7.15. The costs are in acceptable range and well below the DOE 2012

target for large-capacity production. It should be noted that the best case scenario considers all the beneficial elements including high solar intensity, oxygen production, process hybridization, unused spectrum recovery, feed-in-tariff and carbon mitigation incentives. On the other hand, the worst case scenario does not take into account the aforementioned options. The calculations are based on the quantum efficiency of 60%, as measured in the experiments. As presented in Table 7.15, the cumulative effect of these considerations leads to competitive prices, which are indeed reliable providing all the beneficial options can be implemented in the hydrogen production plant. In order to compare the hydrogen production cost by photo-catalytic water splitting with that of the existing large scale production methods, the numbers of the worst case scenario should be adopted, as they are based on more realistic assumptions.

Changing the assumptions would affect the rate price of hydrogen production. The major contributor to the hydrogen selling price is the plant capital cost, which in turn is a function of the process efficiency. Cost of H₂ production can even further be reduced if efficient routs of unused spectrum recovery are implemented and the cost of heliostats can be decreased.

Following the economic assessment of photo-catalytic hydrogen production process, combination of both the exergy analysis and cost accounting is conducted to include the costs of inefficiencies. This analysis aids the investment decisions, and comparing alternative techniques and operating conditions in a more realistic manner. The results are shown in Figure 7.99. Both hydrogen and oxygen are accounted as useful products of the process. Comparing the results in Figure 7.99 and Table 7.15 indicates that exergetic losses have significant effect on the final product price. The exergetic losses have a strong dependence on production capacity. It is observed that the product prices for medium production capacity (100 ton day⁻¹) and high capacity (2000 ton day⁻¹) are very close, whereas the capital costs are about 10 times less for lower production rate. It emphasises the fact that exergy losses in large capacities should be carefully investigated and compared with lower capacity plants to find the most economic option.

Table 7.15: Economic analysis results for cost of hydrogen (\$/kg).

Case 1:H ₂ (Single product)	Capacity (Ton/day)	Best (\$/kg)	Average (\$/kg)	Worst (\$/kg)
Large capacity	2000	0.35	0.58	1.06
Medium capacity	100	0.85	1.12	2.1
Small capacity	1	2.55	3.2	3.95
Case 2: (H₂+O₂) (Dual product)	2H₂O → 2H₂ + O₂			
Large capacity	2000	0.21	0.44	0.89
Medium capacity	100	0.61	0.88	1.53
Small capacity	1	2.21	2.89	3.77

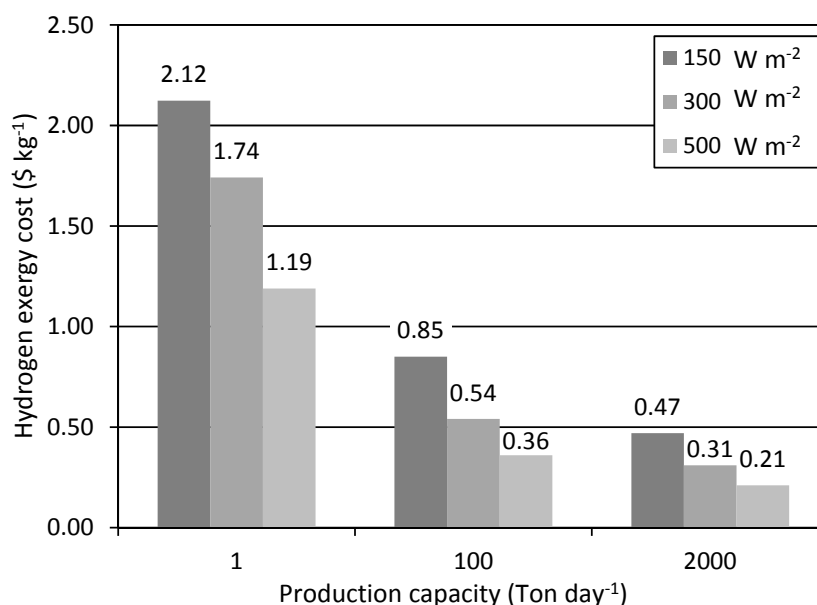


Figure 7.99: Hydrogen exergy cost versus production capacity for different insolation.

7.8. Comparison of electro-catalysis methods

Table 7.16 shows a comparison of different water electro-catalysis technologies. This comparison clearly shows the superiority of alkaline water electro-catalysis as a mature technology with reasonable efficiency relative to other emerging water electrolysis technologies. The PEM electrolyser with highest performance in terms of efficiency still needs to overcome difficulties including costly polymer membranes and porous electrodes, and current collectors. Solid oxide electrolysis cells and PV electrolysis have further challenges due to a severely corrosive operating environment and engineering issues such as high operating temperature and scaling up requirements.

Table 7.16: Comparison of different methods of water electro-catalysis.

Method	Energy Efficiency	Commercial Availability	Reference
PEM electrolyser	65–82%	Commercial	[241]
Solid oxide electrolysis cells	40–60%	Near term	[241]
Alkaline electrolyser	59–70%	Commercial	[241]
Photoelectrolysis	2–12%	Long term	[249]
Molybdenum-oxo	60-69%	Long term	Present study

From an efficiency standpoint, the UCal [10] technology shows a promising and competitive capability for being commercialized. Stability of the molybdenum-oxo catalysts at normal working conditions and extended electrolysis has been shown by UCal experiments. The issue of high over-potential raises concerns for future equipment scale-up. Modifications to $[(PY_5Me_2)MoO](PF_6)_2$ to achieve a better efficiency offer a more promising solution for large scale hydrogen production in the near future.

Chapter 8

Conclusions and Recommendations

8.1. Conclusions

This study provides detailed information for the design, operation and modeling of water splitting photo-catalytic reactors. A new contribution is made in the development of a complete water splitting system for solar-based hydrogen production through modeling and experiments. This design leads to the formation of a continuous reaction system with a stable hydrogen production rate, where photo-catalytic hydrogen production occurs on one manifold and oxygen evolution occurs on another manifold. The results concluded from the scale-up study, and the energy, exergy, and exergo-economic studies of this system confirm the feasibility of the proposed route of photo-catalytic hydrogen production and electro-catalytic oxygen production.

Photo-catalytic hydrogen production using zinc sulfide and cadmium sulfide photo-catalysts is investigated in batch mode, and also a dual-cell with quasi-steady operation. The following remarks are concluded from the present experiments:

- The hydrogen production rate in batch operation is increased by almost 15% following the increase of catalyst concentration from 1% to 3% w/v. The sulfide ions act as hole scavengers to stabilize the ZnS surface against anodic photo-corrosion, but the rate of required replenishment of these chemicals is more than the dual-cell configuration to maintain the productivity of the catalyst constant.
- A higher reaction rate is achieved by supplying higher light intensity with photons within the band gap energy of ZnS, and this effect varies due to competition between ion diffusion and electron-hole recombination. An increase of light intensity from 900 to 1000 W m⁻² leads to more than a 20% increase in productivity of the catalyst in the batch reactor.
- It can be concluded that almost 2.5 times enhancement is achieved by using three times more catalyst concentration. The rate of oxygen formation is increased by almost three times due to the higher rate of hydroxide ion generation. The measured value of the generated oxygen volume is almost half of the hydrogen which confirms

the accomplishment of hydroxide ion decomposition by electro-catalysis. The conversion rate is a direct function of catalyst concentration and light intensity, and simultaneous variation of these parameters in one direction does not make a significant change in photo-reactor productivity.

- Also, an increase of exposed light intensity to dual-cell reactor from 800 W m^{-2} to 1200 W m^{-2} enhances the productivity of the catalyst fivefold. A higher light intensity is more effective at higher catalyst concentrations that facilitate the encountering catalytic active sites and water molecules due to higher ionic diffusion rates.
- A maximum production rate of almost 0.45 mmol h^{-1} corresponding to quantum efficiency of 60% is achieved through illumination of zinc sulfide suspensions in the dual-cell under 1 sun. The quantum efficiency of hydrogen production with the zinc sulfide catalyst is increased by almost 2 times with doubled concentration of the catalyst, and it reaches an optimum point at a certain concentration. Also energy and exergy efficiencies of hydrogen production are improved up to three times, with two times more catalyst concentration. The exergy efficiency of the complete system is almost 25% more than the exergy efficiency of hydrogen production half reaction, due to oxygen production by hydroxide ion decomposition.
- Increase of light intensity from 800 W m^{-2} to $1,200 \text{ W m}^{-2}$ enhances the quantum efficiency by 2.5 times. The results indicate the rapid increase of efficiency due to light intensity increase to 1000 W m^{-2} and fewer enhancements for higher values. About 50% increase in light intensity can lead to a six fold upgrade in exergy efficiency of the complete system during illumination of the zinc sulfide suspension.
- Photo-catalytic hydrogen production with cadmium sulfide incorporates a bottle-neck effect at high catalyst concentrations, in which particle agglomeration limits the effective absorption of light. The productivity is enhanced by almost 6% due to an increase of the catalyst concentration from 1% to 1.5% w/v and it drops about 15% by the further addition of the catalyst to 2% w/v. For every 100 W m^{-2} reductions in light intensity, a decrease of almost 12% of the rate of hydrogen production is observed.
- The quantum efficiency of photo-catalytic hydrogen production using CdS is lower than ZnS, which indicates the higher effectiveness of ZnS catalyst in absorbing the photon energies within the band gap spectra. However, CdS photo-catalyst provides almost 50% higher energy and exergy efficiencies. Utilization of ZnS and CdS photo-

catalysts for simultaneous enhancement of quantum yield and exergy efficiency is achieved.

- Utilization of CdS and ZnS in a mixture suspension enhances the hydrogen production rate by almost 30% compared with ZnS performance. The concentration of cadmium sulfide in favour of enhancing the productivity of zinc sulfide is established depending on the production rate scale and photo-reactor volume.
- The hydrogen production rate of scaled-up photo-reactors can be enhanced by increasing the light intensity. Scale-up methodologies based on a length-to-diameter ratio constraint leads to lower enhancement in productivity at higher light intensities compared with length or diameter constraints. The hydrogen production rate is upgraded five-fold by a 10 times increase of light intensity as the result of light concentration or multi-directional illumination without changing the geometry and dimensions of the photo-reactor. Utilization of the parallel arrangement of small scale photo-reactors versus a large scale unit has to be determined through an economic feasibility study, since the light concentration has a significant impact on capital cost.

The electrochemical performance of the oxygen evolving reactor for the photo-catalytic water splitting system is investigated experimentally. Based on the experimental data, a predictive model was developed, and a transient model of mass and ion transport between the electrodes is presented. The following conclusions are extracted from this study:

- The electrical resistance between electrodes becomes smaller as the electrodes become closer. It is also shown that the electrolyte concentration difference between two half cells has a negative effect on OER over-potential. An approximate 50% decrease in electrode space leads to a 10% decrease in OER over-potential.
- An increase of the rate constant by one order of magnitude leads to an increase of hydroxide ion concentration by almost 2%. When the process is reaction rate controlled, a constant current can be predicted for a longer period of time.
- The cumulative effect of temperature increases in lowering the activation and ohmic over-potential can result in almost a 40% decrease of cell potential for a 50 K temperature rise. It can be concluded that the effect of the temperature increase becomes less beneficial at higher temperatures. It is also shown that, at higher temperatures, the ohmic overpotential is decreased by almost 50% for a 40 K temperature difference.

- There exists an optimum concentration for the electric potential needed for water electro-catalysis, which depends on the membrane-electrode distance and current density.
- The quantification of transient hydroxide ion diffusion inside the bulk solution reveals that the electric potential as a driving force has a linear relation with the rate of diffusion. It is also observed that an increase in current density does not significantly affect the hydroxide ion migration.
- The supramolecular complex with Ph₂phen ligand shows a higher energy efficiency by almost 3 times than the bpy ligand version at low current densities of an OER.

The electrochemical performance of a relatively low-cost and productive molybdenum-oxo catalyst is examined for the complete hydrogen production system. Also, the feasibility of a new seawater electrolysis configuration is reported by supplying a low pH solution from the outlet of the anode compartment to the cathode compartment instead of separate parallel feed of both anolyte and catholyte. The following conclusions can be drawn from the results:

- Neutralization of the hydroxide ions during the course of catalysis is found to be an effective practical way to prevent excess energy demand and also preserve the functionality of the catalyst. The cathodic over-potential is decreased by almost 15% for pH reduction from 9.5 to 7.5 at high current densities.
- Almost three times enhancement in turnover frequency is achieved as a result of the new design in refreshing the seawater and decreasing the pH from 9.5 to 7.5.
- The concentration of dissolved salt in the seawater as a charge carrier from the bulk solution to the active centre of the catalyst is a major parameter to increase the hydrogen production rate.
- Increase of the flow rate leads to mass transport improvement in the bulk and enhances the total precipitate formation, but the effect of improved mass transport can be offset by the decrease in pH at the catholyte active centres.
- The pH difference between the bulk solution and electrode surface is an important factor to increase the diffusion layer thickness. Therefore, the diffusion driving force that accelerates the total precipitate formation is hydroxide ion concentration.

The hybridization of photochemical water splitting, based on supramolecular complexes $[(\text{bpy})_2\text{Ru}(\text{dpp})\text{RhBr}_2](\text{PF}_6)_5$, using an external electric power source, is theoretically investigated. The following concluding remarks are extracted from this study:

- The maximum energy conversion efficiency is improved almost 27% over 6 volts external electric potential, and about 30% enhancement in exergy efficiency is expected.
- The hydrogen production process in the acidic medium is more efficient than a basic medium.
- The ranking of photosensitizers in terms of the degree of enhancement of energy and exergy efficiencies occurred in the following order: Cu-phthalocyanine > $[\text{Ru}(\text{bpy})_3]^{2+}$ > Eosin Y.
- Considering the overall effect of all performance improvements including auxiliary electric power, a light-driven proton pump, and efficient photo-sensitizer, the photochemical production of hydrogen is predicted to achieve about an approximate 42% increase in the energy and exergy efficiencies.
- Investigation of conversion efficiency of light together with exergy efficiency analysis for the scaled-up photo-catalytic system shows a trade-off between the profits of the parallel network of low capacity reactors and a high capacity reactor.

A scaled up photo-catalytic reactor for continuous operation under large-scale process conditions is analyzed with respect to concentrated sunlight and UV-visible lamp irradiation. The energy and exergy efficiencies of a complete catalytic water splitting system are evaluated. The photo-catalytic water splitting and a solar methanol steam reforming system are compared through exergy-environmental analysis of the complete system to evaluate the performance of these two systems in terms of exergy efficiency and CO_2 emission reduction. The following main conclusions are found:

- The energy and exergy efficiencies of the system increase more than 1.5 times by doubling the catalyst concentration, but the hydrogen production rate decreases by increasing the catalyst concentration more than 1.2 g L^{-1} .
- Higher kinetic energy of the solution increases the photochemical interactions in the vicinity of active sites and enhances the hydrogen production rate within a certain range. The optimum flow rate inside the reactor is found to be 6 L min^{-1} , since the

exergy efficiency immediately starts decreasing. The amount of CO₂ reduction by this process increases at higher flow rates.

- Radiation from the reactor surface, due to reflection and scattering, makes the largest contribution to exergy losses (50.6%), and convection heat transfer has the least effect (< 1%).
- Analysis of the light intensity variation shows that energy and exergy efficiencies increase by increasing the intensity. This effect is gradually lowered after a light intensity of 600 Wm⁻² due to light absorptivity limitations of the catalyst. At $\alpha_{nv} = 1.3$ and $\alpha_v = 0.2$, the absorbed light by the catalyst is high enough to provide an optimum hydrogen rate. Further absorptivity can lead to higher energy loss by convection and radiation.
- The energy and exergy efficiency of a complete system decreases by almost 2% per each degree increase in ambient temperature. At higher environment temperatures, the exergy loss due to heat transfer from the reactor surface area decreases, whereas chemical and physical exergy destructions are increased by almost 35% over a 15 degree temperature increase.
- Exergy efficiency and greenhouse gas emissions of the solar methanol steam reforming system increase by increasing the irradiated solar energy. Environmental pollution of the system is higher at a solar input of more than 3,000 W and the exergy efficiency becomes almost constant.
- There is an optimum for methanol feed rate where CO₂ emissions are maximized. This point is associated with the amount of solar flux that drives the conversion of methanol to hydrogen.

The exergo-economic analysis of photo-catalytic water splitting plants at different operational conditions and production scales indicates the following results:

- The hydrogen production capacity has a strong dependency on exergetic losses.
- The hydrogen prices for medium production capacity and high capacity are very close, although the capital costs are about 10 times less for lower production capacity.
- The exergo-economic study reveals the maximum hydrogen exergy price of 2.12, 0.85, and 0.47 \$ kg⁻¹ for production capacities of 1, 100, and 2000 tons day⁻¹, respectively.

8.2. Recommendations for future research

The results obtained from this dissertation also suggest several routes for future studies, as summarized below:

- Design, analysis, and fabrication of a larger scale photo-reactor based on the scale-up analysis presented in this thesis are possible continuations. Investigation of light concentration designs to enhance the productivity of a photo-reactor without manipulation of geometric dimensions is an industrial interest.
- Experimental investigation of photo-catalysts for hydrogen production involves some uncertainties related to the relation between reaction rate and steady state operation. In fact, maintaining a constant reaction rate for several hours of solar hydrogen production requires detailed engineering design of photo-reactors with reaction and regeneration beds. This assists the complete system to be self-sustained and leads to eventual commercialization of this technology.
- Photo-catalytic hydrogen production technology suffers from a lack of realistic models to predict the molecular kinetics and radiation activated steps. The complicated sequence of competing processes in photo-catalytic reactions should be mathematically modeled and verified with experiments.
- Spectrum and band gap engineering is an effective method to enhance the productivity of photo-reactors. Synthesis of photo-catalysts to provide composition of certain semiconductor alloys or utilization of dielectric mirrors and multiple photo-catalysts for specific photon energy range illumination is highly recommended.
- Since most of the available photo-catalysts are able to only absorb the light energy up to visible wavelengths, a large portion of spectrum remains unused during operation. Similar to the hybridization techniques evaluated in this thesis, implementation of energy recovery designs to maximize the benefits of inlet solar energy and exergy is possible. This research focused on electricity generation using photovoltaic cells and use of multiple catalysts to capture the rest of the spectrum. In another approach, the heating value of the rest of the spectrum can be utilized to energize thermochemical hydrogen production cycles.
- The mesh size of a photo-catalyst affects the performance of the photo-catalytic process by contributing in catalyst molecule encounter with water molecules and sacrificial reagents. Further experimental measurements are suggested to quantify the effect of catalyst particle size on hydrogen production rate.

References

- [1] Lewis N. S., Nocera D. G., Powering the planet: chemical challenges in solar energy utilization, *Proc. Natl Acad. Sci. USA*, 103(43):15729-15735, 2007.
- [2] Turner J. A., Sustainable hydrogen production, *Science*, 305(5686): 972-974, 2004.
- [3] Dincer I, Zamfirescu C., Sustainable energy and applications, New York: Springer, 2011.
- [4] Rajeshwar K., McConnell R.D., and Licht S., Solar hydrogen generation: toward a renewable energy future, New York: Springer, 2008.
- [5] U.S. Department of Energy, A national vision of America's transition to a hydrogen economy—to 2030 and beyond (Washington D.C. February 2002) p. iii, http://www1.eere.energy.gov/hydrogenandfuelcells/pdfs/vision_doc.pdf.
- [6] Plunkett J.R., United States. Energy Information Administration., International energy outlook and projections, New York: Nova Science Publishers, 2011.
- [7] Reber J.F., Meier K., Photochemical production of hydrogen with zinc sulfide suspensions, *J. Phys. Chem.*, 88: 5903-5913, 1984.
- [8] Bubler N., Reber J.F., Meier K., Photochemical production of hydrogen with cadmium sulfide suspensions, *J. Phys. Chem.*, 88: 3261-3268, 1984.
- [9] Arachchige S. M., Brown J., Brewer K. J., Photochemical hydrogen production from water using the new photocatalyst $[(\text{bpy})_2\text{Ru}(\text{dpp})]_2\text{RhBr}_2(\text{PF}_6)_5$, *Journal of Photochemistry and Photobiology A: Chemistry* 197: 13-17, 2008.
- [10] Karunadasa H. I., Chang C. J, Long J. R., A molecular molybdenum-oxo catalyst for generating hydrogen from water, *Nature*; 464(7293): 1329-1333, 2010.
- [11] Crabtree R.H., Energy production and storage: Inorganic chemical strategies for a warming world, Hoboken: Wiley, 2010.
- [12] Vayssieres L., Solar hydrogen and nanotechnology, New York: Wiley, 2010.
- [13] Delasa H., Serrano-Rosales B., Advances in chemical engineering, Volume 36: photocatalytic technologies, San Diego: Academic Press, 2009.
- [14] Akkerman I., Janssen M., Rocha J., and Wijffels R.H., Photobiological hydrogen production: photochemical efficiency and bioreactor design. *International Journal of Hydrogen Energy*, 27(11): 1195-1208, 2002.
- [15] Funk J.E., Reinstrom R.M., Energy requirements in production of hydrogen from water, *Industrial & Engineering Chemistry Process Design and Development*, 5(3): 336-342, 1967.

- [16] Naterer G.F., Suppiah S., Stolberg L., Lewis M., Wang Z., Daguppati V., Gabriel K., Dincer I., Rosen M.A., Spekkens P., Lvov S.N., Fowler F., Tremaine P., Mostagimi J., Easton E.B. Trevani L., Rizvi G., Ikeda B.M., Kaye M.H., Lu L., Pioro I., Smith W.R., Seknik E., Jiang J., Avsec J., Canada's program on nuclear hydrogen production and the thermochemical Cu-Cl cycle. *Int. J. Hydrogen Energy*, 35(20): 10905-10926, 2010.
- [17] Kudo A., Miseki Y., Heterogeneous photocatalyst materials for water splitting, *Chem. Soc. Rev.*, 38(1): 253-278, 2009.
- [18] Fujishima A, Honda K., Electrochemical photolysis of water at a semiconductor electrode, *Nature*, 238:37-38, 1972.
- [19] Ni M., Leung M.K.H., Leung D.Y.C., Sumathy K., A review and recent developments in photocatalytic water-splitting using TiO₂ for hydrogen production, *Renewable and Sustainable Energy Reviews*, 11(3): 401-425, 2007.
- [20] Matsuoka M., Kitano M., Takeuchi M., Tsujimaru K., Anpo M., Thomas J.M., Photocatalysis for new energy production: Recent advances in photocatalytic water splitting reactions for hydrogen production, *Catalysis Today*, 122(1-2): 51-61, 2007.
- [21] Archer M.D., Bolton J.R., Requirements for Ideal Performance of Photochemical and Photovoltaic solar-Energy converters, *Journal of Physical Chemistry*, 94(21): 8028-8036, 1990.
- [22] Inoue T., Watanabe T., Fujishima A., Honda K., Kohayakawa K., Suppression of surface dissolution of CDS photoanode by reducing agents, *J. Electrochem. SOC.*, 124(5): 719-722, 1977.
- [23] Serpone N., Pelizzetti E., *Photocatalysis*, New York: Wiley, 1989.
- [24] Goswami D., A review of engineering developments of aqueous phase solar photocatalytic detoxification and disinfection processes. *J. Solar Energy Eng.*, 119: 101-107, 1997.
- [25] Braham R.J., Harris A. T., Review of major design and scale-up considerations for solar photocatalytic reactors, *Ind. Eng. Chem. Res.*, 48: 8890-8905, 2009.
- [26] Roselin L. S., Rajarajeswari G. R., Selvin R., Sadasivam V., Sivasankar B., Rengaraj K., Sunlight/ZnO-mediated photocatalytic degradation of reactive red 22 using thin film flat bed flow photoreactor, *Solar Energy*, 73 (4): 281-285, 2002.
- [27] Turchi C., Ollis D., Photocatalytic degradation of organic water contaminants mechanisms involving hydroxyl radical attack, *J. Catal.*, 122: 178-192, 1990.

- [28] Freudenhammer H., Bahnemann D., Bousselmi L., Geissen S. U., Ghrabi A., Saleh F., Si-Salah A., Siemon U., Vogelpohl A., Detoxification and recycling of wastewater by solar-catalytic treatment, *Water Sci. Technol.*, 35 (4); 149-156, 1997.
- [29] Sun R.D., Nakajima A., TiO₂-coated optical fiber bundles used as a photocatalytic filter for decomposition of gaseous organic compounds, *J. Photochem. Photobiol. A: Chem.*, 136: 111-116, 2000.
- [30] Peill N., Hoffman M., Solar-powered photocatalytic fiber-optic cable reactor for waste stream remediation, *J. Solar Energy Eng.*, 119: 229-236, 1997.
- [31] Pozzo R. L., Brandi R. J., Giombi J. L., Cassano A. E., Baltans M. A., Fluidized bed photoreactors using composites of titania CVD-coated onto quartz sand as photocatalyst: Assessment of photochemical efficiency, *Chem. Eng. J.*, 118 (3): 153-159, 2007.
- [32] Jing DW., Zhang YJ., Guo LJ., Study on the synthesis of Ni doped mesoporous TiO₂ and its photocatalytic activity for hydrogen evolution in aqueous methanol solution, *Chem. Phys. Lett.*, 415:74-8, 2005.
- [33] Liu MY., You WS., Lei ZB., Zhou GH., Yang JJ., Wu GP., Water reduction and oxidation on Pt-Ru/Y₂Ta₂O₅N₂ catalyst under visible light irradiation, *Chem. Commun.*, 19: 2192-3, 2004.
- [34] Kato H., Asakura K., Kudo A., Highly efficient water splitting into H₂ and O₂ over Lanthanum-doped NaTaO₃ photocatalysts with high crystallinity and surface nanostructure, *J Am Chem Soc*, 125: 3082-9, 2003.
- [35] Yoon T.P., Ischay M.A., Juana D., Visible light photocatalysis as a greener approach to photochemical synthesis, *Nature Chemistry*, 2(7): 527-532, 2010.
- [36] Nakata K., Fujishima A., TiO₂ photocatalysis: Design and applications, *Journal of Photochemistry and Photobiology C-Photochemistry Reviews*, 13(3): 169-189, 2012.
- [37] Nowotny J., Sorrell C.C., Sheppard L.R., Bak T., Solar-hydrogen: environmentally safe fuel for the future. *International Journal of Hydrogen Energy*, 30: 521-44, 2005
- [38] U.S. Department of Energy, Hydrogen, fuel cells & infrastructure technologies program, Hydrogen production, DOE/GO-102007-2430. p. 3.1-20., Available from: <http://www.eere.energy.gov/hydrogenandfuelcells/mypp>, 2009.
- [39] Du P., Schneider J., Li F., Zhao W., Patel U., Castellano F., Eisenberg R., Bi- and Terpyridyl Platinum(II) Chloro Complexes: Molecular Catalysts for the Photogeneration of Hydrogen from Water or Simply Precursors for Colloidal Platinum?, *J. Am. Chem. Soc.*, 130: 5056-5058, 2008.

- [40] Lei P., Hedlund M., Lomoth R., Rensmo H., Johansson O., Hammarström L., The Role of Colloid Formation in the Photoinduced H₂ Production with a RuII-PdII Supramolecular Complex: A Study by GC, XPS, and TEM, *J. Am. Chem. Soc.* 130: 26–27, 2008.
- [41] Streich D., Astuti Y., Orlandi M., Schwartz L., Hammarström L., High-Turnover Photochemical Hydrogen Production Catalyzed by a Model Complex of the [FeFe] - Hydrogenase Active Site, *Chem. Eur. J.*, 16: 60-63, 2010.
- [42] Frey M., Hydrogen-activating enzymes, *ChemBioChem* 3(2-3):153-160, 2002.
- [43] Armstrong F. A., Hydrogenases: active site puzzles and progress, *Curr. Opin. Chem. Biol.* 8: 133-140, 2004.
- [44] Evans D. J., Pickett C. J., Chemistry and the hydrogenases, *Chem. Soc. Rev.* 32: 268-275, 2003.
- [45] McConnell I., Li G., Brudvig G. W., Energy conversion in natural and artificial photosynthesis, *Chem. Biol.*, 17: 434 - 447, 2010.
- [46] Barber J.M, Photosynthetic energy conversion: Natural and artificial, *Chem. Soc. Rev.* 38: 185-196, 2009.
- [47] Benniston, A. C., Harriman A., Artificial photosynthesis, *Mater. Today* 11: 26–34, 2008.
- [48] Gust D., Kramer D., Moore A., Moore T. A., Vermaas W., Engineered and artificial photosynthesis: Human ingenuity enters the game. *MRS Bull.* 33: 383-387, 2008.
- [49] Gust D., Moore T. A., Moore A. L., Mimicking photosynthetic solar energy transduction, *Acc. Chem. Res.*, 34: 40-48, 2001.
- [50] Fukuzumi S., Development of bioinspired artificial photosynthetic systems, *Phys. Chem. Chem. Phys.* 10: 2283–2297, 2008.
- [51] Wenger O. S., Long-range electron transfer in artificial systems with d(6) and d(8) metal photosensitizers, *Coord. Chem. Rev.*, 253:1439-1457, 2009.
- [52] Durr H., Bossmann S., Ruthenium polypyridine complexes, On the route to biomimetic assemblies as models for the photosynthetic reaction center, *Acc. Chem. Res.* 34: 905-917 2001.
- [53] Wasielewski M. R., Self-assembly strategies for integrating light-harvesting and charge separation in artificial photosynthetic systems, *Acc. Chem. Res.* 42: 1910-1921, 2009.
- [54] Hasobe T., Supramolecular nanoarchitectures for light energy conversion, *Phys. Chem. Chem. Phys.* 12: 44-57, 2010.
- [55] Andreiadis E. S., Chavarot-Kerlidou M., Fontecave M., Artificial Photosynthesis: From Molecular Catalysts for Light-driven Water Splitting to Photoelectrochemical Cells, *Photochemistry and Photobiology*, 87 (5): 946-964, 2011.

- [56] Masaoka S., Mukawa Y., Sakai K., Frontier orbital engineering of photo-hydrogen-evolving molecular devices: a clear relationship between the H₂-evolving activity and the energy level of the LUMO, *Dalton Trans.*, 39: 5868-5877, 2010.
- [57] Zhang P., Wang M., Li C., Li X., Dong J., Sun L., Photochemical H₂ production with noble-metal-free molecular devices comprising a porphyrin photosensitizer and a cobaloxime catalyst, *Chem. Commun.*, 46(46): 8806-8808, 2010.
- [58] Wang M., Sun L., Hydrogen Production by Noble-Metal-Free Molecular Catalysts and Related Nanomaterials, *ChemSusChem*, 3(5): 551-554, 2010.
- [59] Fihri A., Artero V., Razavet M., Baffert C., Leibl W., Fontecave M., Cobaloxime-based photocatalytic devices for hydrogen production, *Angew. Chem. Int. Ed.* 47: 564-567, 2008.
- [60] Fihri A., Artero V., Pereira A., Fontecave M., Efficient H₂-producing photocatalytic systems based on cyclometalated iridium- and tricarbonylrhenium-diimine photosensitizers and cobaloxime catalysts, *Dalton Trans.*, 39(25): 5567-5569, 2008.
- [61] Li C., Wang M., Pan J. X., Zhang P., Zhang R., Sun L.C., Photochemical hydrogen production catalyzed by polypyridyl ruthenium-cobaloxime heterobinuclear complexes with different bridges, *J. Organomet. Chem.*; 694: 2814-2819, 2009.
- [62] Brauns E., Jones S.W., Clark J.A., Molnar S.M., Kawanishi Y., Brewer K.J., Electrochemical, Spectroscopic and Spectroelectrochemical Properties of Synthetically Useful Supramolecular Light Absorbers with Mixed-Polyazine Ligands, *Inorg. Chem.* 36: 2861-2867, 1997.
- [63] Inagaki A., Akita M., Visible-light promoted bimetallic catalysis, *Coord. Chem. Rev.*, 254: 1220-1227, 2010.
- [64] Kanan M. W., Nocera D. G., Cobalt-phosphate oxygen-evolving compound, *Chem. Soc. Rev.*, 38: 13-17, 2009.
- [65] Tinker L. L., McDaniel N. D., Bernhard S., Progress towards solar-powered homogeneous water photolysis, *J. Mater. Chem.*, 19: 3328-3335, 2009.
- [66] Wang M., Na Y., Gorlov M., Sun L. C., Light-driven hydrogen production catalysed by transition metal complexes in homogeneous systems, *Dalton Trans.*, 33: 6458-6467, 2009.
- [67] Cline E. D., Adamson S. E., Bernhard S., Homogeneous Catalytic System for Photoinduced Hydrogen Production Utilizing Iridium and Rhodium Complexes, *Inorg. Chem.*, 47: 10378-10381, 2008.
- [68] Curtin P. N., Tinker L. L., Burgess C. M., Cline E. D., Bernhard S., Structure-Activity Correlations Among Iridium(III) Photosensitizers in a Robust Water-Reducing System, *Inorg. Chem.*, 48: 10498-10502, 2009.

- [69] Du P. W., Knowles K., Eisenberg R., A Homogeneous System for the Photogeneration of Hydrogen from Water Based on a Platinum(II) Terpyridyl Acetylide Chromophore and a Molecular Cobalt Catalyst, *J. Am. Chem. Soc.*, 130 (38): 12576-12577, 2008.
- [70] Arachchige S.M., Shaw R., White T. A., Shenoy V., Tsui H.M., Brewer K. J., High Turnover in a Photocatalytic System for Water Reduction to Produce Hydrogen Using a Ru, Rh,Ru Photoinitiated Electron Collector, *ChemSusChem*, 4: 1-6, 2011.
- [71] Weber M.F., Dignam M.J.J., Efficiency of Splitting Water with Semiconducting Photoelectrode, *Electrochem. Soc.*, 131 (6): 1258-1263, 1984.
- [72] Zou Z. G., Arakawa H. J., Direct water splitting into H₂ and O₂ under visible light irradiation with a new series of mixed oxide semiconductor photo-catalysts, *Photochem. Photobiol. A*, 158 (2-3): 145-162, 2003.
- [73] Abe R., Sayama K., Sugihara H., *J. Phys. Chem. B*, Development of new photocatalytic water splitting into H₂ and O₂ using two different semiconductor photocatalysts and a shuttle redox mediator IO₃⁽⁻⁾/I⁽⁻⁾, 109 (33): 16052-16061, 2005.
- [74] Fujishima A., Honda K., Electrochemical Photolysis of Water at a Semiconductor Electrode, *Nature*, 238 (5358): 37-42, 1972.
- [75] Kato H., Asakura K. K., Highly efficient water splitting into H₂ and O₂ over lanthanum-doped NaTaO₃ photocatalysts with high crystallinity and surface nanostructure, *A. J. Am. Chem. Soc.*, 125 (10): 3082-3089, 2003.
- [76] Reber J.F., Meier K., Photochemical Production of Hydrogen with Zinc-Sulfide Suspensions, *J. Phys. Chem.*, 88 (24): 5903-5913, 1984.
- [77] Maeda K., Teramura K., Lu D. L., Takata T., Saito N., Inoue Y., Domen K.J., Characterization of ruthenium oxide nanocluster as a cocatalyst with (Ga_{1-x}Zn_x)(N_{1-x}O_x) for photocatalytic overall water splitting, *Phys. Chem. B*, 110 (28): 13753-13758, 2007.
- [78] Maeda K., Teramura K., Lu D. L., Takata T., Saito N., Inoue Y., Domen K., Photocatalyst releasing hydrogen from water - Enhancing catalytic performance holds promise for hydrogen production by water splitting in sunlight, *Nature*, 440 (7082): 295-295, 2007.
- [79] Nowotny J., Sorrell C. C., Bak T., Sheppard L. R., Solar-hydrogen: Unresolved problems in solid-state science, *Sol. Energy*, 78 (5): 593-602, 2005.
- [80] Kayes B. M., Atwater H. A., Lewis N. S., Comparison of the device physics principles of planar and radial p-n junction nanorod solar cells, *J. Appl. Phys.*, 97 (11): 114302-114305, 2005.
- [81] USGS Mineral Commodity Summaries, U.S. Geological Survey, 2010.

- [82] Aharon-Shalom E., Heller A. J., Efficient P-INP (RH-H Alloy) and P-INP (RE-H Alloy) Hydrogen Evolving Photo-Cathods, *Electrochem. Soc.*, 129(12): 2865-2868, 1982.
- [83] Hamann T. W., Lewis, N. S., Control of the stability, electron-transfer kinetics, and pH-dependent energetics of Si/H₂O interfaces through methyl termination of Si(111) surfaces *J. Phys. Chem. B*, 110(45): 22291-22295, 2007.
- [84] Nakato Y., Yano H., Nishiura S., Ueda T., Tsubomura H., Hydrogen Photo-evolution At P-type Silicon Electrodes Coated With Discontinuous Metal Layers, *J. Electroanal. Chem.*, 228(1-2): 97-108, 1987.
- [85] Bookbinder D. C., Bruce J. A., Dominey R. N., Lewis, N. S., Wrighton M. S., Synthesis and Characterization OF A Photosensitive Interface for Hydrogen Generation - Chemically Modified P-Type Semiconducting Silicon Photo-Cathods, *Proc. Natl. Acad. Sci. U.S.A.*, 77: 6280-6286, 1980.
- [86] Levy-Clement C., Heller A., Bonner W.A., Parkinson B. A., Spontaneous Photoelectrolysis of HBR and HL, *J. Electrochem. Soc.*, 129(8): 1701-1706, 1982.
- [87] Valdes A., Kroes G. J., First principles study of the photo-oxidation of water on tungsten trioxide (WO₃), *J. Chem. Phys.*, 130(11): 114701-114705, 2009.
- [88] Liou F.T., Yang C. Y., Hakim, K., Levine, S. N., Polycrystalline In₂O₃ and In₂O₃/Y₂O₃ Photo-anodes, *J. Appl. Electrochem.*, 13(3): 377-383, 1983.
- [89] Veluchamy P., Minoura H., *Appl. Phys. Lett.*, Simple Electrochemical Method for The Preparation Of A Highly Oriented And Highly Photoactive Alpha-PBO Film, 65(19): 2431-2437, 1994.
- [90] Hardee K.L., Bard A.J., *Semiconductor Electrodes* .10. Photoelectrochemical Behaviour of Several Polycrystalline Metal-Oxide Electrodes In Aqueous-Solutions, *J. Electrochem. Soc.*, 124 (2): 215-219, 1977.
- [91] Messier R., White W. B., Optical-Absorbption Spectrum of Hematite, Alpha-Fe₂O₃ Near IR to UV, *J. Phys. Chem. Solids*, 41(9): 981-990, 1980.
- [92] Kennedy J. H., Frese K. W., Photo-oxidation of Water at Alpha-Fe₂O₃ Electrodes, *J. Electrochem. Soc.*, 125(5): 709-712, 1978.
- [93] Sartoretti C. J., Ulmann M., Alexander B. D., Augustynski J., Weidenkaff A., Photoelectrochemical oxidation of water at transparent ferric oxide film electrodes, *Chem. Phys. Lett.*, 376(1-2): 194-199, 2003.
- [94] Sivula K., Formal F. L., Gratzel M., WO₃-Fe(2)O(3) Photoanodes for Water Splitting: A Host Scaffold, Guest Absorber Approach, *Chem. Mater.*, 21(13): 2862-2869, 2009.

- [95] Kay A., Cesar I., Gratzel M., New benchmark for water photooxidation by nanostructured alpha-Fe₂O₃ films, *J. Am. Chem. Soc.*, 128(49): 15714-15719, 2007.
- [96] Tilley S. D., Cornuz M., Sivula K., Gratzel M., *Angew. Chem., Int. Ed.*, Light-Induced Water Splitting with Hematite: Improved Nanostructure and Iridium Oxide Catalysis, 49(36): 6405-6411, 2010.
- [97] Sivula K., Zboril R., Le Formal F., Robert R., Weidenkaff A., Tucek J., Frydrych J., Gratzel M., Photoelectrochemical Water Splitting with Mesoporous Hematite Prepared by a Solution-Based Colloidal Approach, *J. Am. Chem. Soc.*, 132(21): 7436-7441, 2010.
- [98] Ellis A. B., Kaiser S. W., Wrighton M. S., Visible Light to Electrical Energy-Conversion - Stable Cadmium-sulfide and Cadmium selenide Photoelectrodes in Aqueous-Electrolytes, *J. Am. Chem. Soc.*, 98(6): 6855-6862, 1977.
- [99] Kaneko M., Yao G. J., Efficient Water Cleavage with Visible-light by A System Mimicking Photosystem-II, *A. J. Chem. Soc., Chem. Commun.*, 18: 1338-1345, 1989.
- [100] Yamane S., Kato N., Kojima S., Imanishi A., Ogawa S., Yoshida N., Nonomura S., Nakato Y., Efficient Solar Water Splitting with a Composite "n-Si/p-CuI/n-i-p a-Si/n-p GaP/RuO(2)" Semiconductor Electrode, *J. Phys. Chem. C*, 113(32): 14575-14583, 2009.
- [101] Krstajic N. V., Jovic V. D., Gajic-Krstajic L., Jovic B. M., Antozzi A. L., Martelli G. N., Electrodeposition of Ni-Mo alloy coatings and their characterization as cathodes for hydrogen evolution in sodium hydroxide solution, *Int. J. Hydrogen Energy*, 33(14): 3676-3685, 2008.
- [102] Endoh E., Otouma H., Morimoto T., Oda Y., New Raney-nickel Composite-Coated Electrode For Hydrogen Evolution, *Int. J. Hydrogen Energy*, 12(7): 473-485, 1987.
- [103] Raj I.A.J., Nickel-based, Binary-Composite Electrocatalyst for The Cathodes in the Energy-Efficient Industrial-Production of Hydrogen From Alkaline-water Electrolytic Cells, *Mater. Sci.*, 28(16): 4375-4382, 1993.
- [104] Wendt H., Plzak V., Electrocatalytic and Thermal-Activation of Anodic Oxygen and Cathodic Hydrogen Evolution in Alkaline Water Electrolysis, *Electrochim. Acta*, 28(1): 27-34, 1983.
- [105] Conway B. E., Bai L., Determination of the Adsorption Behaviour of Overpotential-deposited Hydrogen-Atom Species in the Cathodic Hydrogen-Evolution by Analysis of Potential-Relaxation Transients, *J. Chem. Soc., Faraday Trans.*, 81: 1841-1850, 1985.
- [106] Jayalakshmi M., Kim, W. Y., Jung K. D., Joo O. S., Effect of different substrates on the electrochemical behaviour of Ni-Mo-Fe-Co-S composite film in alkali solutions, *Int. J. Electrochem., Sci.*, 3(7): 908-914, 2008.

- [107] Kodintsev I. M., Trasatti S., Note on a Method to Interttlate Inner and Outher Electrode Areas – REPLY, *Electrochim. Acta*, 39(11-12): 1803-1810, 1994.
- [108] Manoharan R., Goodenough J. B., Hydrogen Evolution on SRXNBO3-Deta (0.7-Less-Than-or-Equal-to or Less-Than-Or-Equal-to-0.95) in Acid, *J. Electrochem. Soc.*, 137(3): 910-918, 1990.
- [109] Nidola A., Schira R., New Sulfide Coatings for Hydrogen Evolution in KOH electrolysis, *Int. J. Hydrogen Energy*, 11(7): 449-458, 1987.
- [110] Ma C. A., Gan, Y. P., Chu Y. Q., Huang H., Chen D. H., Zhou B. X., Electro-oxidation behaviour of tungsten carbide electrode in different electrolytes, *Trans. Nonferrous Met. Soc. China*, 14(1): 11-20, 2004.
- [111] Walter M.G., Warren E.L., McKone J. R., Boettcher S. W., et al., Solar Water Splitting Cells, *Chem. Rev.*, 110: 6446-6473, 2010.
- [112] Zong X., Yan H., Wu G., Ma G., Wen F., Wang L., Li C., Enhancement of photocatalytic H₂ evolution on CdS by loading MoS₂ as Cocatalyst under visible light irradiation, *J. Am. Chem. Soc.*, 130(23): 7176-7177, 2008.
- [113] Maeda K., Domen K., *J. Phys. Chem. C*, New non-oxide photocatalysts designed for overall water splitting under visible light, 111(22): 7851-7861, 2007.
- [114] Chen X., Mao S., Titanium Dioxide Nanomaterials: Synthesis, Properties, Modifications, and Applications, *Chem. Rev.*, 107 (7): 2891–2959, 2007.
- [115] Kitano M., Takeuchi M., Matsuoka M., Thomas J. M., Anpo M., Photocatalytic water splitting using Pt-loaded visible light-responsive TiO(2) thin film photocatalysts *Catal. Today*, 120(2): 133-140, 2007.
- [116] Selli E., Chiarello G. L., Quartarone E., Mustarelli P., Rossetti I., Forni L., A photocatalytic water splitting device for separate hydrogen and oxygen evolution, *Chem. Commun.*, 47: 5022-5024, 2007.
- [117] Sun LC., Li L., Duan L., Xu Y., Gorlov M., A photoelectrochemical device for visible light driven water splitting by a molecular ruthenium catalyst assembled on dye-sensitized nanostructured TiO(2), *Chem. Commun.*, 46(39): 7307-7309, 2010.
- [118] Sayama K., Yoshida R., Kusama H., Okabe K., Abe Y., Arakawa H., Photocatalytic decomposition of water into H₂ and O₂ by a two-step photoexcitation reaction using a WO₃ suspension catalyst and an Fe³⁺/Fe²⁺ redox system, *Chem Phys Lett*, 277: 387-91, 1997.
- [119] Bae S.W, Ji S.M., Hong S.J., Jang J.W., Lee J.S., Photocatalytic overall water splitting with dual-bed system under visible light irradiation, *Int. J Hydrogen Energy*, 34: 3243-9, 2009.

- [120] Lo C. C., Huang C. W., Liao C., Wu J. C.S., Novel twin reactor for separate evolution of hydrogen and oxygen in photocatalytic water splitting, *Int. J. Hydrogen Energy*, 35(4): 1523-1529, 2010.
- [121] Huang C.W., Liao C.H, Wu J. CS, Liu Y.C., Chang C.L, Wu C.H, Hydrogen generation from photocatalytic water splitting over TiO₂ thin film prepared by electron beam-induced deposition, *Int. J. Hydrogen Energy*, 35 (21): 12005-12010, 2010.
- [122] Santato C., Ulmann M., Augustynski J., Photoelectrochemical properties of nanostructured tungsten trioxide films, *J. Phys. Chem. B*, 105(5): 936-940, 2001.
- [123] Khaselev O., Bansal A., Turner J.A., High-efficiency integrated multijunction photovoltaic/electrolysis systems for hydrogen production, *Int. J. Hydrogen Energy*, 26(2): 127-132, 2001.
- [124] Jahagirdar A.H., Dhere N.G., Photoelectrochemical water splitting using CuIn(1-x)Ga_xS(2)/CdS thin-film solar cells for hydrogen generation, *Solar Energy Materials & Solar Cells*, 91 (15-16):1488-1491, 2007.
- [125] Ampelli C., Passalacqua R., Perathoner S., Centi G., Nanoengineered materials for H₂ production by water photoelectrolysis, *Proceeding of The ninth International Conference on Chemical & Process Engineering*. Available from: <http://www.aidic.it/icheap9/webpapers/392Ampelli.pdf>, 2009.
- [126] Bolton J.R., Solar photoproduction of hydrogen: a review, *Solar Energy*, 57(1):37-50, 1997.
- [127] Murphy A.B., Barnes P.R.F., Randeniya L.K., Plumb I.C., Grey I.E., Horne M.D., Efficiency of solar water splitting using semiconductor electrodes, *International Journal of Hydrogen Energy*, 31: 1999-2017, 2007.
- [128] Varghese O.K., Grimes C.A., Appropriate strategies for determining the photoconversion efficiency of water photoelectrolysis cells: a review with examples using titania nanotube array photoanodes. *Solar Energy Materials and Solar Cells*, 92: 374-84, 2008.
- [129] Chandra N., Wheeler B.L., Bard A.J., Semiconductor electrodes. 59. Photocurrent efficiencies at p-indium phosphide electrodes in aqueous solutions. *Journal of Physical Chemistry*, 89: 5037-40, 1985.
- [130] Kainthla R.C., Khan S., Bockris J.O.M., The theory of electrode matching in photoelectrochemical cells for the production of hydrogen, *International Journal of Hydrogen Energy*, 12: 381-92, 1987.
- [131] Nozik A.J., P-N photoelectrolysis cell, *Applied Physics Letters*, 29:150-154, 1977.

- [132] Grimes CA., Varghese OK., Ranian S., Light, water, hydrogen - the solar generation of hydrogen by water photoelectrolysis (Section 3.3, p. 123), New York: Springer, 2008.
- [133] Minggu L.J, Daud W.R.W, Kassim M.B., An overview of photocells and photoreactors for photoelectrochemical water splitting, *International Journal of Hydrogen Energy*, 35: 5233-5244, 2010.
- [134] Lee K., Seok-Nam W., Young-Han G., Photocatalytic watersplitting in alkaline solution using redox mediator 1: parameter study, *International Journal of Hydrogen Energy*, 29:1343-7, 2004.
- [135] Seok-Nam W., Eun-Young K., Young-Han G., Photocatalytic production of oxygen in a dual bed system using a reversible redox mediator on Ir-TiO₂ catalyst, *Korean Journal of Chemical Engineering*, 25(6):1355-1357, 2008.
- [136] Directed Technologies Inc. (DTI), Technoeconomic Analysis of Photoelectrochemical (PEC) Hydrogen Production, US DOE Report, 2009.
- [137] Balaji R., Kannan B.S., Lakshmi J., An alternative approach to selective sea water oxidation for hydrogen production, *Electrochemistry Communication*, 11: 1700-1702, 2009.
- [138] Kelsall G.H., A Review of Electrodeposited Lead Dioxide Anode Preparation, N.T.I.S., Electricity Council Research Centre, Capenhurst, U.K., Rep. No. PB-277430, 1977.
- [139] Bockris J. O'M., *Energy Options*, New York: Wiley, 257-307, 1980.
- [140] Williams L. O., *Electrolysis of seawater*, New York: Plenum Press, 417-425, 1975.
- [141] Boclous J. O'M., *Energy: The Solar-Hydrogen Alternative*, New York: Wiley, 1977.
- [142] Izumiya K., Akiyama E., Habazaki H., Kumagai N., Kawashima A., Asami K., Hashimoto K. J. Surface activation of manganese oxide electrode for oxygen evolution from seawater. *Journal of Applied Electrochemistry*, 27:1362-68, 1997.
- [143] Izumiya K, Akiyama E, Habazaki H, Kumagai N, Kawashima A, Asami K, Hashimoto K., Effects of additional elements on electrocatalytic properties of thermally decomposed manganese oxide electrodes for oxygen evolution from seawater, *Material Transactions JIM*, 38: 899-905, 1997.
- [144] Izumiya K., Fujimura K., Akiyama E., Habazaki H., Kawashima A., Hashimoto K., Oxygen evolution anodes in seawater electrolysis for global CO₂ recycling. Proc. on Euromat'98, Conf. on Materials in Oceanic Environment: The Federation of European Materials Sciences, 37-45, 1998.
- [145] Fujimura K., Izumiya K., Kawashima A., Habazaki H., Hashimoto K., Anodically deposited manganese-molybdenum oxide anodes with high selectivity for evolving oxygen in electrolysis of seawater, *Journal Applied Electrochemistry*, 29: 765-771, 1999.

- [146] Fujimura K., Matsui T., Habazaki H., Kawashima A., Kumagai N., Hashimoto K., The durability of manganese-molybdenum oxide anodes for oxygen evolution in seawater electrolysis, *Electrochim Acta*, 45: 2297-2303, 2000.
- [147] Habazaki H., Matsui T., Kawashima A., Asami K., Kumagai N., Hashimoto K., Nanocrystalline manganese-molybdenum-tungsten oxide anodes for oxygen evolution in seawater electrolysis, *Scripta Mater*, 44: 1659-1662, 2001.
- [148] Abdel Ghany A.N., Kumagai N., Meguro S., Asami K., Hashimoto K., Oxygen evolution anodes composed of anodically deposited Mn-Mo-Fe oxides for seawater electrolysis, *Electrochimica Acta*, 48: 21-28, 2002.
- [149] El-Moneim A.A., Kumagai N., Asami K., Hashimoto K., Nanocrystalline manganese-molybdenum-tungsten oxide anodes for oxygen evolution in acidic seawater electrolysis, *Mat Trans.*, 46:309-316, 2005.
- [150] Kato Z., Kumagai N., Asami K., Hashimoto K., Corrosion and electrochemistry of advanced materials. In: Hashimoto K, Fujimoto S, Akiyama E, Habazaki H, Macdougall B (eds) *Electrochemical society transactions*, The Electrochemical Society, New Jersey: Pennington, 1:4-8, 2007.
- [151] Kirk D.W., Leda A.E., Precipitate Formation During Sea-water Electrolysis. *International Journal of Hydrogen Energy*, 7: 925-932, 1982.
- [152] Bennett J.E., Electrodes for Generation of Hydrogen and Oxygen From Seawater. *International Journal of Hydrogen Energy*, 5:401-408, 1980.
- [153] Deab M.S.E., Awad M.I., Mohammad A.M., Ohsaka T., Enhanced water electrolysis: Electrocatalytic generation of oxygen gas at manganese oxide nanorods modified electrodes. *Electrochem. Commun.*, 9:2082-2087, 2007.
- [154] AbdeGhany N.A., Kumasai N., Mesuro S., Asami K., Hashimoto K., Oxygen evolution anodes composed of anodically deposited Mn-Mo-Fe oxides for seawater electrolysis. *Electrochim. Acta*, 48: 21-28, 2002.
- [155] Cassano A. E., Martin C. A., Brandi R. J., Alfano O. M., Photoreactor analysis and design: Fundamentals and applications, *Industrial and Engineering Chemistry Research*, 34: 2155-2201, 1995.
- [156] Alfano O. M., Bahnemann D., Cassano A. E., Dillert, R., Goslich R., Photocatalysis in water environments using artificial and solar light, *Catalysis Today*, 58, 199-230, 2000.
- [157] Puma G. L., Yue P. L., A laminar falling film slurry photocatalytic reactor Part I-model development, *Chemical Engineering Sciences*, 53, 2993-3006, 1998.

- [158] Puma G. L., Yue P. L., A novel fountain photocatalytic reactor for water treatment and purification: Modeling and design, *Industrial Engineering Chemical Research*, 40, 5162-5169, 2001.
- [159] Puma G. L., Yue P. L., A novel fountain photocatalytic reactor: Model development and experimental validation, *Chemical Engineering Science*, 56, 2733-2744, 2001.
- [160] Puma G. L., Yue P. L., The modeling of a fountain photocatalytic reactor with a parabolic profile, *Chemical Engineering Science*, 56, 721-726, 2001.
- [161] Grigoriev S.A., Porembsky V.I., Fateev V.N., Pure hydrogen production by PEM electrolysis for hydrogen production, *Int. J Hydrogen Energy*, 31(2): 171-175, 2007.
- [162] Fateev V.N., Archakov O.V., Lyutikova E.K., Kulikova L.N., Porembsky V.I., Electrolysis of water in systems with solid polymer electrolyte, *Russ J Electrochem*, 29(4): 551-557, 1993.
- [163] Linkous C.A., Anderson H.R., Kopitzke R.W., Nelson G.L., Development of new proton exchange membrane electrolytes for water electrolysis at higher temperatures, *Int. J Hydrogen Energy*, 23(7): 525-529, 1998.
- [164] Ni M., Michael K.H. L., Dennis Y.C. L., Energy and exergy analysis of hydrogen production by a proton exchange membrane (PEM) electrolyzer plant, *Energy Conversion and Management*, 49: 2748-2756, 2008.
- [165] Gerischer H., Electrochemical photo and solar cells - principles and some experiments, *Journal of Electro-analytical Chemistry*, 58(263): 263-274, 1975.
- [166] Gerischer H., Stability of semiconductor electrodes against photo-decomposition, *Journal of Electro-analytical Chemistry*, 82:133-139, 1977.
- [167] Ngoya F. N., Thonstad J., On Mass-Transfer Effect Due To Electrolytically Evolved Gas, *Electrochimica Acta*, 30:1659-1664, 1985.
- [168] Ibl N., Mass Transfer in Electrolysis with Gas Agitation, *Chem. Ing. Technik.*, 43: 202-215, 1971.
- [169] Gijsbers H. F. M., Janssen L. J. J., Distribution Of Mass-Transfer Over A 0.5-M-Tall Hydrogen-Evolving Electrode, *J. Appl. Electro-chem.*, 19: 637-648, 1989.
- [170] Muller L., Krenz M., Rubner K., Method For Determining The Relative Solution Flow Velocity Profiles At Electrodes In Electrochemical Gas Evolution, *Electrochimica Acta*, 34: 305-308, 1989.
- [171] Gould I.R., Young R.H., Moody R.E., Farid S., Contact and Solvent-Separated Geminate Radical Ion-Pairs in Electron-Transfer Photochemistry, *J. Phys. Chem.*, 95: 2068-2072, 1991.

- [172] Eads D. D., Dismer B. G., Fleming G. R., A Subpicosecond, Subnanosecond, and Steady-state Study of Diffusion-Influenced Fluorescence Quenching, *J. Chem. Phys.*, 93: 1136-1141, 1990.
- [173] Murata S., Matsuzaki S. Y., Tachiya M., Transient Effect in Fluorescence Quenching by Electron-Transfer .2. Determination of the Rate Parameters Involved in the Marcus Arcus Equation, *J. Phys. Chem.*, 99: 5354-5359, 1995.
- [174] Dorfman R.C., Lin, Y., Fayer, M.D., Photo-induced Electron-Transfer, Geminate Recombination, And Diffusion in Liquid Solution, *J. Phys. Chem.*, 94: 8007-8011, 1990.
- [175] Burshtein A. I., Zharikov A. A., Shokhirev N. V. J., Static and Contact Electron-Transfer Within Photoinduced Geminate Ion-pairs, *Chem. Phys.*, 96: 1951-1956, 1992.
- [176] Barbara P. F., Walker G. C., Smith T. P., Vibrational-Modes and the Dynamic Solvent Effect in Electron and Proton-Transfer, *Science*, 256: 975-979, 1992.
- [177] Cortes J., Heitele, H., Jortner, J., Bandshape Analysis of the Charge-Transfer Fluorescence in Barrelene-based Electron Donor-Acceptor Compounds, *J. Phys. Chem.*, 98: 2527-2532, 1994.
- [178] Baniasadi E., Dincer I., Naterer G.F., Performance analysis of a water splitting reactor with hybrid photochemical conversion of solar energy, *Int. J. Hydrogen Energy*, 37(9): 7464-7472, 2012.
- [179] Moran M.J., Shapiro H.N., *Fundamentals of Engineering Thermodynamics*, second ed., New York: Wiley, 1992.
- [180] Bejan A., *Advanced Engineering Thermodynamics*, New York: Wiley, 1997.
- [181] Planck M., *The Theory of Heat Radiation*, Philadelphia: Blakistons, 1914.
- [182] Petela R., Exergy of undiluted thermal radiation, *Sol. Energy*, 74(6): 469-488, 2003.
- [183] Spanner D.C., *Introduction to Thermodynamics*, London: Academic Press, 1964.
- [184] Jeter S.M., Maximum conversion efficiency for the utilization of direct solar radiation. *Sol Energy*, 26 (3): 231-236, 1981.
- [185] Chagani F., Ha V., Hundt K., Ryan C.J., Solar-catalytic hydrogen reactor, Capstone project, Mechanical Engineering Department, University of Ontario Institute of Technology, April 2011.
- [186] Kinoshita K., *Electrochemical Oxygen Technology*, New York: Wiley-Interscience, 1992.
- [187] Tseung A.C.C., Jasem S., Oxygen Evolution on Semiconducting Oxides, *Electrochim. Acta*; 22(1): 31-34, 1977.

- [188] Wang X., Luo H., Zhou D.-R., Yang H., Sebastian P.J., Gamboa S.A., Oxygen catalytic evolution reaction on nickel hydroxide electrode modified by electroless cobalt coating, *Int. J. Hydrogen Energy*; 29(9): 967-972, 2004.
- [189] Palmas S., Ferrara F., Vacca A., Mascia M., Polcaro A.M., Behaviour of cobalt oxide electrodes during oxidative processes in alkaline medium, *Electrochim. Acta*, 53(2): 400-406, 2007.
- [190] Bocca C., Barbucci A., Delucchi M., Cerisola G., Oxygen evolution on Co_3O_4 and Li-doped Co_3O_4 coated electrodes in an alkaline solution, *Int. J. Hydrogen Energy*, 24(8): 21-26, 1999.
- [191] Singh R.N., Lal B., High surface area lanthanum cobaltate and its A and B sites substituted derivatives for electrocatalysis of O_2 evolution in alkaline solution, *Int. J. Hydrogen Energy*, 27(1): 45-55, 2002.
- [192] Fundo A.M., Abrantes L.M., Electrocatalytic behavior of electroless Ni-P alloys for the oxygen evolution reaction, *Russian J. Electrochem.*, 42(12): 1291-1297, 2007.
- [193] Gennero De Chialvo M.R., Chialvo A.C., Oxygen Evolution Reaction on Thick Hydrous Nickel-Oxide Electrodes, *Electrochim. Acta*, 33(6): 825-830, 1988.
- [194] Bocca C., Barbucci A., Cerisola G., The influence of surface finishing on the electrocatalytic properties of nickel for the oxygen evolution reaction (OER) in alkaline solution, *Int. J. Hydrogen Energy*, 23(4): 247-252, 1998.
- [195] Stojic D.L, Grozdic T.D, Marceta Kaninski M.P, Maksic A.D, Simic ND, Intermetallics as advanced cathode materials in hydrogen production via electrolysis, *Int. J Hydrogen Energy*, 31(7):841-6, 2007.
- [196] Kim S., Koratkar N., Karabacak T., Lu T-M, Water electrolysis activated by Ru nanorod array electrodes, *Appl Phys Lett*, 88(26): 2631061-2631063, 2007.
- [197] Kline S.J., McClintock F., Describing uncertainties in single-sample experiments, *Mech. Eng.* 75: 3-8, 1953.
- [198] Abernethy R., Benedict R., Dowdell R., ASME measurement uncertainty, *Trans ASME: J. Fluids Eng.*, 107: 161-164, 1985.
- [199] Malato S., Blanco J., Campos A., Caceres J, Guillard C, Herrmann JM., Effect of operating parameters on the testing of new industrial titania catalysts at solar pilot plant scale. *Appl Catal B*, 42(4):349-357, 2003.
- [200] Liu Q., Hong H., Yuan J., Jin H., Cai R., Experimental investigation of hydrogen production integrated methanol steam reforming with middle-temperature solar thermal energy, *Applied Energy*, 86: 155-162, 2009.

- [201] Puma G.L., Yue P. L., A laminar falling film slurry photocatalytic reactor Part I-model development, *Chemical Engineering Sciences*, 53, 2993-3006, 1998.
- [202] Bruce Nauman E., *Chemical reactor design, optimization, and scale-up: 2nd ed.*, New York: Wiley, 2008.
- [203] Bisio A., Kabal R.L., *Scale up of Chemical Processes*, New York: Wiley, 1985.
- [204] Norwood K.W., Metzner A.B., Flow Patterns and Mixing Rates in Agitated Vessels, *AIChE J.*, 6(3): 432-437, 1960.
- [205] Zamfirescu C., Naterer G.F., Dincer I., Solar Light-Based Hydrogen Production Systems, In *Encyclopedia of Energy Engineering and Technology*, New York: Taylor and Francis, 1-22, 2012.
- [206] Yan H., Yang J., Ma G., Wu G., Zong X., Lei Z., Shi J., Visible-light-driven hydrogen production with extremely high quantum efficiency on Pt-PdS/CdS photocatalyst, *Journal of Catalysis* 266:165-168, 2009.
- [207] Klan P., Wirz J., *Photochemistry of organic compounds; from concepts to practice*, New York: Wiley, 2009.
- [208] Zamfirescu C., Dincer I., Naterer G.F., Molecular Charge Transfer Simulation and Quantum Efficiency of a Photochemical Reactor for Solar Hydrogen Production, *International Journal of Hydrogen Energy*, 37: 9537-9549, 2012.
- [209] Verhaert I., De Paepe M., Mulder G., Thermodynamic model for an alkaline fuel cell, *J. Power Sources*, 193:233, 2009.
- [210] Zhang H., Lin G., Chen J., The performance analysis and multi-objective optimization of a typical alkaline fuel cell, *Energy*, 36(7): 4327-4332, 2011.
- [211] O'Hayre R., Cha S-W, Colella W., Prinz F.B., *Fuel cells fundamentals*. New York: Wiley, 2007.
- [212] Aal-saleh M. A., Gultekin S., Al-zakr A. S., Celiker H., Performance of Porous Nickel Electrode for Alkaline H₂/O₂ Fuel Cell, *Int. J. Hydrogen Energy*, 19 (8): 713-718, 1994.
- [213] Jorne J., Roayaie E., Experimental Studies of Flow-Through Porous-Graphite Chlorine Electrode, *J. of The Electrochemical Society*, 133(4): 696-701, 1987.
- [214] Duso A.B., Chen D.D.Y., Proton and Hydroxide Ion Mobility in Capillary Electrophoresis, *Anal. Chem.*, 74: 2938-2942, 2002.
- [215] Gilliam R. J., Graydon J. W., Kirk D. W., Thorpe S. J., A review of specific conductivities of potassium hydroxide solutions for various concentrations and temperatures, *Int. J. Hydrogen Energy*, 32(3): 359, 2007.

- [216] Andrade L., Lopes T., Ribeiro H. A., Mendes A., Transient phenomenological modeling of photoelectrochemical cells for water splitting - Application to undoped hematite electrodes, *Int. J. Hydrogen Energy*, 36 (1): 175-188, 2011.
- [217] Kortum G., Bockris J., *Textbook of Electrochemistry*, Vol. 1, Chapter VIII. Amsterdam: Elsevier, 1951.
- [218] Shaw P., Reiss L. P., Hanratty T. J., An Experimental Study of the Unsteady Nature of the Viscous Sublayer, *A.I.Ch.E. JI*, 9: 154-160, 1963.
- [219] Schatz G., Untersuchung des Stoffaustausch-Anlaufgebietes in einem Rohr bei vollausgebildeter hydrodynamischer strömung mit einer elektrochemischen Methode, *Int. J. Heat Mass Transfer*, 7: 1077-1082, 1964.
- [220] Dincer I., Rosen M. A., *Exergy: energy, environment, and sustainable development*, 1st Ed., Oxford: Elsevier, 2007.
- [221] Kondratiew K. Ya., *Radiation energy of the Sun*, GIMIS, 1954.
- [222] Gueymard, C.A., The sun's total and spectral irradiance for solar energy applications and solar radiation models, *Solar Energy* 76 (4): 423-453, 2004.
- [223] Rosen M.A., Dincer I., Kanoglu M., Role of exergy in increasing efficiency and sustainability and reducing environmental impact, *Energy Policy* 36 (1): 128-137, 2008.
- [224] Dincer I., Naterer G.F., Assessment of exergy efficiency and Sustainability Index of an air water heat pump, *International Journal of Exergy*, 7 (1): 37-50, 2010.
- [225] Kwak H.Y., Kim D.J., Jeon J.S., Exergetic and thermoeconomic analyses of power plants, *Energy* 28 (4): 343-360, 2003.
- [226] Michigan Department of Environmental Quality Remediation and Redevelopment Division Financial Assurance Mechanisms (DOE), Present Worth analysis, Guidance document, 2003.
- [227] Zamfirescu C., Dincer I., Stern M., Wagar W. R., Exergetic, environmental and economic analyses of small-capacity concentrated solar-driven heat engines for power and heat cogeneration, *International Journal of Energy Research*, 36:397-408, 2012.
- [228] Rosen M.A., *The Relation Between Thermodynamic Losses and Capital Costs for a Modern Coal*, American Society of Mechanical Engineers, New York, 21: 69-78, 1990.
- [229] Ozgener L., Hepbasli A., Dincer I., Rosen M.A., Exergo-economic analysis of geothermal district heating systems: A case study, *Applied Thermal Engineering*, 27(8-9): 1303-1310, 2007.
- [230] Tokumura M., Znad H.T., Kawase Y., Modeling of an external light irradiation slurry photoreactor: UV light or sunlight-photoassisted Fenton discoloration of azo-dye Orange II

with natural mineral tourmaline powder, *Chemical Engineering Science*, 61: 6361-6371, 2006.

[231] Bongenaar-Schlenter B.E., Janssen L.J.J., Van Stralen S.J.D., Barendrecht E., The Effect of the Gas Void Distribution on the Ohmic Resistance During Water-Electrolytes, *J. Appl. Electrochem.*, 15: 537-48, 1985.

[232] Zamfirescu C., Dincer I., Naterer G.F., Analysis of a photochemical water splitting reactor with supramolecular catalysts and a proton exchange membrane, *International Journal of Hydrogen Energy*, 36 (17): 11273-11281, 2011.

[233] Senftle F.E., Grant J.R., Senftle F.P., Low-voltage DC/AC electrolysis of water using porous graphite electrodes, *Electrochimica Acta*. 55(18): 5148-5153, 2010.

[234] Bagotsky V., *Fundamentals of Electrochemistry*, 2nd Ed. (Chapter 17), New York: Wiley-Interscience, 2007.

[235] Ghosh P.K., Smirnov A. Yu., Nori F., Modeling light-driven proton pumps in artificial photosynthetic reaction centers, *The Journal of Chemical Physics* 131 (3), 035102-035108, 2009.

[236] Paluselli D., Marsen B., Miller E. L., Rocheleau R. E., Nitrogen Doping of Reactively Sputtered Tungsten Oxide Films, *Electrochemical and Solid-State Letters*, 8 (11): G301-G303, 2005.

[237] Cervera-March S., Smotk E. S., A Photoelectrode Array System for Hydrogen Production From Solar Water Splitting, *Int. J. Hydrogen Energy* 16 (4): 243-247, 1991.

[238] Smotkin E.S., Cerveramarch S., Bard A.J., Campion A., Fox M.A., Mallouk T, Webber S.E., Bipolar CDSE/COS Semiconductor Photoelectrode Arrays for Unassisted Photolytic Water Splitting, *Journal of Physical Chemistry*, 91(1): 6-8, 1987.

[239] Khan S., Akikusa J., Photoelectrochemical splitting of water at nano-crystalline n-Fe₂O₃ thin-film electrodes, *Journal of Physical Chemistry* 103(34): 7184-7189, 1999.

[240] Leygraf C., Hendewerk M., Somorjai G.A., Photo-dissociation of Water by PARA-Type and Normal-Type Polycrystalline Iron-Oxides by Using Visible-Light (Less-Than-or-Equal-to 2.7 eV) in the Absence of External Potential, *Proceedings of the National Academy of Sciences of the United States of America-Physical Sciences*, 79 (18): 5739-5741, 1982.

[241] Bird R.B., Stewart W.E., Lightfoot E.N., *Transport phenomena*, 2nd Ed, New York: Wiley, 2007.

[242] Jiang N., Meng, H. M., Song L. J., Yu H.Y., Study on Ni-Fe-C cathode for hydrogen evolution from seawater electrolysis, *Int. J. Hydrogen Energy*, 35(15): 8056-8062, 2010.

- [243] Abdel-aal H. K., Hussein I. A., Parametric study for saline water electrolysis: Part I-hydrogen production, *Int. J. Hydrogen Energy*, 18:485-489, 1993.
- [244] Jing D., Guo L., Zhao L., Zhang X., Liu H., Li M., Efficient solar hydrogen production by photocatalytic water splitting: From fundamental study to pilot demonstration, *Int. J. Hydrogen Energy*, 35(13): 7087-7097, 2010.
- [245] Lasher S., Marion M., Kromer M., An Assessment of Renewable-Hydrogen Costs, Infrastructure, and Resource Constraints, *Proceeding of Clean Technology and Sustainable Industries Conference and Trade Show*, 319-322, 2008.
- [246] Dincer I., Rosen M.A., Sustainability aspects of hydrogen and fuel cell systems, *Energy for Sustainable Development*, 15(2): 137-146, 2011.
- [247] Edenhofer O., Madrugá R.P., Sokoma Y., Renewable energy sources and climate change mitigation, *Special report of the Intergovernmental Panel of Climate Change*, Cambridge: Cambridge University Press, 2012.
- [248] U.S. Department of Energy, Oxygen Production, Advanced Carbon Dioxide Capture R&D Program: Technology Update, May 2011.
- [249] Licht S., Wang B., Mukerji S., Soga T., Umeno M., Tributsch H., Over 18% solar energy conversion to generation of hydrogen fuel; theory and experiment for efficient solar water splitting, *Int. J Hydrogen Energy*; 26 (7):653-659, 2001.
- [250] Press W.H., Teukolsky S.A., Vetterling W.T., Flannery B.P., *Numerical Recipes in FORTRAN: The Art of Scientific Computing (second ed.)*, New York: Cambridge University Press, 1992.

Appendix I

Optimization

In this research, the experiments and post-processing the data are followed by parametric optimization and data fitting through a systematic procedure. Assuming there is a function $F(p_1, p_2, \dots)$ called the objective function that depends on the parameters p_1, p_2 , etc., the goal is to determine the best values for the parameters (best in the sense that these values will maximize or minimize F).

One of the methods to implement this is the simplex method of Nelder and Mead, based on a subroutine that is given by Press et al. [250]. Other sources and codes for other languages are available in versions of commercial packages (e.g., MATLAB). Some more efficient but more complicated, gradient-based methods are available from the same sources.

Curve fitting by optimization is one of the useful toolboxes in MATLAB software that will be utilized during the course of this research. This toolbar can be used to fit an optional function to some data. The sub-routine code uses the `fminsearch` solver to minimize the sum of squares of errors between the data and selected function for varying parameters. The following shows an example of a data fitting procedure to an exponential function of the form $Ae^{-\lambda t}$.

- a) Accepts vectors corresponding to the x- and y-coordinates of the data
- b) Returns the parameters of the exponential function that best fits the data using the following MATLAB code.

```
-----  
function [estimates, model] = fitcurvedemo(xdata, ydata)  
% Call fminsearch with a random starting point.  
start_point = rand(1, 2);  
model = @expfun;  
estimates = fminsearch(model, start_point);  
% expfun accepts curve parameters as inputs, and outputs sse, the sum of squares error  
for %A*exp(-lambda*xdata)-ydata,  
% and the FittedCurve. FMINSEARCH only needs sse, but we want to plot the FittedCurve  
at %the end.  
function [sse, FittedCurve] = expfun(params)  
A = params(1);
```

```
lambda = params(2);
FittedCurve = A .* exp(-lambda * xdata);
ErrorVector = FittedCurve - ydata;
sse = sum(ErrorVector .^ 2);
end
end
```

The file calls the function `fminsearch`, which finds parameters `A` and `lambda` that minimize the sum of squares of the differences between the data and the exponential function $A \times \exp(-\lambda x)$. The nested function *expfun* computes the sum of squares.

Appendix II

Sample codes for simulation of hydrogen and oxygen evolution process

```
.....  
% This m file (MATLAB code) evaluate the over-potentials  
associated with%oxygen evolving reactor. Energy and exergy  
efficiencies are%also calculated.  
.....  
F=96485;  
R=8.314;  
alpha=0.52;  
M=12;  
T=300;  
k=(-2.041*M (0.0028*(M^2)))+(0.005332*M*T)+  
(207.2*M/T)+(0.001043*(M^3))-(0.0000003*(M^2)*(T^2));  
j0Ni=6e-6;  
j0G=4.6e-5;  
jLNi=0.400;  
jLG=0.150;  
tele1=1;  
j=linspace(0.005,0.05,20);  
V_act=R*T/2/F/alpha*log(j/j0Ni);  
V_con=R*T/2/F/alpha*log(jLNi./(jLNi-j));  
V_ohm=j*5/k;  
V_actual=1./2./F*((237200*0.41./1.23)+(R*T./alpha*log(j./j0Ni)  
)+(R*T/alpha*log(jLNi./(jLNi-j)))+(j*2*F/k*5));  
eta=V_actual-0.41;  
plot (j,V_con)  
Pelec=j.*20.*V_actual;  
eta_energy=100*2400e-  
6/20/3600*286000./(Pelec+(1240/470*1.602e-19*7.27e19/60));  
eta_exergy=1.5*0.08988/2/3600*286000./(Pelec+(518*0.024));
```

```

.....
%This m file (MATLAB code) solve the continuity equation for
transient%diffusion of hydroxide ions in oxygen production
reactor.
.....

```

```

function [pl,ql,pr,qr] = pdexlbc(xl,nl,xr,nr,t)

```

```

pr=0;

```

```

qr=1;

```

```

j=0.25;

```

```

E=3/10;

```

```

pl=nl-(j*0.95/96485/1/20.5e-4./E);

```

```

ql=0;

```

```

function n0 = pdexlic(x)

```

```

n0=0.001;

```

```

function [c,f,s] = pdexlpde(x,t,n,DnDx)

```

```

c=19011.406;

```

```

f=DnDx;

```

```

T=300;

```

```

E=3/10;

```

```

s=20.5e-4/5.26e-5*E;

```

```

.....
%This m file (MATLAB code) simulates the photo-catalytic
hydrogen production%process by considering all intermediate
steps of forming%hydrogen molecule and quantum efficiency.
.....

```

```

phi=0.020;

```

```

k_GS=0.035;

```

```

k_enc=25;

```

```

ndotH2d=1.96e-9;

```

```

ndotph=7.34E-5;

```

```

V=0.0002;

```

```

CH2=ndotH2d/V;

```

```

gama=7.96e-2;
deltaro=991;
d_bubb=0.035e-3;
beta=deltaro*9.81*((d_bubb/2)^2)/gama;
nu=2/0.08988/1000;
ta_bubb=0.004;
C=((1/phi)-1-k_GS)/k_enc/CH2)-1;
C_bubb=C*CH2;
s=solve('2*x/ndotph=(1/(1+k_GS+(k_enc*((ndotH2d/V)+90+(x/V))))
)')

```

```

.....
%This EES code simulates the radiative heat transfer and
%catalyst performance of a large scale continuous
flow%photoreactor for water splitting.
.....

```

```

Js=1.3678 [kW/m2];
Jv=0.5446 [kW/m2];
Bs=1.2835 [kW/m2];
Bv=0.5155 [kW/m2];
Ss=0.307e-3 [kW/K/m2];
Sv=0.113e-3 [kW/K/m2];
Radius=11 [mm];
V=25.6 [cm/s];
H2=1.25 [L/h];
gama=0.2;

VH2Oin=Radius*Radius*3.14/4*V*3600*0.00001;
nH2=102000*H2*0.001/8.314/303/3600;
nO2=nH2/2;
nH2Oin=VH2Oin*1000/18.05/3600;
nH2Oout=(VH2Oin-(nH2*18*3600))*1000/18.05/3600;
alphav=0.31;
alphaL=1.8;

```

```

"Exergy of solar irradiation"
{lamda[1]=470;
K_lamba[1]=100;
L_lamda[1]=2.998e8*138.03e-
28/(lamda[1]^4)*((1+(lamda[1]^5*K_lamba[1]/5.95e-
20*ln(1+(lamda[1]^5*K_lamba[1]/5.95e-20)))));
b_s=4.329e-5*pi*((3e-
12*(T0^4))+SUM(K_lamba[j]*lamda[j],j=1,1)-
(T0*SUM(L_lamda[j]*lamda[j],j=1,1)));}

```

```

"Natural convection loss"
Gr=g*B*(Ts-Tinf)*(L^3)/nu;
g=9.81;
{T[2]=ConvertTemp(C,K,30);}
Ts=ConvertTemp(C,K,35);
Tinf=ConvertTemp(C,K,20);
T[1]=Tinf+5;
L=0.5;
Tf=(Ts+Tinf)/2;
B=1/Tf;
mu=Viscosity('Air', T=Tf);
ro=density('Air',T=Tf, P=101.325);
nu=mu/ro;
Pr=Prandtl('air', T=Tf);
Ra=Gr*Pr;
Nusselt=0.1*Ra^(1/3);
Nusselt=h*L/k;
k=conductivity('Air', T=Tf);
D=0.011;
A=pi*D*L;
Qconv=h*A*(T[2]-T[1]);
Qconv=0.1*Js*A;

```

delbconv=Tinf*Qconv*((1/Tinf)-1/Tf);

"Radiation loss"

Qrad=0.8*5.667e-8*A*((Ts^4)-(Tinf^4));

{delBrad=Tinf*Qrad*((1/Tinf)-1/Ts);}

{delBrad=Tinf*((0.9*5.667e-8*A*((Ts^3)-(Tinf^3)))-
((Qrad+Qconv)/((A*alphav*Jv)+(A*gama*alphaL*(Js-
Jv))))*((A*alphav*Sv)+(A*gama*alphaL*(Ss-Sv))))};

delBrad=0.8/3*5.667e-8*A*((3*(Ts^4))+(Tinf^4)-
(4*Tinf*(Ts^3)));

"Chemical loss"

delBch=(nH2/1000*(ENTHALPY('hydrogen',T=T[2],P=101.325)-
(Tinf*ENTROPY('hydrogen',T=T[2],P=101.325))))+(nO2/1000*(ENTHA
LPY('oxygen',T=T[2],P=101.325)-
(Tinf*ENTROPY('oxygen',T=T[2],P=101.325))))+(nH2Oout/1000*(ENT
HALPY('water',T=T[2],P=101.325)-
(Tinf*ENTROPY('water',T=T[2],P=101.325))))-
(nH2Oin/1000*(ENTHALPY('water',T=T[1],P=101.325)-
(Tinf*ENTROPY('water',T=T[1],P=101.325))));

"Physical loss"

delBph=(nH2Oout/1000*(ENTHALPY('water',T=T[2],P=101.325)-
(Tinf*ENTROPY('water',T=T[2],P=101.325))))-
(nH2Oin/1000*(ENTHALPY('water',T=T[1],P=107.325)-
(Tinf*ENTROPY('water',T=T[1],P=107.325))));

"Input Exergy"

Exin=(A*alphav*Bv)+(A*gama*alphaL*(Bs-
Bv))+(nH2Oin/1000*((ENTHALPY('water',T=T[2],P=101.325)-
ENTHALPY('water',T=T[1],P=107.325))-
(Tinf*(ENTROPY('water',T=T[2],P=101.325)-

```
ENTROPY('water',T=T[1],P=107.325)))))+((V/100)^2)/2)+
(VH2Oin/1000/3600*5/0.85);
```

```
{Exin=(A*alphav*Bv)+(A*gama*alphaL*(Bs-
Bv)))+(nH2Oin/1000*((ENTHALPY('water',T=T[1],P=107.325)-
ENTHALPY('water',T=Tinf,P=101.325))-
(Tinf*(ENTROPY('water',T=T[1],P=107.325)-
ENTROPY('water',T=Tinf,P=101.325)))))+((V/100)^2)/2)+
(VH2Oin/1000/3600*5/0.85);}
```

"Input Energy"

```
Ein=(A*alphav*Jv)+(A*gama*alphaL*(Js-Jv))
+(nH2Oin/1000*(ENTHALPY('water',T=T[2],P=101.325)-
ENTHALPY('water',T=T[1],P=107.325)))+(VH2Oin/1000/3600*5/0.85;
```

"Exergy efficiency"

```
{eta_ex=(nH2/1000*((ENTHALPY('hydrogen',T=T[2],P=101.325)-
ENTHALPY('hydrogen',T=Tinf,P=101.325))-
(Tinf*(ENTROPY('hydrogen',T=T[2],P=101.325)-
ENTROPY('hydrogen',T=Tinf,P=101.325)))))/Exin;}
eta_ex=nH2*237/Exin;
```

"Energy Efficiency"

```
eta_en=nH2*286/Ein;
```